T2R2 東京科学大学 リサーチリポジトリ
Science Tokyo Research Repository

論文 / 著書情報
Article / Book Information

題目(和文)	II 型超新星爆発のHe層とH層で合成される軽元素
Title(English)	Light elements synthesized in the He-layer and the H-rich envelope of type II supernovae
著者(和文)	吉田敬
Author(English)	
出典(和文)	学位:博士(理学), 学位授与機関:東京工業大学, 報告番号:甲第4289号, 授与年月日:2000年3月26日, 学位の種別:課程博士, 審査員:中澤 清
Citation(English)	Degree:Doctor (Science), Conferring organization: Tokyo Institute of Technology, Report number:甲第4289号, Conferred date:2000/3/26, Degree Type:Course doctor, Examiner:
学位種別(和文)	博士論文
Type(English)	Doctoral Thesis

Powered by T2R2 (Science Tokyo Research Repository)

Light Elements Synthesized in the He-layer and the H-rich Envelope of Type II Supernovae

Takashi YOSHIDA

Department of Applied Physics (Earth and Planetary Sciences)
Tokyo Institute of Technology
Meguro-ku, Tokyo 152-8551, Japan

(Doctoral Thesis)

March 2000

Abstract

The explosive nucleosynthesis of the light elements, i.e., the CNO-elements and the X-elements (Li, Be, and B), in the He-layer and the H-rich envelope of Type II supernovae was numerically investigated aimed at the establishment of a suitable manner for identifying presolar grains originated from supernovae. The ranges of the abundances and the elemental ratios of the light elements produced in the supernovae were evaluated by changing the neutrino emission model, the initial chemical compositions, and the mass of progenitors. Further, the influence of the nuclear reprocessing after the mixing on the light element synthesis was investigated. Our nuclear reaction network contains 52 species of nuclei extended to ^{23}Mg. Neutrino induced nuclear reactions are taken into account. The explosion model of the supernova explosion is used a spherically symmetrical strong shock propagation model in a medium with the power law density profile. In this thesis, about half of Sections 2 and 3 and most of Sections 4 and 5 are reprinted from "*Light Elements Synthesized in the He-layer and the H-rich Envelope of a Type II Supernova -Influence of the Adopted Neutrino Emission Model-*" (Yoshida, Emori, and Nakazawa 2000) and Section 6 is reprinted from "*Light Elements Synthesized in the He-layer and the H-rich Envelope of a Type II Supernova, II -Influence of Initial Chemical Compositions-*" (Yoshida, Nakazawa, and Emori 1999).

Appreciable amounts of ^{7}Li, ^{10}B, and ^{11}B are produced in the He-layer and the inner H-rich envelope (except ^{10}B) of supernova ejecta. The neutrino emission model and the stellar mass affect their amounts within several orders of magnitude. However, the ^{11}B/^{7}Li ratio is confined within a factor of 180. The amounts of ^{6}Li and ^{9}Be produced in the supernovae are very small: the ^{6}Li/^{7}Li and ^{9}Be/^{7}Li ratios are smaller than 4×10^{-5} and 4×10^{-3}, respectively. In the CNO-elements, ^{13}C, ^{14}N, ^{15}N, and ^{17}O are synthesized in the convective He-layer. Their abundances are affected by the neutrino emission model within

a factor of 10 or so. The amounts of the CNO-elements in the radiative He-layer and the H-rich envelope do not change in the supernova explosions, so that they depends on the initial chemical compositions. The X-elements suffer from the nuclear reprocessing after large scale mixing but the CNO-elements do not. We propose the following isotopic/elemental ratios of the light elements useful for identifying supernova originated presolar grains: ^{6}Li/^{7}Li, ^{9}Be/^{7}Li, ^{11}B/^{7}Li, ^{12}C/^{13}C, ^{14}N/^{15}N, and ^{16}O/^{17}O. Their varieties are within the regions shown in this study by the use of diagrams between two elemental ratios: ^{6}Li/^{16}O-^{7}Li/^{16}O, ^{9}Be/^{16}O-^{7}Li/^{16}O, ^{11}B/^{7}Li-^{12}C/^{13}C, ^{14}N/^{15}N-^{12}C/^{13}C, and ^{16}O/^{17}O-^{12}C/^{13}C.

Contents

1. Introduction

1.1. Presolar grains

In the last decade, remarkable progress of chemical/isotopic analyses (e.g., the Secondary Ion Mass Spectrometry, SIMS), have made it possible to determine precisely chemical/isotopic compositions in a very tiny area of a cosmochemical sample (e.g., Mckeegan *et al.* 1985; Hoppe *et al.* 1995a). By the use of such superior tools, many authors have tried to determine chemical compositions of small components in meteorites (such as μm-size refractory grains) and found a lot of μm-size grains of which isotopic ratios are quite different from the solar-system composition. Such exotic grains are called presolar grains (Zinner 1998). A large isotopic heterogeneity of presolar grains would be kept so far from their birth and would reflect physical and chemical birth conditions.

Evidence for presolar grains was firstly provided by large isotopic anomalies in carbon (Swart *et al.* 1983). Since the measurement of the chemical compositions of μm-size isolated grains was established by the use of SIMS (Zinner *et al.* 1989), single presolar grains were found in SiC (Zinner *et al.* 1989), graphite (Amari *et al.* 1990), corundum (Hutcheon *et al.* 1994), and so on (reviewed in Zinner 1998). By the discovery of presolar grains, our new interest is aroused: where were they born? how were the isotopic heterogeneities brought about? As the origin of presolar grains, two possibilities are proposed until now; one is the supernova origin and the other is the AGB (asymptotic giant branch) star origin.

Presolar grains originated from supernovae are identified by comparing their isotopic ratios with those predicted by supernova nucleosynthesis theory. Most of the identifications have been conducted in Washington Univ. group (reviewed in Zinner 1998). Until now, some presolar grains have been certainly identified as supernova origin on the basis of their ^{15}N excesses, large $^{26}Al/^{27}Al$ ratios, ^{28}Si excesses (e.g., Amari *et al.* 1992, 1995a, 1996a; Nittler *et al.* 1995, 1996), ^{44}Ca excesses (Amari *et al.* 1992; Nittler *et al.* 1996), ^{48}Ti excesses (Amari *et al.* 1992, 1995a, 1996a; Nittler *et al.* 1996), and so on. However, some of these grains also show silicon or nitrogen isotopic ratios beyond the range of the ratios predicted by the supernova nucleosynthesis theory (Travaglio *et al.* 1999) (identifications of supernova originated presolar grains is presented in detail in Section 1.3). Since these unsolved problems still remain, we can say nothing about their origin definitely. This is due, partly, to the facts that we have still a small number of sample grains and that isotopic species, which we can analyze precisely, are limited owing to the smallness of sample particles. However, the most significant reason is that we have not an enough and a general knowledge on the nucleosynthesis in the supernova explosion. Thus, it is very important to investigate extensively the nucleosynthesis in the supernova explosion and to grasp a general behavior of isotopic variation of the supernova ejecta.

1.2. Theoretical studies of supernova nucleosynthesis

Since Arnett (1969), many efforts have been dedicated to studying the nucleosynthesis in supernovae on the basis of the stellar evolution of massive stars as well as the model of hydrodynamical explosion. Weaver *et al.* (1978) first calculated the evolution of entire 15 $M_\odot$ and 25 $M_\odot$ stars (where $M_\odot$ denotes the solar mass; 1 $M_\odot = 1.989 \times 10^{33}$ g) from the zero-age main sequence stage to the stage of the iron core collapse. Weaver and Woosley (1980) demonstrated the nucleosynthesis during supernova explosions starting from the presupernova models of Weaver *et al.* (1978). Their nuclear reaction network consists of 39 species of nuclei from ^{1}H to ^{56}Ni and they obtained the final composition of α-elements, like ^{16}O and ^{28}Si, in the supernovae.

Discovery of SN 1987A in Large Magellanic Cloud (e.g., Bethe 1990) has been given a lot of information about supernova explosions through observations with wide wave bands including X-rays and γ-rays. Progenitor's radius, the explosion energy, and the stellar mass were precisely deduced on the basis of the observations of the early light curve (Shigeyama *et al.* 1987, 1988; Woosley *et al.* 1987; Woosley 1988). Furthermore, Hashimoto *et al.* (1989) first presented the abundances of isotopes lighter than Ge in the ejecta of SN 1987A by calculating the explosive nucleosynthesis by the use of the hydrodynamical model of a 6 $M_\odot$ helium star. Thielemann *et al.* (1990) recalculated the explosive nucleosynthesis of elements lighter than Ge in SN 1987A using the more extensive nuclear reaction network containing 300 species of nuclei. They compared their final composition of synthesized elements with the solar-system composition and evaluated the mass of the neutron star.

Woosley *et al.* (1990) calculated the explosive nucleosynthesis using a nuclear reaction network containing interactions between high energy neutrinos emitted from the collapsed core and nuclei in the surrounding layers. The neutrino induced nucleosynthesis, which is called generically the ν-process, was first suggested by Domogatskii *et al.* (1977) and Woosley *et al.* (1990) employed the ν-process to many species of nuclei. Since a huge number ($\sim 10^{57}$) of high energy (~ 10 MeV) neutrinos is emitted from the collapsed core, the ν-process plays an important role on the nucleosynthesis in the supernova explosions despite small cross sections of the neutrino interactions. Woosley *et al.* (1990) constructed the neutrino emission model on the basis of observation of SN 1987A and showed that some nuclei, e.g., ^{7}Li, ^{11}B, and ^{19}F, are produced through the ν-process. The ν-process is a strong candidate of the X-element synthesis other than the spallation by the galactic cosmic rays.

In 1995 and 1996, two kinds of extensive studies of supernova nucleosynthesis were conducted: Woosley and Weaver (1995) and Thielemann *et al.* (1996). Woosley and Weaver (1995) investigated the explosive nucleosynthesis of 78 different supernova models with masses ranging from 11 to 40 $M_\odot$ and with metallicities ranging from 0 to the solar metallicity. The final abundances of isotopes lighter than Zn are shown and main synthetic processes of each element are discussed. They applied their results to the model of the galactic chemical evolution (Timmes *et al.* 1995). Thielemann *et al.* (1996) also calculated explosive nucleosynthesis of isotopes lighter than Ge in supernovae of which progenitors are 3.3, 4.0, and 8.0 $M_\odot$ helium stars. In their study, the mass of neutron star remaining after the explosion as well as the time when the explosion occurs after the core collapse were regarded as parameters since precise values of the parameters are poorly understood. They first evaluated the composition of iron group nuclei in the innermost region of the ejecta and compared their results with the abundances found from specific supernova observations (e.g., SN 1987A, 1993J) and supernova remnants (e.g., G292.0+18, N132D). As a result, they obtained probable values of the neutron star masses and the time interval from the collapse till the explosion.

After the publication of the last version of nuclear reaction tables (Caughlan and Fowler 1988), experimental reaction rates have been revised. Woosley *et al.* (1997) investigated the sensitivity of the abundances of the elements produced in a 25 $M_\odot$ supernova to recent revisions in the reaction rates. They also demonstrated the explosive nucleosynthesis above the iron group nuclei using a reaction network of isotopes lighter than ^{106}Ru.

Through the series of the theoretical studies of supernova nucleosynthesis, many studies were conducted with the aim of constructing global scenario on the formation of elements (Weaver *et al.* 1978; Weaver and Woosley 1980; Woosley *et al.* 1990; Woosley and Weaver 1995) or explaining observational features (e.g., γ-ray spectra) of special supernova events (Hashimoto *et al.* 1989; Thielemann *et al.* 1990, 1996). For the above purposes, it is important to obtain the compositions over almost all isotopes in whole stars. On the other hand, in order to distinguish presolar grains originated from supernovae, the isotopic ratios of elements in grains should be compared with those in supernova ejecta. Note, here, that the composition of a presolar grain reflect the local composition where the grain condensed. In addition, the materials in supernova ejecta are very heterogeneous and the local compositions are different from the averaged composition of the star (e.g., Woosley and Weaver 1995). So, in order to find suitable manners for distinguishing presolar grains originated from supernovae, it is important to investigate the varieties of the elemental ratios of the elements produced in supernovae rather than the averaged composition in the whole stars.

1.3. Identification of supernova originated presolar grains

Until now, several kinds of presolar grains originated from supernovae have been identified on qualitative and quantitative comparison between the analyzed isotopic ratios and the isotopic ratios predicted by nucleosynthesis theories of supernova explosions. Zinner *et al.* (1991) first found a presolar grain of which C, N, and Si isotopic compositions are quite different from those of the other grains they had found. Amari *et al.* (1992) also found additional four SiC presolar grains. These SiC grains are named "grains of type X" (which is sometimes abbreviated as "grains X"). Grains of type X have the following isotopic characters; the $^{12}C/^{13}C$ ratios are larger than the ratios of the solar-system composition, the $^{14}N/^{15}N$ ratios are smaller than the ratios of the solar-system composition, the $^{26}Al/^{27}Al$ ratios are up to 0.1, and the grains have ^{28}Si excesses to the solar-system composition. One of the grains X has ^{44}Ca excess, which comes from the decay of ^{44}Ti. Four of the grains X have also ^{49}Ti excesses, which come from the decay of ^{49}V.

Amari *et al.* (1992) suggested that the grains of type X are formed in supernovae on the basis of qualitative comparison between the isotopic characters of the grains of type X and those of supernovae (Woosley 1986). In the convective He-layer, the $^{12}C/^{13}C$ ratio is extremely large and the $^{14}N/^{15}N$ ratio is small compared with those of the solar-system composition. Large amount of ^{28}Si is formed in the O-burning stage and during the explosive O-burning. During the explosive He-, O-, and Si-burning ^{44}Ti is formed and decays to ^{44}Ca with a half life of 47 years. Similarly, ^{49}V is formed during the explosive He-, Ne-, and O-burning and decays to ^{49}Ti with a half life of 331 days. Amari *et al.* (1992) concluded that if a large scale mixing occurs during the supernova explosions, these characters of the isotopic ratios are in qualitative agreement with the isotopic ratios of grains of type X.

Amari *et al.* (1995a) identified 47 low density graphite grains from the Murchison meteorite as supernova originated grains. Most of the identified grains have ^{15}N excesses, small ^{16}O/^{18}O ratios, large ^{26}Al/^{27}Al ratios (up to 0.15), and ^{28}Si excesses. The ^{16}O/^{17}O ratios are roughly equal to or less than the ratio of the solar-system composition. The obtained ratios were qualitatively compared with those in the model of a 15 $M_{\odot}$ supernova (Woosley and Weaver 1995); the ^{16}O/^{18}O ratio in the convective He-layer is as low as 0.3, the ^{16}O/^{17}O ratio in the convective He-layer is less than that of the solar-system composition, large amount of ^{28}Si is formed in inner layers through the O-burning. Thus, Amari *et al.* (1995a) obtained that these graphite grains have qualitative traces of nucleosynthesis in the supernova. Nittler *et al.* (1995) found seven Si_3N_4 grains expected to be originated from supernovae. The isotopic ratios of C, N, Al, Si of three of the grains and the ^{30}Si/^{28}Si ratios of the other four grains were measured. These three grains showed ^{15}N and ^{28}Si excesses and large ^{26}Al/^{27}Al ratios ranging from 0.006 to 0.6 and the other grains showed the ^{30}Si/^{28}Si ratios smaller than the solar-system composition. These isotopic ratios were similar to those of SiC grains X which had been identified before (Amari *et al.* 1992; Nittler *et al.* 1993, 1995; Hoppe *et al.* 1994b). Thus, Si_3N_4 grains are expected to be of the supernova origin.

Nittler *et al.* (1996) observed large ^{44}Ca excesses, the decay product of ^{44}Ti, relative to the solar ^{44}Ca/^{40}Ca ratio in four low-density graphite grains and five SiC grains of type X. They also observed small ^{42}Ca and ^{43}Ca excesses in three graphite grains. In the supernova explosions, ^{44}Ca is produced through n-captures in the He-layer and comes from the decay of ^{44}Ti in the O-, Si-, and Ni-layers (Woosley and Weaver 1995). In the case of the n-capture production, however, ^{42}Ca and ^{43}Ca excesses larger than ^{44}Ca excesses are shown. So, Nittler *et al.* (1996) concluded that the ^{44}Ca excesses shown in these grains are traces of the ^{44}Ti production in supernovae. They also measured the isotopic ratios of C, N, Si, and Ti in the graphite grains and the SiC grains and the O isotopic ratios in the graphite grains. The isotopic ratios of most of the grains were qualitatively similar to the low-density graphite grains and the SiC grains of type X they have analyzed before (e.g., Amari *et al.* 1992, 1995a). The problems of the ^{15}N excesses, the ^{26}Al/^{27}Al ratios, and the Si isotopic ratios arose in this study.

Amari *et al.* (1996a) observed large ^{41}K excesses in five graphite grains. The maximum value of the observed ^{41}K/^{39}K ratios is four times larger than the maximum ratio (which is excluded the contribution of the decay of ^{41}Ca) predicted from a 15 $M_\odot$ supernova model (Woosley and Weaver 1995). Further, since graphite is one of the first solids condensed in supernova ejecta when C/O > 1 (Lattimer *et al.* 1978) and K is more volatile than Al and Mg, K is not expected to be contained in graphites. So, Amari *et al.* (1996a) expected that the large ^{41}K excesses are the evidence for the decay of ^{41}Ca produced in supernovae. The excesses of ^{42}Ca and ^{43}Ca were also measured. The large ^{41}Ca/^{40}Ca ratio is produced in the He/C-layer and ^{42}Ca and ^{43}Ca excesses are produced in the O/C and O/Ne-layers (Woosley and Weaver 1995).

Until now, only one supernova originated presolar oxide grain has been found. Nittler *et al.* (1998) found one presolar oxide grain that is extremely rich in ^{16}O in the Tieschitz meteorite. They considered that the grain had been probably formed in the ejecta of a type II supernova because the grain is extremely rich in ^{16}O.

Among these studies, the isotopic ratios of C, N, O, Al, Si, Ca, and Ti in SiC, graphite, and Si_3N_4 grains have been measured. Most of supernova originated grains were identified qualitatively on the basis of the ^{15}N excesses, ^{18}O excesses, large ^{26}Al/^{27}Al ratios, and ^{28}Si excesses. The ^{15}N and ^{18}O excesses are formed in the convective He-layer in supernovae. The large ^{26}Al/^{27}Al ratio is formed in the radiative He-layer. In the O-burning layers a large amount of ^{28}Si is produced. Some of the grains were also identified based on the large excesses of ^{41}K, ^{44}Ca, and ^{49}Ti, which are the decay product of the short lived ^{41}Ca, ^{44}Ti, and ^{49}V, respectively. These radioactive isotopes are formed in supernovae. Thus, on the condition that a large scale microscopic mixing occurs in order to match several kinds of isotopic anomalies of the grains with those in the supernovae, the isotopic ratios of presolar grains originated from supernovae are in qualitative agreement with those predicted by nucleosynthesis theory of supernova explosions. Despite the qualitative agreement, some problems on the isotopic ratios are also shown; the depletion of ^{30}Si relative to ^{29}Si measured in these grains are not reproduced by the addition of ^{28}Si in the inner layers of the supernova ejecta (Nittler *et al.* 1995). Large ^{26}Al/^{27}Al ratios combined with ^{15}N excesses in the grains are not reproduced by the supernova models. In the radiative He-layer, where the large ^{26}Al/^{27}Al ratio is formed, the extremely excess of ^{14}N is shown. The ^{15}N excess is shown in the convective He-layer. Because of the large amount of ^{14}N in the radiative He-layer, the large ^{26}Al/^{27}Al ratios is scarcely combined with ^{15}N excesses even in the mixture between the two layers (Nittler *et al.* 1995).

After Woosley and Weaver (1995), quantitative evaluations of the varieties of the isotopic ratios of the elements produced in supernovae have been conducted by the use of numerical results of Woosley and Weaver (1995) (Zinner and Amari 1995; Amari and Zinner 1997a, 1997b; Travaglio *et al.* 1996, 1999). The isotopic ratios of the presolar SiC (Amari *et al.* 1992; Hoppe *et al.* 1995b, 1996; Nittler *et al.* 1995, 1996), graphite (Hoppe *et al.* 1992; Amari *et al.* 1994, 1995a, 1995b, 1995c, 1996a, 1996b; Nittler *et al.* 1996; Amari and Zinner 1997a, 1997b; Travaglio *et al.* 1999), and Si_3N_4 (Nittler *et al.* 1995) grains qualitatively identified as supernova origin were compared with the isotopic ratios in the C-rich layer, i.e., the convective and the radiative He-layers of supernovae with masses of 13 $M_\odot$ to 25 $M_\odot$ by the use of diagrams between two isotopic ratios: $^{14}N/^{15}N$-$^{12}C/^{13}C$, $^{16}O/^{18}O$-$^{12}C/^{13}C$, and $\delta^{29}Si/^{28}Si$-$\delta^{30}Si/^{28}Si$ (e.g., Zinner and Amari 1995; Amari and Zinner 1997a, 1997b; Travaglio *et al.* 1999). These diagrams clearly showed that the isotopic ratios in the grains are not reproduced by those in the C-rich layers of the supernovae. These disagreements require a large scale microscopic mixing containing O-rich regions. In practice, theoretical study aiming at reproducing the light curve of SN 1987A (e.g., Shigeyama and Nomoto 1990) or hydrodynamical calculations of the mixing in supernovae (e.g., Hachisu *et al.* 1994) also require a large scale mixing containing inner and outer regions. The mixing process during the supernova explosions is described in detail on page 13.

Zinner and Amari (1995) and Travaglio *et al.* (1996) conducted diffusive mixing calculation in the supernova ejecta of a 15 $M_\odot$ model given by Woosley and Weaver (1995) and compared the isotopic ratios in the ejecta with those in low-density graphite grains (Amari *et al.* 1994, 1995b; Hoppe *et al.* 1992; Zinner 1995). The diffusive mixing is proceeded preserving the condition of $C/O > 1$ in the He-layer. They evaluated the isotopic ratios in the diffusively mixed ejecta in the diagrams between two isotopic ratios: $^{14}N/^{15}N$-$^{12}C/^{13}C$, $^{16}O/^{17}O$-$^{12}C/^{13}C$, $^{26}Al/^{27}Al$-$^{12}C/^{13}C$, and $\delta^{29}Si/^{28}Si$-$\delta^{30}Si/^{28}Si$. Although they showed that the isotopic ratios in the diffusive mixture reproduce those found in the grains, assumptions that ^{15}N and ^{28}Si are selectively injected into the convective He-layer or that only a 1/200 of the N abundance in the radiative He-layer contributes the formation of presolar grains are required in order to reproduce the isotopic ratios in the graphite grains. Amari and Zinner (1997a, 1997b) compared the isotopic ratios of the elements in the supernova mixtures obtained in Travaglio *et al.* (1996) with those of the supernova originated SiC (Amari *et al.* 1992, 1995a, 1996a; Nittler *et al.* 1995, 1996; Hoppe *et al.* 1996) and Si_3N_4 (Nittler *et al.* 1995) grains. The obtained results are similar to the results of Travaglio *et al.* (1996).

In addition to the isotopic ratios in the C-rich layers and in the diffusively mixed ejecta, Travaglio *et al.* (1999) considered the mixing of discrete layers, each of which composition is averaged, of a 15 $M_\odot$ supernova. They divided the supernova from the He/N-layer to the Ni core into seven distinct layers; the He/N-, He/C-, O/C- and O/Ne-, O/Si-, Si/O- and Si/S-, and Ni-layers of the supernova are denoted by M1 to M7. They mentioned that they had investigated many combinations of mixing ratios but presented only a few of most typical results. In their paper they assumed that the mixing ratios of M4/M2 is equal to 0.05, the ratios of M5/M2 and M6/M2 are given as parameters and they decided the ratios of M1/M2 and M3/M2 in order to obtain given $^{12}C/^{13}C$ ratios from 5 to 1×10^4. From the obtained compositions they calculated N, O, Al, Si, Ca, and Ti isotopic ratios. They showed diagrams of $^{14}N/^{15}N$-, $^{16}O/^{18}O$-, and $^{26}Al/^{27}Al$-$^{12}C/^{13}C$, $^{16}O/^{18}O$- and $^{26}Al/^{27}Al$-$^{14}N/^{15}N$ and $\delta^{30}Si/^{28}Si$-$\delta^{29}Si/^{28}Si$. They also showed the diagrams between Ca isotopic ratios and $^{12}C/^{13}C$, Ti isotopic ratios and $^{12}C/^{13}C$, Ti isotopic ratios and $\delta^{30}Si/^{28}Si$ and investigated whether the isotopic ratios of the low-density graphite grains qualitatively identified as supernova origin (Amari *et al.* 1995a, 1996a, 1996b; Nittler *et al.* 1996) are reproduced by the supernova mixing models.

Their obtained results are summarized as follows. The ratios of $^{12}C/^{13}C$, $^{16}O/^{18}O$, $^{44}Ti/^{48}Ti$, and $^{41}Ca/^{40}Ca$ in the supernova mixing model reproduced the whole ranges of the isotopic ratios of low-density graphite grains qualitatively identified as supernova origin. The ratios of $^{26}Al/^{27}Al$ in the supernova reproduced the maximum isotopic ratios in the grains but did not reproduce the low ones. The Si isotopic ratios reproduced the ^{28}Si excesses in the grains but had large $^{30}Si/^{29}Si$ ratios compared with those in the grains. The $^{14}N/^{15}N$ ratios were too large compared with those in the grains where the $^{12}C/^{13}C$ ratios were within the range in the grains. For stable Ca and Ti isotopes, they failed to reproduce large ^{43}Ca and ^{44}Ca excesses and large ^{49}Ti and ^{50}Ti excesses found in some of the grains. The $^{12}C/^{13}C$, $^{14}N/^{15}N$, and $^{26}Al/^{27}Al$ ratios were almost completely determined by contributions of layers M1, M2, and M3. The $^{16}O/^{18}O$ ratios and the Si isotopic ratios were also affected by the ratios of layers M4 and M5 and layers M5 and M6, respectively. Travaglio *et al.* (1999) indicated possible solutions for the failures: different reaction rates for several nuclear reactions and elemental fractionation during the mixing.

Conjecturing from their results, we have to identify presolar grains as supernova origin on the basis of the match of several kinds of the isotopic ratios found in the grains with those in supernovae. The match of all kinds of the isotopic ratio is expected to be very rare. After the identification of the supernova originated presolar grains, we probably have to consider elemental fractionations of the grains which have suffered. In order to determine whether given isotopic ratios found in the grains are inside the regions of the ratios of supernovae, we should clarify definite ranges of the isotopic ratios of elements produced in supernovae. Although Travaglio *et al.* (1999) investigated many kinds of the isotopic ratios in the mixtures of discrete layers of a 15 $M_{\odot}$ supernova (probably they investigated the mixing of supernovae with the other masses), their study is still insufficient for identification of supernova originated presolar grains; their predicted ranges of the isotopic ratios of the elements in supernovae are not clear. Since the composition in each layer is averaged, the adopted ranges of the isotopic ratios obtained by the use of their mixing model do not cover all isotopic ranges in the supernova. We should find probable ranges of isotopic ratios of elements produced in supernovae taking account of the varieties on the supernovae such as the chemical compositions and the stellar mass. At the same time, it is preferred to use the isotopic or the elemental ratios insensitive to uncertainties in the supernova explosion models when we identify supernova originated grains. As the first step of obtaining probable ranges of the isotopic ratios in supernovae, we will clarify the ranges of several kinds of isotopic/elemental ratios of light elements produced in supernovae.

1.4. Purposes of this study

In this paper, we pay special attention to the explosive nucleosynthesis of light elements, i.e., the CNO-elements and Li, Be, and B (hereafter we call them the X-elements). Oxygen is one of the main constituents of silicate grains. Carbon and Nitrogen are generally abundant and a part of them, at least, would be extracted into dust grains when they condense in the cooling stage of supernova explosion. In the case of the X-elements, despite the low solar-system abundances, abundance values in the silicate bearing particles are relatively high because of high chemical affinity with Si-Mg grains and their high refractory features. In this sense, we can expect that the grains of supernova origin would certainly contain these elements. In addition, the X-elements and the CNO-elements behave quite differently in the nucleosynthesis. Extensive study of the explosive nucleosynthesis of these two kinds of elements will give us one of the suitable way to identify supernova originated presolar grains. In our present study, we concentrate on the nucleosynthesis only in the He-layer and the H-rich envelope during the supernova explosions. Previous studies on the explosive nucleosynthesis indicated that the CNO-elements (except ^{12}C and ^{16}O) as well as the X-elements are produced by appreciable amounts in these layers (Woosley *et al.* 1990; Woosley and Weaver 1995; Meyer *et al.* 1995).

In order to overcome various kinds of uncertainties and to obtain definite ranges of the isotopic ratios considering varieties on supernova explosions, we simulate light element synthesis during the supernova explosions by changing the following four parameters which are expected to affect the nucleosynthesis in supernovae:

1. The model of the neutrino emission.

2. Initial chemical compositions.

3. Nuclear reprocessing due to mixing.

4. Mass of a progenitor.

Neutrino-induced reactions play important roles on the synthetic processes of the X-elements. Woosley *et al.* (1990) first clarified the explosive nucleosynthesis including the neutrino-induced nuclear processing under the realistic stellar conditions. They investigated production processes of the X-elements and the sensitivity of the production processes to the neutrino temperatures. However, they did not investigate the influence of the decay time of the neutrino flux and the total energy carried by neutrinos on the X-element production. In order to obtain varieties of the amounts and the elemental ratios of the X-elements produced in the supernovae, we should also take account of the uncertainties of the neutrino emission model such as the decay time of the neutrino flux and the total energy carried by neutrinos and we should find the isotopic or elemental ratios insensitive to the uncertainties of the neutrino emission model.

The behavior of the light element synthesis may be modified by the initial chemical compositions, i.e., the chemical compositions in the presupernova stage. During the stellar evolution the chemical compositions are changed thoroughly through several burning processes as well as mixing processes. The difference of the stellar evolution mainly due to the stellar mass may affect the chemical compositions in the presupernova stage. So, it is important to investigate how the light element production responses to the adopted chemical compositions at the presupernova stage.

There is a possibility that the explosive nucleosynthesis is influenced by the mixing between discrete layers during the supernova explosion and, as a result, gives different results on the isotopic/elemental ratios of the light elements. Many authors pointed out theoretically that there occurs the Rayleigh-Taylor instability during the supernova explosion (e.g., Chevalier 1976; Ebisuzaki *et al.* 1989) and the instability develops to large scale mixing in the ejecta (e.g., Hachisu *et al.* 1990, 1992, 1994; Herant and Woosley 1994). Existence of such a large scale mixing is supported by γ-ray observations of SN 1987A (e.g., Shigeyama and Nomoto 1990).

Large scale mixing during the supernova explosion would vary the compositions in the He-layer and the H-rich envelope by two different ways; one is that the mixing brings about only a chemical blend between two mixed fluid elements (hereafter such a mixing will be called "the mechanical mixing"). The other is that new nucleosynthetic reactions are induced by the material mixing and the chemical abundances of the mixture vary not only by "the mechanical mixing" but also by "the nuclear reprocessing after the mixing". Since the Rayleigh-Taylor instability occurs just after the shock arrival to the He/H boundary and develops with a free fall time due to an effective gravity (e.g., Herant and Woosley 1994), the temperature of the mixture may be high enough to induce new kind of nucleosynthesis. So, we will also investigate the nuclear reprocessing driven by the large-scale mixing between the He-layer and the H-rich envelope.

In most of this study, we adopt a model with the power-law distribution approximated on the basis of a 16.2 $M_{\odot}$ progenitor model, which is obtained numerically by Shigeyama and Nomoto (1990) (14E1 model), as for the stellar density distribution of a progenitor. Of course, supernovae occur at the end of the evolution of massive stars with various masses. Since difference of the stellar evolutions due to the stellar mass affects not only the composition of the progenitors but also their stellar structure, the difference of the stellar structure may affect the final chemical composition of the supernova ejecta. In order to take account of the influence of the mass of the progenitor, we additionally investigate explosive nucleosynthesis of the light elements in the cases where the mass of the progenitor is 25 $M_{\odot}$, 20 $M_{\odot}$, and 15 $M_{\odot}$.

We will introduce a specific term of "detection limit". Roughly speaking, most of dust grains are piles of oxygen atoms and, hence, the amounts of other species (except Si, Mg, and Fe) are much less than that of oxygen. When dust grains contain some kind of rare elements with the content of 1×10^{-7} times as small as that of ^{16}O, it is difficult to detect such rare elements, even by using the most sensitive instruments such as the ion probe technique. Expecting an extensive progress of isotopic analyzers in near future, we hereafter put to be 1×10^{-9} of ^{16}O as the detection limit of rare isotopes.

This paper is organized as follows: in Section 2, we will present our nuclear reaction network and add a short comment on the reaction rates. In addition, we will present reactions of the ν-process briefly. The reactions and their references are listed in Appendix. In Section 3, we will construct a dynamical model of a supernova explosion based on a strong shock propagation in a medium with a power-law density profile. We will also construct a model of the neutrino emission and the method of handling the material mixing which occurs during the supernova explosion. We will explain initial chemical compositions of the He-layer and the H-rich envelope. About half of Sections 2 and 3 are reprinted from the corresponding sections of Yoshida, Emori, and Nakazawa (2000).

In Section 4, we will demonstrate the synthetic processes of the light elements during the supernova explosion for a model, which we call the standard model. In Section 5, we will discuss in detail the influence of the adopted neutrino emission model on the production of light elements, i.e., the influence of the decay time of the neutrino flux and the total energy carried by neutrinos. Most of Sections 4 and 5 are reprinted from the corresponding sections of Yoshida, Emori, and Nakazawa (2000).

In Section 6, in order to investigate how the adopted initial chemical compositions affects the produced amounts of the light elements, we will first set up the models of the initial chemical compositions that the He-layer and the H-rich envelope consist of only four elements, ^{1}H, ^{4}He, ^{12}C, and ^{16}O with various contents. In addition, in order to see the degree of decomposition of pre-existing elements, we will also consider an artificial case where there are large amounts of the light elements in the presupernova stage. Next, results of numerical simulations will be shown: we will describe in detail the sensitivity of the light element production to the adopted initial chemical compositions. Furthermore, presuming the chemical composition in the presupernova stage on the basis of studies of the stellar evolution as well as atmospheric chemical compositions of stars, and combining it with our numerical results, we will evaluate probable ranges of the isotopic/elemental ratios of the light elements observed in supernova ejecta. This section is reprinted from Yoshida, Nakazawa, and Emori (1999).

In Section 7, we will investigate the results of the nuclear reprocessing of the light element after the mixing, which are obtained by numerical simulations. We will see that the abundances of the X-elements vary mainly through proton-capture reactions induced after the mixing but the CNO-elements suffer from only the mechanical mixing. In Section 8, we will investigate the varieties of the synthetic processes of the light elements due to the stellar mass as well as the adopted model of the neutrino emission and the nuclear reprocessing after the mixing. In Section 9, we will change a point of view to the other synthetic processes: synthesis due to low and intermediate mass stars on the red giant branch (RGB) and the asymptotic giant branch (AGB) as well as the cosmic ray interactions. We will deduce the ranges of the isotopic/elemental ratios of the CNO-elements based on theoretical studies of the RGB star and the AGB stars and those of the X-elements based on the studies of the cosmic rays. We will compare them with the results obtained in this study. Conclusions of this study will be presented in Section 10. The region of the ratios of $^{14}N/^{15}N$-$^{12}C/^{13}C$ will be compared with that shown in Travaglio *et al.* (1999). The isotopic/elemental ratios of the light elements taken into account of the mixing of the O- and Si-layers will be also discussed.

2. Nuclear Reaction Network

After the passage of the shock wave, the temperature in the He-layer and the H-rich envelope rises and many channels of nuclear reactions open. Just before the shock passage, huge amount of neutrinos pass through the layers and neutrino-induced nuclear reactions occur. In this section we describe a nuclear reaction network for investigating the light element synthesis in the supernova explosions. About a half of this section is reprinted from Section 2 in Yoshida, Emori, and Nakazawa (2000).

2.1. Thermonuclear reactions, beta-decays, and electron captures

In this study, we are interested in the abundances and isotopic ratios of nuclear species from H to O synthesized inside the He-layer and the H-rich envelope of supernovae. During the supernova explosion, the maximum temperature of these layers is kept to be lower than the temperature at which the explosive C-burning ignites so that we can expect that the abundances of elements heavier than Na do not change. Thus, we construct a reaction network including 52 species of isotopes from H to Mg illustrated in Fig. 2.1.

We consider various kinds of nuclear reactions in our network: (n,γ)-, (p,γ)-, (α,γ)-, (n,p)-, (n,α)-, and (p,α)- reactions as well as their inverse reactions, β-decays, and electron captures. They are tabulated in Tables A.1 to A.9 in Appendix together with the Q-values and the references from which the reaction rates are taken. The total number of the nuclear reactions is 412. In tables, we include all reactions relevant not only to the pp chains and the CNO cycles, but also to the hot pp chains, rap-processes (Wiescher *et al.* 1989) which are a chain p- and α-capture reactions starting from ^{7}Be to form O isotopes, and NeNa cycle (Rolfs and Rodney 1988).

The atomic weights of these species, A_i, are adopted from Audi and Wapstra (1995). Most of the reaction rates are taken from Caughlan and Fowler (1988) which is abbre-

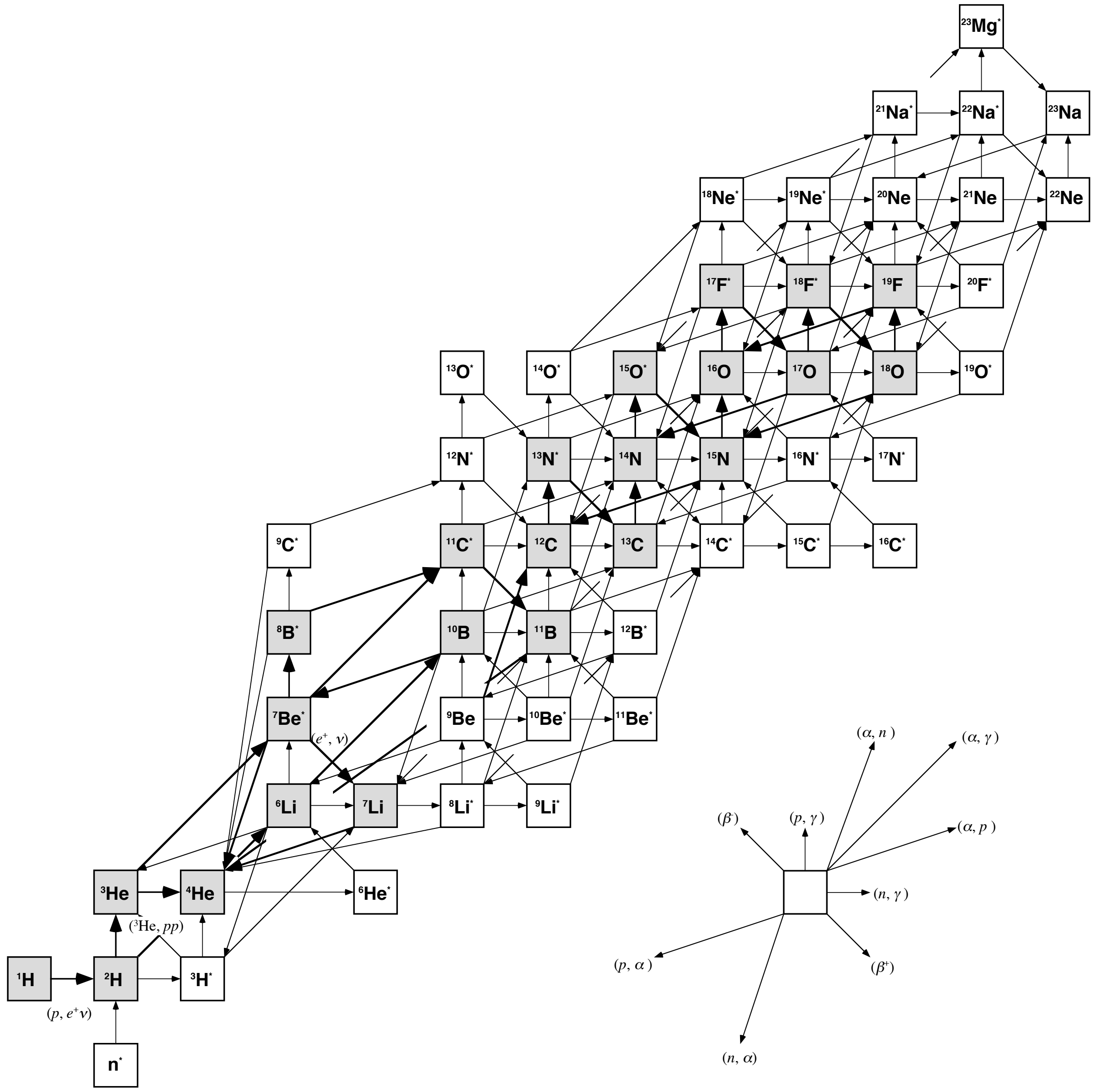

Fig. 2.1. Isotopic species and the nuclear reaction network adopted in our present study. Arrows denote the nuclear reactions considered in the simulations of explosive nucleosynthesis. A small network, which is composed of shaded isotopic species connected by bold arrows, is used for evaluating the initial chemical composition of light elements in the H-rich envelope. Species with an asterisk are radioactive isotopes.

viated as CF88 hereafter. However, some reactions are not listed up in CF88; for such reactions, we use the reaction rates presented in other sources (which are listed in tables mentioned above). Furthermore, some of the reaction rates tabulated in CF88 are reevaluated recently; for such reactions we adopt new ones in our reaction network. For example, for $^{12}C(\alpha,\gamma)^{16}O$ we use a new reaction rate reevaluated by Buchmann (1996, 1997) and for $^{17}O(p,\alpha)^{14}N$ and $^{17}O(p,\gamma)^{18}F$ we evaluate the reaction rates using the rate formula given by Landré *et al.* (1990) and the proton width of 5.673 MeV excited state of ^{18}F (Γ_p=22 neV) newly found by Blackman *et al.* (1995) (the proton width of 5.786 MeV excited state is put to be 0.44 meV without a strong evidence since this state does not contribute so much). The reaction rate of $^{18}O(\alpha,\gamma)^{22}Ne$ is adopted from Käppeler *et al.* (1994) which includes a resonance of 10.05 MeV of excited state of ^{22}Ne.

2.2. Neutrino induced nuclear reactions

In addition to the ordinary nuclear reactions, the reaction processes induced by neutrinos, which are emitted from the stellar core, play an important role on the light elements synthesis (Woosley *et al.* 1990). Such processes are called generically the ν-process. According to theoretical studies of the type II supernova explosions, the explosion is ignited by the central core collapse due to photodisintegration of iron group elements (e.g., Woosley and Weaver 1986). As many authors pointed out (e.g., Cooperstein 1988), strong neutrino flux should be released from the collapsing core prior to the explosion and neutrinos react with nuclei in He- and H-layers of the type II supernova through the neutral and charged current interactions (Domogatsky *et al.* 1977; Epistein *et al.* 1988; Woosley and Haxton 1988; Woosley *et al.* 1990). Woosley *et al.* (1990) evaluated the cross sections of these reactions by the use of the nuclear shell model and applied the ν-process to their simulations of nucleosynthesis. In our study, we employ the ν-process reactions in our nuclear reaction network in order to evaluate the amounts of the ν-process products.

We consider three flavors of neutrinos, μ-, τ-, and e- neutrinos as well as their antiparticles. In the cases of μ- and τ-neutrinos and their antineutrinos, only the inelastic scattering due to neutral current is important. This process leads to the nuclear excitation to unbounded states, which is followed by a spontaneous emission of neutron, proton, or α-particle. The reactions are written schematically as

$$(Z, A) + \nu \rightarrow (Z, A)^* + \nu', \tag{2.1}$$

$$(Z, A)^* \rightarrow \begin{cases} (Z, A-1) + n \ , \\ (Z-1, A-1) + p \ , \\ (Z-2, A-4) + \alpha \ , \end{cases} \tag{2.2}$$

where (Z, A) represents a nucleus specified by the atomic number Z and the total nucleon number A.

On the other hand, in the case of e-neutrinos (and their antineutrinos), there are the following six reactions through the charged current interaction in addition to the inelastic mentioned above:

$$(Z, A) + \nu_e \rightarrow \begin{cases} (Z+1, A) + e^- + \gamma \ , \\ (Z+1, A-1) + n + e^- \ , \\ (Z, A-1) + p + e^- \ , \end{cases} \tag{2.3}$$

and

$$(Z, A) + \bar{\nu_e} \rightarrow \begin{cases} (Z-1, A) + e^+ + \gamma \ , \\ (Z-1, A-1) + n + e^+ \ , \\ (Z-2, A-1) + p + e^+ \ . \end{cases} \tag{2.4}$$

The reaction rates of the ν-process are determined by the cross sections of the neutrino interactions and the neutrino flux. Roughly speaking, the cross sections of the neutral current interactions, σ_ν, are evaluated as $\sigma_\nu \sim 10^{-43} A$ cm^2 (e.g., Woosley *et al.* 1990) and, as shown in Section 3.3 (see page 35), the neutrino flux, ϕ_ν, is of the order of 10^{37}

cm^2/s in the He-layer. Thus, a typical value of the reaction rates of the ν-process is evaluated as the orders of 10^{-6} s^{-1}. The cross sections of these neutrino reactions and branching ratios are taken from those deduced by Hoffman and Woosley (1992). All neutrino reactions taken into account in our reaction network are listed in Table A.10 in Appendix. The number of the neutrino reactions in our reaction network is 148. It is worth to note that neutral current reactions dominate the ν-processes and that τ- and ν-neutrinos with higher energies contribute more than e-neutrinos. In order to evaluate the reaction rates of the ν-processes, it is also necessary to have a knowledge about the mean neutrino temperatures, the number flux of neutrinos, and its time variation. These will be described in Section 3.3 (see page 35).

Combined with the above thermonuclear reactions, β-decays, the ν-process, and so on, the time evolution of the mass fraction of nucleus i, X_i, is given symbolically by

$$\begin{aligned} \frac{1}{A_i}\frac{dX_i}{dt} &= -N_i\lambda_i\frac{X_i}{A_i} + \sum_j N_i\lambda_j\frac{X_j}{A_j} \\ &\quad - \sum_j \frac{N_i}{1+\delta_{ij}}[ij]\frac{X_i}{A_i}\frac{X_j}{A_j} + \sum_{j,k}\frac{N_i}{1+\delta_{jk}}[jk]\frac{X_j}{A_j}\frac{X_k}{A_k} \\ &\quad - \sum_{j,k}\frac{N_i}{1+\Delta_{ijk}}[ijk]\frac{X_i}{A_i}\frac{X_j}{A_j}\frac{X_k}{A_k} + \sum_{j,k,l}\frac{N_i}{1+\Delta_{jkl}}[jkl]\frac{X_j}{A_j}\frac{X_k}{A_k}\frac{X_l}{A_l} \\ &\quad - \sum_\zeta < \sigma_{\nu\zeta} >_i \phi_{\nu\zeta}\frac{X_i}{A_i} + \sum_j\sum_\zeta < \sigma_{\nu\zeta} >_j \phi_{\nu\zeta}\frac{X_j}{A_j}. \end{aligned} \tag{2.5}$$

In the above, A_i denotes the atomic weight of nucleus i, λ_i is the reaction rates of $\beta^{\pm}$-decays, photodisintegrations, or electron captures, $[ij] = \rho N_{\rm A} < \sigma v >_{ij}$, $[ijk] = \rho^2 N_{\rm A}^2 < \sigma v >_{ijk}$, ρ is the density, $N_{\rm A}$ is Avogadro's number, $< \sigma v >_{ij}$ and $< \sigma v >_{ijk}$ are reaction rate of two- and three-particle reactions. The cross section of the interaction between the ζ-flavor of neutrino and the nucleus i averaged over the energy distribution of the neutrinos is denoted by $< \sigma_{\nu\zeta} >_i$ and the flux of the ζ-flavor of the neutrinos is $\phi_{\nu\zeta}$. The number, N_i, means the number of species i created or annihilated in a reaction, δ_{ij} is the Kronecker delta, and $\Delta_{ijk} = \delta_{ij} + \delta_{jk} + \delta_{ki} + 2\delta_{ij}\delta_{jk}\delta_{ki}$.

3. Model of Supernova Explosion

In a type II supernova, a shock wave generated at the surface of the central core propagates outward and heats up the outer materials. So, nuclear reactions begin newly to work to form various kinds of light elements. Neutrinos and antineutrinos, which are produced in the collapsing central core, induce some nucleosyntheses before the shock arrival and have a good contribution to the synthesis of light elements. After the shock arrival at the He/H boundary, fluid near the boundary becomes unstable against the Rayleigh-Taylor instability. The instability develops to the large scale mixing and there occurs the nuclear reprocessing of the light elements in the mixture. In order to reproduce properly the nucleosynthesis during the supernova explosion, we have to know the physical parameters which govern the explosive nucleosynthesis of the light elements: the chemical compositions in the presupernova stage, the neutrino flux, its time variation, the arrival time of the shock wave, the post shock thermal evolution, the time when two layers mix, and the physical conditions of the mixture. About a half of Sections 3.1, 3.2, and 3.3 and most part of Section 3.5 are reprinted from Sections 3.1, 3.2, 3.3, and 3.4 in Yoshida, Emori, and Nakazawa (2000) except description of models of 25 $M_\odot$, 20 $M_\odot$, and 15 $M_\odot$ supernovae.

3.1. Internal stellar model in the presupernova stage

We first construct a stellar model in the presupernova stage (i.e., a model of a progenitor) on the basis of a 16.2 $M_\odot$ progenitor model (14E1 model) obtained numerically by Shigeyama and Nomoto (1990). The corresponding main-sequence mass of the progenitor is 20 $M_\odot$. The stellar mass is adopted in order to reproduce the light curve properties of SN 1987A (Saio *et al.* 1988; Shigeyama and Nomoto 1990). In Fig. 3.1 we show a rough sketch of the outer region of the progenitor together with the radii, r, and the internal mass coordinates, M_r, at the boundaries between layers. The density distribution , $\rho_0(r)$, of 14E1 model is shown in Fig. 3.2. For the later convenience, we will approximate $\rho_0(r)$ by the power-law:

$$\rho_0(r) = \rho_{00} \left(\frac{r}{r_0} \right)^{-\omega} . \tag{3.1}$$

Constants r_0, ρ_{00} and ω are determined by fitting the density distribution of the numerical model, 14E1. Fitting is made in a range between the bottom of the Oxygen-layer and a middle position in the H-rich envelope, i.e., from 2.9×10^8 cm to 1.0×10^{12} cm (in the outer region where the radius is larger than 1.0×10^{12} cm the shock wave becomes weak and the temperature does not increase so much; no nuclear processes proceed in this region). As a result, we find

$$r_0 = 1.0 \times 10^9 \, \mathrm{cm}, \;\; \rho_{00} = 6.7 \times 10^4 \, \mathrm{g/cm^3}, \;\; \text{and} \;\; \omega = 2.636. \tag{3.2}$$

The density distribution given by Eqs.(3.1) and (3.2) is shown by the dashed line in Fig. 3.2. The power-law density distribution fits well to that of the numerical model 14E1 (the solid line) over the wide range we consider.

In order to investigate the variety of the nucleosynthesis of the light elements due to the stellar mass (Section 8), we consider progenitor models with different masses. The models are constructed on the basis of presupernova models obtained numerically by Iwamoto (1998) for 25 $M_\odot$ and 20 $M_\odot$ stars and by Nomoto *et al.* (1993) for a 15 $M_\odot$ star. The progenitors with masses of 25 $M_\odot$, 20 $M_\odot$, and 15 $M_\odot$ consist of 8 $M_\odot$, 6 $M_\odot$, and 4 $M_\odot$ He star models calculated by Nomoto and Hashimoto (1988), respectively, and the H-rich envelope models. The internal mass coordinates and the radii at the boundaries between layers of these models are listed in Table 3.1. Constants ρ_{00} and ω in the approximated density distribution of Eq. (3.1) in the case of these models are tabulated in Table 3.2 together with the regions of the fitting. Schematic pictures of the internal stellar structure of the 25 $M_\odot$, 20 $M_\odot$, and 15 $M_\odot$ progenitors are shown in Fig.

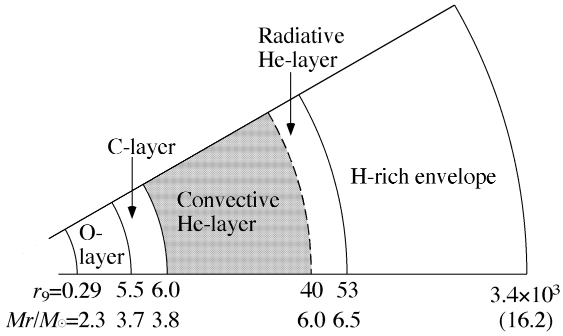

Fig. 3.1. Schematic picture of the internal stellar structure of a progenitor (14E1 model). Radii, r_9, and the internal mass coordinates, M_r, of the boundaries between layers are shown in the units of 1×10^9 cm and the solar mass, $M_\odot$, respectively.

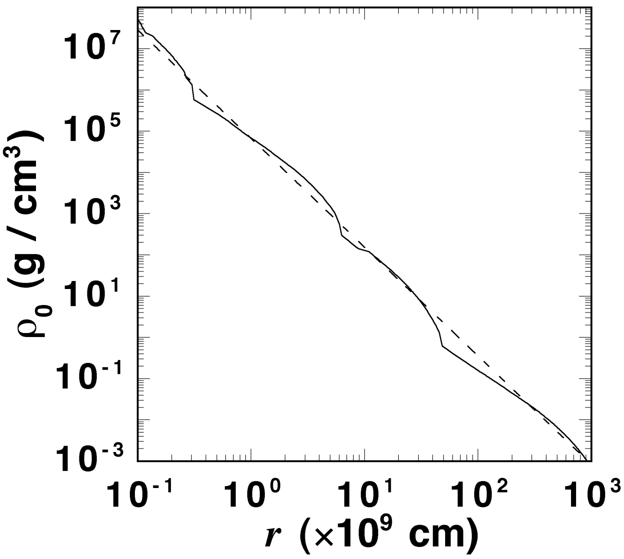

Fig. 3.2. Stellar density distribution $\rho_0(r)$, of 14E1 progenitor model (after Shigeyama and Nomoto 1990). The approximate power-law density distribution given by Eqs. (3.1) and (3.2) is also shown by the dashed line.

8.1 (see page 136). The density distributions of the numerical models of the 25 $M_\odot$, 20 $M_\odot$, and 15 $M_\odot$ progenitors and the corresponding power-law density distributions are shown in Fig. 8.2 on page 137. We will discuss the differences of the internal structures and the explosions due to the stellar mass in detail in Section 8.1 (see page 134).

Table 3.1. The internal mass coordinates and radii at the C/He-, the convective He/the radiative He-, and the He/H-boundaries in the cases of 16.2 $M_\odot$, 25 $M_\odot$, 20 $M_\odot$, and 15 $M_\odot$ progenitor models. In this table C/He, conv/rad, and He/H denote the boundaries between the C-layer and the He-layer, the convective He-layer and the radiative He-layer, and the He-layer and the H-rich envelope, respectively.

	C/He boundary		conv-He/rad-He boundary		He/H boundary	
	$M_{\rm C/He}$ ($M_\odot$)	$r_{\rm C/He}$ (cm)	$M_{\rm conv/rad}$ ($M_\odot$)	$r_{\rm conv/rad}$ (cm)	$M_{\rm He/H}$ ($M_\odot$)	$r_{\rm He/H}$ (cm)
16.2 $M_\odot$ model	3.8	6.0×10^9	6.0	4.0×10^{10}	6.5	5.3×10^{10}
25 $M_\odot$ model	6.0	7.7×10^9	8.1	3.5×10^{10}	8.5	4.4×10^{10}
20 $M_\odot$ model	3.8	6.0×10^9	5.7	4.0×10^{10}	6.0	4.9×10^{10}
15 $M_\odot$ model	2.1	3.6×10^9	3.5	5.8×10^{10}	4.3	1.6×10^{11}

Table 3.2. Constants ω and ρ_{00} in the approximated density distribution of Eq. (3.1) and the lower and upper radii of the fitting range, i.e., r_{in} and r_{out}, respectively, in the cases of 16.2 $M_\odot$, 25 $M_\odot$, 20 $M_\odot$, and 15 $M_\odot$ progenitor models. A constant r_0 in Eq. (3.1) is set commonly to be 1×10^9 cm in all cases.

	16.2 $M_\odot$ model	25 $M_\odot$ model	20 $M_\odot$ model	15 $M_\odot$ model
ω	2.636	2.740	2.662	2.711
ρ_{00} (g/cm^3)	6.7×10^4	8.9×10^4	6.4×10^4	3.5×10^4
r_{in} (cm)	2.9×10^8	4.0×10^8	3.0×10^8	6.4×10^8
r_{out} (cm)	1.0×10^{12}	2.3×10^{12}	2.0×10^{12}	8.9×10^{10}

3.2. Dynamical model of supernova explosion

Numerical simulations of supernova explosions have been carried out by several authors (e.g., Woosley and Weaver 1995; Thielemann *et al.* 1996). Some of them mentioned that the shock propagation can be well approximated by the simple and famous "Sedov solution" in a medium with uniform density distribution (Woosley 1988; Woosley *et al.* 1990). Since we are concerned with the outer parts of the stellar interior (i.e., the He-layer and the H-rich envelope), we rather employ another Sedov solution, called the generalized Sedov solution, of a spherically symmetric strong shock wave in a medium with a power law initial density profile (Sedov 1959).

Now, we consider a spherically symmetric star which is composed of an ideal gas with the ratio of specific heat, γ. The density distribution of the gas is given by Eq. (3.1) and the gas is initially at rest in the star. Suppose that an explosion is ignited with explosion energy E_0 at the center of the star and that the propagating shock wave is strong enough to ignore the fluid pressure in front of the shock front compared with the pressure produced by the explosion behind the shock front. In this case, the fluid velocity, v_2, the density, ρ_2, and the pressure just behind the shock, P_2, are found from the condition of the strong shock wave, i.e., that the preshock pressure is negligible compared with the postshock pressure, as

$$v_2 = \frac{2}{\gamma+1} v_s, \quad \rho_2 = \frac{\gamma+1}{\gamma-1}\rho_0, \quad \text{and} \quad P_2 = \frac{2}{\gamma+1}\rho_0 v_s^2, \tag{3.3}$$

where v_s and r_s are the velocity and the radius of the shock front, respectively. Sedov (1959) derived the velocity of the shock front by the usage of a self-similar solution and dimensional analysis. In the case of the limit of the strong shock, as far as the description of the fluid motion behind the shock front, we can ignore the self gravity term in the equation of fluid motion. So, the equation of motion, the equation of continuity, and the equation of entropy are described as

$$\frac{\partial v}{\partial t} + v\frac{\partial v}{\partial r} + \frac{1}{\rho}\frac{\partial P}{\partial r} = 0, \tag{3.4}$$

$$\frac{\partial \rho}{\partial t} + \frac{\partial}{\partial r}(\rho v) + 2\frac{\rho v}{r} = 0, \tag{3.5}$$

and

$$\frac{\partial}{\partial t}\left(\frac{P}{\rho^\gamma}\right) + v\frac{\partial}{\partial r}\left(\frac{P}{\rho^\gamma}\right) = 0, \tag{3.6}$$

respectively. Here, v, ρ, and P is the fluid velocity, the fluid density, and the fluid pressure, respectively.

As seen from Eqs. (3.4) to (3.6), we have no parameters which bring characteristic scales of length and time. In such a case, we can obtain solutions to these equations in the form of a self-similarity. Note that we have two parameters characterizing a point explosion, the explosion energy, E_0, and a coefficient of the power-law density distribution, $\rho_{00} r_0^\omega$. Here, we look for the self-similar solutions described by a dimensionless variable containing two independent variables r and t. The only one dimensionless parameter we can make is λ defined as

$$\lambda = \left(\frac{\rho_{00} r_0^\omega \alpha}{E_0 t^2}\right)^{1/(5-\omega)} r, \tag{3.7}$$

where α is a dimensionless constant. By an introduction of λ, Eqs. (3.4) to (3.6) are transferred to the ordinary differential equations of λ. It should be noted that we can set the scale of the new parameter λ arbitrarily. So we choose it as $\lambda = 1$ at the shock front. Then, the constant α is determined by the following condition.

$$r_s = \left(\frac{E_0 t^2}{\rho_{00} r_0^\omega \alpha}\right)^{1/(5-\omega)}, \tag{3.8}$$

where r_s is the radius of the sphere of the shock front. Then, the velocity of the shock front is represented by time derivative of the radius of the shock front, r_s, as

$$v_s = \frac{2}{5-\omega}\frac{r_s}{t}. \tag{3.9}$$

Furthermore, according to Sedov (1959), we also introduce a variable V, which relates to λ as

$$\lambda^{-1} = \left[\frac{(5-\omega)(\gamma+1)}{4}V\right]^{2/(5-\omega)} \left[\frac{(5-\omega)(\gamma+1)}{7-\gamma-(\gamma+1)\omega}\left(1-\frac{3\gamma-1}{2}V\right)\right]^{\alpha_1} \times \left[\frac{\gamma+1}{\gamma-1}\left(\frac{\gamma(5-\omega)}{2}V-1\right)\right]^{\alpha_2}, \tag{3.10}$$

where α_1 and α_2 are functions of ω and γ (expressions of α_1 and α_2 will be given later together with other coefficients). Physically V means the ratio of the characteristic time of expansion at r_s and r. By the use of dimensionless variables λ and V, the density behind the shock front is expressed as

$$\rho = \rho_2\lambda^{-\omega}\left[\frac{\gamma+1}{\gamma-1}\left(\frac{\gamma(5-\omega)}{2}V-1\right)\right]^{\alpha_3} \times \left[\frac{(5-\omega)(\gamma+1)}{7-\gamma-(\gamma+1)\omega}\left(1-\frac{3\gamma-1}{2}V\right)\right]^{\alpha_4} \times \left[\frac{\gamma+1}{\gamma-1}\left(1-\frac{5-\omega}{2}V\right)\right]^{\alpha_5} \tag{3.11}$$

and the pressure is given by

$$P = P_2\left[\frac{(5-\omega)(\gamma+1)}{4}V\right]^{6/(5-\omega)} \times \left[\frac{(5-\omega)(\gamma+1)}{7-\gamma-(\gamma+1)\omega}\left(1-\frac{3\gamma-1}{2}V\right)\right]^{\alpha_4+\alpha_1(\omega-2)} \left[\frac{\gamma+1}{\gamma-1}\left(1-\frac{5-\omega}{2}V\right)\right]^{\alpha_5+1}. \tag{3.12}$$

Coefficients α_1 to α_5 used in the above expressions are defined as follows (Sedov, 1959):

$$\alpha_1 = \frac{(5-\omega)\gamma}{3\gamma-1}\left[\frac{2(6-3\gamma-\omega)}{\gamma(5-\omega)^2} - \frac{1-\gamma}{2\gamma+1-\gamma\omega}\right], \tag{3.13}$$

$$\alpha_2 = \frac{1-\gamma}{2\gamma+1-\gamma\omega}, \tag{3.14}$$

$$\alpha_3 = \frac{-\omega+3}{2\gamma+1-\gamma\omega}, \tag{3.15}$$

$$\alpha_4 = \frac{(5-\omega)(3-\omega)\alpha_1}{6-3\gamma-\omega}, \tag{3.16}$$

and

$$\alpha_5 = \frac{\omega(1+\gamma)-6}{6-3\gamma-\omega}. \tag{3.17}$$

Because we ignore the preshock pressure of the fluid and self gravity of the star in the equation of motion, the explosion energy E_0 must be equal to the total energy of explosion which is the sum of the kinetic energy and the internal energy of the fluid behind the shock front. So, E_0 must be expressed as

$$E_0 = \int_0^{r_s} \left(\frac{1}{2}\rho v^2 + \frac{P}{\gamma - 1} \right) 4\pi r^2 dr. \tag{3.18}$$

Substituting Eqs. (3.11) and (3.12) into Eq. (3.18) and by the usage of the expression of the fluid velocity in the postshock region given by

$$v = v_2 \frac{(5-\omega)(\gamma+1)}{4} \lambda V, \tag{3.19}$$

we can express the total energy by dimensionless variables ρ/ρ_2 and P/P_2. Furthermore, substituting the definition of v_2, ρ_2 and P_2 given by Eq. (3.3), we finally obtain the expression of α as

$$\alpha = \int_{V_2}^{V_1} \left\{ \frac{1}{2} \frac{\gamma+1}{\gamma-1} \frac{\rho(V)}{\rho_2} \lambda^2 V^2 + \frac{2}{(\gamma+1)(\gamma-1)} \left(\frac{2}{5-\omega} \right)^2 \frac{P(V)}{P_2} \right\} 4\pi \lambda^2 \frac{d\lambda}{dV} dV. \tag{3.20}$$

In this expression we use the variable V instead of λ as an independent variable. This is for the convenience of numerical treatment as mentioned on page 28 (see also Eq. (3.10)). The upper and lower values of V (i.e., V_1 and V_2) correspond to the lower boundary, within which a vacuum is obtained, and the shock front, respectively. From Eq. (3.19), it is clear that V_2 is equal to $4/(5-\omega)(\gamma+1)$, because v and λ is equal to v_2 and unity at the shock front, respectively. In the self-similar solution, owing to the strong explosion the fluid is blown away from the center of the star and we have a cavity inside of the star. So, at the lower boundary of the fluid we adopt the condition that $P = 0$. From Eq. (3.12), as far as ω is larger than $(7-\gamma)/(\gamma+1)$ we have $2/(5-\omega)$ for the boundary V_1. The sound velocity is also equal to zero there. It is worth to mention that, in the Eq. (3.20), $d\lambda/dV$ is negative and V_2 is smaller than V_1.

We evaluate the relation of the radius and the density to the mass coordinate at an arbitrary time. By the usage of the power law density profile, mass $M_{r,ej}$ contained in the sphere with the radius r is shown as

$$M_{r,ej} = \frac{4\pi\rho_{00}r_0^{\omega}}{3-\omega}r^{3-\omega}, \tag{3.21}$$

and, hence, Eq. (3.8) can be written as

$$t = \beta\left(\frac{3M_{s,ej}}{4\pi E_0}\right)^{\frac{1}{2}} r_s \quad \text{with} \quad \beta = \sqrt{\frac{(3-\omega)\alpha}{3}}, \tag{3.22}$$

where $M_{s,ej}$ is a mass contained within the shock front. We find that Eq. (3.22) differs systematically from the relation between the mass coordinate, M_r, and the radius, r, given by the corresponding numerical model. This is because the mass of the ejecta containing the radius, $M_{r,ej}$, in Eq. (3.22) does not contain the mass of the core, $M_{\rm core}$, which remains as a neutron star after the explosion. Furthermore, the power-law density profile does not well approximate to the density profile of the numerical model. In order to avoid the troublesome, we set the mass coordinate, M_r, contained within the radius, r, to be

$$M_r = \frac{4\pi\rho_{00}r_0^{\omega}}{3-\omega}r^{3-\omega} + M_{\rm core} + M_0 \tag{3.23}$$

where the constant, M_0, is determined by fitting the relation between the radius and the mass coordinate at the inner boundary of the He-layer given by the numerical model. Then, the shock arrival time is evaluated as Eq. (3.22) substituted $M_s - M_{\rm core}$ in place of $M_{s,ej}$ where M_s is the mass coordinate at the shock front. We evaluate the relation of the radius, r, to the mass coordinate, M_r, behind the shock front. By the use of Eqs. (3.10) and (3.11), the mass coordinate, M_r, behind the shock front is given by

$$\begin{aligned} M_r &= \int_V^{V_1} 4\pi r_s^3 \rho(V')\lambda^2 \frac{d\lambda}{dV'}\, dV' + M_{\rm core} + M_0 \\ &= (3-\omega)M_{s,ej}\int_V^{V_1} \frac{\gamma+1}{\gamma-1}\frac{\rho(V')}{\rho_2}\lambda^2\frac{d\lambda}{dV'}\, dV' + M_{\rm core} + M_0. \end{aligned} \tag{3.24}$$

From this equation we find a variable V as a function of M_r. Hence, we evaluate the radius as a function of M_r through the variable, V, and using Eq. (3.10). Following to the radius, we also find the density and the pressure using Eqs. (3.11) and (3.12), respectively. In the exploding supernova, the pressure behind the shock front is almost determined by the radiative pressure owing to the high temperature (Weaver and Woosley 1980). So, the ratio of specific heats, γ, can be put to be 4/3 and, thus, the temperature behind the shock front is written by

$$T = \left(\frac{3P}{a}\right)^{1/4}, \tag{3.25}$$

where a is the radiation density constant.

In Sections 4 to 7, we will investigate the light element synthesis during the supernova explosion by the use of the 16.2 $M_\odot$ progenitor model of which density profile is approximated by the power-law in Eqs. (3.1) and (3.2). In order to evaluate thermal evolution of the supernova explosion starting from the 16.2 $M_\odot$ progenitor, we set the relation of the radius to the mass coordinate of the 16.2 $M_\odot$ progenitor. According to Shigeyama and Nomoto (1990), the radius and the ejected mass coordinate at the He/H boundary are given by (see Fig. 3.1)

$$M_r = 6.05 \times 10^9 \quad \text{cm} \quad \text{and} \quad M_r = 3.8 \quad M_\odot \,. \tag{3.26}$$

Substituting Eq. (3.2) into Eq. (3.23) and taking account of the condition Eq. (3.26), we obtain

$$M_r = 1.166 {r_9}^{0.364} + 1.553 \quad M_\odot \,, \tag{3.27}$$

where r_9 is the radius in the units of 1×10^9 cm.

In Section 8, we will investigate the varieties of the light element production due to the stellar mass. As same as the explosive model based on the 16.2 $M_\odot$ progenitor, we obtain the relation between the mass coordinate and the radius in the cases of 25 $M_\odot$, 20

$M_\odot$, and 15 $M_\odot$ progenitor models as

$$M_r = 2.572 r_9^{0.260} + 1.627 M_\odot \quad \text{for 25 } M_\odot \text{ model,} \tag{3.28}$$

$$M_r = 1.189 r_9^{0.338} + 1.615 M_\odot \quad \text{for 20 } M_\odot \text{ model,} \tag{3.29}$$

and

$$M_r = 0.763 r_9^{0.289} + 0.992 M_\odot \quad \text{for 15 } M_\odot \text{ model.} \tag{3.30}$$

We also list the dimensionless constant α in Eq. (3.7) and the core mass of the 16.2 $M_\odot$, 25 $M_\odot$, 20 $M_\odot$, and 15 $M_\odot$ progenitor models in Table 3.3. These relations and constants are evaluated by the use of a constant ω, the mass coordinates, M_r, the ratio of specific heats, $\gamma = 4/3$, and the radii at the bottom of the He-layer listed in Tables 3.1 and 3.2.

Table 3.3. The dimensionless constant α in Eq. (3.7) and the core masses in the cases of the 16.2 $M_\odot$, 25 $M_\odot$, 20 $M_\odot$, and 15 $M_\odot$ progenitor models.

	16.2 $M_\odot$	25 $M_\odot$	20 $M_\odot$	15 $M_\odot$
α	9.96	13.76	10.71	12.42
$M_{\rm core}$ ($M_\odot$)	1.61	1.77	1.61	1.33

Hereafter, we discuss the temperature evolution of the supernova explosion model of which progenitor is the 16.2 $M_\odot$ model. In the cases of the 25 $M_\odot$, 20 $M_\odot$, and 15 $M_\odot$ progenitors, we will discuss in detail in Section 8.1 (see page 134). Peak temperature, defined as the temperature at the passage of the shock wave, is illustrated in Fig. 3.3. The explosion energy, E_0, is put to be 1×10^{51} erg according to Shigeyama and Nomoto (1990). When the shock wave arrives at the inner boundary of the He-layer ($r = 6.05 \times 10^9$ cm and $M_r = 3.8 M_\odot$), the temperature rises from 2.0×10^8 K to 5.8×10^8 K. The shock arrival time is 6.8 s. When the shock wave arrives at the boundary between the convective He-layer and the radiative He-layer at 63 s, the temperature at the boundary rises from

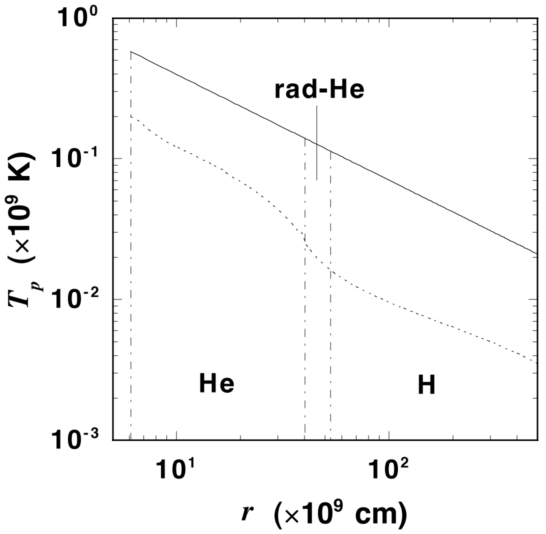

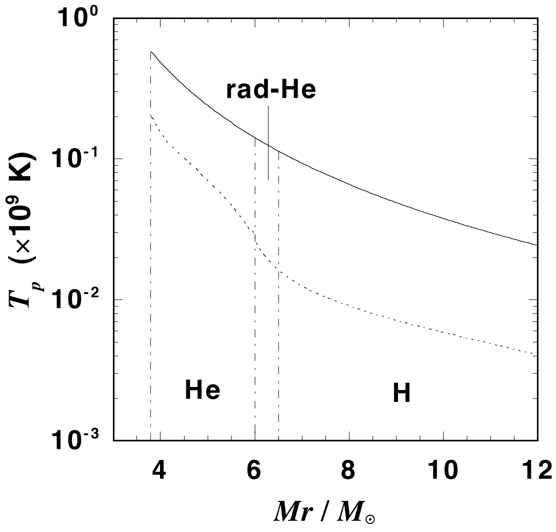

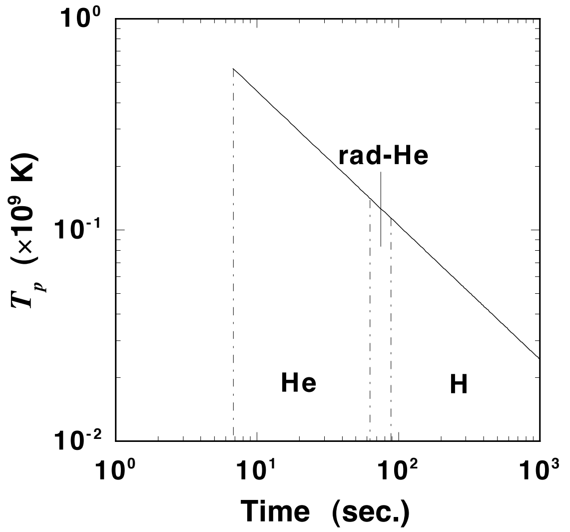

Fig. 3.3. The peak temperature, T_p, (solid line) at a give radius, r, (panel (a)), at a given mass coordinate, M_r, (panel (b)), and at a given time (panel (c)) and the temperature distribution in the presupernova stage (dashed line in panels (a) and (b)) in the case of the 16.2 $M_\odot$ supernova. Regions between two vertical dash-dotted lines and denoted by "He", "rad-He", and "H" are the convective He-layer, the radiative He-layer, and the H-rich envelope, respectively.

2.6×10^7 K to 1.4×10^8 K. Further, at the bottom of the H-rich envelope peak temperature of 1.1×10^8 K reaches at 88 s at the shock arrival. Peak temperatures in the cases of the 25 $M_\odot$, 20 $M_\odot$, and 15 $M_\odot$ supernovae are shown in Fig. 8.3 on page 139.

In order to confirm the validity of our explosion model, we will compare the propagation profile of the shock, which is evaluated from the 16.2 $M_\odot$ progenitor model, with that of the 14E1 model (Shigeyama and Nomoto 1990). Since numerical simulations of the shock propagations during the supernova explosions are not performed in the cases of the numerical models of the 25 $M_\odot$ and 20 $M_\odot$ progenitors (Iwamoto 1998) and thermal evolution during the supernova explosion of the 15 $M_\odot$ supernova is not written (Nomoto *et al.* 1993), we do not compare the thermal evolution of these supernovae and those of the corresponding numerical models. As a whole, the evaluated shock profiles of the 16.2 $M_\odot$ model coincide well with those of the 14E1 model. However, at the regions just outside the boundaries between the C-layer and the He-layer and between the He-layer and the H-rich envelope, the differences of the shock profiles become relatively large; especially the evaluated shock density is larger by a factor of 3 or 4 compared to that of 14E1 model. Nevertheless, we do not pay special attention to the density difference because we know that the material density does not play any important roles on the nucleosynthesis. The evaluated temperature is higher by 30% or so at the regions just outside the boundaries. In order to see how the inaccurate model temperature affects the final result of isotopic ratios in which we are interested (see, e.g., Fig. 5.5 on page 71), we calculated, as a test case, the explosive nucleosynthesis at the bottom of the He-layer ($r = 6.05 \times 10^9$ cm) assuming that the temperature during the explosion is decreased by 30% artificially. By the test calculations we found that the isotopic ratios can be reproduced properly within a factor of 3. The difference is not so important because in our study we take notice on the isotopic ratios of light elements in order of magnitude.

3.3. Model of neutrino emission

In Section 2.2 we briefly described reactions of the ν-process. In order to evaluate the reaction rates of the ν-process, we need to know the number flux of neutrinos, their energy spectra, and the time variations as well as the cross sections of the ν-process. Hereafter, we adopt a model of the flux evolution of neutrinos and antineutrinos adopted by Woosley *et al.* (1990), in which there are eight parameters, i.e., the total energy carried by neutrinos, E_ν, the temperature of each neutrino flavor, $T_{\nu i}$ ($\nu_i = \nu_{\rm e}, \nu_\mu, \nu_\tau, \bar{\nu}_{\rm e}, \bar{\nu}_\mu$, and $\bar{\nu}_\tau$), and the decay time of the neutrino flux, τ_ν.

A core collapse in a type II supernova liberates an enormous amount of gravitational energy, most of which is carried by neutrinos and antineutrinos. So, the total energy carried by neutrinos is almost equal to the gravitational binding energy of a formed neutron star. From these reasons, Woosley *et al.* (1990) evaluated E_ν to be 3×10^{53} erg based on a neutron star model proposed by Cooperstein (1988). The energy spectrum of i-flavor neutrinos was presented as the Fermi-Dirac distribution with a temperature, $T_{\nu i}$, and zero chemical potential. Cooperstein (1988) also showed that one half of the total neutrino energy is released within the first 2 s and most of the rest energy comes out over the next 10 s. On the basis of his results, Woosley *et al.* (1990) adopted a model that the number flux of i-flavor neutrino, $\phi_{\nu i}$, decreases exponentially with a decay time, $\tau_\nu = 3$ s:

$$\phi_{\nu i} = \frac{1}{6}\frac{1}{4\pi r^2}\frac{E_\nu}{\varepsilon_i}\frac{1}{\tau_\nu}e^{-\frac{t-r/c}{\tau_\nu}}\Theta(t - r/c), \tag{3.31}$$

where $\Theta(x)$ is the step function ($\Theta(x) = 1$ for $x > 0$ and 0 otherwise) and ε_i is the mean energy per particle of i-flavor neutrino, $\varepsilon_i = 3.15T_{\nu i}$ (Woosley *et al.* 1990). In most of this study we adopt the standard values of the total energy carried by neutrinos, E_ν, and the decay time of the neutrino flux, τ_ν, as (see also Section 4.1 on page 48)

$$E_\nu = 3 \times 10^{53}\ \text{ergs} \quad \text{and} \quad \tau_\nu = 3\ \text{sec}\ . \tag{3.32}$$

It should be noted that there are yet uncertainties in the equation of state of neutron star matter as well as the mass of the neutron star (e.g., Lattimer and Yahil 1989) and that τ_ν is determined by the diffusion transport which is affected in a complicated manner by the physical conditions of the deep stellar interior. So it is not always certain whether the above values of E_ν and τ_ν are proper or not. We will investigate sensitivities of the abundances and the isotopic/elemental ratios of the light elements to E_ν and τ_ν in Section 5. Hereafter, we set additional values of the decay time of the neutrino flux, τ_ν, and the total energy carried by neutrinos, E_ν, taking account of their uncertainties, as well as the temperature of each neutrino flavor, $T_{\nu i}$. The total energy carried by neutrinos in the cases of 25 $M_\odot$, 20 $M_\odot$, and 15 $M_\odot$ supernovae, adopted in Section 8, will be also presented.

The decay time of the neutrino flux is determined by the neutrino diffusion time of the interior of the collapsed core. According to the textbook of Bahcall (1989), the characteristic time of the neutrino irradiation is in a range between 1 s and 10 s. Arnett *et al.* (1989a) also estimated the neutrino emission time scale, which is from 1 s to 10 s. The time scale is equal to the total energy carried by neutrinos divided by the luminosity from all flavors of the neutrinos. Thus, for τ_ν we consider additional two cases where

$$\tau_\nu = 1 \text{ s} \quad \text{and} \quad 10 \text{ s}. \tag{3.33}$$

When we investigate the sensitivity of the light element production to the decay time of the neutrino flux, E_ν is fixed to be 3×10^{53} erg.

Cooperstein (1988) and Lattimer and Yahil (1989) evaluated the binding energy of a neutron star considering uncertainties of the equation of state of neutron star's matter. In Section 5 where we investigate the sensitivity of the light element production to the uncertainty of the total energy carried by neutrinos, we artificially set the mass of a neutron star to be ranging between 1 $M_\odot$ and 2 $M_\odot$ as the uncertainty though the progenitor's mass is fixed to be 16.2 $M_\odot$. The lowest value of the mass is smaller than the mass of the core of 11 $M_\odot$ presupernova and the highest is more than the mass of the core of 40 $M_\odot$ progenitor in Woosley and Weaver (1995). In this mass range, the evaluated energy range is between 1×10^{53} and 4×10^{53} erg in Cooperstein (1988) and 1.5×10^{53} and 6×10^{53} erg in Lattimer and Yahil (1989). Thus, we consider additional two cases, i.e.,

$$E_\nu = 1 \times 10^{53} \quad \text{and} \quad 6 \times 10^{53} \quad \text{erg} . \tag{3.34}$$

In these cases, τ_ν is fixed to be 3 s.

The total energy carried by neutrinos depends on the stellar mass through the mass of the formed neutron star. In Section 8 we adopt the total energy carried by neutrinos considering the stellar mass as follows. Lattimer and Yahil (1989) evaluated the relation between the gravitational mass of a neutron star, M_g, and the binding energy, $E_{\rm bin}$, by the use of observational data of SN 1987A. The obtained relation is written as

$$E_{\rm bin} = 1.5(M_g/M_\odot)^2 \times 10^{53} \quad \text{erg}. \tag{3.35}$$

Thielemann *et al.* (1996) evaluated the gravitational mass of the neutron star as well as the mass of progenitor's core in the cases of 25 $M_\odot$, 20 $M_\odot$, and 15 $M_\odot$ supernovae. Substituting the gravitational masses of the formed neutron stars of the 25 $M_\odot$, 20 $M_\odot$, and 15 $M_\odot$ supernovae obtained in Thielemann *et al.* (1996) into Eq. (3.35), we evaluate the total energies carried by neutrinos in the cases of these supernovae. The obtained total energy carried by neutrinos is tabulated in Table 3.4 together with the gravitational mass of the neutron star, M_g.

Woosley *et al.* (1990) estimated theoretically neutrino temperatures and obtained the result with some uncertainties that temperatures of $e-$, μ-, and τ-neutrinos are $T_{\nu e} \simeq 4$ to 5 MeV/k (k being the Boltzmann constant), $T_{\nu\mu} \simeq 8$ to 10 MeV/k, and $T_{\nu\tau} \simeq 8$ to 10 MeV/k, respectively. Considering the observational data of 1987A which suggest

Table 3.4. Total energy carried by neutrinos and the gravitational mass of the neutron star in the cases of the 25 $M_\odot$, 20 $M_\odot$, and 15 $M_\odot$ supernova models.

	E_0 (erg)	M_g ($M_\odot$)
25 $M_\odot$ model	3.7×10^{53}	1.56
20 $M_\odot$ model	3.2×10^{53}	1.45
15 $M_\odot$ model	2.2×10^{53}	1.21

$T_{\nu e} \simeq 3$ to 4 MeV/k (Burrows and Lattimer 1987), they used the smallest values estimated theoretically. Although there are still uncertainties on the neutrino temperatures, we also adopt the same values as Woosley *et al.* (1990) in the present study:

$$T_{\nu e} = T_{\bar{\nu} e} = 4 \text{ MeV}/k \quad \text{and} \quad T_{\nu\mu} = T_{\bar{\nu}\mu} = T_{\nu\tau} = T_{\bar{\nu}\tau} = 8 \text{ MeV}/k \; . \tag{3.36}$$

Woosley *et al.* (1990) investigated the sensitivity of the X-element production to $T_{\nu i}$. Their result shows that the variety of the amounts of the X-elements is within a factor of 3. As we will present in Section 5, the variety due to the uncertainties of τ_ν and E_ν extends over five orders of magnitude in some cases, so that the variety due to $T_{\nu i}$ is not so important. Woosley *et al.* (1990) also checked the sensitivity to the chemical potentials and found again that the varieties are small. So, we do not investigate the sensitivity to the chemical potentials of the neutrino energy spectra.

3.4. Model of mixing between the He-layer and the H-rich envelope

A progenitor of a type II supernova consists of multiple layers with different chemical compositions. At a boundary between adjacent layers, there appears a density gap owing to the difference of the mean molecular weights, μ, and the continuity of the temperature and the pressure. In the case of the boundary between the He-layer and the H-rich envelope, the density gap is given by

$$\frac{\rho_{\rm He} - \rho_{\rm H}}{\rho_{\rm He} + \rho_{\rm H}} = \frac{\mu_{\rm He} - \mu_{\rm H}}{\mu_{\rm He} + \mu_{\rm H}} = 0.32, \qquad (3.37)$$

where $\rho_{\rm He}$ and $\rho_{\rm H}$ are the densities at the top of the He-layer and the bottom of the H-rich envelope, respectively. As for the mean molecular weight we put to be $\mu_{\rm He} = 1.34$ and $\mu_{\rm H} = 0.69$ (which correspond to the adopted chemical compositions of the two layers; see Section 3.5). When a shock front passes across the chemical boundary, fluid near the boundary becomes unstable against the Rayleigh-Taylor instability (Ebisuzaki *et al.* 1989). In the case of $\omega < 3$ where ω is the power law index of the density profile (i.e., $\omega = -d\ln\rho/d\ln r$; see Eq. (3.1)), the velocity of the shock front decreases gradually with time because the shock front pushes outer fluid and, as a result, the fluid behind the shock is decelerated oppositely. In other words, fluid feels outward inertia force. Thus, the fluid near the boundary sphere, across which there is an appreciable density gap, becomes unstable under the action of the outward inertia force. Since the inertia force per unit mass is equal to the acceleration due to pressure force (Chevalier 1976), the fluid of the heavy He-layer component penetrate into the light H-rich envelope with a time of the order of

$$\tau_m \sim 1/\sqrt{\frac{1}{l}\left|\left(-\frac{1}{\rho}\right)\frac{\partial P}{\partial r}\right|} \quad , \qquad (3.38)$$

where l is the mixing length and $\partial P/\partial r$ is the pressure gradient at the boundary just after the shock passage. According to the linear analysis of the Rayleigh-Taylor instability, the characteristic growth time of the instability, $\tau_{\rm RT}$, is given by (Chandrasekhar 1981)

$$\tau_{\rm RT} = 1/\sqrt{\frac{\rho_{\rm He} - \rho_{\rm H}}{\rho_{\rm He} + \rho_{\rm H}}\,\kappa\,\left|\left(-\frac{1}{\rho}\right)\frac{\partial P}{\partial r}\right|}, \qquad (3.39)$$

where κ is the azimuthal wave number of perturbations. When the mixing length is of the order of a reciprocal of κ, τ_m is nearly the same as $\tau_{\rm RT}$.

Many authors investigated the Rayleigh-Taylor instability during the supernova explosions by numerical simulations and presented us snapshots of the development of

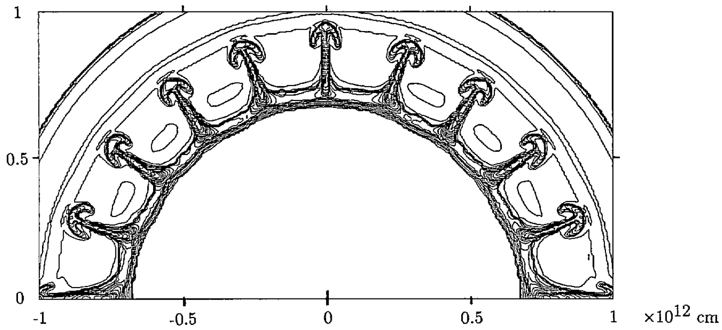

Fig. 3.4. Mushroom-like structure of plumes due to the Rayleigh-Taylor instability during the supernova explosion. This figure is reprinted from Fig. 1 in Hachisu *et al.* (1990).

stellar-scale mixing inside a supernova (e.g., Arnett *et al.* 1989b; Hachisu *et al.* 1990, 1991, 1992, 1994; Fryxell *et al.* 1991; Herant and Woosley 1994; Iwamoto *et al.* 1997). An example of the snapshots is illustrated in Fig. 3.4. As seen from this figure, fluid element originated from the He-layer (and also from the deeper layers) penetrates into the H-rich envelope in the form of plumes (i.e., mushroom-like structure). Although we cannot see a detailed process of material mixing from the numerical simulations, plumes seem to grow into the H-rich envelope keeping its original chemical components as well as the proper entropy because the plumes arise up within a short time interval (i.e., the time of dynamical change).

So, we can expect that material mixing is described by the following simple fashion:

(1) The fluid element originated from the He-layer is transported to a certain point of the H-rich envelope and mixes there with the fluid element of the H-rich envelope (the former and the latter fluid components which will be mixed are hereafter called simply the He- and H-components, respectively).

(2) Material mixing occurs after a certain time interval since the shock arrives at the He/H boundary. The temperature and the pressure of the mixture become suited

quickly to the surrounding gas.

In order to include material mixing in our nucleosynthetic simulation, we have to know the following quantities.

1. Original location of the He-component, M_m(He) (note that the location is described in term of the internal mass coordinate).

2. Location of the material mixing in the H-rich envelope, M_m(H).

3. Time of the material mixing, t_m (which will be hereafter called the mixing time).

4. The mixing ratio between the two fluid components, x.

5. Temperature and density of the mixture.

Since we have no knowledge about these quantities, we adopt a simply parameterized model as stated below.

As for M_m(He) and M_m(H), we consider eight and seven cases, respectively, for the 16.2 $M_\odot$ model. They are tabulated in Table 3.5 (on page 43) together with the corresponding radial distance r_m(He) and r_m(H) at a time when the shock arrives at the He/H boundary. According to Hachisu *et al.* (1992) and Herant and Woosley (1994), plumes originated from the He-layer penetrate to the outermost part of the H-rich envelope. However, we do not consider such a distant mixing because the plume temperature becomes too low to bring about any nuclear reactions (see also Section 7).

The mixing time, t_m, would be properly written as

$$t_m = t_a + \tau_m \,, \tag{3.40}$$

where t_a is a time of the shock arrival at the H/He boundary. Furthermore, τ_m is the time interval between the shock arrival and the occurrence of the mixing and is given by

Eq. (3.38) as an order of magnitude. In this study, we define the mixing time interval as

$$\tau_m = c_m \sqrt{\kappa l} \tau_{\rm RT}, \tag{3.41}$$

where we introduce c_m as a numerical parameter of the order of unity to take account of uncertainties: c_m is put to be 1 (the standard value), 0.5, 2, and 5. In evaluating τ_m, the mixing length l is taken to be $r_m(\rm H) - r_m(\rm He)$. Note that we need not provide the value of κ.

It is difficult to determine theoretically the mixing ratio between the two layer's components, x, which is defined as the mass fraction of a mixed fluid of the H-component. In our present study, we consider the following cases:

$$\begin{aligned} x \;=\; & 0,\, 1\times10^{-5},\, 1\times10^{-4},\, 1\times10^{-3},\, 2\times10^{-3},\, 5\times10^{-3},\, 1\times10^{-2}, \\ & 2\times10^{-2},\, 5\times10^{-2},\, 0.1,\, 0.3,\, 0.5,\, 0.7,\, 0.9, 0.999, 0.99999, \text{ and } 1.0. \end{aligned} \tag{3.42}$$

The cases of x=0 and 1.0 correspond to the pure He-component and the pure H-component, respectively. Since most of the X-elements are decomposed by a small amount of protons in the mixture (see Section 7), we set many cases of the mixing with a small ratio of the H-component.

As mentioned earlier, plumes stand up almost adiabatically in their growing stage. However, after the He-component mixes with the gases of the H-rich envelope, the temperature and the pressure of the mixture should become the same as those of the surrounding gas of the H-rich envelope. Thus, we presume that the density and the temperature of the mixture is determined by the following simple manner:

$$\rho_m = \frac{\mu_m}{\mu_{\rm H}} \rho_{\rm H} \quad \text{and} \quad T_m = T_{\rm H}, \quad \text{for} \quad t \geq t_m \tag{3.43}$$

where $\rho_{\rm H}$ and $T_{\rm H}$ are, respectively, the density and the temperature at the location of mixing(i.e., $M_r = M_m(\rm H)$). Furthermore, μ_m is the mean molecular weight of the mixture and is given by

$$\mu_m^{-1} = \frac{1-x}{\mu_{\rm He}} + \frac{x}{\mu_{\rm H}}\,. \tag{3.44}$$

Table 3.5. Original location of a fluid component in the He-layer, M_m(He), and location of mixing in the H-rich envelope, M_m(H). The radii, r_m(He) and r_m(H), corresponding to M_m(He) and M_m(H) are also shown in the units of $r_0 = 1 \times 10^9$ cm. The mixing time interval, τ_m, is presented in the case of c_m=1. The positions of 7 and 8 of the He-layer components are in the radiative He-layer.

	He-layer component			H-rich envelope component		
	Location (M_m(He)/$M_\odot$)	Radius (r_m(He)/r_0)	τ_m (s)	Location (M_m(H)/$M_\odot$)	Radius (r_m(H)/r_0)	τ_m (s)
1	3.80	40.0	1.76×10^2	6.50	52.7	7.19×10
2	4.00	41.1	1.68×10^2	6.80	62.1	1.68×10^2
3	4.50	43.6	1.49×10^2	7.20	62.1	2.89×10^2
4	5.00	46.0	1.27×10^2	7.60	91.6	3.17×10^2
5	5.50	48.4	1.03×10^2	8.00	109	3.79×10^2
6	6.00	50.57	7.19×10	8.40	129	4.38×10^2
7	6.03	50.65	7.04×10	8.80	151	4.94×10^2
8	6.40	52.3	3.14×10			

3.5. Initial chemical compositions

The chemical compositions just before the supernova explosion are generally to be determined as a result of the evolution of its progenitor. Until now, many works were made on the evolution of progenitors of supernovae (e.g., Weaver and Woosley 1993; Nomoto and Hashimoto 1988). In such works, however, some authors concentrated on special supernova events and other authors did not take account of nuclear species which play an important role on our study. So, in the present study, we prepare by ourselves the chemical compositions just before the supernova explosion by the following way.

It should be noted that the chemical compositions in the H-rich envelope depend strongly on whether the convective region develops in the envelope or not. Lamb *et al.*

(1976) pursued the evolution of a 25 $M_\odot$ star after the main sequence stage and showed that there is a convective region in the inner part of the H-rich envelope. Furthermore, Saio *et al.* (1988) pursued the evolution of the progenitor of SN1987A and showed that a large scale convection occurs in the H-rich envelope. So we expect that there is a convective region in the inner H-rich envelope of a 16.2 $M_\odot$ star. In the convective region, the chemical compositions would be determined by the steady-flow equilibrium condition of the H-burning. The equilibrium chemical abundance is calculated by using a small reaction network composed of shaded nuclear species in Fig. 2.1 (see page 18). The temperature and the density at the bottom of the H-rich envelope are, respectively, taken to be 4×10^7 K and 5 g/cm^3 after Lamb *et al.* (1976) and the mass fractions of ^{1}H and ^{4}He are put to be 0.565 and 0.430, respectively (Shigeyama and Nomoto 1990). For isotopes which do not take part in the small reaction network (i.e., unshaded isotopes in Fig. 2.1 on page 18), the mass fractions are set artificially to be 1×10^{-50}, which is the smallest value in our calculation. Note that we adopt ^{7}Be abundance in the steady-flow equilibrium as initial ^{7}Li abundance in the H-rich envelope and initial ^{7}Be abundance is set to be 1×10^{-50} because it is expected that ^{7}Be produced in the H-burning shell is converted to ^{7}Li by the electron-capture process in outer and cooler part of the H-rich envelope. Although the abundances of ^{1}H and ^{4}He, exactly speaking, change in the course of the H-shell burning, the steady-flow equilibrium abundances of the CNO-elements are hardly affected by the ^{1}H and ^{4}He abundances. The abundances of X-elements (i.e., Li, Be, and B) vary with the ^{4}He abundance almost proportionally. However, these variations are not important because their abundances are very small compared with those produced by the explosive nucleosynthesis.

Shigeyama and Nomoto (1990) studied the chemical compositions in the He-layer of a 6.0 $M_\odot$ He star (corresponding to a 16.2 $M_\odot$ star) modeled by Nomoto and Hashimoto (1988). Unfortunately, they did not give a detailed description on the time variation of the chemical composition nor take account of some species in which we are interested. So we adopt the radial locations of the boundaries of distinct layers from Nomoto and Hashimoto (1988) and we prepare the chemical compositions originally. In this model the inner region of the He-layer ($3.8M_\odot \leq M_r \leq 6.0M_\odot$) is convective and the outer region ($6.0M_\odot \leq M_r \leq 6.5M_\odot$) is radiative. In the outer radiative region, the chemical compositions would be determined originally at the stage of the H-burning and may not suffer from further nuclear burning processes. So, as the initial chemical compositions in this region, we adopt those of ashes of the H-burning; the chemical compositions are evaluated by solving the nuclear reaction network until the mass fraction of ^{1}H decreases to 1×10^{-5} (e.g., Woosley *et al.* 1990) under the same physical condition at the bottom of the H-rich envelope. For the compositions in the inner convective region of the He-layer, we adopt those of the He-burning products when the mass fraction of ^{4}He decreases to 0.930 (i.e., when the stellar core begins to collapse (Nomoto and Hashimoto 1988)). The chemical compositions are calculated by using our nuclear reaction network (see Fig. 2.1). The obtained initial mass fractions of important species are illustrated in Fig. 3.5. Note that the abundances of X-elements are very little in the whole regions of the He-layer and the H-rich envelope.

The initial chemical compositions are different from those of Woosley *et al.* (1990). After Woosley *et al.* (1990), some reaction rates, especially concerned to oxygen, are updated as mentioned in Section 2 (see page 19). As a result, the initial amounts of the CNO-elements should be recalculated. Convective mixing during the stellar evolution is also expected to affect the initial composition, so that we include this effect for the determination of the initial composition.

In order to evaluate the variety of the light element production due to the initial chemical compositions, we will set 4-component models of the initial chemical composition which consist of ^{1}H, ^{4}He, ^{12}C, and ^{16}O in Section 6.1 (see page 73). Further, we will set another model of the initial chemical composition in order to investigate the decomposition processes of the light elements (see Section 6.1.2 on page 75).

We also prepare the initial compositions of the He-layer and the H-rich envelopes of 25 $M_\odot$, 20 $M_\odot$, and 15 $M_\odot$ presupernovae. Among these presupernovae, the chemical compositions in the H-rich envelope are determined by the steady-flow equilibrium composition. The temperatures and the densities are commonly taken to be 4×10^7 K and 5 g/cm^3, respectively, and the mass fractions of ^{1}H and ^{4}He are 0.565 and 0.430, respectively. The chemical compositions in the radiative He-layer are commonly determined as the compositions of the ashes of H-burning when the mass fraction of ^{1}H decreases to 1×10^{-5}. The chemical compositions in the convective He-layer are determined as the compositions of the He-burning products when the mass fraction of ^{4}He decreases to 0.950, 0.930, and 0.940 in the cases of 25 $M_\odot$, 20 $M_\odot$, and 15 $M_\odot$ progenitors (i.e., when the corresponding stellar cores begin to collapse (Nomoto and Hashimoto 1988)).

The initial mass fractions of important species in the three presupernovae are also presented in Fig. 3.5 (see the next page). The abundances of the X-elements are very small in the He-layer and the H-rich envelope of all progenitors. Only ^{7}Li in the H-rich envelope is the level of 1×10^{-11} and these of the other elements are much smaller. Hence, almost all of the X-elements are produced by the explosive nucleosynthesis. In the all presupernova models the abundances of ^{12}C and ^{16}O are large in the convective He-layer and the abundance of ^{14}N is large in the radiative He-layer and the H-rich envelope. So, most of the light elements are expected to be produced from ^{1}H, ^{4}He, ^{12}C, and ^{16}O. In the convective He-layer, the abundances of ^{14}N and ^{18}O are large in the cases of the 15 $M_\odot$ progenitor (Fig. 3.5h) but small in the case of the 25 $M_\odot$ progenitor (Fig. 3.5d). The triple α-reactions proceed effectively in the case of the 15 $M_\odot$ star because the density at the bottom of the He-layer of the 15 $M_\odot$ progenitor is large compared with those of the 20 $M_\odot$ and 25 $M_\odot$ progenitors.

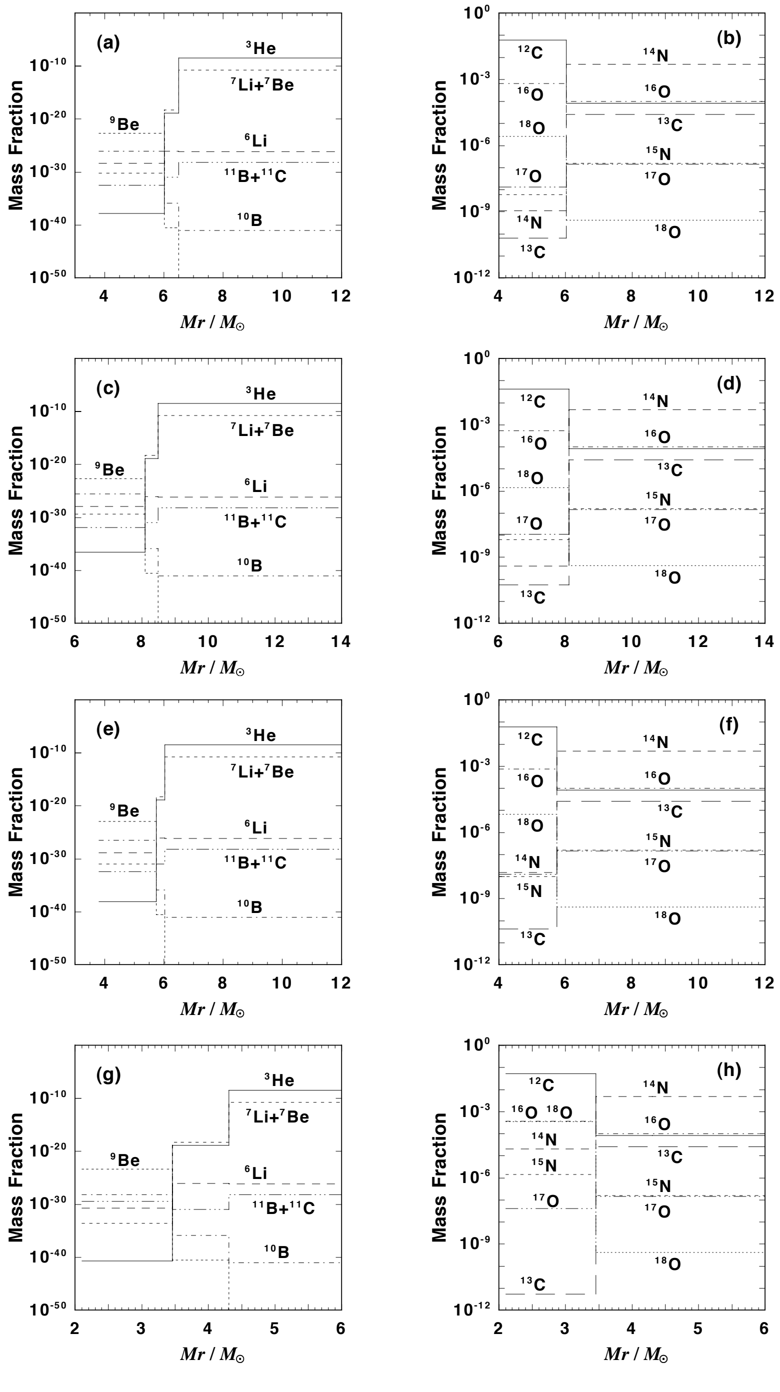

Fig. 3.5. Initial mass fractions of ^{3}He, ^{6}Li, ^{7}Li+^{7}Be, ^{9}Be, ^{10}B, and ^{11}B+^{11}C (left panels) and ^{12}C, ^{13}C, ^{14}N, ^{15}N, ^{16}O, ^{17}O, and ^{18}O (right panels). Panels (a) and (b) show the distribution of the light elements in 16.2 $M_\odot$ progenitor. Panels (c) and (d), (e) and (f), and (g) and (h) show those in 25 $M_\odot$, 20 $M_\odot$, and 15 $M_\odot$ progenitors. Horizontal axis shows the internal mass coordinates, M_r, in the unit of the solar mass, $M_\odot$.

4. Light Element Synthesis in the Case of the Standard Model

The amounts of isotopes synthesized in the supernova explosion depend, by a complicated manner, on the neutrino emission model, the chemical compositions of the progenitors, the mixing between the He-layer and the H-rich envelope and the following nuclear reprocessing, and the stellar mass as well as the temporal and spatial points we observe. So, at first, we should confirm in general how the light elements are synthesized in the supernova explosions. In this section, we first define the structure of the progenitor, the explosion model, the neutrino emission model, the chemical composition of the progenitor, and the mixing process of the standard model of the supernova explosion in order to grasp its general behaviors of the light element synthesis in the supernova explosion. Next, we will show the explosive nucleosynthesis of the light elements in the He-layer and the H-rich envelope of the supernova only in the case of the standard model. Sections 4.2 to 4.4 are reprinted from Sections 4.1 to 4.3 in Yoshida, Emori, and Nakazawa (2000) and Section 4.5 is reprinted from a part of Section 6 in Yoshida, Emori, and Nakazawa (2000).

4.1. The standard model

We define physical parameters characterizing the structure of the progenitor, the dynamics of the supernova explosion, the neutrino emission, the mixing process, and the chemical composition of the progenitor of the standard model as follows:

- The density structure of the progenitor is given by Eqs. (3.1) and (3.2), which is approximated by the 16.2 $M_\odot$ progenitor model calculated numerically by Shigeyama and Nomoto (1990).

- The explosion model is adopted from the 16.2 $M_\odot$ supernova explosion model constructed in Section 3.2.

- The decay time of the neutrino flux, τ_ν, is put to be 3 s, and the total energy carried by neutrinos, E_ν, is put to be 3×10^{53} erg.

- The chemical compositions of the progenitor is determined by the way described in Section 3.5 in the case of the 16.2 $M_\odot$ progenitor. The mass fractions of the main components of the light elements are taken from the compositions shown in Figs. 3.5 (a) and (b).

- The mixing process between the He-layer and the H-rich envelope and the following the nuclear reprocessing in the mixture are not considered.

In the case of the standard model, i.e., the above physical parameters, we will see the explosive nucleosynthesis of the light elements and their produced amounts. On the basis of the results, we will investigate the varieties of the light element synthesis due to the various physical parameters such as the neutrino emission, the initial chemical compositions, the mixing process, and the mass of the progenitor.

4.2. General behavior of X-element synthesis

In Fig. 4.1, we illustrate the time variation of the amount of ^{7}Li for typical internal mass coordinates. Although, at a glance, the abundance curves behave quite differently from point to point of the internal mass coordinates, the abundance evolution is generally divided into three stages: the preshock stage, the shock-induced (explosive) burning stage, and the freezing stage. In the first stage (i.e., the preshock stage) before the arrival of the explosive shock wave, the X-elements are synthesized through various kinds of the ν-processes and subsequent nuclear reactions. For ^{7}Li, ^{4}He$(\nu, \nu' p)^3$H$(\alpha, \gamma)^7$Li and/or ^{4}He$(\nu, \nu' n)^3$He$(\alpha, \gamma)^7$Be$(e^-, \nu_e)^7$Li are the major formation reactions in the He-layer. In the inner region ($M_r \lesssim 5 M_\odot$, see Fig. 4.3 on page 52), the neutrino flux is so intensive that a large amount of ^{7}Li is synthesized. In the outer region the amount of synthesized ^{7}Li decreases with a decrease in the neutrino flux and ^{7}Li is hardly formed near the bottom of the H-rich envelope (i.e., at $M_r = 6.5M_\odot$), since neutrino flux is 1.3×10^{-2} times as small as that at the innermost region of the He-layer (i.e., at $M_r = 3.8M_\odot$).

The second (the shock-induced burning) stage starts at the moment of the shock arrival and ends when the temperature becomes sufficiently low owing to the expansion accompanied with the adiabatic cooling. By a sudden increase in temperature, new channels of nuclear reactions open; some isotopes which are synthesized by the ν-processes are changed to ^{11}B and some isotopes are newly formed through various kinds of nuclear reactions. For example, ^{7}Li produced by the ν-process is destroyed abruptly and almost completely through ^{7}Li$(\alpha,\gamma)^{11}$B in the innermost region whereas ^{7}Li is formed by ^{3}H$(\alpha,\gamma)^7$Li in the outer region. In the last stage where the temperature is too low, there occurs no nuclear reactions except the beta processes and the abundance is frozen to the level of the end of the second stage if no beta processes play an important role.

Similar behavior is seen from Fig. 4.2 where the abundance evolution of ^{11}B is shown. Spikes observed at $t = 7$ s ($M_r = 3.8M_\odot$) and $t = 27$ s ($M_r = 5.0M_\odot$) are the result of the sudden production of ^{11}B through ^{7}Li(α,γ) ^{11}B, as mentioned in the last paragraph, just after the shock arrival and of the rapid disruption due to ^{11}B$(p,\alpha\alpha)^4$He and ^{11}B$(\alpha,n)^{14}$N. In the case of ^{11}B, the abundance increase gradually even in the third stage. This is due to the β^+-decay of ^{11}C with the decay time of 1.8×10^3 s (Thomas *et al.* 1993).

As seen from Figs. 4.1 and 4.2, the amounts of the X-elements vary from point to point of the internal mass coordinates. The distribution of the final abundances of the X-elements are illustrated in Fig. 4.3. The final abundance depends complicatedly on the initial chemical composition, neutrino flux, and time of the shock arrival. In the He-layer, the most abundant X-elements are ^{7}Li and ^{11}B. Production of all X-elements

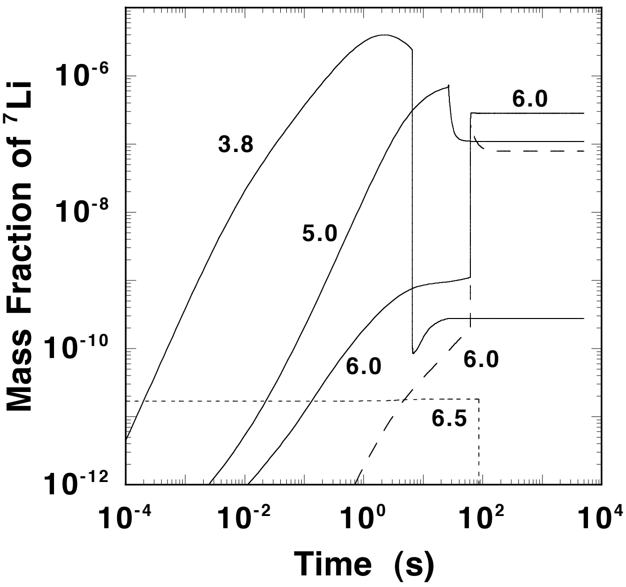

Fig. 4.1. Time variation of the amount of ^{7}Li. Solid lines are of the time evolution in the convective He-layer. Attached numbers indicate the internal mass coordinates. Dashed and dotted lines show the time evolutions at the bottom of the radiative He-layer and at the bottom of the H-rich envelope, respectively.

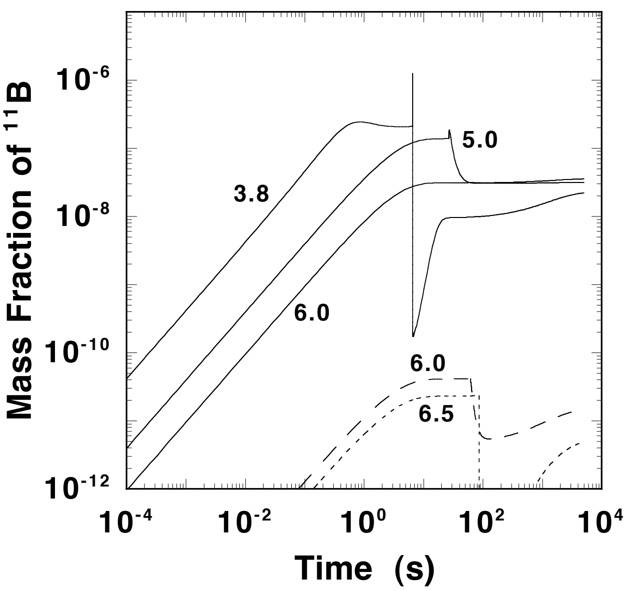

Fig. 4.2. The same as Fig. 4.1, but for ^{11}B.

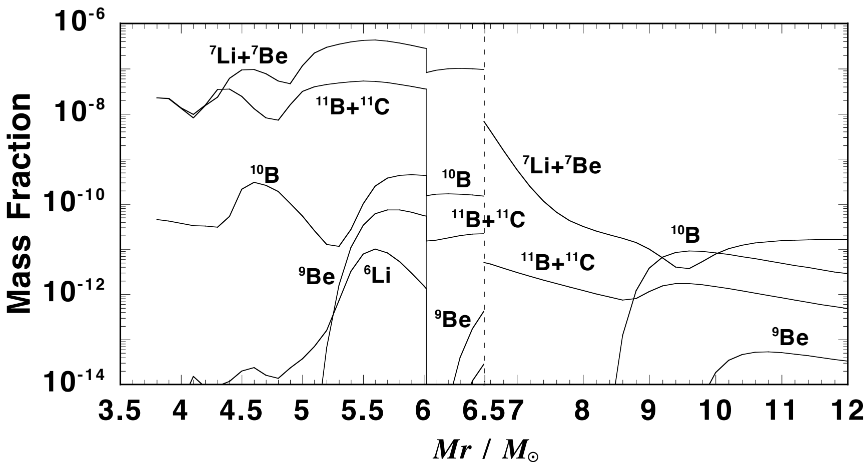

Fig. 4.3. Distribution of the final abundances of the X-elements. Discontinuities of the curves appear at the boundaries between the convective and the radiative He-layers ($M_r = 6.0 M_\odot$) and between the radiative He-layer and the H-rich envelope ($M_r = 6.5 M_\odot$).

(as well as ^{11}C) is initiated by the ν-processes, ^{4}He+ν and ^{12}C+ν, and the amounts produced during the preshock stage are almost same. However, after the shock passage, they are recooked by hot nuclear reactions; especially, ^{6}Li and ^{9}Be are disrupted almost completely. In the H-rich envelope (but $M_r \lesssim 8.0 M_\odot$), only ^{7}Li is synthesized through $^4\mathrm{He}(\nu, \nu' n)^3\mathrm{He}(\alpha, \gamma)^7\mathrm{Be}(e^-, \nu_\mathrm{e})^7\mathrm{Li}$ by an appreciable amount. The production of the other X-elements are inactive in the H-rich envelope: their mass fractions are lower than a level of 1×10^{-10}.

Key reactions (production and decomposition reactions) which play important roles on determining the abundances of the light elements are shown in Table 4.1. As a matter of course, key reactions vary from point to point as well as from time to time so that in the table only typical reactions are tabulated. In the preshock stage, the X-elements are synthesized, mainly, through the ν-processes with the target nuclei of ^{4}He and ^{12}C. In the shock-induced burning stage, various kinds of nuclear reactions take part in the formation and destruction of the X-elements.

Table 4.1. Typical key reactions of light element synthesis. The upper and lower columns show the formation and decomposition reactions, respectively. Furthermore, empty columns mean that there are no appreciable formation (or decomposition) processes.

	Convective He-layer			Radiative He-layer	H-rich envelope
$M_r/M_\odot$	4.0 4.2 4.4 4.6 4.8 5.0	5.6		6.0	6.5 7.2 7.5
^{6}Li	^{9}Be$(p,\alpha)^6$Li				
	^{6}Li$(p,\alpha)^3$He				
^{7}Li	^{4}He$(\nu,\nu'n)^3$He$(\alpha,\gamma)^7$Be$(e^-,\nu_e)^7$Li, ^{7}Be$(n,p)^7$Li	^{4}He$(\nu,\nu'p)^3$H$(\alpha,\gamma)^7$Li			^{3}He$(\alpha,\gamma)^7$Be$(e^-,\nu_e)^7$Li, ^{14}N$(\nu,\nu'\alpha)^{10}$B$(p,\alpha)^7$Be$(e^-,\nu_e)^7$Li
	^{7}Be$(\alpha,\gamma)^{11}$C	^{7}Li$(\alpha,\gamma)^{11}$B	^{7}Li$(p,\alpha\gamma)^4$He		
^{9}Be	^{7}Li$(t,n)^9$Be, ^{12}C$(\nu,\nu'\,^3$He$)^9$Be				
	^{9}Be$(p,\alpha)^6$Li, ^{9}Be$(p,d\alpha)^4$He, ^{9}Be$(\alpha,n)^{12}$C				
^{10}B	^{12}C$(\nu,\nu'np)^{10}$B			^{14}N$(\nu,\nu'\alpha)^{10}$B	
	^{10}B$(\alpha,p)^{13}$C	^{10}B$(p,\alpha)^7$Be	^{10}B$(n,\alpha)^7$Li	^{10}B$(p,\alpha)^7$Be	
^{11}B	^{12}C$(\nu,\nu'n)^{11}$C$(,e^+\nu_e)^{11}$B or ^{11}C$(n,p)^{11}$B, ^{7}Li$(\alpha,\gamma)^{11}$B	^{12}C$(\nu,\nu'p)^{11}$B, ^{12}C$(\nu,\nu'n)^{11}$C$(,e^+\nu_e)^{11}$B			
	^{11}B$(\alpha,n)^{14}$N	^{11}B$(p,\alpha\alpha)^4$He			
^{13}C	^{12}C$(p,\gamma)^{13}$N$(n,p)^{13}$C or ^{13}N$(,e^+\nu_e)^{13}$C	^{12}C$(n,\gamma)^{13}$C			
	^{13}C$(\alpha,n)^{16}$O				
^{14}N	^{11}B$(\alpha,n)^{14}$N				
^{15}N	^{18}O$(p,\alpha)^{15}$N				
	^{15}N$(\alpha,p)^{12}$C				^{14}N$(p,\gamma)^{15}$O$(,e^+\nu_e)^{15}$N
^{17}O	^{16}O$(n,\gamma)^{17}$O				
^{18}O					^{17}O$(p,\gamma)^{18}$F$(,e^+\nu_e)^{18}$O
	^{18}O$(\alpha,\gamma)^{22}$Ne ^{18}O$(p,\alpha)^{15}$N				^{18}O$(p,\alpha)^{15}$N

4.3. ^{6}Li and ^{9}Be production

As mentioned briefly in the previous subsection, ^{6}Li and ^{9}Be are scarcely produced during the supernova explosion. Here we will see in detail the formation processes of these two isotopes and discuss the reasons of the rare production.

In the He-layer ^{6}Li is commonly produced through ^{9}Be$(p,\alpha)^6$Li. Nevertheless, we cannot find the curve of ^{6}Li in Fig. 4.3 except the narrow region where 5.3 $M_\odot \lesssim M_r \lesssim$ 6.0 $M_\odot$. In the inner region where $M_r \lesssim 5.3 M_\odot$ ^{6}Li is formed by an appreciable amount (say, a level of 3×10^{-10} by mass fraction) owing to the neutrino irradiation. However, as soon as the shock front reaches ^{6}Li is completely decomposed through ^{6}Li$(p,\alpha)^3$He. In the outer region where $5.3 M_\odot \lesssim M_r \lesssim 6.0 M_\odot$, a little amount of ^{6}Li can survive because the temperature is not so high (compared with that in the inner region) even just after the passage of the explosive shock. In the radiative He-layer and the H-rich envelope ^{6}Li is produced and decomposed through the same processes as those in the convective He-layer. However, in these regions the initial abundance of ^{12}C, which is a seed isotope of ^{6}Li, is very low (about three orders of magnitude below) and the neutrino flux dilutes by about two orders of magnitude compared with those in the inner convective region. As a result, the amount of produced ^{6}Li is suppressed under the low level. Furthermore, ^{6}Li (as well as ^{7}Li) is hardly produced (nor decomposed) in the outermost H-rich envelope ($M_r \gtrsim 11 M_\odot$) since the shock temperature is very low and the neutrino flux is very weak. Thus, the amount of produced ^{6}Li is less than 1×10^{-15} by mass fraction throughout the H-rich envelope.

For ^{9}Be, the situation is quite the same as in the case of ^{6}Li. In the convective He-layer, ^{9}Be is produced through ^{12}C$(\nu,\nu'^3\text{He})^9$Be in the preshock stage, ^{7}Li$(t,n)^9$Be in the shock-induced burning stage. In the radiative He-layer and the H-rich envelope, ^{13}C$(\nu,\nu'\alpha)^9$Be is a dominant reaction in the preshock stage. In the He-layer as well as the H-rich envelope, ^{9}Be is commonly decomposed through ^{9}Be$(p,\alpha)^6$Li, ^{9}Be$(p,n\alpha)^4$He or ^{9}Be$(\alpha,n)^{12}$C in the shock-induced burning stage. With an increase in radius in the convective He-layer, the amount of ^{9}Be firstly becomes larger owing to less decomposition and becomes smaller again since the neutrino flux becomes smaller owing to the geometrical effect. As in the case of ^{6}Li, the amount of ^{9}Be becomes appreciable only in the outer region where 5.3 $M_\odot \lesssim M_r \lesssim$ 6.0 $M_\odot$ in the He-layer.

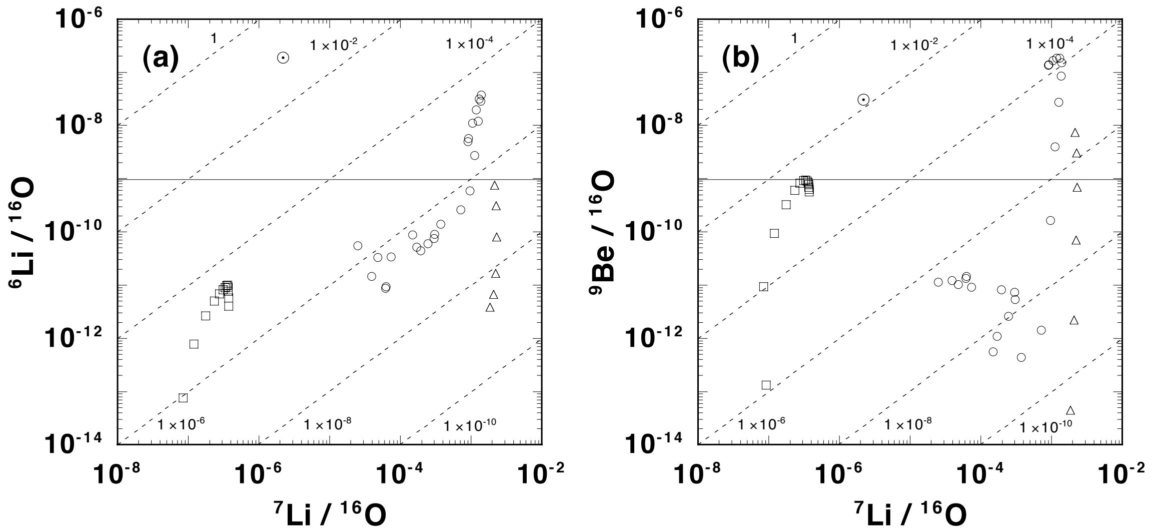

Fig. 4.4. Diagrams between ^{6}Li/^{16}O and ^{7}Li/^{16}O ratios (panel (a)) and between ^{9}Be/^{16}O and ^{7}Li/^{16}O ratios (panel (b)). The ratios are all in number. Circles, triangles, and squares show the ratios in the convective He-layer, in the radiative He-layer, and in the H-rich envelope, respectively. A mark $\odot$ shows the ratios of the solar-system composition. A solid horizontal line indicates the detection limit, i.e., the number ratio of species to ^{16}O equal to 1×10^{-9}. Furthermore, dotted lines indicate values of constant ^{6}Li/^{7}Li ratio (a) and ^{9}Be/^{7}Li ratio (b): $1.0, 1 \times 10^{-2}$, 1×10^{-4}, 1×10^{-6}, 1×10^{-8} and 1×10^{-10}.

In Figs. 4.4(a) and 4.4(b), the same results (but only ^{6}Li, ^{7}Li, and ^{9}Be) as in Fig. 4.3 are transferred to the diagrams of ^{6}Li/^{16}O-^{7}Li/ ^{16}O and ^{9}Be/ ^{16}O- ^{7}Li/ ^{16}O where ^{i}X/ ^{16}O is the number ratio of ^{i}X-isotope synthesized in the supernova explosion to ^{16}O. We can see clearly that ^{6}Li produced in the supernova explosion is very small compared with the number of ^{16}O; only in the narrow region where $5.3M_\odot \lesssim M_r \lesssim 6.0M_\odot$ (see Fig. 4.3) we have ^{6}Li/^{16}O greater than the detection limit, 1×10^{-9} (see Introduction), and we can never detect ^{6}Li produced in the other places. It should be also noted that, even if we can observe a trace of ^{6}Li, the ^{6}Li/^{7}Li ratio is less than 3×10^{-5} and much smaller than the solar-system value (about 8.1×10^{-2}; Anders and Grevesse 1989). The same things can be said in the case of ^{9}Be: ^{9}Be/^{16}O is equal to or smaller than 2×10^{-7} and the ^{9}Be/^{7}Li ratio is less than 2×10^{-4}. Although the abundance ratio of ^{9}Be to ^{16}O (if we adopt the maximum value) is almost comparable to the solar-system value, ^{9}Be/ ^{7}Li is far from the solar-system value by two orders of magnitude or more.

The above results seem to depend on the adopted models of the neutrino emission, the chemical composition of the progenitor, the mixing process, and the stellar mass as well as the dynamical model of the supernova explosion. However, we will see in the following sections that these results do not depend on the adopted model and, hence, ^{6}Li and ^{9}Be to ^{7}Li ratios as well as ^{6}Li and ^{9}Be to ^{16}O ratios are important measures for finding presolar grains of supernova origin.

4.4. Production of C-, N-, and O-elements

Almost all of C-, N-, and O-isotopes are not produced by an appreciable amount (say, compared with the solar-system abundances) in the He-layer nor in the H-rich envelope as seen from Fig. 4.5. Especially, the abundances of ^{12}C and ^{16}O (also ^{18}O) do not change from their initial abundances. Isotopes traced by the horizontal lines in Fig. 4.5 keep their initial abundances without addition and annihilation due to nuclear processes (see also Figs. 3.5(a) and 3.5(b) on page 47). Key reactions relevant to the formation of these isotopes are summarized in Table 4.1 (on page 53). Only in the convective region of the He-layer ($M_r \leq 6.0 M_\odot$), a small amount of ^{13}C is synthesized through mainly ^{12}C(n,γ) ^{13}C and ^{12}C(p,γ) ^{13}N(n,p) ^{13}C where protons and neutrons are supplied from ^{4}He$(\nu,\nu' p)$ ^{3}H and ^{4}He$(\nu,\nu' n)^{3}$He. In the innermost region, a part of synthesized ^{13}C is decomposed by ^{13}C(α,n) ^{16}O after the shock passage and the resultant abundance of ^{13}C remains at relatively low level (about $1{\times}10^{-6}$ by mass fraction). It is conjectured that the amount of synthesized ^{13}C depends on the initial abundance of ^{12}C. However, the ratio ^{12}C/ ^{13}C,

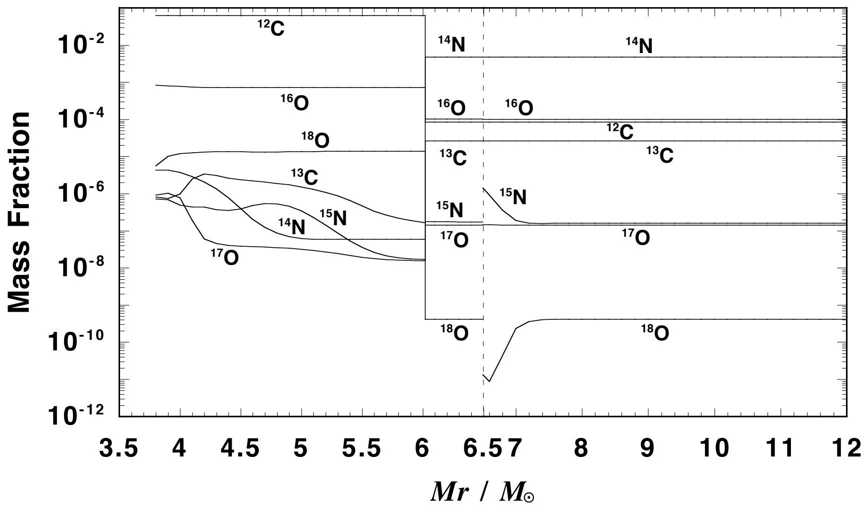

Fig. 4.5. The same as Fig. 4.3, but for the CNO-elements.

which will be shown in Fig. 5.4 (on page 68), would be almost independent of the initial abundance of ^{12}C since only ^{12}C is a parent isotope of ^{13}C.

In the inner region of the He-layer, ($M_r \lesssim 5.0 M_\odot$) N-isotopes are also produced. Almost all of ^{14}N comes from the decomposition product of ^{11}B, i.e., $^{11}\mathrm{B}(\alpha, n)\,^{14}\mathrm{N}$, in the shock-induced burning stage. The final abundance of ^{14}N increases with an increase in the shock temperature (i.e., with a decrease in radius): it is of the order of 4×10^{-6} (by mass fraction) in the innermost region ($M_r \lesssim 4.0 M_\odot$). When $M_r \gtrsim 5.0 M_\odot$, it decreases below the level of its initial abundance (about $6{\times}10^{-8}$). Heavy isotope, ^{15}N, is synthesized through $^{18}\mathrm{O}(p, \alpha)\,^{15}\mathrm{N}$ in the preshock stage, one of the reactions of the hot CNO-cycle (protons are formed by the ν-process, $^{4}\mathrm{He}(\nu, \nu' p)\,^{3}\mathrm{H}$). However, the amount of ^{15}N is relatively low, 7×10^{-7} (the innermost region) to 2×10^{-8} (the outer region) by mass fraction. Among O-isotopes, only ^{17}O is synthesized in the convective He-layer, through $^{16}\mathrm{O}(n, \gamma)\,^{17}\mathrm{O}$ in the preshock and the shock-induced burning stages. As in the case of ^{15}N, the abundance level is very low and the ratio, $^{16}\mathrm{O}/\,^{17}\mathrm{O}$, is as large as 1×10^{4} or

5×10^4 except the innermost region ($M_r \lesssim 4.0 M_\odot$) where the ratio is comparable to the solar-system ratio, 1×10^3.

In the radiative He-layer all CNO-elements keep their initial amounts. In this region protons are not much enough to change the initial abundances of CNO-elements in a small time interval during the explosion. Productions of ^{13}C and ^{17}O through n-captures do not proceed effectively in the radiative He-layer because the initial amounts of ^{12}C and ^{16}O are less than those in the convective He-layer and because the amount of neutrons is less than one-tenth as little as that in the convective He-layer. In the deep region of the H-rich envelope, only ^{15}N and ^{18}O change from their initial values. During the explosion ^{15}N is produced through ^{14}N(p,γ) ^{15}O(β^+) ^{15}N and ^{18}O is decomposed through ^{18}O(p,α) ^{15}N. In the region where $M_r \gtrsim 7.6 M_\odot$, all CNO-elements keep their initial compositions of the presupernova stage because the shock temperature is too low to proceed nuclear reactions appreciably.

4.5. Summary

In this section we demonstrated light element synthesis in the He-layer and the H-rich envelope in the case of the standard model (see Section 4.1). We calculated their final abundances and clarified their synthetic processes in detail on the basis of the standard model. The results obtained in this section are as follows:

1. Among the X-elements, ^{7}Li, ^{10}B, and ^{11}B are synthesized appreciably (i.e., beyond the level of the detection limit) in the He-layer and the inner H-rich envelope of a supernova (except ^{10}B in the inner H-rich envelope). The abundances of these isotopes vary over several orders of magnitude owing to the internal mass coordinate, M_r.

2. The amounts of ^{6}Li and ^{9}Be produced in the exploding He-layer and the H-rich

envelope are much smaller than that of, for example, ^{7}Li. The ratios of ^{6}Li/^{7}Li and ^{9}Be/^{7}Li are less than 3×10^{-5} and 2×10^{-4}, respectively, as long as we are concerned with the case where the isotopic abundance exceeds beyond the detection limit (i.e., the number ratio to ^{16}O is greater than 1×10^{-9}). The above ratios of ^{6}Li/ ^{7}Li and ^{9}Be/ ^{7}Li are far from the corresponding solar-system values.

3. The tightly bounded isotopes, ^{12}C and ^{16}O, are never synthesized in the He-layer nor in the H-rich envelope and the abundances are completely determined by their initial values. Heavy isotope, ^{18}O, keeps, in most case, its initial abundance.

4. The other CNO-elements, ^{13}C, ^{14}N, ^{15}N, and ^{17}O are synthesized in the convective He-layer by small fractions (but not outside the radiative He-layer). The amounts of these elements vary with the internal mass coordinate, M_r, by two or more orders of magnitude.

In the following sections, we will see that most of the production and the destruction processes of the light elements obtained in this section occur in the cases of the other physical parameter sets of the supernova explosions. We will also see that the special varieties of the abundances of the light elements are qualitatively in common among the supernova explosions. Hence, we will evaluate how the abundances and the abundance ratios of the light elements vary from the results obtained in this section owing to the change of the various physical parameters.

5. Influence of the Adopted Neutrino Emission Model

Since the light elements are produced mainly through neutrino interactions with helium and carbon as seen in the previous section, we expect that the production of the light elements is influenced essentially by the adopted model of the neutrino emission during the supernova explosion. In other words, uncertainties of the neutrino emission model give a confusion on studying the nucleosynthesis of the light elements. To examine the influence and to find a suitable manner to discuss freely from the uncertainties of the neutrino emission model in this section, we will calculate the abundances of the light elements by changing the two parameters of the neutrino emission model, namely, the decay time of the neutrino flux, τ_ν, and the total energy carried by neutrinos, E_ν (see Section 3.3). The explosion model and the chemical compositions of the progenitor used in this section are the same model and the compositions that we defined in Section 4.1 (see page 48), i.e., the 16.2 $M_\odot$ progenitor model and the chemical compositions shown in Figs. 3.5(a) and (b) (see page 47). The mixing process will not be considered in Sections 5.1 to 5.4. We will consider the mechanical mixing between the He-layer and the H-rich envelope in Section 5.5. Sections 5.1 to 5.4 are reprinted from Sections 5.1 to 5.4 in Yoshida, Emori, and Nakazawa (2000). A part of Section 5.5 is reprinted from Section 6 in Yoshida, Emori, and Nakazawa (2000).

5.1. Abundance response to τ_ν and E_ν

As mentioned in the previous section, the abundance of a light element is determined by three kinds of processes, i.e., synthesis due to the ν-process in the preshock stage, rapid production and decomposition at the stage of the shock heating, and re-synthesis in the shock-induced burning stage. If τ_ν is much shorter than the arrival time of the shock, too small number of neutrinos remain at the stage of re-synthesis. In this case the final abundances of the light elements are almost determined by the decomposition due to the shock heating. Because the inner region of the He-layer is exposed to the higher shock temperature, the light elements survive in the outer region more than in the inner region. On the other hand, in the case where τ_ν is much longer than the shock arrival time, enough number of neutrinos take part in the re-synthesis of light elements even after the decomposition due to the shock heating and the loss is recovered.

The other parameter, E_ν, also affects the production rates of the light elements. In our present study, E_ν means directly the total number flux of emitted neutrinos because we assume that, as mentioned in Section 3.3 (see Eq.(3.31) on page 35), the neutrino temperatures are fixed. So, it may be conjectured that the amounts of synthesized light elements increase proportionally with E_ν. However, the ν-processes also produce, sometimes, "poison" to some kind of elements, so that the final abundances response to the adopted value of E_ν complicatedly. In this subsection we will see, as an example, how τ_ν and E_ν influence the final abundance of ^{11}B.

In Fig. 5.1(a), we present the amount of ^{11}B produced in the He-layer in the three cases with different τ_ν, i.e., 1 s, 3 s, and 10 s (E_ν is fixed to be 3×10^{53} erg). In the outer region where $M_r \gtrsim 5.0 M_\odot$ ^{11}B is mainly produced through ^{12}C$(\nu, \nu' p)^{11}$B and the shock temperature is not high enough to decompose ^{11}B (^{11}B is decomposed above 2.5×10^8 K). As a result, the abundance of ^{11}B does not depend appreciably on τ_ν. In the radiative He-layer where $M_r \geq 6.0 M_\odot$, the ^{11}B abundance is much less than that in the inner convective He-layer. This is due to the fact that there exists a small number of ^{12}C in the radiative He-layer compared with that in the inner convective He-layer. In the inner region where $M_r \lesssim 5.0 M_\odot$, ^{11}B is produced through ^{12}C$(\nu, \nu' n)^{11}$C$(, e^+ \nu_e)^{11}$B and ^{4}He$(\nu, \nu' n)^3$He$(\alpha, \gamma)^7$Be$(\alpha, \gamma)^{11}$C$(, e^+ \nu_e)^{11}$B. This region is characterized by the high shock temperature; ^{11}B produced through the ν-process is decomposed almost completely through α- and p-capture reactions and, thus, the final abundance depends on the total

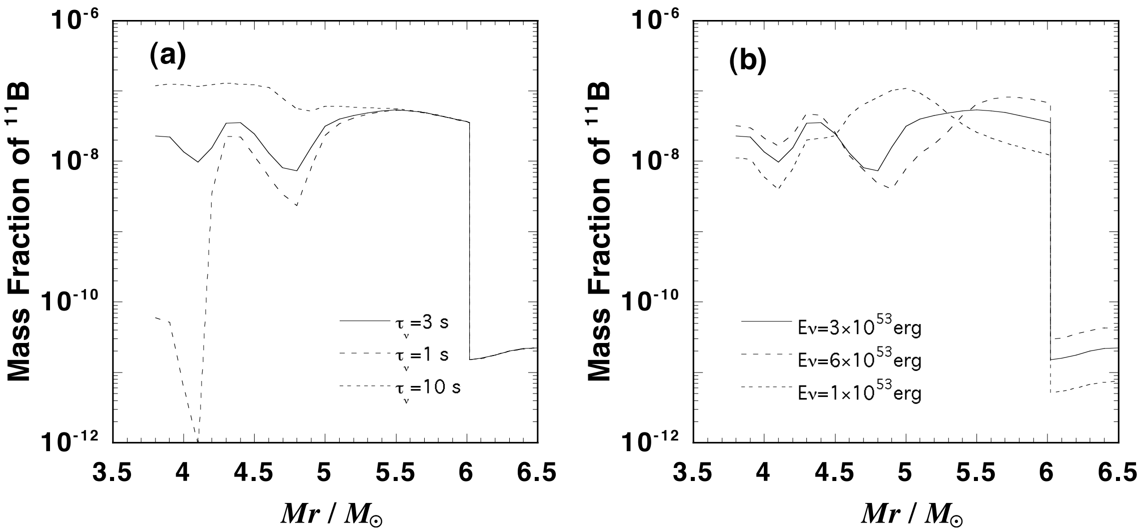

Fig. 5.1. Distribution of the final mass fraction of ^{11}B in the He-layer. Panel (a) shows the cases of $\tau_\nu = 1$ s (dashed curve), 3 s (solid curve), and 10 s (dotted curve) with common E_ν ($= 3 \times 10^{53}$ erg) and panel (b) the cases of $E_\nu = 6 \times 10^{53}$ erg (dashed curve), 3×10^{53} erg (solid curve), and 1×10^{53} erg (dotted curve) with common τ_ν ($= 3$ s).

neutrino flux as well as the shock temperature. In the case where $\tau_\nu = 10$ s, the loss due to decomposition is recovered almost completely through the thermonuclear reaction sequence in the postshock stage as in the case of the outermost region (the shock reaches a sphere of $M_r = 5.0 M_\odot$ at 27.3 s) and the abundance pattern becomes almost uniform independently of the mass coordinate, M_r. In the case of $\tau_\nu = 3$ s, ^{11}B is decomposed owing to the shock heating but a part is re-produced. However, in the case of $\tau_\nu = 1$ s almost all of ^{11}B is decomposed by the shock heating (especially, in the innermost region where $M_r \lesssim 4.2 M_\odot$) and the final abundance is about one to five orders of magnitude lower than that in the case of $\tau_\nu = 10$ s.

In Fig. 5.1(b) the distribution curves of produced ^{11}B are illustrated for the three cases with different E_ν (but τ_ν is fixed to be 3 s). As a whole, the distribution curves behave moderately in contract to the case of Fig. 5.1(a) and the variation of the amount is confined within an order of magnitude or so. As conjectured earlier, as long as we are concerned with the outermost region where $M_r \gtrsim 5.7 M_\odot$, the amount of ^{11}B is almost proportional to E_ν. But in the inner region, the distribution curves behave in a different manner from point to point. Especially, in the middle region where $4.5 M_\odot \lesssim M_r \lesssim 5.5 M_\odot$, the amount of ^{11}B decreases with an increase in E_ν. This is due to the fact that (p, α)-reaction, by which ^{11}B is decomposed (see Table 4.1 on page 53), becomes inactive with an decrease in E_ν because protons are supplied mainly by ^{4}He$(\nu, \nu' p)$ ^{3}H.

5.2. Abundance ratios among the X-elements

We can expect that, at least qualitatively, the X-elements are processed by a similar manner and that the abundance ratios among them are less sensitive to the adopted values of τ_ν and E_ν than the amounts themselves. In Figs. 5.2(a) and 5.2(b), the number ratios of ^{11}B/ ^{7}Li are shown in the cases with various τ_ν and with various E_ν, respectively. Except a narrow region between $M_r = 4.1 M_\odot$ and $4.3 M_\odot$, ^{11}B/ ^{7}Li has a value between 7×10^{-2} and 2 in the convective He-layer; the ratio of the maximum to the minimum in the convective He-layer is much smaller than those of the abundance curves shown in Fig. 5.1(a). In the outer region where $M_r \gtrsim 5.0 M_\odot$ ^{7}Li as well as ^{11}B are produced through the ν-processes in the preshock stage and scarcely decomposed by the shock heating. So the amounts of ^{7}Li as well as ^{11}B (and, hence, their ratio) are independent of τ_ν. In the region between 4.3 $M_\odot$ and 5.0 $M_\odot$, the ^{11}B/^{7}Li ratios have almost the same values for the cases of $\tau_\nu = 1$ s and 3 s where most of neutrinos pass through before the shock passage. Both ^{7}Li and ^{11}B are firstly produced through ν-processes but decomposed almost completely during the shock-induced burning stage. In the case of $\tau_\nu = 10$ s, only ^{11}B is recovered almost completely and, as a result, ^{11}B/^{7}Li becomes slightly large compared with the cases of $\tau_\nu \lesssim 3$ s. In the innermost region where $M_r \lesssim 4.1 M_\odot$, the amounts of ^{7}Be and

^{11}C, which are parent nuclei of ^{7}Li and ^{11}B, respectively, are almost determined by a steady-flow equilibrium condition of ^{4}He even in the case of $\tau_\nu = 1$ s so that the ^{11}B/^{7}Li ratio scarcely depends on τ_ν.

In the case of $\tau_\nu = 1$ s, the ^{11}B/ ^{7}Li ratio becomes exceptionally large in the narrow region between $M_r = 4.1 M_\odot$ and 4.3 $M_\odot$. In this case, neutrino irradiation stops before the shock arrival and both ^{7}Be and ^{11}C decrease exponentially in the post shock stage. Since the decomposition rate of ^{7}Be is larger than that of ^{11}C and the ^{11}B/^{7}Li ratio becomes very large. As seen in Fig. 5.2(b), ^{11}B/ ^{7}Li varies moderately with E_ν. In the inner ($M_r \lesssim 4.3 M_\odot$) and the outer ($M_r \gtrsim 5.5 M_\odot$) regions, the ratio does not depend on E_ν. In the middle region the ratio increases with a decrease in E_ν because of ^{11}B behavior mentioned in the last paragraph.

Compared with the ^{11}B/^{7}Li ratio, the ^{11}B/^{10}B ratio behaves in a different way against τ_ν. We see from Fig. 5.3(a) that the ^{11}B/^{10}B ratio depends sensitively on τ_ν, especially, in the inner region where $M_r \lesssim 5.3 M_\odot$. This is due, mainly, to the fact that the amount of ^{10}B is influenced strongly by the adopted value of τ_ν. In the He-layer, ^{10}B is commonly synthesized through ^{12}C$(\nu, \nu' np)$ ^{10}B. On the other hand, ^{10}B is decomposed by (p, α)-, (n, α)-, and (α, p)-reactions; in the innermost He-layer ($M_r \lesssim 4.5 M_\odot$) (α, p)-reactions dominates and in the radiative He-layer ($M_r \geq 6.0 M_\odot$) (p, α)-reaction does. Furthermore, it should be noted that protons are supplied by the ν-process ^{4}He$(\nu, \nu' p)$ ^{3}H and neutrons are formed mainly by ^{4}He$(\nu, \nu' n)$ ^{3}He and ^{3}H(t, nn) ^{4}He in the preshock stage. Thus, the final abundance of ^{10}B varies in a complicated manner owing to τ_ν as well as the mass coordinates, M_r. The ratio of ^{11}B/^{10}B, as shown in Figs. 5.3(b), does not depend strongly on the adopted value of E_ν in the inner region where $M_r \lesssim 5.0 M_\odot$. However, in the outer region it scatters widely: from Fig. 5.3(b) we observe a difference of two or more orders of magnitude between cases with small and large E_ν.

Thus, we can say that the abundance ratio ^{11}B/ ^{7}Li is less sensitive to uncertainties

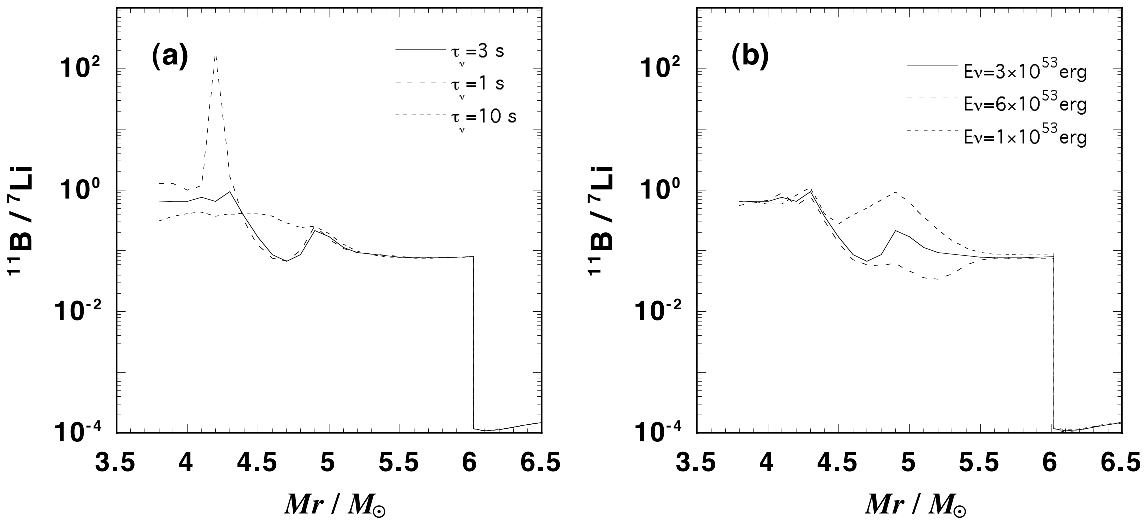

Fig. 5.2. Distribution of the number ratio, $^{11}B/^{7}Li$ in the He-layer. Panels (a) and (b) are illustrated by the same manner as in Fig. 5.1.

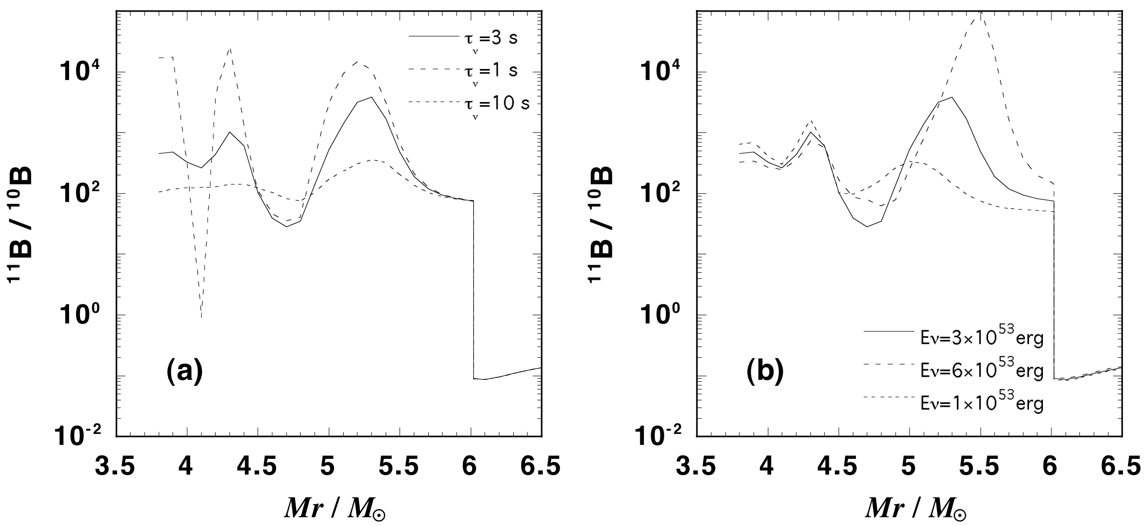

Fig. 5.3. The same as Fig. 5.2 but for $^{11}B/^{10}B$.

on the neutrino emission model than other quantities such as ^{11}B/ ^{10}B and the amounts of the X-elements themselves. Nevertheless, it should be noted that there remains a difference more than one order of magnitude in ^{11}B/ ^{7}Li among the cases with various τ_ν and E_ν.

5.3. Influence on ^{6}Li and ^{9}Be

Only in the inner region ($M_r \lesssim 5.0 M_\odot$) of the convective He-layer where the shock wave passes through within a first 30 s after the beginning of the explosion, the amounts of produced ^{6}Li and ^{9}Be are affected by the value of τ_ν. Especially, in the case of $\tau_\nu = 10$ s the final abundances become large by two or three orders of magnitude compared with the standard case ($\tau_\nu = 3$ s) since the neutrino irradiation lasts even after the passage of the shock. However, the influence of the neutrino irradiation time on the amounts of ^{6}Li and ^{9}Be is of no importance since the abundance level is still below the detection limit. In the outer region where $M_r \gtrsim 5.0 M_\odot$, the amounts of ^{6}Li and ^{9}Be do not depend so much on τ_ν as long as we are concerned with the cases where $\tau_\nu \leq 10$ s.

Roughly speaking, on the other hand, ^{6}Li and ^{9}Be are produced in proportion to the adopted value of E_ν (i.e., to the total number of neutrinos) since they are formed commonly through the ν-processes with the target nuclei of ^{12}C and ^{13}C. For example, when $E_\nu = 6 \times 10^{53}$ erg their maximum amounts (which are realized near $M_r = 5.5 M_\odot$) become two times larger than those in the standard case ($E_\nu = 3 \times 10^{53}$ erg). However, the amount of ^{7}Li increases similarly and, as a result, both ^{6}Li/ ^{7}Li and ^{9}Be/ ^{7}Li are still less than 2×10^{-4}. Thus, the conclusions mentioned in Section 4.3 (see page 53) hold as they are irrelevant to the adopted model of neutrino emission.

5.4. Influence on the CNO-elements

In Fig. 5.4 we show how the isotopic ratios of CNO-elements depend on τ_ν and E_ν. In most part of the He-layer where $M_r \gtrsim 4.0 M_\odot$, isotopic ratios are very insensitive to the adopted value of τ_ν; all of their variations are confined within a factor of 4. The CNO-elements (except ^{12}C and ^{16}O) are produced by various kind of the ν-processes whereas they are hardly decomposed by the shock heating, after they are once produced. As a result, the final abundances of these elements are governed entirely by the total number of neutrinos but not by the time variation of the neutrino flux.

Only in the innermost region ($M_r \lesssim 4.0 M_\odot$) where the shock temperature is relatively high, the isotopic ratios depend weakly on τ_ν. The ratio ^{12}C/ ^{13}C (or ^{14}N/ ^{15}N) decreases (or increases) with an increase in τ_ν. As described in Section 4.3, ^{13}C is decomposed through $^{13}\mathrm{C}(\alpha, n)\,^{16}\mathrm{O}$ owing to the shock heating. After the shock passage ^{13}C is reproduced through $^{12}\mathrm{C}(n, \gamma)\,^{13}\mathrm{C}$; neutrons are supplied by the ν-process originated by the remaining neutrino flux. Thus, the final amount of ^{13}C becomes large when τ_ν is long. Even in the case of $\tau_\nu = 1$ s, about one-thousandth of the total number of neutrinos pass through a sphere of $M_r = 3.8 M_\odot$ after the shock arrival.

The ratio ^{14}N/ ^{15}N behaves inversely against τ_ν compared to the case of ^{12}C/ ^{13}C. Owing to the shock heating, ^{14}N and ^{15}N are decomposed through (α, γ)- and (p, α)-reaction, respectively. When τ_ν is long, ^{14}N is reproduced from ^{11}B, which is formed through a reaction sequence of α-captures starting from $^{4}\mathrm{He}(\nu, \nu' p)\,^{3}\mathrm{H}$ after the shock passage. On the contrary, when τ_ν is short, ^{14}N is not reproduced and ^{15}N is hardly decomposed because of lack of protons. Hence, ^{14}N/ ^{15}N becomes small compared to the case of long τ_ν. In the case of oxygen, ^{17}O, once formed, is hardly decomposed by the shock heating even in the innermost region and, hence, the variation of ^{16}O/ ^{17}O is very small (within a factor of 2).

As conjectured earlier and seen from Fig. 5.4, the final amount of ^{13}C increases,

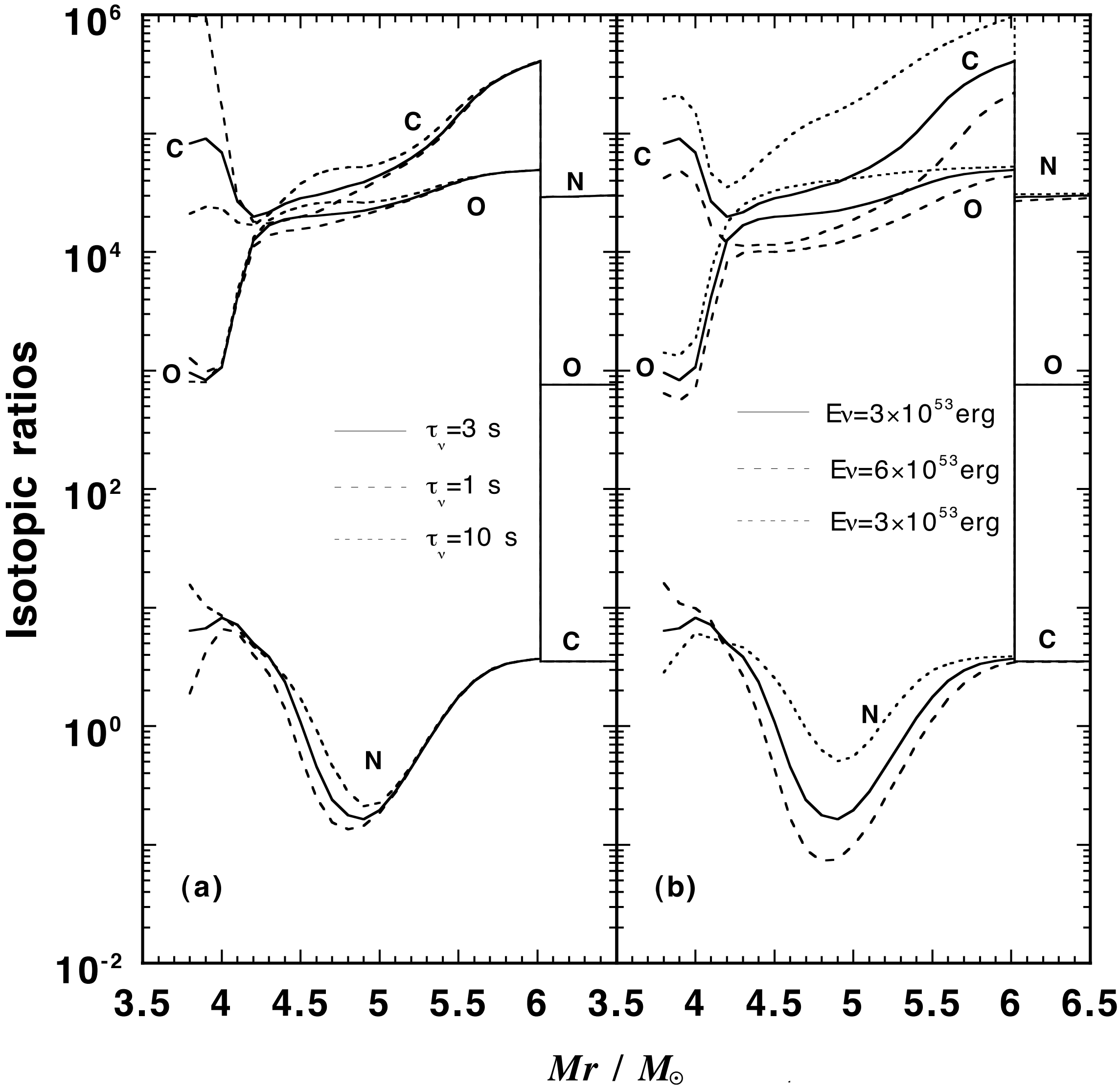

Fig. 5.4. The same as Fig. 5.2 but in the cases of $^{12}C/^{13}C$, $^{14}N/^{15}N$, and $^{16}O/^{17}O$, of which curves are denoted by C, N, and O, respectively.

more or less, in proportion to E_ν, i.e., the total number of neutrinos, irrelevant to the internal mass coordinate M_r. As shown in Table 4.1, ^{13}C is produced through the ν-process due to ^{12}C and hardly decomposed by the shock heating. The ratio ^{16}O/^{17}O changes with E_ν similarly to the case of ^{12}C/^{13}C. However, ^{14}N/^{15}N behaves differently against E_ν. In the outer region where $M_r \gtrsim 4.3 M_\odot$, ^{15}N, which is mainly produced through $^{18}\mathrm{O}(p,\alpha)\,^{15}\mathrm{N}$ and $^{16}\mathrm{O}(\nu,\nu' p)\,^{15}\mathrm{N}$, is increased with E_ν. The amount of ^{14}N, however, scarcely depends on E_ν because the amount of ^{11}B, parent nucleus of ^{14}N, is determined by a balance between production and decomposition reactions, both of which are originated by the ν-processes. Thus, ^{14}N/^{15}N becomes low when E_ν is large. In the inner region, however, ^{14}N/^{15}N ratio increases with an increase in E_ν because the amount of ^{14}N increases and that of ^{15}N decreases. The reason is as follows. As seen in Table 4.1, ^{14}N is produced through an α-capture reaction sequence originated by the ν-process. Increase in E_ν brings about an increment of ^{14}N production and, simultaneously, the same reaction provides more protons which are the poison of ^{15}N.

5.5. Summary and diagrams between two isotopic/elemental ratios

The abundances of the light elements are affected by various kinds of physical parameters which govern the models of the supernova explosion as well as the neutrino emission. Of these parameters, the decay time of the neutrino flux, τ_ν, and the total energy carried by neutrinos, E_ν, are most important since the explosive synthesis of the light elements is initiated, in most cases, by the ν-processes. In this section, we concentrated ourselves on investigating the influence of uncertainties in the adopted model of the neutrino emission on the abundances of the light elements. The obtained results are summarized as follows:

1. The ratios of ^{6}Li/^{7}Li and ^{9}Be/^{7}Li do not depend on the neutrino emission model so much when ^{6}Li and ^{9}Be are produced more than a level of the detection limit. Thus,

the ratios of ^{6}Li/^{7}Li and ^{9}Be/^{7}Li are less than 3×10^{-5} and 2×10^{-4}, respectively, even if we consider uncertainties in the adopted model of the neutrino emission.

2. The abundances of ^{7}Li, ^{10}B, and ^{11}B vary over several orders of magnitude owing to the neutrino emission model (i.e., τ_ν and E_ν), as well as the internal mass coordinate, M_r. However, the ratio of ^{11}B/ ^{7}Li is confined within a relatively small range (but, ^{11}B/ ^{10}B or ^{10}B/ ^{7}Li scatters widely as the abundances do).

3. The abundances of ^{12}C, ^{16}O, and ^{18}O keep their abundances at the presupernova stage in most cases even if we consider the uncertainties of the adopted model of the neutrino emission.

4. The other CNO-elements, ^{13}C, ^{14}N, ^{15}N, and ^{17}O synthesized in the convective He-layer depend on τ_ν and E_ν but are confined within a factor of 10 or so if we observe at fixed M_r.

As pointed out in Section 1, several procedures for distinguishing presolar grains of supernova origin have been proposed (e.g, Nittler *et al.* 1996; Travaglio *et al.* 1999). So, it may be worthwhile to compile our numerical results for applying to the study of presolar grains of supernova origin. According to familiar ways of cosmochemists, we make useful three diagrams between two isotopic (elemental) ratios overwriting all of numerical results presented in this study: diagrams of ^{11}B/ ^{7}Li- ^{12}C/ ^{13}C, ^{14}N/ ^{15}N- ^{12}C/ ^{13}C, and ^{16}O/ ^{17}O- ^{12}C/ ^{13}C, which are illustrated in Figs. 5.5(a) to 5.5(c). As described in the above, these ratios vary both with the adopted values of τ_ν and E_ν and with the internal mass coordinate we observe. Nevertheless, they are confined within relatively small, two regions in the diagram: one is of the H-rich envelope (including the radiative He-layer) and the other is of the inner convective He-layer. The corresponding solar-system value (marked by $\odot$ in the figures) does not fall onto the two regions mentioned above. These three

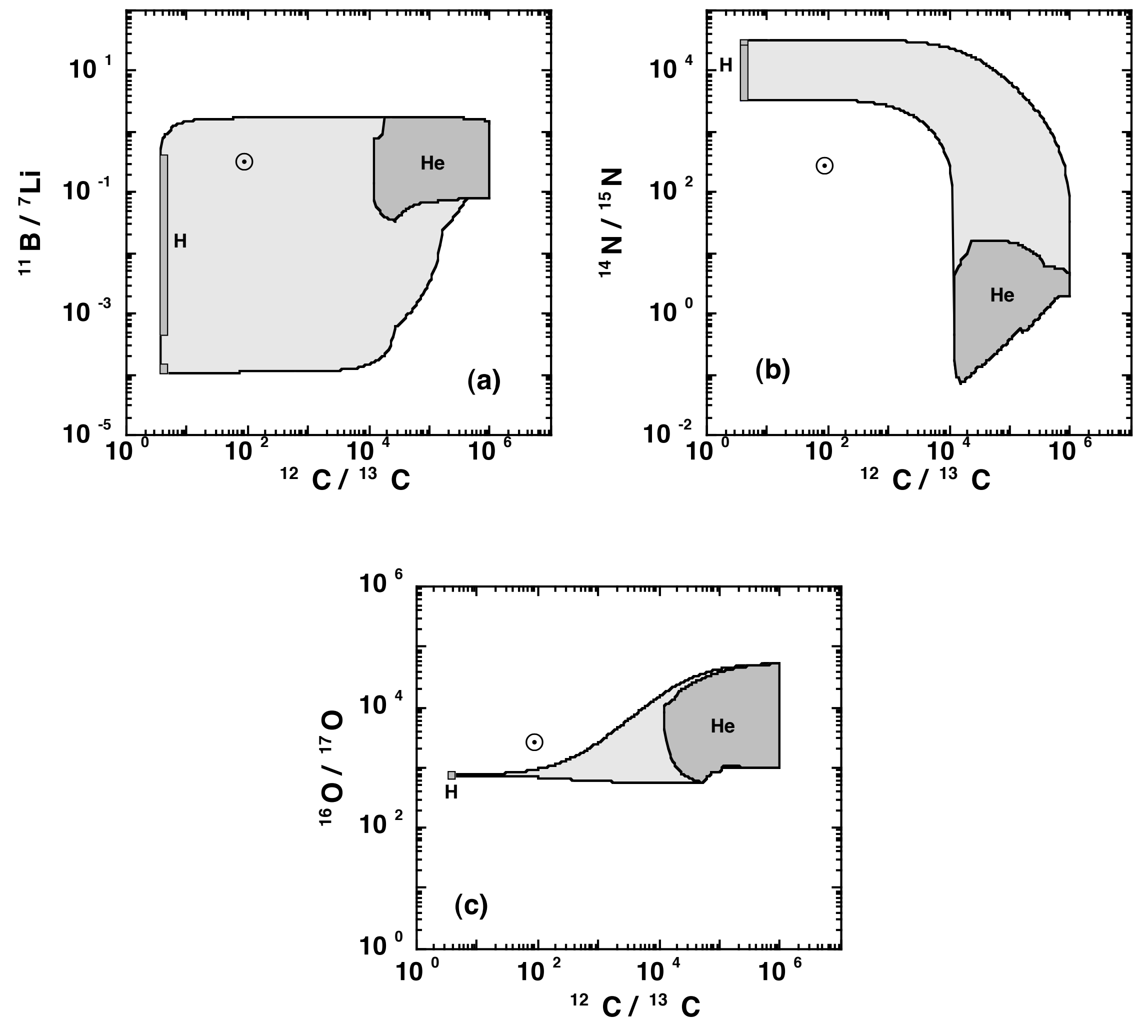

Fig. 5.5. The number ratios of ^{11}B/ ^{7}Li (panel (a)), ^{14}N/ ^{15}N (panel (b)), and ^{16}O/ ^{17}O (panel (c)) versus ^{12}C/ ^{13}C. Three regions with a dark shade are of the convective He-layer (denoted by He), the radiative He-layer (denoted by rad-He), and the H-rich envelope (denoted by H) whereas a region with a light shade denotes the ratios made of the mechanical mixing between these regions. In panel (c), the region of the radiative He-layer overlaps with that of the H-rich envelope. A mark ⊙ shows the ratio of the solar-system composition. (In panel (a), exceptional spike appeared in Fig. 5.2(a) is excluded.)

figures would help us to distinguish presolar grains of supernova origin from solar-system materials.

It should be noted here that, as will be mentioned in detail in Section 7, there happens to occur a material mixing among the exploding layers, which is caused by the Rayleigh-Taylor instability (e.g., Hachisu *et al.* 1994). The mixing disturbs inevitably the isotopic (elemental) ratios of materials through, at least, the mechanical mixing. When there occurs a mixing between two arbitrary fluid elements outside the He-burning shell (i.e., the He-layer and the H-rich envelope), we can readily evaluate the mixing effect on the isotopic ratios using our present results. The variation of the isotopic ratios due to the mechanical mixing are shown in Figs. 5.5(a) to 5.5(c) by light shadows. Thus, dust-grains originated from the 16.2 $M_\odot$ supernova model should have the following cosmochemical features of isotopic (elemental) ratios of the light elements:

(a) Among the X-elements, ^{6}Li and ^{9}Be should be both very rare. Presolar grains with ^{6}Li/^{7}Li less than 3×10^{-5} and with ^{9}Be/^{7}Li less than 2×10^{-4} should be originated from the supernova.

(b) Presolar grains with the ratios ^{11}B/^{7}Li, ^{12}C/^{13}C, ^{14}N/^{15}N, and ^{16}O/^{17}O confined within relatively narrow two regions with dark shade shown in Figs. 5.5(a) to 5.5(c) should be also originated from the supernova. If there occurs a mixing between the He-layer and the H-rich envelope, the ratio would fall onto the regions with light shade.

6. Influence of Initial Chemical Compositions

In this section we will investigate the sensitivity of the light element synthesis to the initial chemical compositions using artificial 4-component model, which consists of ^{1}H, ^{4}He, ^{12}C, and ^{16}O, and investigate how the abundances of the light elements change owing to the amounts of the four species. We will also investigate the decomposition processes of the light elements by the use of another artificial initial composition. Combining the numerical results and probable ranges of the light element abundances at the presupernova stage deduced by the use of theoretical studies of massive stars and the observations of stellar atmosphere, we will evaluate the probable ranges of the light element abundances in the supernova taking account of the uncertainty of the initial chemical compositions. The explosion model, the neutrino emission model, and the mixing model are identical to those of the standard model (see Section 4.1 on page 48) in Sections 6.1 to 6.4. We will consider the mechanical mixing in Section 6.5. Sections 6.1, 6.2, 6.3, 6.4 and 6.5 are reprinted from Sections 2, 3, 4, 5, and 6 in Yoshida, Nakazawa, and Emori (1999).

6.1. Initial chemical compositions

6.1.1. Four-component models

In Section 4 we showed that the X-elements and most of the CNO-elements are mainly produced from ^{4}He, ^{12}C, and ^{16}O through neutrino-induced reactions. So it is expected, at least qualitatively, that the production of the X-elements and the CNO-elements essentially depends on the amounts of ^{4}He, ^{12}C, and ^{16}O in the presupernova stage. However, it is difficult to estimate quantitatively from the results of the standard model how the abundance ratios of the light elements are changed by the adopted initial chemical compositions. In order to answer such a question, we set artificially 4-component models of the initial chemical composition which consist of only ^{1}H, ^{4}He, ^{12}C, and ^{16}O.

The amounts of the other elements included in our nuclear reaction network are put practically to be zero. Note that in the above models we omit ^{14}N completely from the initial constituents in order to see clearly the formation processes of ^{14}N and ^{15}N although ^{14}N is the most abundant element among the CNO-elements in the radiative He-layer and the H-rich envelope. The effects of this simplification will be discussed in Section 6.4 where we will see such a simplification does not affect the main conclusions of the this section.

In this section, we will consider the following initial chemical composition: in the convective and the radiative He-layers, the mass fractions of ^{4}He are taken to be 0.9372 and 0.9800, respectively. The remainder is divided into ^{12}C and ^{16}O equally by weight (their mass fractions are 0.0314 and 0.0100, respectively, in the convective and the radiative He-layers). In the H-rich envelope, the mass fractions of ^{1}H and ^{4}He are set to be 0.55 and 0.43, respectively, the values of which are almost equal to those we set in Section 3.5 (see page 47). Note that in this model the initial metallicity is equal to 0.02. Hereafter, this model will be called model SII and the chemical composition of the standard model, mentioned in Section 3.5, will be called that of model SI.

In order to investigate in detail the influence of choice of the initial chemical composition on the light element synthesis, we prepare additional six models of the initial chemical compositions other than models SI and SII. They are tabulated in Table 6.1 together with models SI and SII. Models A1 and A2 are of seeing the role of ^{12}C and ^{16}O separately on the light element synthesis and correspond to C-rich and O-rich compositions, respectively. In models A3 and A4, we see the influence of a variety of the He abundances. In these models, taking account of the depletion of ^{4}He due to the He-shell burning, we adopt less abundant ^{4}He-content (i.e., 0.8 and 0.5 in models A3 and A4, respectively) in the convective He-layer but the same chemical composition as in model SII in the radiative He-layer. Furthermore, in the H-rich envelope, in model A3 the mass fractions of ^{1}H and ^{4}He are taken to be 0.73 and 0.25 (almost the same as the solar-system abundances) whereas in model A4 the mass fractions of ^{1}H and ^{4}He are set to be 0.25 and 0.73, respectively. In all cases mentioned above, the metallicity (i.e., the total mass fractions of ^{12}C and ^{16}O in our present study) is put to be the same value as in model SII. In models A5 and A6 we consider the effect due to a variety of the metallicities. In models A5 and A6, the metallicity is set to be 0.002 and 0.0002, respectively. In both cases the metal component consists of ^{12}C and ^{16}O with equal mass fraction. The mass fractions of ^{1}H and ^{4}He are taken to be nearly equal to those of model SII.

It should be noted that, in some cases, the model compositions are far extremely from those expected properly in the presupernova stage: in the convective He-layer, models A2 and A4 give extraordinarily large ^{16}O/^{12}C and too much metallicity, respectively. Furthermore, in model A1 ^{16}O/^{12}C is too low in the radiative He-layer and the H-rich envelope. So, we will exclude these models when we discuss the probable elemental/isotopic ratios of supernova ejecta in Section 6.5.

6.1.2. Over-abundant model of rare light elements

In the models mentioned above, we ignore completely the initial abundances of the X-elements and the rare CNO-elements. We are interested in, not only the production of the light elements from ^{4}He, ^{12}C, and ^{16}O, but also the destruction of these rare elements which have been formed through other processes and existed just before the supernova explosion. So we make a simulation in the alternative and artificial case where the initial amounts of the X-elements and the rare CNO-elements are set to be 1×10^{-10} and 1×10^{-6}, respectively, in all mass coordinates (such a model is called "model B"). The four major components, i.e., ^{1}H, ^{4}He, ^{12}C, and ^{16}O, are fixed to be the same as in model SII.

Table 6.1. Initial chemical compositions of the 4-component models and model SI (by mass fraction). In all models except model SI, the mass fractions of species other than tabulated ones (including ^{1}H in the He-layer) are set to be zero. In model SI, ^{14}N and the other rare light elements are also included. The mass fractions are as follows; ^{1}H=0 (conv. He) and 1.0×10^{-5} (rad. He), ^{14}N=5.8×10^{-8} (conv. He) and 4.8×10^{-3} (rad. He and H-env.), the X-elements $\leq 1.0 \times 10^{-10}$, and the rare CNO elements $\leq 3.0 \times 10^{-5}$.

<table>
<tr><th rowspan="2">Model</th><th colspan="4">H-rich Envelope</th><th colspan="3">Radiative He-layer</th><th colspan="3">Convective He-layer</th></tr>
<tr><th>^{1}H</th><th>^{4}He</th><th>^{12}C</th><th>^{16}O</th><th>^{4}He</th><th>^{12}C</th><th>^{16}O</th><th>^{4}He</th><th>^{12}C</th><th>^{16}O</th></tr>
<tr><td>SII</td><td>0.5500</td><td>0.4300</td><td>0.0100</td><td>0.0100</td><td>0.9800</td><td>0.0100</td><td>0.0100</td><td>0.9372</td><td>0.0314</td><td>0.0314</td></tr>
<tr><td>A1</td><td rowspan="2">0.5500</td><td rowspan="2">0.4300</td><td>0.0190</td><td>0.0010</td><td rowspan="4">0.9800</td><td>0.0190</td><td>0.0010</td><td rowspan="2">0.9372</td><td>0.0622</td><td>0.0006</td></tr>
<tr><td>A2</td><td>0.0010</td><td>0.0190</td><td>0.0010</td><td>0.0190</td><td>0.0006</td><td>0.0622</td></tr>
<tr><td>A3</td><td>0.7300</td><td>0.2500</td><td rowspan="2">0.0100</td><td rowspan="2">0.0100</td><td rowspan="2">0.0100</td><td rowspan="2">0.0100</td><td>0.8000</td><td>0.1000</td><td>0.1000</td></tr>
<tr><td>A4</td><td>0.2500</td><td>0.7300</td><td>0.5000</td><td>0.2500</td><td>0.2500</td></tr>
<tr><td>A5</td><td rowspan="2">0.5500</td><td>0.4480</td><td>0.0010</td><td>0.0010</td><td>0.9980</td><td>0.0010</td><td>0.0010</td><td rowspan="2">0.9372</td><td rowspan="2">0.0314</td><td rowspan="2">0.0314</td></tr>
<tr><td>A6</td><td>0.4498</td><td>0.0001</td><td>0.0001</td><td>0.9998</td><td>0.0001</td><td>0.0001</td></tr>
<tr><td>SI</td><td>0.5650</td><td>0.4300</td><td>8.5×10^{-5}</td><td>0.0001</td><td>0.9950</td><td>8.5×10^{-5}</td><td>0.0001</td><td>0.9300</td><td>0.0619</td><td>0.0007</td></tr>
</table>

6.2. Sensitivity to the initial compositions

6.2.1. Light element production due to 4-component model

At first, we will see, in brief, the general features of element synthesis due to the 4-component model, comparing the produced amounts of the light elements between models SI and SII. The initial chemical compositions of main constituents of models SI and SII are shown in Table 6.1; in short, differences among the two models are summarized as follows:

1. In the convective He-layer ^{12}C/^{16}O (by weight) are equal to 1 and about 100 in models SII and SI, respectively.

2. In the radiative He-layer and the H-rich envelope, the mass fractions of ^{12}C and ^{16}O in model SII are about 100 times as large as those of model SI.

3. There exist initially no X-elements and rare CNO-elements in model SII.

Distributions of the mass fractions of the X-elements and the CNO-elements are presented in Figs. 6.1(a) and 6.1(b), respectively. Main production and decomposition processes of the X-elements and the CNO-elements in model SII are tabulated in Table 6.2. In the convective He-layer, the amounts of the X-elements in model SII are very similar to those in model SI; the final abundances of ^{6}Li, ^{7}Li, and ^{9}Be are quite the same between the two models as long as the mass fractions are larger than the level of 1×10^{-14}. For ^{10}B and ^{11}B, the mass fractions are lower than those in model SI by a factor of about two, in accordance with the abundance ratio of ^{12}C between the two models.

In the H-rich envelope, the amounts of ^{6}Li, ^{7}Li, and ^{9}Be in model SII are also similar to those in model SI except the ^{7}Li-abundance in the outer region (i.e., $M_r \gtrsim 9.0 M_{\odot}$) which, in the case of model SI, is mainly governed by the initial abundance (the initial amount of ^{7}Li is about 2×10^{-11} in model SI). The amount of ^{11}B is remarkably different among the two models: the abundance in model SII is two orders of magnitude larger than that in model SI (also in the radiative He-layer). The large amount of ^{12}C in model SII, about two orders of magnitude larger than that in model SI, brings about this difference (note that ^{11}B is commonly formed from ^{12}C through the ν-processes in both models). It is interesting to note that, although the amounts of ^{10}B are quite similar between models SI and SII, the production process is different. In the case of model SII, ^{10}B is produced through $^{12}\mathrm{C}(\nu, \nu' np)^{10}\mathrm{B}$ because of the large amount of ^{12}C and no initial amount of ^{14}N. In the case of model SI, ^{10}B is produced through $^{14}\mathrm{N}(\nu, \nu' \alpha)^{10}\mathrm{B}$ since ^{14}N is abundant.

In the radiative He-layer, the abundances of ^{6}Li and ^{9}Be are different between the two models in contrast to the case of the H-rich envelope; the difference comes from the fact that, in model SII, they are scarcely decomposed because there are no protons initially (see Table 6.1). The abundance behavior of the other X-elements are similar with those in the H-rich envelope.

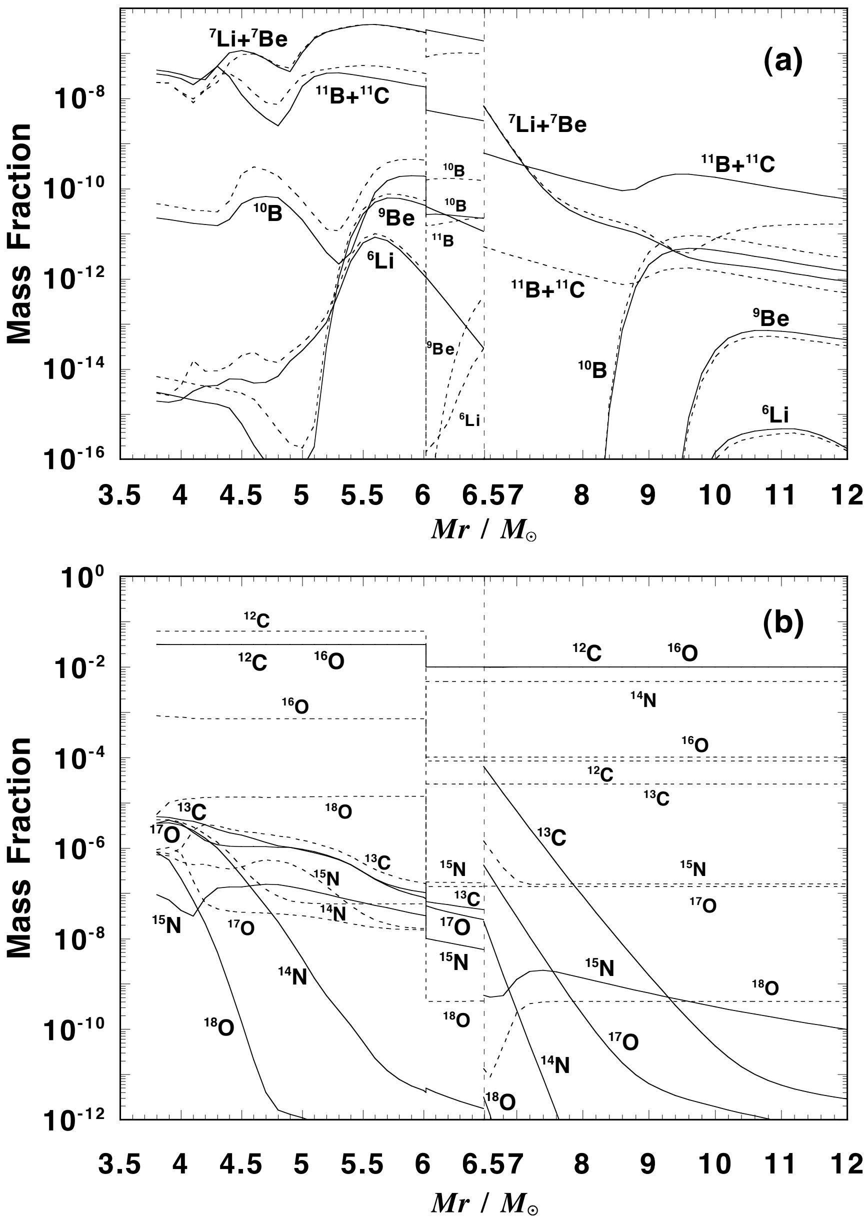

Fig. 6.1. Distributions of the final abundances of the X-elements (panel(a)) and the CNO-elements (panel(b)). Horizontal axis, M_r, denotes the internal mass coordinate. Solid lines and dashed lines show the mass fractions in model SII and model SI, respectively (see also Table 6.1). Discontinuities of the curves appear at the boundaries between the convective and the radiative He-layers ($M_r = 6.0M_\odot$) and between the radiative He-layer and the H-rich envelope ($M_r = 6.5M_\odot$).

Distributions of the amounts of the CNO-elements are different between models SI and SII. Difference in ^{12}C- and ^{16}O-abundances observed in all regions is due, simply, to the adopted initial abundances because, as shown in Sections 4 and 5, they are neither formed nor decomposed appreciably during the supernova explosion. In the convective He-layer, the final abundances of ^{13}C and ^{15}N are similar, within one order of magnitude or so, to those of model SI. The initial abundances of these isotopes adopted in model SI are below the level of 1×10^{-8} which is comparable to or lower than that of the explosive production and, hence, we cannot see an appreciable difference between the two models. The distribution of the ^{17}O abundance behaves also similarly to that in Fig. 4.5 (on page 57) but the abundance strongly reflects that of ^{16}O. On the other hand, for ^{14}N and ^{18}O the abundance patterns are quite different; this is due, mainly, to the fact that the initial abundances govern essentially the final abundances in model SI. In the case of model SII, the abundances in the innermost region are comparable to those of model SI but decrease abruptly with an increase in M_r. This behavior is brought about by large temperature dependence of their α-capture production processes (see Table 6.2).

In the radiative He-layer and the H-rich envelope, the abundance patterns of the rare CNO elements are different between the two models, SI and SII. This is because, in model SI, these elements are scarcely produced during the supernova explosion and their final abundances are almost determined by their initial abundances. In the H-rich envelope, the CNO-elements are produced only in the inner region. The maximum amounts of ^{13}C and ^{17}O, of which seed nuclei are ^{12}C and ^{16}O, respectively, are larger than those in model SI. This is simply because the amounts of ^{12}C and ^{16}O are larger than those in model SI by a factor of 100. Heavy nitrogen, ^{15}N, is produced from ^{16}O through the ν-process in model SII but from ^{14}N in model SI, so that the abundance pattern differs from each other. In model SII, ^{14}N and ^{18}O are hardly produced because their parent nuclei, ^{13}C and ^{17}O, are much less compared with the case of model SI.

Table 6.2. Typical key reactions of light element synthesis in model SII. The upper and lower columns show the formation and decomposition reactions, respectively. Empty columns mean that there are no appreciable formation (or decomposition) processes.

$M_r/M_\odot$		Convective He-layer (4.0 4.2 4.4 4.6 4.8 5.0 5.6 6.0) / Radiative He-layer (6.0–6.5)	H-rich envelope (6.5 7.0 8.0 9.0 10.0)
^{6}Li	formation	$^{2}\mathrm{H}(\alpha,\gamma)^{6}\mathrm{Li}$ / $^{9}\mathrm{Be}(p,\alpha)^{6}\mathrm{Li}$	$^{9}\mathrm{Be}(p,\alpha)^{6}\mathrm{Li}$ (continued)
	decomposition	$^{6}\mathrm{Li}(\alpha,\gamma)^{10}\mathrm{B}$, $^{6}\mathrm{Li}(p,\alpha)^{3}\mathrm{He}$ /	$^{6}\mathrm{Li}(p,\alpha)^{3}\mathrm{He}$
^{7}Li	formation	$^{4}\mathrm{He}(\nu,\nu'n)^{3}\mathrm{He}(\alpha,\gamma)^{7}\mathrm{Be}(n,p)^{7}\mathrm{Li}$ / $^{4}\mathrm{He}(\nu,\nu'p)^{3}\mathrm{H}(\alpha,\gamma)^{7}\mathrm{Li}$	$^{3}\mathrm{He}(\alpha,\gamma)^{7}\mathrm{Be}(e^{-},\nu_e)^{7}\mathrm{Li}$ / $^{10}\mathrm{B}(p,\alpha)^{7}\mathrm{Be}$ / $^{12}\mathrm{C}(\nu,\nu'n\alpha)^{7}\mathrm{Be}$
	decomposition	$^{7}\mathrm{Be}(\alpha,\gamma)^{11}\mathrm{C}$ / $^{7}\mathrm{Li}(\alpha,\gamma)^{11}\mathrm{B}$ / $^{7}\mathrm{Li}(p,\alpha\gamma)^{4}\mathrm{He}$	
^{9}Be	formation	$^{12}\mathrm{C}(\nu,\nu'\,^{3}\mathrm{He})^{9}\mathrm{Be}$ / $^{7}\mathrm{Li}(t,n)^{9}\mathrm{Be}$	$^{12}\mathrm{C}(\nu,\nu'\,^{3}\mathrm{He})^{9}\mathrm{Be}$
	decomposition	$^{9}\mathrm{Be}(\alpha,n)^{12}\mathrm{C}$, $^{9}\mathrm{Be}(p,\alpha)^{6}\mathrm{Li}$, $^{9}\mathrm{Be}(p,\alpha\alpha)^{2}\mathrm{H}$ /	$^{9}\mathrm{Be}(p,\alpha)^{6}\mathrm{Li}$, $^{9}\mathrm{Be}(p,\alpha\alpha)^{2}\mathrm{H}$
^{10}B	formation	$^{12}\mathrm{C}(\nu,\nu'np)^{10}\mathrm{B}$	$^{12}\mathrm{C}(\nu,\nu'np)^{10}\mathrm{B}$ (continued)
	decomposition	$^{10}\mathrm{B}(\alpha,p)^{13}\mathrm{C}$ / $^{10}\mathrm{B}(p,\alpha)^{7}\mathrm{Be}$ / $^{10}\mathrm{B}(n,\alpha)^{7}\mathrm{Li}$ / $^{10}\mathrm{B}(p,\alpha)^{7}\mathrm{Be}$	$^{10}\mathrm{B}(p,\alpha)^{7}\mathrm{Be}$ (continued)
^{11}B	formation	$^{12}\mathrm{C}(\nu,\nu'n)^{11}\mathrm{C}(,e^{+}\nu_e)\mathrm{or}(n,p)^{11}\mathrm{B}$, $^{7}\mathrm{Li}(\alpha,\gamma)^{11}\mathrm{B}$ / $^{12}\mathrm{C}(\nu,\nu'p)^{11}\mathrm{B}$, $^{12}\mathrm{C}(\nu,\nu'n)^{11}\mathrm{C}(,e^{+}\nu_e)^{11}\mathrm{B}$	$^{12}\mathrm{C}(\nu,\nu'p)^{11}\mathrm{B}$, $^{12}\mathrm{C}(\nu,\nu'n)^{11}\mathrm{C}(,e^{+}\nu_e)^{11}\mathrm{B}$ (continued)
	decomposition	$^{11}\mathrm{B}(\alpha,n)^{14}\mathrm{N}$ / $^{11}\mathrm{B}(p,\alpha\alpha)^{4}\mathrm{He}$	$^{11}\mathrm{B}(p,\alpha\alpha)^{4}\mathrm{He}$ (continued)
^{13}C	formation	$^{12}\mathrm{C}(p,\gamma)^{13}\mathrm{N}(,e^{+}\nu_e)\mathrm{or}(n,p)^{13}\mathrm{C}$ / $^{12}\mathrm{C}(n,\gamma)^{13}\mathrm{C}$	$^{12}\mathrm{C}(p,\gamma)^{13}\mathrm{N}(,e^{+}\nu_e)^{13}\mathrm{C}$ / $^{12}\mathrm{C}(n,\gamma)^{13}\mathrm{C}$
	decomposition	$^{13}\mathrm{C}(\alpha,n)^{16}\mathrm{O}$ /	
^{14}N	formation	$^{11}\mathrm{B}(\alpha,n)^{14}\mathrm{N}$ / $^{17}\mathrm{O}(n,\alpha)^{14}\mathrm{C}(,e^{-}\nu_e)^{14}\mathrm{N}$	$^{13}\mathrm{C}(p,\gamma)^{14}\mathrm{N}$
	decomposition		
^{15}N	formation	← / $^{14}\mathrm{N}(\alpha,\gamma)^{18}\mathrm{F}(n,\alpha)^{15}\mathrm{N}$ / $^{16}\mathrm{O}(\nu,\nu'p)^{15}\mathrm{N}$	$^{16}\mathrm{O}(\nu,\nu'p)^{15}\mathrm{N}$ (continued)
	decomposition	$^{15}\mathrm{N}(p,\alpha)^{12}\mathrm{C}$ /	$^{15}\mathrm{N}(p,\alpha)^{12}\mathrm{C}$ /
^{17}O	formation	$^{16}\mathrm{O}(n,\gamma)^{17}\mathrm{O}$	$^{16}\mathrm{O}(p,\gamma)^{17}\mathrm{F}(,e^{+}\nu_e)^{17}\mathrm{O}$ / $^{16}\mathrm{O}(n,\gamma)^{17}\mathrm{O}$
	decomposition		
^{18}O	formation	$^{14}\mathrm{N}(\alpha,\gamma)^{18}\mathrm{F}(n,p)\mathrm{or}(,e^{+}\nu_e)^{18}\mathrm{O}$ / $^{17}\mathrm{O}(n,\gamma)^{18}\mathrm{O}$	$^{17}\mathrm{O}(p,\gamma)^{18}\mathrm{F}(,e^{+}\nu_e)^{18}\mathrm{O}$
	decomposition		

The above comparison between models SI and SII (and also Table 6.2) suggests the following interesting points which are important to our later arguments. That is,

(1) Roughly speaking, the light elements are classified into three groups, i.e., (a) ^{6}Li, ^{7}Li, ^{9}Be, ^{14}N, and ^{18}O, (b) ^{10}B, ^{11}B, and ^{13}C, and (c) ^{15}N and ^{17}O. The produced amounts of elements of groups (a), (b), and (c) are mainly determined by the contents of ^{4}He, ^{12}C, and ^{16}O, respectively.

(2) In the cases of ^{10}B, ^{15}N, and ^{18}O, another production channel opens possibly if there exist appreciable amounts of ^{14}N and ^{18}O in the presupernova stage.

(3) In the radiative He-layer and the H-rich envelope, the final abundances of the CNO-elements are essentially governed by the initial chemical composition in a sense that pre-existing elements survive as they were.

In the later subsections, we will confirm these conjectures.

6.2.2. Sensitivity of individual isotope

6.2.2.1. ^{13}C

As an example, we will first see how the amount of ^{13}C depends on the adopted abundances of the major four components. The distributions of the final mass fractions of ^{13}C are illustrated in Fig. 6.2(a) for all models. In most part of the convective He-layer, we see the similar distributions of the final ^{13}C in all models other than model A2. In the case of model A2, the amount of ^{13}C is smaller than those of the others by a factor of 40. As seen from Table 6.2, ^{13}C is formed through (n, γ)-reaction of ^{12}C. Almost all of neutrons are produced from ^{4}He through the ν-process and consumed by ^{12}C and ^{16}O with a similar probability per nucleus in the temperature range of the convective He-layer. Hence, the amount of ^{13}C is nearly proportional to the number ratio of ^{12}C to ^{12}C+^{16}O. In model A2 where the ratio of ^{12}C/(^{12}C+^{16}O) is very small compared with those of the other models, the resultant abundance of ^{13}C is very small.

In the radiative He-layer, the maximum and minimum amounts of ^{13}C are seen in models A1 and A2, respectively. Among models SII, A1, and A2, the total amount of ^{12}C and ^{16}O is identical, so that the production of ^{13}C is governed by the ^{12}C/^{16}O ratio, as in the case of the convective He-layer, i.e., the large ^{12}C/^{16}O ratio brings out a large amount of ^{13}C, and vice versa. In models A5 and A6, an appreciable amount of ^{13}C is produced in spite of the low metallicity because of the small abundances of neutron poisons, ^{12}C and ^{16}O. In the H-rich envelope, ^{13}C is simply produced through ^{12}C$(p, \gamma)^{13}$N$(, e^{+}\nu_{e})^{13}$C and

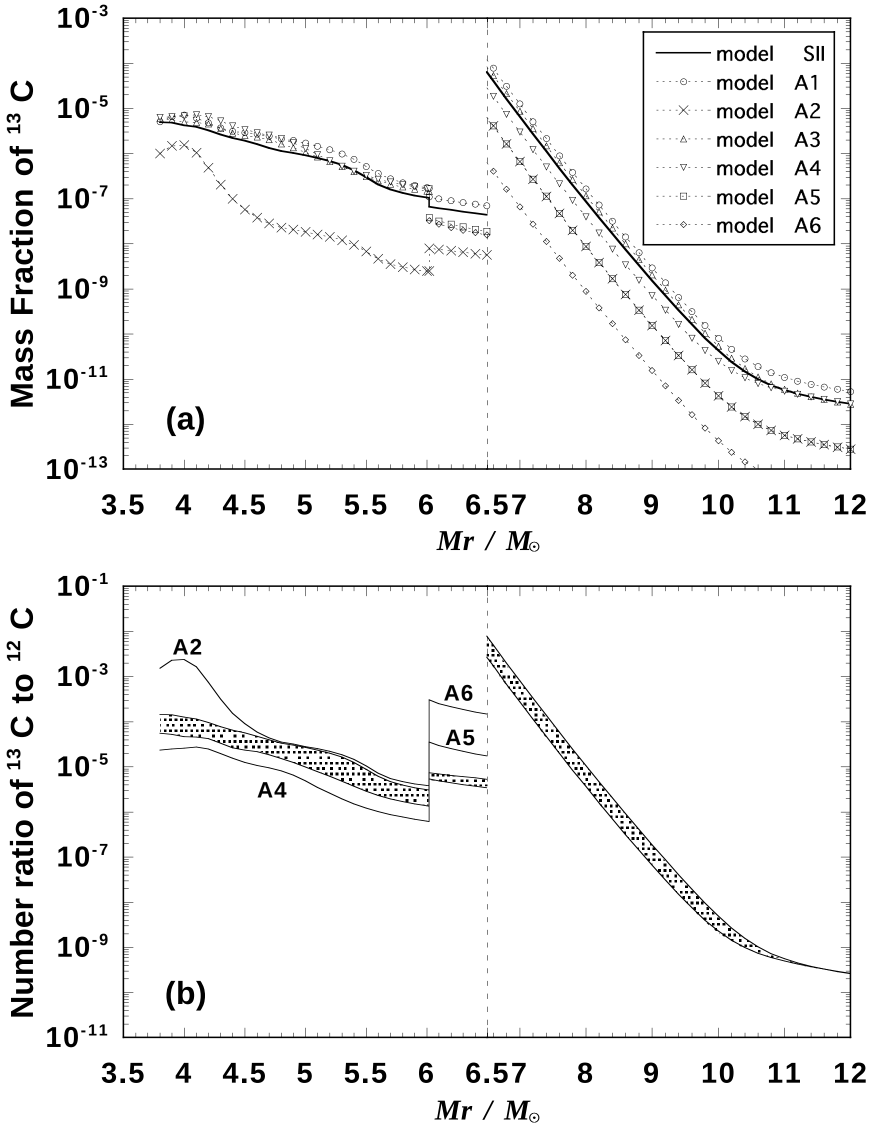

Fig. 6.2. Distributions of the final mass fraction of ^{13}C (panel(a)) and the number ratio of ^{13}C to ^{12}C (panel(b)). In panel (a), some lines overlap each other: models SII, A5, and A6 in the convective He-layer and models SII, A3, and A4 in the radiative He-layer. In panel (b), the shaded regions show ^{13}C/^{12}C ratio in most models which give the similar results. Exceptional curves are labeled model names.

its amount is roughly proportional to those of ^{12}C and protons. So, the largest amount of ^{13}C is formed in model A1 and the smallest in model A6.

In Fig. 6.2(b), we show the distribution of the number of ^{13}C normalized by that of its parent isotope, ^{12}C. The shaded regions show the ^{13}C/^{12}C ratio in most models which give the similar results, whereas the curves present those of the exceptional cases (the following figures are also illustrated by the same manner). Note that the widths of the shaded regions are confined within a factor of 3 or so. This means that the amount of ^{13}C is almost proportional to that of ^{12}C as conjectured in the previous subsection. It should be also noted that the ratios, ^{13}C/^{4}He and ^{13}C/^{16}O, scatter widely from two to four orders of magnitude. In model A2 where the ^{12}C content is as low as 0.0006 in the convective He-layer, the ^{13}C/^{12}C ratio becomes large in the innermost region. In the radiative He-layer, the ^{13}C/^{12}C ratio is larger by a factor of 3 to 30 in models A5 and A6. The reasons are mentioned earlier. In the H-rich envelope, the ^{13}C/^{12}C ratio scarcely depends on initial chemical composition among all models; only difference attributes to the amount of protons and is only within a factor of 3 ($\simeq 0.73/0.25$).

6.2.2.2. ^{10}B and ^{11}B

The amounts of boron isotopes are also scaled well by that of ^{12}C. The distributions of ^{10}B/^{12}C and ^{11}B/^{12}C are presented in Figs. 6.3(a) and 6.3(b), respectively. We see that both ratios are insensitive to the initial chemical compositions as in the case of ^{13}C/^{12}C ratio except a few models.

In the He-layer, the band width of the shaded region is small (within one order of magnitude). This is due to the fact that ^{10}B is mainly produced through $^{12}\mathrm{C}(\nu, \nu' np)^{10}\mathrm{B}$ and decomposed by the neutrons with the similar number density. In models A3 and A4 where both ^{12}C and ^{16}O which are poison to neutrons are very abundant in the convective He-layer, ^{10}B decomposition is less effective and the resultant ^{10}B/^{12}C ratio becomes large. On the contrary, ^{10}B is decomposed by neutrons more effectively in the radiative He-layer

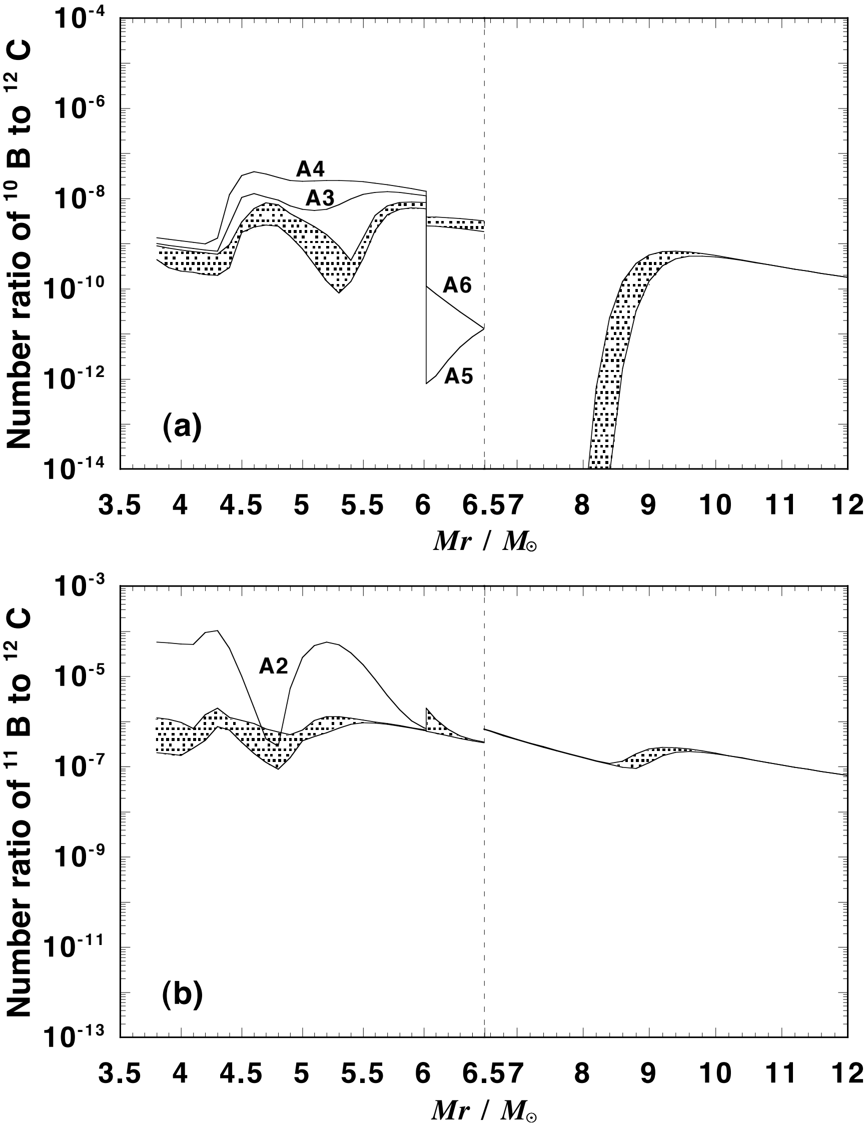

Fig. 6.3. Distribution of the number ratio of ^{10}B to ^{12}C (panel(a)) and that of ^{11}B to ^{12}C (panel(b)). The shaded regions show the ratios in most models which give the similar results. In the exceptional cases, we show curves independently.

in the case of the low metallicity models (models A5 and A6). In the H-rich envelope, ^{10}B is decomposed completely by protons in the inner region but not in the outer region ($M_r \gtrsim 10 M_\odot$). Hence, the abundance of ^{10}B is determined only by that of ^{12}C.

In the case of ^{11}B, the behavior is somewhat different from the case of ^{10}B. In the H-rich envelope, there is no difference from model to model. In the inner part of the H-rich envelope, ^{11}B remains as the daughter isotope of ^{11}C produced from ^{12}C$(\nu, \nu' n)^{11}$C and in the outer part ^{11}B is produced directly from ^{12}C through the ν-process. In the He-layer, even if ^{12}C and ^{16}O are very rich (models A3 and A4), the effect is small because ^{11}B and ^{11}C are not so decomposed by neutrons. The variety of the ratios is within a factor of about 6. Only in the case of model A2 where ^{12}C is less abundant in the convective He-layer, we see a large excess of the ^{11}B/^{12}C ratio. This is due to the fact that, since the abundance of ^{12}C is small, contribution of another production sequence ^{3}H$(\alpha, \gamma)^{7}$Li$(\alpha, \gamma)^{11}$B becomes important. In evaluating probable ratio of ^{11}B/^{12}C in Section 6.4.2, we will exclude the result of model A2.

6.2.2.3. ^{15}N and ^{17}O

Now, we consider the species of which parent isotope is ^{16}O. The distribution of the number ratio of ^{15}N to ^{16}O is presented in Fig. 6.4(a). Except the innermost regions of the He-layer and the H-rich envelope, ^{15}N/^{16}O ratio is almost independent of the initial chemical composition. As seen from Table 6.2, in almost all regions ^{15}N is produced through ^{16}O$(\nu, \nu' p)^{15}$N and is not decomposed. In the innermost regions of the He-layer and of the H-rich envelope, the ratio of ^{15}N/^{16}O depends, more or less, on the initial composition since the decomposition reaction, ^{15}N$(p, \alpha)^{12}$C becomes effective. The effect of decomposition is seen apparently for the ^{12}C-poor model (model A2) because protons are mainly captured by ^{12}C.

The ratio of ^{17}O/^{16}O is illustrated in Fig. 6.4(b). The ratio is confined within a factor of about 10 in the convective He-layer except model A4. In the H-rich envelope,

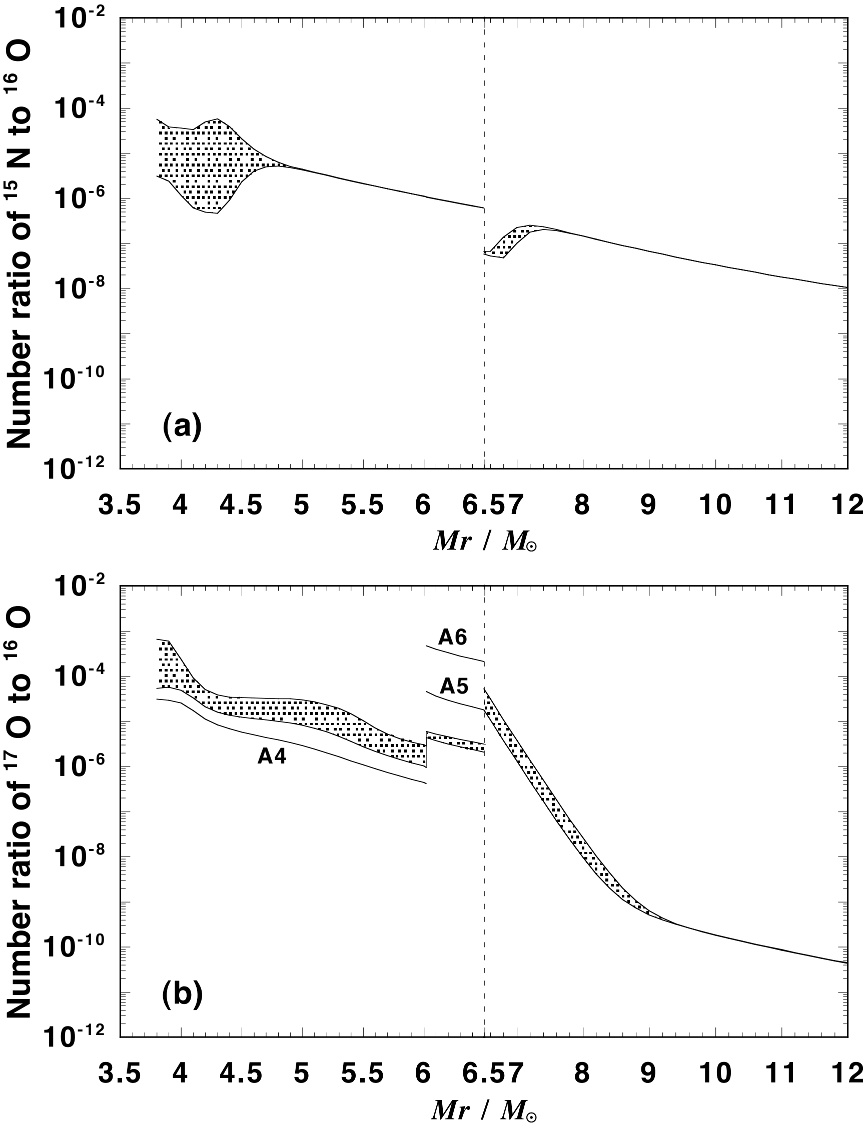

Fig. 6.4. As same as Fig. 6.3, but for the number ratio of ^{15}N to ^{16}O (panel(a)) and that of ^{17}O to ^{16}O (panel(b)). Discontinuities of the curves appear at the boundaries between the convective and the radiative He-layers ($M_r = 6.0M_\odot$) and between the radiative He-layer and the H-rich envelope ($M_r = 6.5M_\odot$).

^{16}O/^{17}O ratio scarcely depends on the initial chemical compositions since ^{17}O is produced from ^{16}O without an appreciable decomposition. The behavior of ^{17}O/^{16}O, shown in Fig. 6.4(b), is very similar to ^{13}C/^{12}C ratio illustrated in Fig. 6.2(b) in a sense that the lack of the parent isotope brings about the high ratio. In model A1 where the ^{16}O content is as low as 0.0006, the ^{17}O/^{16}O ratio becomes large in the innermost region of the convective He-layer (note that the upper edge of the shaded band comes from model A1). Similarly, in the radiative He-layer, ^{17}O/^{16}O ratio becomes also large by a factor of 6 and of 60 in models A5 and A6 (the low metallicity models), respectively.

6.2.2.4. ^{14}N and ^{18}O

As seen from Table 6.2, both ^{14}N and ^{18}O are produced from different parent isotopes (through different types of nuclear reactions) owing to the internal mass coordinate, M_r. So, their abundances are not always scaled thoroughly by any of the major constituents over the whole regions of M_r. Nevertheless, it is reasonable to normalize their abundances by that of ^{4}He because they are formed from ^{4}He originally with a good productivity in the innermost region of the He-layer.

The distribution of the ^{14}N/^{4}He ratio is shown in Fig. 6.5(a). An appreciable amount of ^{14}N is produced only in the inner region where $M_r \lesssim 5.0 M_\odot$ (see also Fig. 6.1(b)) and, in such a region, the ^{14}N/^{4}He ratio is confined within a small region (note that ^{14}N is mainly produced through ^{11}B$(\alpha, n)^{14}$N). On the contrary, in the outer region of the He-layer where $M_r \gtrsim 5.0 M_\odot$, ^{14}N is less abundant and the ^{14}N/^{4}He ratio scatters widely owing to the adopted initial composition; since the temperature during the explosion does not become high enough to proceed α-capture reaction, ^{14}N is produced through ^{17}O$(n, \alpha)^{14}$C in place of ^{11}B$(\alpha, n)^{14}$N. In the H-rich envelope, ^{14}N is produced through ^{12}C$(p, \gamma)^{13}$N$(, e^+\nu_e)^{13}$C$(p, \gamma)^{14}$N and the range of the ^{14}N/^{4}He ratio naturally becomes large owing to the difference of the ^{12}C content.

The distribution of the ^{18}O/^{4}He ratio, shown in Fig. 6.5(b), behaves very similarly to

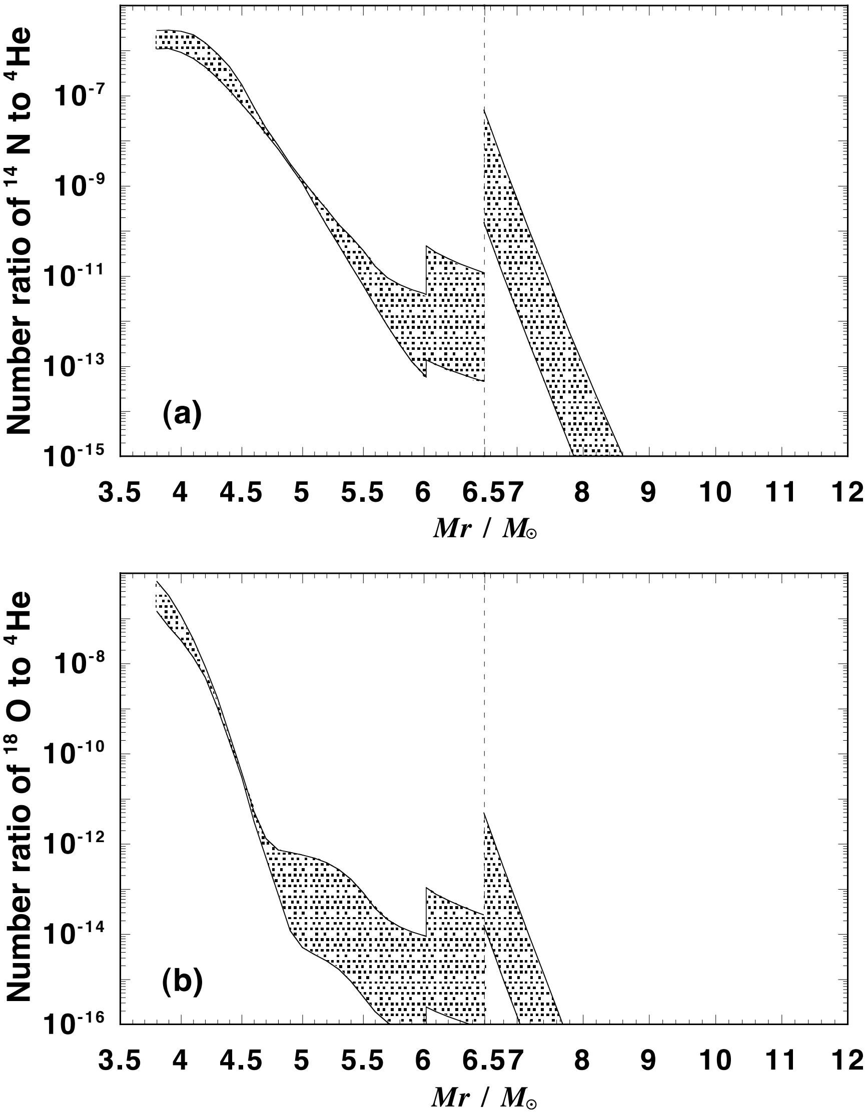

Fig. 6.5. As same as Fig. 6.3, but for the number ratio of ^{14}N to ^{4}He (panel(a)) and that of ^{18}O to ^{4}He (panel(b)).

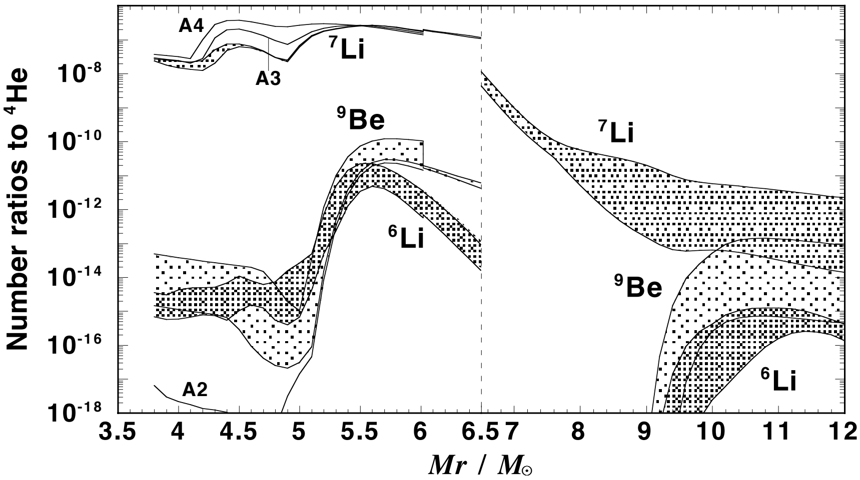

Fig. 6.6. Distributions of the number ratios of ^{6}Li, ^{7}Li, and ^{9}Be to ^{4}He. Dark shaded regions, medial shaded regions, and light shaded regions show ^{6}Li/^{4}He, ^{7}Li/^{4}He, and ^{9}Be/^{4}He ratios in most models, respectively. A curve labeled A2 is of ^{9}Be/^{4}He ratio.

the case of the ^{14}N/^{4}He ratio. In the inner region of the He-layer where $M_r \lesssim 4.7 M_\odot$, ^{18}O is abundant and is scaled well by ^{4}He. In the outer He-layer and in the H-rich envelope, ^{18}O is produced from ^{16}O through two n-captures and two p-captures, respectively. As a result, ^{18}O is less abundant in such regions and the ^{18}O/^{4}He ratio varies over a wide range owing to the ^{16}O-content.

6.2.2.5. ^{6}Li, ^{7}Li, and ^{9}Be

Finally, we present distributions of the numbers of ^{6}Li, ^{7}Li, and ^{9}Be normalized by the ^{4}He content in Fig. 6.6. In the He-layer, the ^{7}Li/^{4}He ratio is insensitive to the initial chemical compositions; the ratio is confined within a factor of 2 or so. As seen from Table 6.2, the production path of ^{7}Li is ^{3}He$(\alpha,\gamma)^7$Be$(n,p)^7$Li$(\alpha,\gamma)^{11}$B in the inner region of the He-layer. In most models, the amounts of ^{4}He and neutrons are almost identical, so that the final ^{7}Li/^{4}He ratio scarcely changes in these models. In models A3 and A4 with the abundant ^{12}C content, the number of neutrons decreases and ^{7}Be is left as it is. In the outer region of the He-layer where $M_r \gtrsim 5.4 M_\odot$, the ^{7}Li/^{4}He ratio is determined uniquely irrelevant to the adopted model. In this region, ^{7}Li is produced from ^{4}He and ^{3}H through ^{4}He$(\nu, \nu' p)^{3}$H$(\alpha, \gamma)^{7}$Li and is not decomposed. In the inner region of the H-rich envelope where $M_r \lesssim 7.6 M_\odot$, the variety of ^{7}Li/^{4}He is relatively small but becomes large in the outer region. In the outer region ^{7}Li is produced from ^{12}C mainly during the ν-process stage. As a result, the ^{7}Li/^{12}C ratio is confined within a factor of 3.

For ^{6}Li and ^{9}Be, their ratios to ^{4}He scatters very widely in most of regions but not in the middle region ($5.4 M_\odot \lesssim M_r \lesssim 6.5 M_\odot$) where they are abundant (the ratios are confined within a factor of 6 or so). In the middle region, ^{9}Be is produced from ^{7}Li through ^{7}Li$(t, n)^{9}$Be and ^{6}Li is produced through ^{9}Be$(p, \alpha)^{6}$Li. Or, more explicitly, they are produced from ^{4}He originally (see Table 6.2). In the other regions, ^{9}Be is produced from ^{12}C, so that it is natural that both ^{9}Be/^{4}He and ^{6}Li/^{4}He ratios have large varieties due to the initial chemical compositions. However, it is not so important because of their extremely small amounts.

6.2.3. Decomposition of the light elements

It is also interesting to see the decomposition process of the light elements which would exist in the presupernova stage. As mentioned in Section 6.1.2, we put 1×10^{-6} and 1×10^{-10} as the initial mass fractions of the rare CNO-elements and the X-elements, respectively, keeping the amounts of the four major elements of model SII (such a model is called model B). The mass fractions of the X-elements in model B are presented in Fig. 6.7(a). In the convective He-layer, the X-elements, which exist initially, are decomposed or hidden completely by those produced during the explosion. In fact, the distribution of the mass fractions of the X-elements in the convective He-layer is almost same as those in model SII (compare with Fig. 6.1(a) on page 78). In the radiative He-layer, a small part of

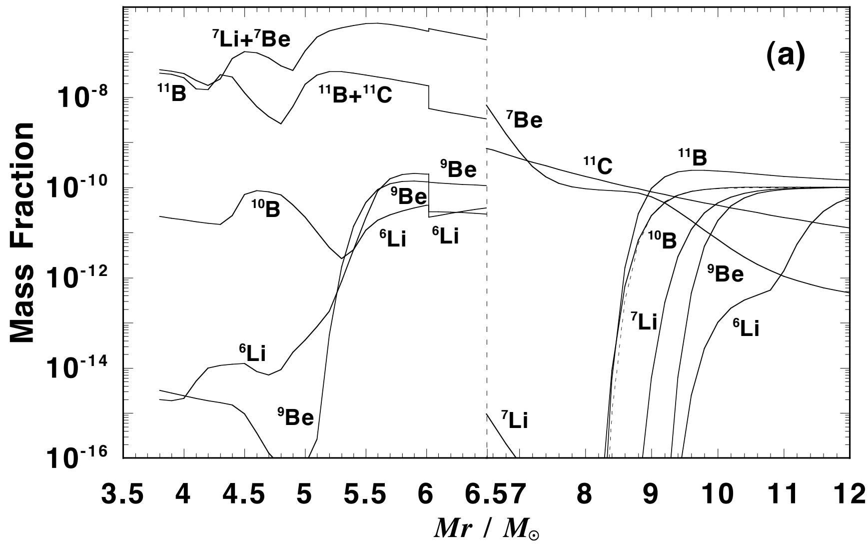

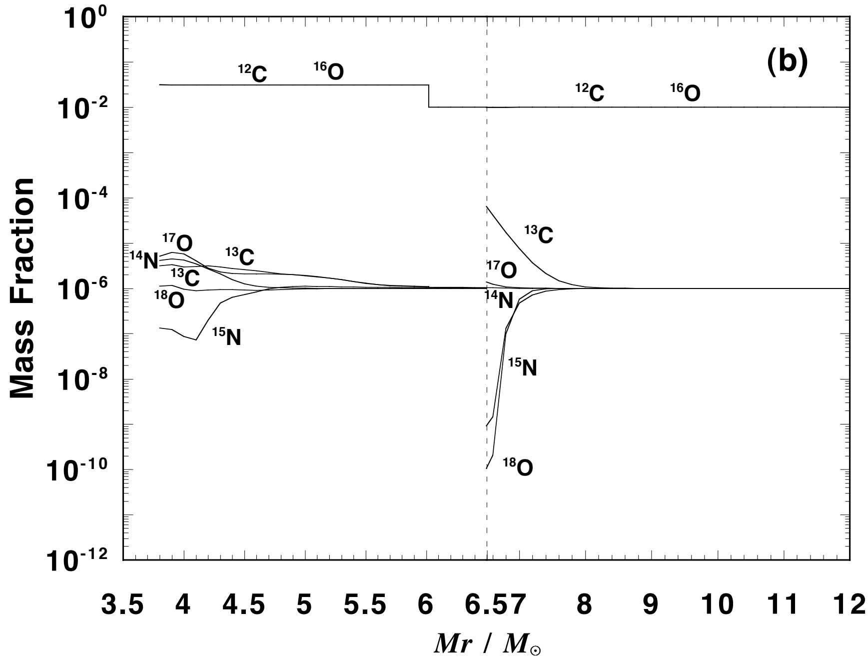

Fig. 6.7. Distribution of the abundances of the X-elements (panel(a)) and the CNO-elements (panel (b)) in model B. In panel(a) dashed line denotes the fraction of survival ^{11}B of the shock heating.

initially existing ^{6}Li and ^{9}Be can survive against (p, α)-reactions. In the H-rich envelope, only ^{7}Be and ^{11}C, both of which are p-rich unstable elements, are newly produced and remain against p-capture process. However, all of the stable X-elements (except ^{11}B) are not formed through the ν-process but decomposed effectively owing to the shock heating. For ^{11}B, we can see from Fig. 6.7(a) that a small amount of ^{11}B is produced through the ν-process. In other words, for the X-elements (except ^{11}B) the distribution curves in the H-rich envelope mean the fractions of survival of the shock heating; in the inner region they are completely decomposed and in the outer region ($M_r \gtrsim 12 M_\odot$) they can survive and keep their initial compositions in the presupernova stage. For the later convenience, we also show the survival fraction of ^{11}B by dashed line in Fig. 6.7(a), which is obtained from a numerical calculation without the ν-process.

The distributions of the mass fractions of the CNO-elements are shown in Fig. 6.7(b). In the innermost region of the convective He-layer, only ^{15}N is decomposed through ^{15}N$(p, \alpha)^{12}$C. The other isotopes are produced and reach the abundance level in model SII. In the outer region where $M_r \gtrsim 4.5 M_\odot$ (including the radiative He-layer), all of the CNO-elements conserve their initial abundances. In the H-rich envelope, ^{15}N and ^{18}O are decomposed at the narrow region inner than 7.2 $M_\odot$. When the CNO-cycle is in quasi-steady state, both ^{15}N/^{14}N and ^{18}O/^{16}O ratios are quite small, since ^{15}N$(p, \alpha)^{12}$C and ^{18}O$(p, \alpha)^{15}$N have relatively large cross sections compared with the other reactions of the CNO-cycle. So it is natural that only ^{15}N and ^{18}O are decomposed during the explosion. In the region outer than $M_r \gtrsim 7.8 M_\odot$, the CNO-elements keep completely their initial abundances.

6.3. Probable chemical composition in the presupernova stage

The light elements, which are produced on the way of the stellar evolution to the presupernova stage, affect, more or less, the nucleosynthesis during the supernova explosion by two ways; one is that relatively abundant elements govern the production and/or decomposition processes and the other is that the pre-existing light elements survive after the supernova explosion. So, it is important to evaluate probable values of the amounts and the isotopic ratios of the light elements in the He-layer and the H-rich envelope in order to see the reliable light element composition of the supernova ejecta.

6.3.1. The CNO-elements

First, we consider the abundances of the CNO-elements in the H-rich envelope. According to Lamb *et al.* (1976), during the time when a 25 $M_{\odot}$ star evolves from the helium burning stage to the carbon burning stage, the temperature of the H-burning shell varies from 3.0×10^7 K to 5.0×10^7 K. Using this temperature range and assuming that the corresponding density is in the range between $0.1 \mathrm{g/cm^3}$ and $10 \mathrm{g/cm^3}$ and the metallicity is 2 % by weight, we evaluate possible ranges of the steady-flow equilibrium abundances of the CNO-elements. In this calculation we used a small nuclear reaction network in Fig. 2.1 (on page 18). The possible ranges of the elemental abundances of the major components and the isotopic ratios are tabulated in Table 6.3 as "the equilibrium values" (the He content is assumed to be 0.25 to 0.60). One of the most remarkable points is that ^{14}N is the most abundant element among the CNO-elements. For comparison, numerical results found by Woosley *et al.* (1990) and Weaver and Woosley (1993) (which hereafter are referred to W90 and WW93, respectively) are also shown in Table 6.3. The values due to WW93 are those in the presupernova stage of a 25 $M_{\odot}$ star found from their evolutionary calculation. In WW93, the contents of some isotopes are beyond the ranges of the steady-flow equilibrium abundances, probably because the CNO-cycle may not be in the steady-flow equilibrium. On the other hand, W90 gives the abundances consistent with those predicted by the steady-flow equilibrium condition. For the later use, we will define probable ranges of the contents of the CNO-elements in the H-rich envelope of a progenitor; probable ranges are determined so as to include all the values of the three examples (except ^{17}O; see the next paragraph) and are shown in Table 6.3 as the "probable values".

It should be noted that the amount of ^{17}O given by WW93 is rather large compared with that of the steady-flow equilibrium value in this study. Almost all of ^{17}O is produced through $^{16}\mathrm{O}(p,\gamma)^{17}\mathrm{F}\ (,e^{+}\nu_{\mathrm{e}})^{17}\mathrm{O}$ and decomposed by $^{17}\mathrm{O}(p,\alpha)^{14}\mathrm{N}$ at the H-burning shell (Woosley and Weaver 1995). The reaction rate of $^{17}\mathrm{O}(p,\alpha)^{14}\mathrm{N}$ used in WW93 (Caughlan and Fowler 1988) is much smaller than that of Landré *et al.* (1990) which we adopted. Woosley *et al.* (1997) pointed out that the total amount of ^{17}O of a 25 $M_{\odot}$ supernova ejecta (Model S25A in Woosley and Weaver 1995) decreases by a factor of 14 by the use of the reaction rate of Landré *et al.* (1990) and Blackmon *et al.* (1995) compared with that by the use of Caughlan and Fowler (1988). So, the amount of ^{17}O given by WW93 is reduced by a factor of 14 in evaluating the probable values in Table 6.3 (as well as in Tables 6.4 and 6.5).

In the radiative He-layer, it is natural to consider that the initial abundances are those of ashes of the hydrogen burning. In Table 6.4, the steady-flow equilibrium abundances of the CNO-cycle, calculated by the same way as earlier (but the He-content is assumed to be 0.95 to 0.97), are shown together with those of W90 and WW93. The probable abundances in the radiative He-layer are deduced from the three examples.

In the convective He-layer, the probable amounts of the CNO-elements (except ^{14}N) are deduced from W90, WW93, and model SI by the similar way as earlier. They are tabulated in Table 6.5. Note that the three references give quite different values in the abundance of ^{14}N from each other. Especially, the amount of ^{14}N given by WW93 is extraordinarily large. In the typical temperature range of the He-burning ($\sim 2\times10^{8}$ K) ^{14}N reacts with ^{4}He very rapidly to form ^{18}F compared with the triple α-reaction. So, it is reasonable to expect that in the presupernova stage only a small amount of ^{14}N is

Table 6.3. Probable initial mass fractions and isotopic ratios (in number) of the CNO-elements in the H-rich envelope. For comparison, we also present the chemical compositions given by Woosley *et al.* (1990) and Weaver and Woosley (1993) (referred to as W90 and WW93, respectively, in the text) as well as the steady-flow equilibrium compositions of the CNO-cycle.

	Probable values	W90	WW93	Equilibrium values
^{4}He	$0.25 \sim 0.6$	~ 0.5	0.39	$0.25 \sim 0.60$
^{12}C	$2 \times 10^{-4} \sim 2 \times 10^{-3}$	2.1×10^{-4}	2×10^{-3}	$2.2 \times 10^{-4} \sim 4.4 \times 10^{-4}$
^{14}N	$5 \times 10^{-3} \sim 2 \times 10^{-2}$	1.2×10^{-2}	5×10^{-3}	1.9×10^{-2}
^{16}O	$3 \times 10^{-4} \sim 7 \times 10^{-3}$	6.6×10^{-4}	7×10^{-3}	$2.9 \times 10^{-4} \sim 6.3 \times 10^{-4}$
^{12}C/^{4}He	$1 \times 10^{-4} \sim 2 \times 10^{-3}$	1.4×10^{-4}	1.7×10^{-3}	$1.2 \times 10^{-4} \sim 5.9 \times 10^{-4}$
^{14}N/^{1}H	$9 \times 10^{-4} \sim 5 \times 10^{-3}$	1.7×10^{-3}	9.2×10^{-4}	$2.3 \times 10^{-3} \sim 5.4 \times 10^{-3}$
^{12}C/^{13}C	$3 \sim 2 \times 10$	3.4	2.4×10	3.5
^{14}N/^{15}N	3×10^{4}	3.2×10^{4}	–	$2.9 \times 10^{4} \sim 3.4 \times 10^{4}$
^{16}O/^{17}O	$2 \times 10^{2} \sim 2 \times 10^{3}$	–	1.2×10^{2}	$2.2 \times 10^{2} \sim 9.1 \times 10^{2}$

left unless there happens to occur, for example, a large scale mixing through which ^{14}N is newly formed just before the supernova explosion. In fact, in 6 $M_\odot$ and 8 $M_\odot$ He-star models which correspond to 20 $M_\odot$ and 25 $M_\odot$ main sequence stars, respectively (Nomoto and Hashimoto 1988), very small amount of ^{14}N (compared to that of WW93) is left in the presupernova stage (Hashimoto 1999). Thus, the initial amount of ^{14}N is deduced only from W90 and model SI. The probable mass fraction of ^{18}O is adopted from the result of model SI neglecting those of W90 and WW93 which are much larger than ours. This is because the reaction rate of $^{18}\mathrm{O}(\alpha,\gamma)^{22}\mathrm{Ne}$ increases recently by a factor of 10 to 200 in the temperature range of the He-burning (Giesen *et al.* 1994) compared with that used in W90 and WW93.

Table 6.4. Probable initial mass fractions and isotopic ratios (in number) of the CNO-elements in the radiative He-layer. In the table, W90 and WW93 denote a composition of the ashes of hydrogen-burning in W90 and that of the radiative He-layer in WW93, respectively.

	Probable values	W90	WW93	Equilibrium values
^{4}He	$0.95 \sim 1$	0.985	0.98	$0.95 \sim 0.97$
^{12}C	$2 \times 10^{-4} \sim 4 \times 10^{-4}$	2.2×10^{-4}	2×10^{-4}	$2.2 \times 10^{-4} \sim 4.4 \times 10^{-4}$
^{14}N	$1 \times 10^{-2} \sim 2 \times 10^{-2}$	1.2×10^{-2}	1.3×10^{-2}	1.9×10^{-2}
^{16}O	$2 \times 10^{-4} \sim 6 \times 10^{-4}$	2.6×10^{-4}	2×10^{-4}	$2.9 \times 10^{-4} \sim 6.3 \times 10^{-4}$
^{12}C/^{4}He	$7 \times 10^{-5} \sim 2 \times 10^{-4}$	7.4×10^{-5}	6.8×10^{-5}	$7.6 \times 10^{-5} \sim 1.5 \times 10^{-4}$
^{12}C/^{13}C	$3 \sim 4$	3.5	2.7	3.5
^{14}N/^{15}N	3×10^{4}	3.1×10^{4}	–	$2.9 \times 10^{4} \sim 3.4 \times 10^{4}$
^{16}O/^{17}O	$2 \times 10^{2} \sim 9 \times 10^{2}$	–	1.1×10	$2.2 \times 10^{2} \sim 9.1 \times 10^{2}$

Table 6.5. Probable initial mass fractions and isotopic ratios (in number) of the CNO-elements in the convective He-layer. In the table W90 denotes a composition of the He-layer with 95% He estimated by W90 and WW93 denotes that of the convective He-layer given in WW93.

	Probable values	W90	WW93	model SI
^{4}He	$0.91 \sim 0.95$	0.95	0.91	0.93
^{12}C	$3 \times 10^{-2} \sim 6 \times 10^{-2}$	3.0×10^{-2}	6×10^{-2}	6.2×10^{-2}
^{14}N	$1 \times 10^{-12} \sim 6 \times 10^{-8}$	1.1×10^{-12}	$6 \times 10^{-7} \sim 5 \times 10^{-6}$	5.8×10^{-8}
^{16}O	$4 \times 10^{-4} \sim 1 \times 10^{-2}$	4.1×10^{-4}	1.1×10^{-2}	7.2×10^{-4}
^{18}O	1×10^{-5}	8.0×10^{-3}	2.0×10^{-3}	1.4×10^{-5}
^{12}C/^{4}He	$1 \times 10^{-2} \sim 2 \times 10^{-2}$	1.1×10^{-2}	2.2×10^{-2}	2.2×10^{-2}
^{12}C/^{16}O	$7 \sim 1 \times 10^{2}$	9.8×10	7.3	1.1×10^{2}
^{12}C/^{13}C	$9 \times 10^{7} \sim 2 \times 10^{9}$	9.3×10^{7}	–	2.3×10^{9}
^{14}N/^{15}N	$4 \times 10^{-5} \sim 4$	3.7×10^{-5}	–	4.0
^{16}O/^{17}O	$5 \times 10^{4} \sim 8 \times 10^{4}$	–	5.8×10^{3}	5.5×10^{4}
^{16}O/^{18}O	$5 \times 10^{1} \sim 1 \times 10^{3}$	5.8×10^{-2}	6.2	5.8×10^{1}

6.3.2. The X-elements

It is reasonable to presume that, in the presupernova stage, there are no X-elements in the He-layer as well as in the inner (convective) H-rich envelope because they are all decomposed at the H-burning shell. Even if they existed in these regions, they would be eliminated by the nuclear processes during the supernova explosion as already seen in Section 6.2.3. Thus, we are interested in the initial abundances of the X-elements only in the outer H-rich envelope.

The initial abundances of the X-elements can be deduced only on the basis of observations of the atmospheric chemical compositions of stars. For Li, unfortunately, we have no definite answer although many observations have been made for various kinds of stellar objects (e.g., Andersen *et al.* 1984; Rebolo *et al.* 1986; Lemoine *et al.* 1997; Hobbs and Thorburn 1997; Smith *et al.* 1998; Cayrel *et al.* 1999); we have now only upper limits on the elemental ratio, Li/H, and the isotopic ratio, ^{6}Li/^{7}Li (in number):

$$\mathrm{Li/H} \lesssim 1 \times 10^{-9} \qquad \text{and} \qquad {}^6\mathrm{Li}/{}^7\mathrm{Li} \leq 0.1\,. \tag{6.1}$$

It should be noted that there exist Li-deficient stars of which Li abundance is lower than the above by one or two orders of magnitude (e.g., Soderblom *et al.* 1993). It is believed that in such stars the surface materials are transported to a hot region by a large scale mixing and, as a result, light elements such as ^{2}H, ^{6}Li, and ^{7}Li are decomposed.

The Be/Li ratio is evaluated from observations of stars of which surface temperature is higher than 6700 K; Meneguzzi *et al.* (1971) gave the ratio of Be/Li between 2×10^{-3} and 1.5×10^{-2} (in number) from the observations of eight main-sequence stars with masses between 1 $M_\odot$ and 2 $M_\odot$. Furthermore, Boesgaard and Budge (1989) reported 4.7×10^{-3} and 5.0×10^{-2} for two Li-deficient F-type stars in Hyades. Since ^{6}Li/^{7}Li $\lesssim$ 0.1, the probable range of ^{9}Be/^{7}Li in the presupernova stage may be given as (in number)

$$2 \times 10^{-3} \lesssim {}^9\mathrm{Be}/{}^7\mathrm{Li} \lesssim 5 \times 10^{-2}\,. \tag{6.2}$$

As will be seen later, the above abundance of ^{9}Be is one or two orders of magnitude larger than that produced in the exploding H-rich envelope.

There are also many observational studies on the B/Li ratio of stars. Lemke *et al.* (1993) reported the B/Li ratio to be 2.9×10^{-2} and 1.4×10^{-2} (in number) from the observations of HD82328 and HD211027, respectively, both of which are population I stars with the surface temperature higher than 6000 K. Furthermore, Boesgaard *et al.* (1998) found 2.1×10^{-1} and 1.0 in Li- and Be-deficient two stars. On the basis of these observational studies, the probable range of the ^{11}B/^{7}Li ratio is evaluated as

$$1 \times 10^{-2} \lesssim {}^{11}\mathrm{B}/{}^{7}\mathrm{Li} \lesssim 1\,. \qquad (6.3)$$

6.4. Probable Isotopic/Elemental Diagrams

Combining the numerical results found in Section 6.2 and the probable initial composition evaluated in the last section, we will consider the probable ranges of the isotopic/elemental ratios, ^{6}Li/^{7}Li, ^{9}Be/^{7}Li, ^{11}B/^{7}Li, ^{12}C/^{13}C, ^{14}N/^{15}N, and ^{16}O/^{17}O, which are to be observed in supernova ejecta.

6.4.1. The ^{6}Li/^{7}Li and ^{9}Be/^{7}Li ratios

In Sections 4 and 5, we showed that only small amounts of ^{6}Li and ^{9}Be are produced in the He-layer and the H-rich envelope during the supernova explosion and that the ratios of them to ^{7}Li are very small compared with, say, the solar ratios. These are the remarkable features of nucleosynthesis in the supernova explosion and, hence, it is important to confirm whether these arguments are proper or not even when we choose the different initial chemical compositions from model SI.

As conjectured from Fig. 6.6 (on page 89), the produced amounts of ^{6}Li and ^{9}Be become large compared with the detection limit (which is an abundance level of 1×10^{-9} times as small as the number of ^{16}O; see Section 1) only in the outer regions of the

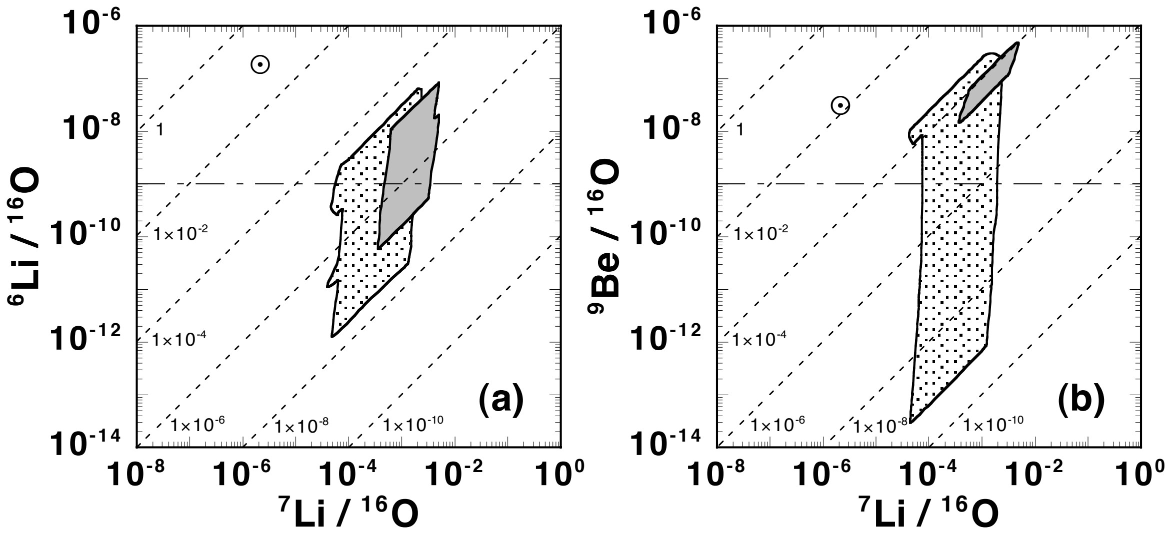

Fig. 6.8. Diagrams between ^{6}Li/^{16}O and ^{7}Li/^{16}O ratios (panel (a)) and between ^{9}Be/^{16}O and ^{7}Li/^{16}O ratios (panel (b)). The ratios are all in number. Light and dark shaded regions show the varieties of the ratios in the convective He-layer outer than 5.1 $M_{\odot}$ and in the radiative He-layer, respectively. A dash-dotted horizontal line indicates the detection limit (see text). Furthermore, dotted lines show the values of constant ^{6}Li/^{7}Li ratio (a) and ^{9}Be/^{7}Li ratio (b). A mark $\odot$ denotes the ratios of the solar-system composition.

convective He-layer. This is always true irrelevant to the initial contents of ^{6}Li and ^{9}Be because, as mentioned in Section 6.2.3, pre-existing ^{6}Li and ^{9}Be are almost completely decomposed in the He-layer and the inner H-rich envelope. In Figs. 6.8(a) and 6.8(b), we show the probable ranges of the final ^{6}Li and ^{9}Be contents in ^{6}Li and ^{9}Be abundant region in the convective He-layer ($M_r \geq 5.1 M_{\odot}$) and in the radiative He-layer. In these diagrams, the results of models A2 and A4 in the convective He-layer and model A1 in the radiative He-layer are excluded because of a mismatch in the ^{12}C and ^{16}O contents. Furthermore, the amount of ^{16}O of each model is replaced by that within the probable range. Figures show that the ^{6}Li/^{7}Li and the ^{9}Be/^{7}Li ratios are always less than 3×10^{-5}

and 2×10^{-4}, respectively. Thus, we can say that ^{6}Li and ^{9}Be are not produced so much during the supernova explosion in the He-layer and in the H-rich envelope and that their ratios to ^{7}Li are much smaller than those of the solar-system composition. It should be noted, however, that it is possible to conserve their initial ratios (of the levels given by Eqs. (6.2) and (6.3)) in the outermost part of the H-rich envelope where $M_r \gtrsim 10 M_\odot$ (see Fig. 6.7(a)).

6.4.2. The ^{11}B/^{7}Li ratio

As seen in Section 6.2.2, the amounts of ^{11}B and ^{7}Li are scaled conveniently by those of different major constituents (i.e., ^{12}C and ^{4}He, respectively) and their final abundances suffer from their initial contents in the H-rich envelope (see Section 6.2.3), which we do not know precisely. Moreover, since the amount of ^{14}N is relatively large in the H-rich envelope (see Section 6.3.1), we should take account of ^{7}Li production through $^{14}\mathrm{N}(\nu, \nu'\alpha)^{10}\mathrm{B}(p, \alpha)^7\mathrm{Be}(e^-, \nu_\mathrm{e})^7\mathrm{Li}$ which may play an important role on the ^{7}Li production in the intermediate mass region (see Table 4.1). Thus, it is not so easy to find the probable ratio of ^{11}B/^{7}Li. Here, by the help of the result in Section 4 (see Fig. 4.3 on page 52) as well as our numerical simulations mentioned in Section 6.2, we evaluate the probable range of ^{11}B/^{7}Li ratio by the following way. The result is illustrated in Fig. 6.9(a).

In the convective He-layer, pre-existing ^{7}Li and ^{11}B are completely decomposed on the way to the presupernova stage and the ^{11}B/^{7}Li ratio is determined by the nuclear processes during the supernova explosion. In the inner region of the He-layer the probable range of the ^{11}B/^{7}Li ratio is evaluated almost uniquely from our results of models SII, A1, and A3, of which ^{12}C and ^{16}O-contents are consistent with the probable initial abundances shown in Table 6.5. In the outer convective He-layer (where $M_r \gtrsim 5.2 M_\odot$) as well as in the radiative He-layer, ^{7}Li and ^{11}B are produced mainly from ^{4}He and ^{12}C, respectively.

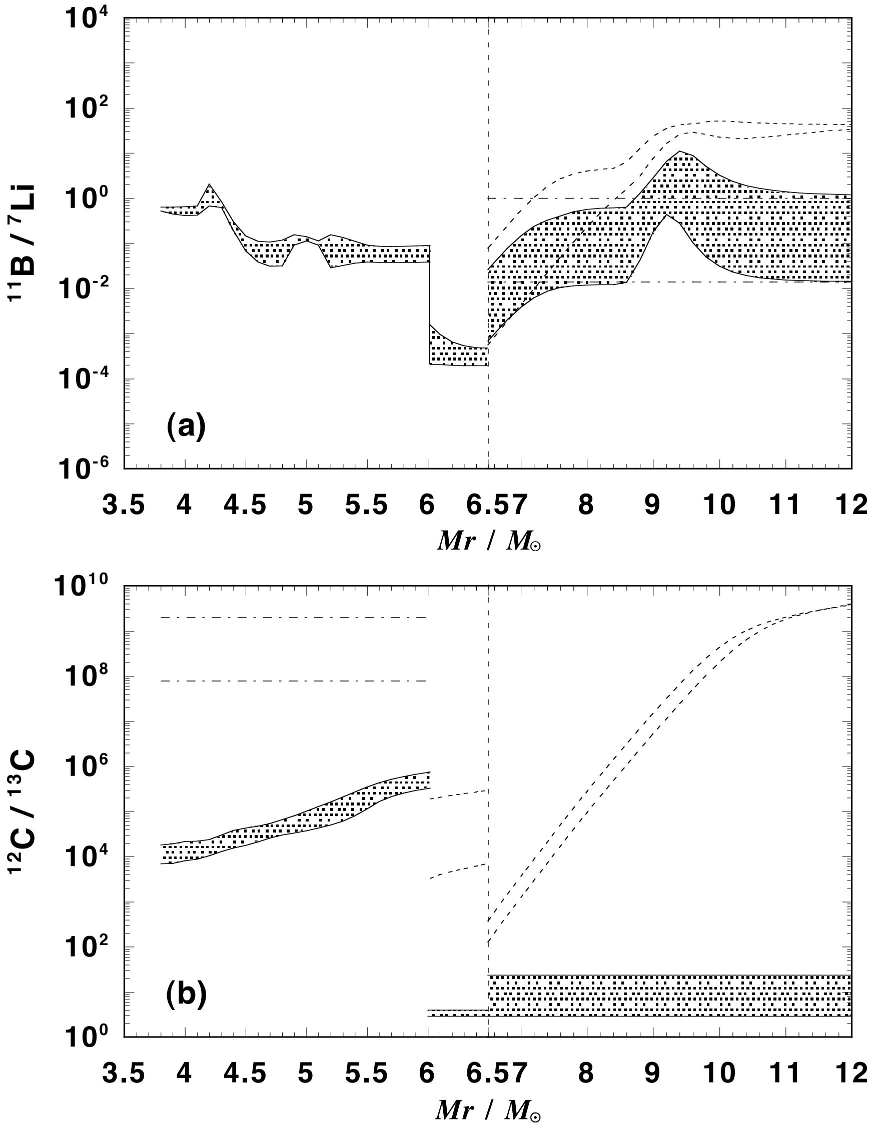

Fig. 6.9. Distributions of the number ratios of $^{11}B/^{7}Li$ (panel(a)), $^{12}C/^{13}C$ (panel(b)), $^{14}N/^{15}N$ (panel(c)), and $^{16}O/^{17}O$ (panel(d)). Shaded regions show the probable ratios evaluated from the results of numerical simulations and the probable chemical compositions in the presupernova stage. Regions between two dashed lines correspond to the shaded regions in Figs. 6.2 to 6.5, i.e., the probable ranges of the ratios of the produced elements and regions between two dash-dotted lines present the probable ranges of the elemental ratios in the presupernova stage evaluated in Section 6.3.

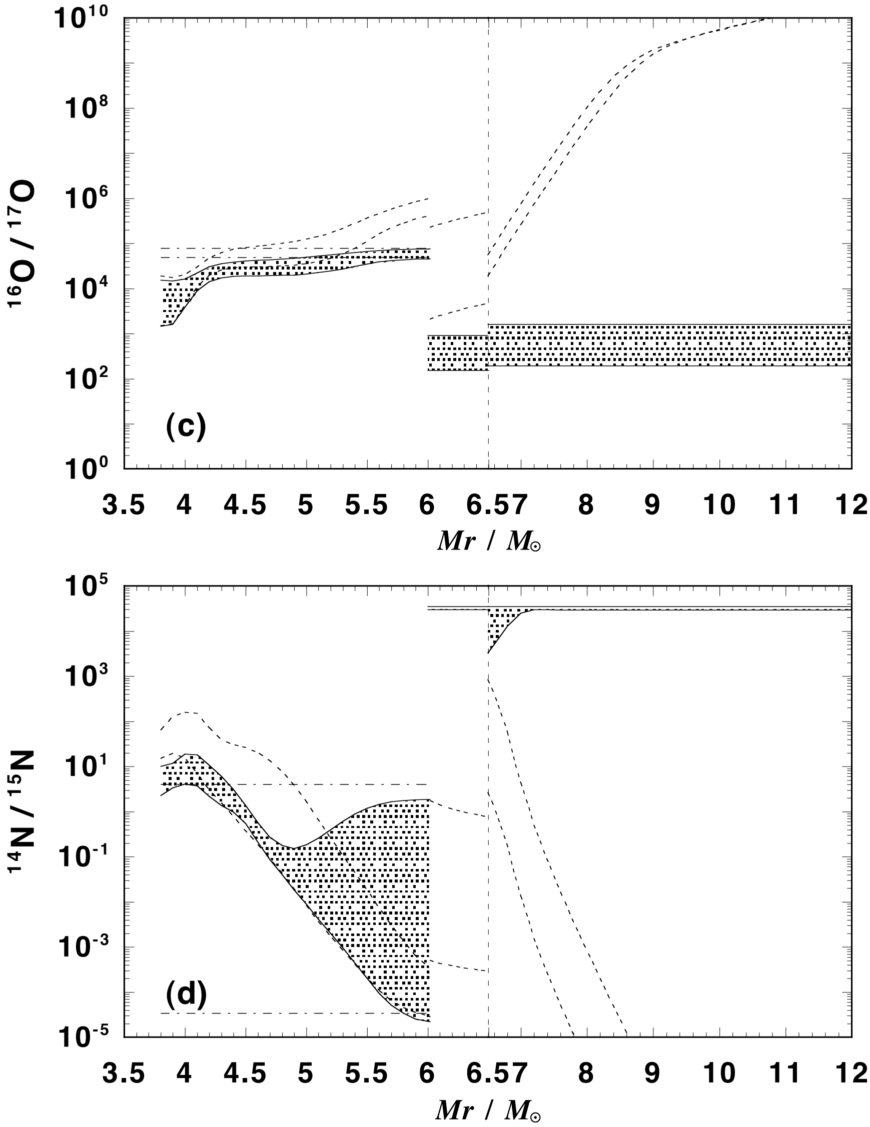

Fig. 6.9. *Continued*

Hence, the range of the ^{11}B/^{7}Li ratio is governed essentially by the ^{12}C/^{4}He ratio and evaluated from

$$\frac{^{11}\mathrm{B}}{^{7}\mathrm{Li}} = \left(\frac{^{12}\mathrm{C}}{^{4}\mathrm{He}}\right)_{\mathrm{o}} \left(\frac{^{11}\mathrm{B}}{^{12}\mathrm{C}}\right)_{\mathrm{m}} \left(\frac{^{7}\mathrm{Li}}{^{4}\mathrm{He}}\right)_{\mathrm{m}}^{-1} \quad . \tag{6.4}$$

In the above, $(^{12}\mathrm{C}/^{4}\mathrm{He})_{\mathrm{o}}$ is the initial elemental ratio given in Tables 6.4 and 6.5. The ratios $(^{11}\mathrm{B}/^{12}\mathrm{C})_{\mathrm{m}}$ and $(^{7}\mathrm{Li}/^{4}\mathrm{He})_{\mathrm{m}}$ are found from the results of our calculations mentioned in Section 6.3 (i.e., the shaded bands in Figs. 6.3(b) and 6.6).

In the inner H-rich envelope where $M_r \lesssim 8.5 M_\odot$, both ^{7}Li and ^{11}B existing in the presupernova stage are decomposed almost completely by the shock heating and re-produced through the ν-processes and the explosive nucleosynthesis (see Section 6.2.3). In the outer region of the H-rich envelope ($M_r \gtrsim 10 M_\odot$), both ^{7}Li and ^{11}B are formed commonly through the ν-process from ^{12}C during the supernova explosion but their produced amounts are very small, as seen in Fig. 6.1(a) (on page 78), compared with those of ^{7}Li and ^{11}B observed in stellar surfaces (see Section 6.3.2). Thus, in such regions of the H-rich envelope, the ^{11}B/^{7}Li ratio is described by

$$\frac{^{11}\mathrm{B}}{^{7}\mathrm{Li}} = \frac{\left(\frac{^{11}\mathrm{B}}{^{12}\mathrm{C}}\right)_{\mathrm{m}} \left(\frac{^{12}\mathrm{C}}{^{1}\mathrm{H}}\right)_{\mathrm{o}} + \left(\frac{^{11}\mathrm{B}}{^{7}\mathrm{Li}}\right)_{\mathrm{o}} \left(\frac{^{7}\mathrm{Li}}{^{1}\mathrm{H}}\right)_{\mathrm{o}} \xi_{11\mathrm{B}}}{\left(\frac{^{7}\mathrm{Li}}{^{4}\mathrm{He}}\right)_{\mathrm{m}} \left(\frac{^{4}\mathrm{He}}{^{1}\mathrm{H}}\right)_{\mathrm{o}} + \left(\frac{^{7}\mathrm{Li}}{^{1}\mathrm{H}}\right)_{\mathrm{o}} \xi_{7\mathrm{Li}}} \quad , \tag{6.5}$$

where subscripts m and o denote the elemental ratios found in our model calculations and the probable ratios predicted in Section 6.3.2, respectively. Furthermore, ξ_i denotes the fraction of survival of the shock heating to the initial amount of i-th constituent and is shown in Fig. 6.7(a).

In the intermediate region where $8.5 M_\odot \lesssim M_r \lesssim 10 M_\odot$, as mentioned at the top of this subsection, we should add the amount of ^{7}Li produced from ^{14}N to denominator of Eq. (6.5), i.e., $(^{7}\mathrm{Be}/^{14}\mathrm{N})_{\mathrm{m}} \cdot (^{14}\mathrm{N}/^{1}\mathrm{H})_{\mathrm{o}}$. Here the ratio of $(^{7}\mathrm{Be}/^{14}\mathrm{N})_{\mathrm{m}}$ is evaluated from the numerical result in Section 4 * and the adopted range of the ratio is between 2×10^{-10}

and 8×10^{-9} in the corresponding mass region. The probable range of ^{14}N, that is, $(^{14}N/^{1}H)_{o}$, is written in Section 6.3.1.

6.4.3. The $^{12}C/^{13}C$ and $^{16}O/^{17}O$ ratios

We can readily find the probable $^{12}C/^{13}C$ ratio as long as the initial chemical compositions are included in the probable ranges listed in Tables 6.3 to 6.5. In the H-rich envelope and the radiative He-layer, the probable content of ^{13}C is much larger than that produced during the supernova explosion (see Fig. 6.2(b) on page 82) and, as seen in Section 6.2.3, ^{13}C is hardly decomposed. Thus, in these regions the $^{12}C/^{13}C$ ratio is entirely determined by the initial ratio. On the other hand, in the convective He-layer, the amount of ^{13}C expected in the presupernova stage is of the order of 1×10^{-10}, which is much less than that produced during the supernova explosion (see Table 6.5 and Fig. 6.2(b)); in this region, the $^{12}C/^{13}C$ ratio is a result of the nuclear processes during the explosion and the distribution is well described by the shaded band illustrated in Fig. 6.2(b). Here we exclude models A2 and A4 because of an extreme mismatch in the initial contents of ^{12}C and ^{16}O (compare Table 6.1 with Table 6.5). The result is shown in Fig. 6.9(b).

Evaluation of the probable $^{16}O/^{17}O$ ratio is slightly complicated compared with the case of $^{12}C/^{13}C$. In the radiative He-layer and the H-rich envelope, the amount of ^{17}O in the presupernova stage is much larger than that produced in the supernova explosion similarly to the case of ^{13}C. Furthermore, ^{17}O is hardly decomposed, as seen in Section 6.2.3, in these regions and thus, the $^{16}O/^{17}O$ ratio is simply determined by that of the presupernova stage. However, the amount of ^{17}O produced in the supernova explosion is slightly larger than that expected in the presupernova stage in the inner region but not

*The ratio of $(^{7}Be/^{14}N)_{m}$ is evaluated as the difference between the $^{10}B/^{14}N$ ratio produced through $^{14}N(\nu, \nu'\alpha)^{10}B$, which is not apparently written in Section 4, and the final $^{10}B/^{14}N$ ratio.

in the outer region of the convective He-layer. Thus, the distribution of the ^{16}O/^{17}O ratio is given, as shown in Fig. 6.9(c), by the inverse of the sum of the ^{17}O/^{16}O ratio shown by the shaded band of Fig. 6.4(b) and that of the probable initial ratio shown in Table 6.5. The ^{16}O/^{17}O ratio is determined by the explosive nucleosynthesis in the inner region ($M \lesssim 5M_\odot$) and by the initial ratio in the outer region.

6.4.4. The ^{14}N/^{15}N ratio

In evaluating the probable range of the ^{14}N/^{15}N ratio, we have to pay special attention to the following four. The first is that, ^{14}N is not included as an initial constituent of 4-component models though ^{14}N is the most abundant isotope among the CNO-elements in the radiative He-layer and the H-rich envelope. Secondly, ^{18}O is not included too though ^{15}N is possibly formed from ^{18}O in the convective He-layer (see Table 4.1). Thirdly, it is quite uncertain how much amount of ^{14}N is contained in the convective He-layer (see Table 6.5) in the presupernova stage. Finally, the two isotopes are formed from different parent isotopes: ^{15}N is mainly produced through ^{16}O$(\nu, \nu' p)^{15}$N and ^{14}N through ^{11}B$(\alpha, n)^{14}$N. Therefore, the ^{14}N/^{15}N ratio depends on the contents of ^{4}He and ^{16}O in a complicated manner.

Now, we will evaluate the probable range of the ^{14}N/^{15}N ratio in the convective He-layer. Since ^{14}N is not decomposed during the explosion, the final abundance is given by the sum of the abundance in the presupernova stage and that produced during the explosion. For ^{15}N, we first note that, as seen in Table 6.5, the content of ^{14}N is very small in the convective He-layer and, hence, the produced amount of ^{15}N is not so affected by the initial content of ^{14}N. In the innermost region, ^{15}N is decomposed to the level of 10 % of the initial abundance (see Fig. 6.7(b)). However, it is re-produced probably through ^{18}O$(p, \alpha)^{15}$N to the abundance level more than the initial composition (see Table 4.1). The produced amount of ^{15}N from ^{16}O is readily found from Fig. 6.4 (on page 86).

The amount of ^{15}N from ^{18}O is also estimated from the result in Section 4 in which we found that the final ratio of ^{15}N/^{18}O is 3×10^{-3} to 3×10^{-1} (for the probable values of ^{18}O/^{16}O, see Table 6.5). Thus, we find the amount of ^{15}N as the sum of the initial abundance and that produced by the two ways during the explosion. The probable range of the ^{14}N/^{15}N ratio in the convective He-layer, evaluated by the way mentioned above (note that we exclude the results of models A2 and A4 because of a mismatch in the ^{12}C and ^{16}O-contents), is shown in Fig. 6.9(d). In the inner region where $M_r \lesssim 5.0 M_\odot$, the uncertainty in the ^{14}N/^{15}N ratio attributes mainly to that of the ^{16}O/^{4}He ratio. In the outer region, the maximum value of the ratio is determined by the initial ratio and the minimum one is determined by the ratio obtained from our present results. The range of the probable ratio becomes larger with an increase in the mass coordinate because of the large uncertainty in the abundance of pre-existing ^{14}N.

In the radiative He-layer and most part of the H-rich envelope, the contents of ^{14}N and ^{15}N in the presupernova stage are much larger than those produced during the explosion. Furthermore, ^{15}N production from ^{14}N can be excluded as mentioned before. As a result, the probable range of the ^{14}N/^{15}N ratio is entirely governed by the isotopic ratio in the presupernova stage. However, in the innermost region of the H-rich envelope the ^{14}N/^{15}N ratio differs from the initial values. According to the result of model B mentioned in Section 6.2.3, pre-existing ^{15}N is decomposed during the explosion in such a region and, at the same time, ^{15}N would be produced from ^{14}N by the shock heating through $^{14}\mathrm{N}(p,\gamma)^{15}\mathrm{O}(,e^{+}\nu_{\mathrm{e}})^{15}\mathrm{N}$, if there exists a sufficient amount of ^{14}N. In fact, Paper I tells us this is true in the present case since the initial ^{14}N/^{15}N ratio is as large as 3×10^{4} (see Table 6.3). Thus, in the innermost region of the H-rich envelope the ^{14}N/^{15}N ratio is governed by the explosive nuclear processes; from Fig. 4.3, the ratio is in the range between 3×10^{3} and 3×10^{4}.

6.5. Summary and diagrams between two isotopic/elemental ratios

In this section, we investigated the influence of choice of the initial chemical composition on the light element synthesis by the use of artificially modeled compositions which consist of only ^{1}H, ^{4}He, ^{12}C, and ^{16}O. We also made a simulation of decomposition processes of the light elements during the supernova explosion using a model with overabundant rare light elements. The main results of numerical simulations are summarized as follows:

1. Roughly speaking, the light elements produced in the supernova explosion are classified into three groups, i.e., (a)^{6}Li, ^{7}Li, ^{9}Be, ^{14}N, and ^{18}O, (b)^{10}B, ^{11}B, and ^{13}C, and (c)^{15}N and ^{17}O. The final productions of elements of groups (a), (b), and (c) can be properly scaled by the amounts of ^{4}He, ^{12}C, and ^{16}O contained in the presupernova stage, respectively.

2. In the radiative He-layer and the H-rich envelope, the final abundances of the CNO-elements are governed by the chemical composition in the presupernova stage in a sense that pre-existing elements survive as they were.

Furthermore, in Section 6.3 we deduced probable ranges of the amounts and the isotopic ratios of the light elements in the presupernova stage on the basis of the previous studies of stellar evolution and atmospheric compositions of stars. Combining the results presented in Sections 6.2 and 6.3, we constructed the probable distributions of the final elemental/isotopic ratios of the light elements of ^{11}B/^{7}Li, ^{12}C/^{13}C, ^{16}O/^{17}O, and ^{14}N/^{15}N. We also confirmed the results in Sections 4 and 5 that the amounts of ^{6}Li and ^{9}Be produced in the He-layer and the inner region of the H-rich envelope are much smaller than that of ^{7}Li and that in the outermost region of the H-rich envelope the initial ratios are conserved.

Now, as same as Section 5.5, we make three diagrams between two isotopic (elemental) ratios which are useful for the study of presolar grains of supernova origin: diagrams of $^{11}B/^{7}Li$-$^{12}C/^{13}C$, $^{14}N/^{15}N$-$^{12}C/^{13}C$, and $^{16}O/^{17}O$-$^{12}C/^{13}C$. They are illustrated in Figs. 6.10(a) to 6.10(c). In these figures, four kinds of regions are overwritten: hatched regions, dark shadow regions, light shadow regions, and regions enclosed by dashed curves. A combined set of the dark shadow region and the hatched region, constructed from the shaded regions of Fig. 6.9, show the probable ranges of the isotopic/elemental ratios. The probable ratios are confined within relatively small two regions in each diagram; one is of the H-rich envelope (including the radiative He-layer) and the other is of the convective He-layer. The hatched regions mean that the ratios are completely determined by the nuclear processes during the supernova explosion irrelevant to the chemical compositions in the presupernova stage. In other words, the isotopic (elemental) ratios belonging to the hatched regions are of peculiar to the nucleosynthesis during the supernova explosion. Furthermore, the light shadow regions denote the dispersion of the ratios due to a mechanical mixing between the He-layer and the H-rich envelope, which would be triggered by the Rayleigh-Taylor instability during the explosion (e.g., Hachisu *et al.* 1994). The regions enclosed by dashed curves correspond to the dark shadow regions drawn in Fig. 5.5 (on page 71), in which we investigated the isotopic (elemental) ratios under a variety of the neutrino emission models.

The three isotopic/elemental diagrams shown in Fig. 6.10 are nearly identical to those shown in Fig. 5.5. In the convective He-layer, the regions of the isotopic/elemental ratios are almost included in the regions in Fig. 5.5, which are enclosed by dashed curves in Fig. 6.10, except the $^{14}N/^{15}N$ ratio. In the radiative He-layer, the regions of the isotopic/elemental ratios in Fig. 6.10 are almost similar to those in the corresponding figures in Fig. 5.5. In the H-rich envelope, the regions of the ratios are mainly determined by the probable regions of the ratios in the presupernova stage. So, the regions of the ratios obtained in this study are larger than those obtained in Fig. 5.5 (in which we did not take into account a variety of the initial chemical compositions). The regions of the

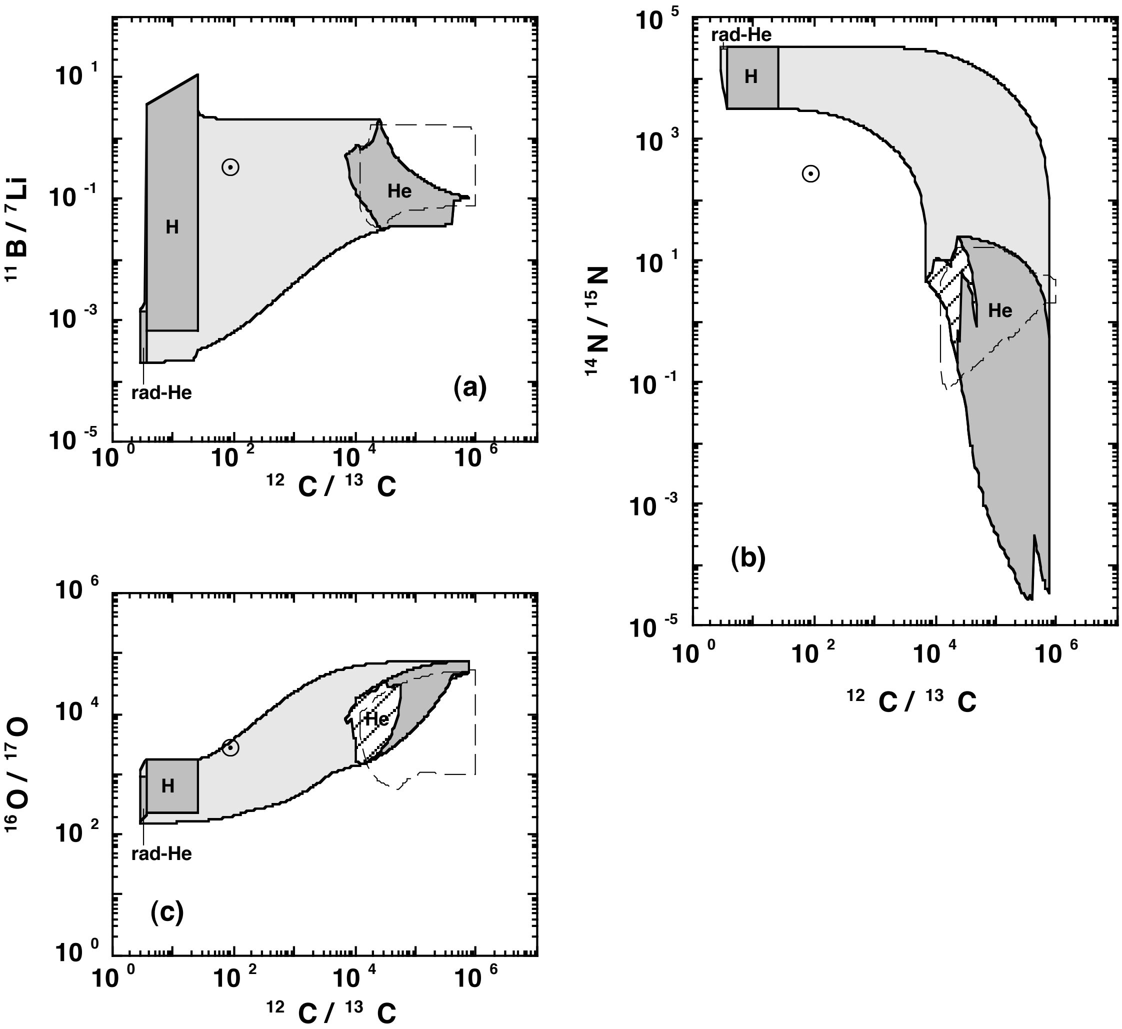

Fig. 6.10. The number ratios of $^{11}B/^{7}Li$ (panel(a)), $^{14}N/^{15}N$ (panel(b)), and $^{16}O/^{17}O$ (panel(c)) versus $^{12}C/^{13}C$. Three regions with a dark shade are of the convective He-layer (denoted by He), of the radiative He-layer (denoted by rad-He), and of the H-rich envelope (denoted by H) whereas a region with a light shade denotes the spread of the ratios due to the mechanical mixing between the two regions. The hatched regions denote the ratios which are peculiar to the nucleosynthesis in the supernova explosion determined independently of the chemical composition in the presupernova stage. Furthermore, the region enclosed by dashed curves corresponds to the dark shaded region of the convective He-layer shown in Fig. 5.5.

ratios due to the material mixing are essentially similar to those shown in Fig. 5.5.

We should note on the $^{14}N/^{15}N$ ratio which shows a different feature between Fig. 6.10 and Fig. 5.5; in the outer region of the convective He-layer (where $M_r \gtrsim 5M_\odot$), the $^{14}N/^{15}N$ ratio becomes very small, as seen in Fig. 6.10(b), compared with that in Fig. 5.5(b) where the minimum value of the $^{14}N/^{15}N$ ratio is about 3×10^{-2} (see the dashed curve in Fig. 6.10(b)). This is due to the large uncertainty of the amount of ^{14}N in the presupernova stage (see Section 6.4.4). However, the region of $^{14}N/^{15}N$ below 1×10^{-2} is not so important on the study of the presolar grains of supernova origin because the abundance of ^{14}N is extremely small compared with that of ^{16}O.

Thus, we arrive at the following conclusions in this section.

1. A variety of the chemical compositions in the presupernova stage does not affect so much the isotopic/elemental ratios (which we perceive) compared with a variety of the neutrino emission models investigated in the previous section as long as we adopt the initial chemical composition within the probable range mentioned in Section 6.3.

2. The hatched regions in Fig. 6.10, in which the ratios are determined by the nuclear processes during the supernova explosion irrelevant to the adopted chemical composition in the presupernova stage, are almost included in the regions brought about by the uncertainty in the neutrino emission model in the previous section.

3. In the H-rich envelope, the ranges of the ratios are almost determined by the chemical composition in the presupernova stage, and, thus, the results of the previous section should be replaced by those of this section.

4. As mentioned in Section 5.5, presolar grains with $^{6}Li/^{7}Li$ less than 3×10^{-5} and with $^{9}Be/^{7}Li$ less than 2×10^{-4} should be originated from the supernova, even if we consider an uncertainty in the chemical composition in the presupernova stage.

In short, we can say that the conclusions found in the previous section are proper without any significant modification even if we take into account of the uncertainty in the chemical composition in the presupernova stage. Furthermore, as pointed out in Section 5.5, the isotopic diagrams shown in Figs. 6.8 and 6.10 are useful for studying the presolar grains of supernova origin.

7. Influence of the Nuclear Reprocessing after the Mixing

During the supernova explosions, large scale mixing occurs between the He-layer and the H-rich envelope owing to the development of the Rayleigh-Taylor instability at the He/H boundary. The chemical compositions of the He-layer and the H-rich envelope are changed by the mixing through not only the chemical blend between two mixed fluid elements (the mechanical mixing) but also through the nuclear reactions proceeded in the mixture (the nuclear reprocessing after the mixing). The former process has been already considered when the diagrams between two isotopic/elemental ratios in Sections 5 and 6. The latter process also occurs possibly: a proton free He-component is exposed to protons in the H-component and new kind of *p*-capture reactions occur in the mixture. In order to investigate the nuclear reprocessing after the mixing in detail and obtain the varieties of isotopic/elemental ratios of the light elements due to the nuclear reprocessing, we will perform numerical simulations of the nuclear reprocessing after the mixing during the supernova explosion by the use of the mixing model described in Section 3.4 (see page 38). On the physical parameters other than the mixing model, those of the standard model are adopted.

7.1. Nuclear reprocessing after the mixing

7.1.1. Typical example of the nuclear reprocessing - Case of ^{7}Li

Mixing between two kinds of fluid elements originated from the He-layer and the H-rich envelope (which are called, respectively, the He-component and the H-component) brings about new nuclear processes; a proton-free He-component is exposed to protons and new kinds of proton-capture reactions occur in the mixture. Hereafter, we will see in detail how the nuclear reprocessing due to material mixing affects the final abundance of, as an example, ^{7}Li.

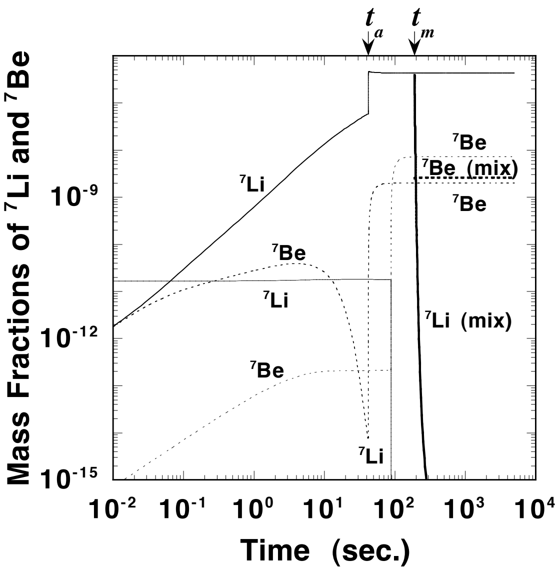

Fig. 7.1. Time variation of the amounts of ^{7}Li (solid lines) and ^{7}Be (dotted lines). Ordinary and thin lines are of the He-component at $M_m(\mathrm{He}) = 5.5\ M_\odot$ and of the H-component at $M_m(\mathrm{H}) = 6.5\ M_\odot$, respectively. Bold lines are of the mixture of which mixing ratio, x, is equal to 0.1. Furthermore, t_a, and t_m are the time of the shock arrival at the bottom of the H-rich envelope and of the mixing, respectively.

Figure 7.1 shows the time variations of the abundances of ^{7}Li and its unstable isobar ^{7}Be. We first see the case where the He-component at $M_m(\mathrm{He}) = 5.5 M_\odot$ mixes with the H-component at $M_m(\mathrm{H}) = 6.5 M_\odot$ (i.e., at the bottom of the H-rich envelope) with the mixing ratio, 0.1 (c_m is put to be 1). Before the arrival of the shock wave, both ^{7}Li and ^{7}Be are produced through the ν-processes in the He-layer: main reactions are $^4\mathrm{He}(\nu, \nu' p)^3\mathrm{H}(\alpha, \gamma)^7\mathrm{Li}$ and $^4\mathrm{He}(\nu, \nu' n)^3\mathrm{He}(\alpha, \gamma)^7\mathrm{Be}$ for ^{7}Li and ^{7}Be, respectively. Only ^{7}Be in the He-component is decomposed through (n, p)-reaction. In the H-rich envelope, ^{7}Be is produced through the ν-process but ^{7}Li keeps its amount at the presupernova stage because the amount produced through the ν-process is vary small. The shock wave reaches $M_r = 5.5 M_\odot$ in the He-layer at 42 s and the bottom of the H-rich envelope at 88 s. When the shock wave arrives there, explosive nucleosynthesis starts: ^{7}Li is further produced through ^{3}H$(\alpha,\gamma)^7$Li in the He-layer but completely decomposed through ^{7}Li$(p,\alpha\gamma)^4$He in the H-rich envelope, and ^{7}Be is commonly produced through ^{3}He$(\alpha,\gamma)^7$Be in these locations. After 103 s from the shock passage of the He/H boundary, there occurs a mixing between the two components. In the mixture ^{7}Li is rapidly decomposed by protons through ^{7}Li$(p,\alpha\gamma)^4$He. However, proton-rich isobar ^{7}Be is not decomposed. Thus, the final abundance of ^{7}Li is determined by that of ^{7}Be undecomposed in the mixture. Note that the final ^{7}Li abundance becomes small compared with that of the mixture in the case without nuclear reprocessing after mixing.

The final abundance of ^{7}Li after the mixing depends on the original location of the He-component, M_m(He), as well as the mixing ratio, x, as shown in Fig. 7.2 where the He-component comes from the inner region, $M_m(\mathrm{He}) = 3.8M_\odot$ (Fig. 7.2(a)) and from the outer region, $M_m(\mathrm{He}) = 6.0M_\odot$ (Fig. 2(b)). In these figures, solid and dashed curves denote, respectively, the final abundance of ^{7}Li and the abundance of ^{7}Be in the case where we consider only the mechanical mixing (that is, the case where we ignore the nuclear reprocessing after the mixing). We see from Fig. 7.2(a) that the final abundances of ^{7}Li fit well to the solid line, i.e., they are not affected by the nuclear reprocessing induced by the mixing. This is due to the following reason. First, note that the solid line almost overlaps with the dotted line. As shown in Section 4.1, in the convective He-layer inner than 5 $M_\odot$ ^{7}Li is mainly produced as ^{7}Be (see Table 4.1 on page 53): ^{7}Li is produced in the shock-induced burning stage but captured quickly by ^{4}He in the same stage. As seen in Fig. 7.1, proton-rich isobar ^{7}Be, which is produced in the after-shock stage, is undecomposed even if ^{7}Be mixes with proton-rich material. Thus, the final abundance of ^{7}Li is not influenced by the nuclear reprocessing after the mixing. On the other hand, in the case of $M_r \gtrsim 5M_\odot$ where the He-component contains an appreciable amount of ^{7}Li, we have a different picture (see Fig. 7.2(b)). The final abundance of ^{7}Li is nearly the

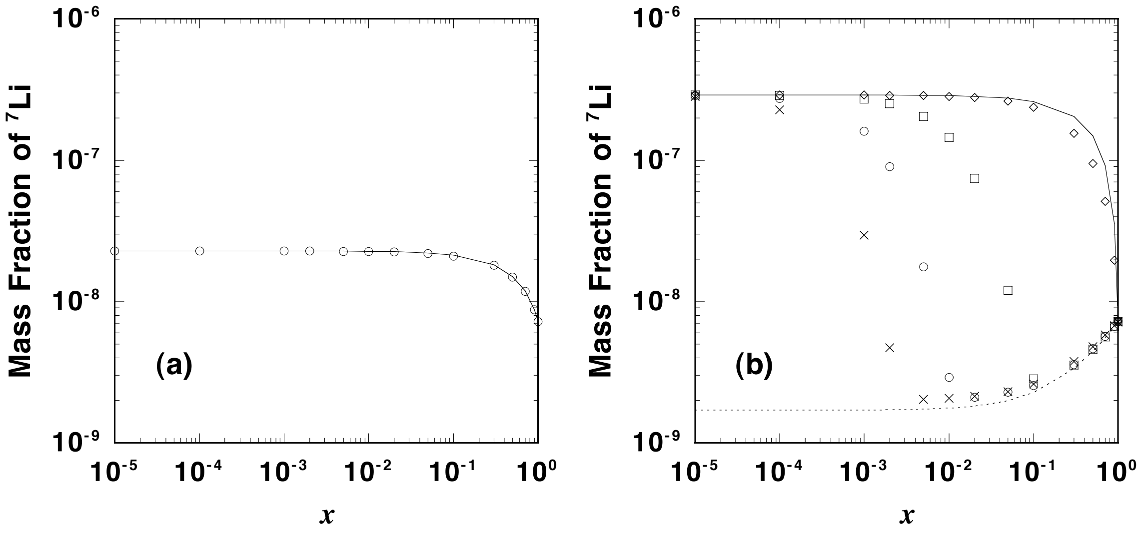

Fig. 7.2. The final abundances of ^{7}Li in the mixture in the cases of M_m(He)=3.8 $M_\odot$ (panel(a)) and 6.0 $M_\odot$ (panel(b)). The location of the H-component is fixed to be $M_m(\mathrm{H}) = 6.5 M_\odot$. The horizontal axis denotes the mixing ratio of the H-component, x. Open circles are the abundances of ^{7}Li in the mixtures in the case of $c_m = 1$ (see Section 3.4 on page 42). In panel(b) crosses, squares, and diamonds are the ratios in the cases of $c_m = 0.5$, 2, and 5, respectively. Solid line and dotted line show the final abundance of ^{7}Li and the abundance of ^{7}Be produced during the explosion, respectively, in the case of the mechanical mixing.

same as that shown by the solid line when $x < 1 \times 10^{-3}$ but fits to the dotted line when $x \gtrsim 2 \times 10^{-2}$. It should be noted that ^{7}Li is decomposed partly by the nuclear reprocessing after the mixing even if the fraction of the H-component is as low as 1×10^{-3}. When the mass ratio of the H-component is more than 2×10^{-2}, ^{7}Li originally produced in the He-layer is completely decomposed through $^7\mathrm{Li}(p, \alpha\gamma)^4\mathrm{He}$ after the mixing. On the other hand, ^{7}Be produced in the He-layer and the H-rich envelope remain undecomposed and the final abundance of ^{7}Li in the mixture is determined by the ^{7}Be content. In the case of the mixture with the radiative He-layer component, the behavior of the abundance of ^{7}Li is similar to that in the case of Fig. 7.2(b).

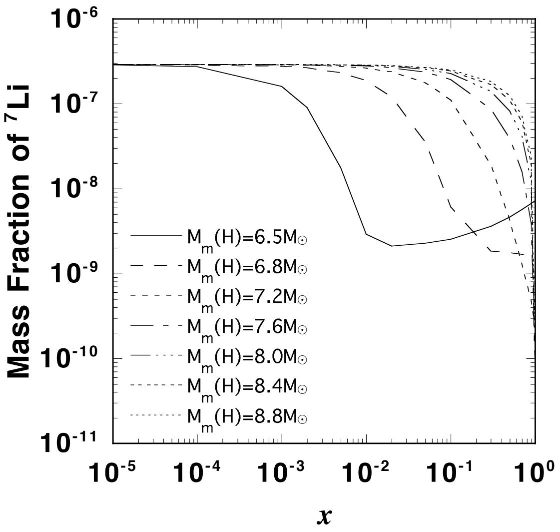

Fig. 7.3. The same as Fig. 7.2 but in the cases with various M_m(H). The location of the He-component is fixed to be M_m(He) =6.0 $M_\odot$.

In Fig. 7.2(b) we also demonstrate the influence of choice of the mixing time parameter, c_m, on the final abundance of ^{7}Li in the case where $M_m(\mathrm{He}) = 6.0M_\odot$ and $M_m(\mathrm{H}) = 6.5M_\odot$. When c_m is large, it takes long time to mix, so that the maximum temperature of the mixture is low and the nuclear reprocessing after the mixing is less effective. In the case of $c_m = 5$, the abundances of ^{7}Li are almost on the solid line because ^{7}Li is hardly decomposed owing to the decrease in the maximum temperature of the mixture. On the other hand, in the case of $c_m < 5$ the abundances of ^{7}Li become small in the range of the large mixing ratio and fit to the dotted line.

In Fig. 7.3, we show how the final abundances of ^{7}Li depend on the adopted values of M_m(H) (M_m(He) is fixed to be 6.0 $M_\odot$). We see that the mixing ratio where mass fraction of ^{7}Li decreases from the value in the He-component becomes large with increase in M_m(H), i.e., the decomposition of ^{7}Li is less effective with increase in M_m(H). In practice, although ^{7}Li originally produced in the He-component is completely decomposed when the mixing ratio is more than 0.3 in the case of $M_m(\mathrm{H}) = 6.8M_\odot$, the amount of ^{7}Li is almost same as in the case of the mechanical mixing in the mixtures with $M_m(\mathrm{H}) = 8.4M_\odot$ and 8.8 $M_\odot$. It takes long time to mix with the H-component at outer part and the maximum temperature in the mixture is low. Thus, there occurs no appreciable nuclear reprocessing on ^{7}Li in the case where $M_m(\mathrm{H}) > 8.4M_\odot$. Note that in the pure H-component (x=1) mass fraction of ^{7}Li decreases with an increase in $M_m(\mathrm{H})$. See also Fig.4.3 (on page 52). For the other elements the situation is almost the same as in the case of ^{7}Li and, hence, we do not consider the distant mixing beyond $M_m(\mathrm{H}) = 8.8M_\odot$.

7.1.2. Reprocessing on the other X-elements

7.1.2.1. ^{11}B

Figure 7.4 presents the abundances of ^{11}B in the mixture as a function of the mixing ratio, x. Figure 7.4(a) (and 7.4(b)) shows the case of mixing between the He-component at $M_m(\mathrm{He}) = 3.8M_\odot$ (and 6 $M_\odot$) and the H-component at $M_m(\mathrm{H}) = 6.5M_\odot$. Apparently the behavior of the abundance of ^{11}B is quite similar to that of ^{7}Li. This is due, at least partly, to the fact that there exists proton-rich unstable isobar ^{11}C which corresponds to ^{7}Be in the case of ^{7}Li. Remember that ^{11}B and ^{11}C are produced through $^7\mathrm{Li}(\alpha,\gamma)^{11}\mathrm{B}$ and $^{12}\mathrm{C}(\nu,\nu'p)^{11}\mathrm{B}$, and $^7\mathrm{Be}(\alpha,\gamma)^{11}\mathrm{C}$ and $^{12}\mathrm{C}(\nu,\nu'n)^{11}\mathrm{C}$, respectively, in the He-layer during the explosion (see Section 4.1 and Table 4.1 on page 53). Produced ^{11}B is decomposed by protons through $^{11}\mathrm{B}(p,\alpha\alpha)^4\mathrm{He}$ after the mixing. In Figs. 7.4(a) and 7.4(b), ^{11}B is decomposed in the cases of $x \gtrsim 0.1$ and $x \gtrsim 2\times10^{-3}$, respectively. Similarly to the case of ^{7}Li, the final abundance of ^{11}B is determined by the abundance of undecomposed ^{11}C when x is large. Note that ^{11}B of the He-component at $M_m(\mathrm{He}) = 3.8M_\odot$ (Fig. 7.4(a)) is decomposed in the mixture with larger mixing ratio than that at $M_m(\mathrm{He}) = 6.0M_\odot$ (Fig. 7.4(b)) because it takes longer time to mix with the He-component at the inner location and the maximum temperature of the mixture becomes low.

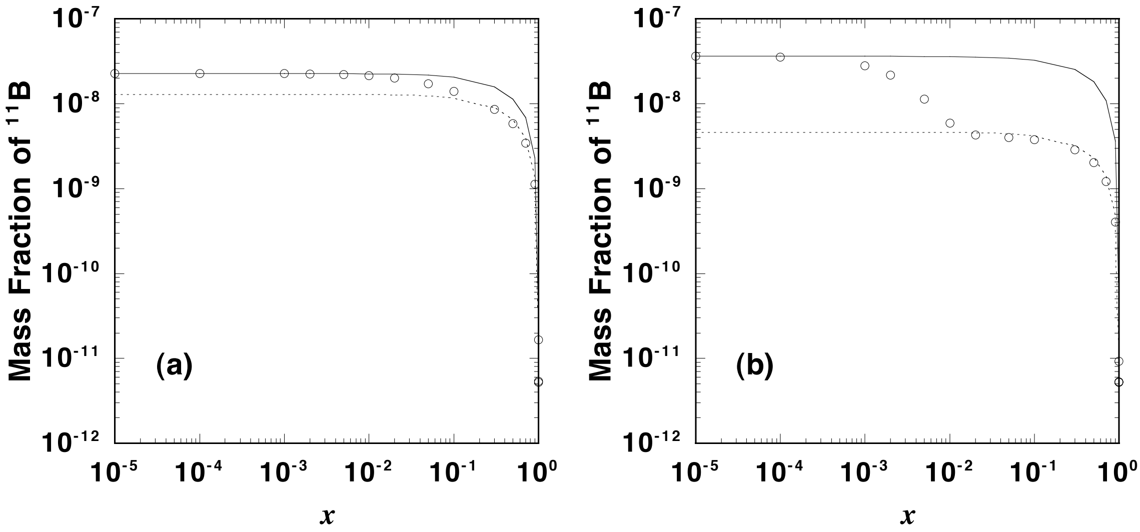

Fig. 7.4. As same as Fig. 7.2, but for the final abundances of ^{11}B. Solid line and dotted line show the final abundance of ^{11}B in the case of the mechanical mixing and that of ^{11}C at the shock arrival to the He/H boundary, respectively.

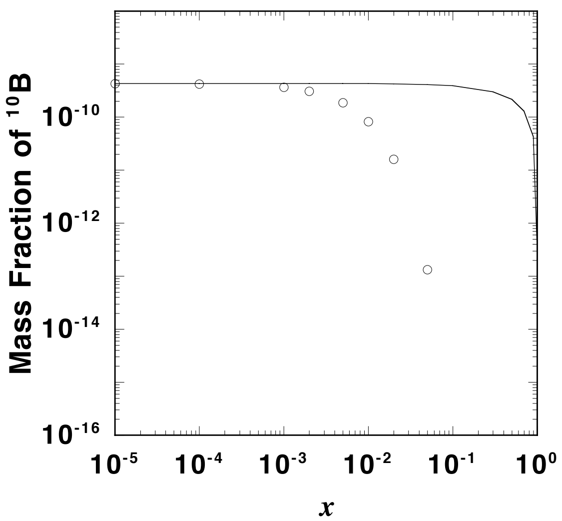

Fig. 7.5. The final abundances of ^{10}B (open circles) in the mixture between the He-component at M_m(He)= 6.0 $M_\odot$ and the H-component at M_m(H)= 6.5 $M_\odot$ (c_m=1). Solid line shows the abundance in the case of the mechanical mixing.

7.1.2.2. ^{10}B

Figure 7.5 shows the abundance of ^{10}B in the mixture between the He-component at $M_m(\mathrm{He}) = 6.0M_\odot$ and the H-component at $M_m(\mathrm{H}) = 6.5M_\odot$. When the mixing ratio, x, is smaller than 1×10^{-3}, the abundance of ^{10}B is almost equal to the corresponding value of the mechanical mixing which is denoted by the solid line. In the case of $x \gtrsim 5 \times 10^{-3}$, ^{10}B is decomposed after the mixing through $^{10}\mathrm{B}(p,\alpha)^{7}\mathrm{Be}$. In contrast to the case of ^{7}Li and ^{11}B, ^{10}B is decomposed completely after the mixing and the abundance becomes less than 1×10^{-20} when $x \gtrsim 0.2$. This is because there are no proton-rich isobars of ^{10}B, which are produced sufficiently and tolerate protons.

In the case of the mixture with the radiative He-layer component, the abundance of ^{10}B in the mixture decreases similarly to the above case with an increase in x. On the other hand, in the case of the mixing with the inner He-component, ^{10}B is decomposed under the mixing ratio larger than the above since it takes longer time to mix and the maximum temperature of the mixture becomes low. For example, in the mixture with the He-component at $M_m(\mathrm{He}) = 3.8M_\odot$, the abundance of ^{10}B becomes smaller than the value of the mechanical mixing when $x > 0.3$.

7.1.2.3. ^{6}Li and ^{9}Be

In Sections 4.2, 5.3, and 6.4.1, we showed that ^{6}Li and ^{9}Be are produced only in the outer part ($M_r \gtrsim 5.2M_\odot$) of the He-layer during the supernova explosion and that their amounts are very small compared with that of ^{7}Li. Since ^{6}Li and ^{9}Be are very fragile, nuclear reactions induced by the mixing would lead to the further decrease in their amounts. In fact, as presented in Figs. 7.6(a) and 7.6(b) where the abundances of ^{6}Li and ^{9}Be, respectively, in the mixture between the He-component at $M_m(\mathrm{He}) = 6.0M_\odot$ and the H-component at $M_m(\mathrm{H}) = 6.5M_\odot$ are shown, the abundances of ^{6}Li and ^{9}Be are obviously smaller than those of mechanical mixing when $x > 1 \times 10^{-3}$; ^{6}Li and ^{9}Be are decomposed through $^{6}\mathrm{Li}(p,\alpha)^{3}\mathrm{He}$ and $^{9}\mathrm{Be}(p,\alpha)^{6}\mathrm{Li}$ and $^{9}\mathrm{Be}(p,\alpha\alpha)^{2}\mathrm{H}$, respectively. As

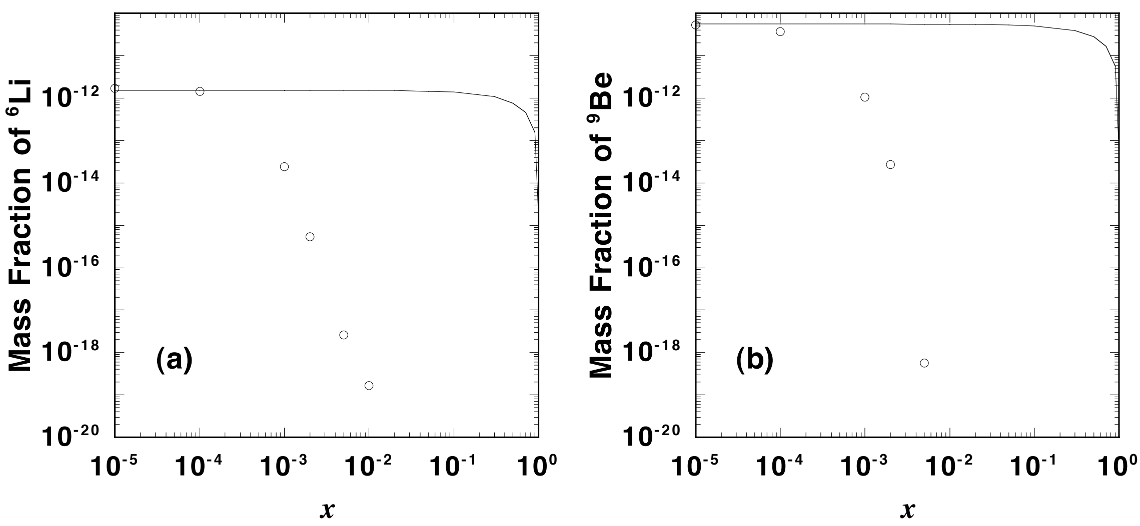

Fig. 7.6. As same as Fig. 7.5, but for the abundances of ^{6}Li (panel (a)) and those of ^{9}Be (panel (b)).

same as ^{10}B, there are no isobars of ^{6}Li and ^{9}Be produced sufficiently and undecomposed by protons.

As a result, the abundances of ^{6}Li and ^{9}Be become extremely small in the mixture with only a small fraction of the H-component. In the cases of the mixtures between the radiative He-layer component and the H-component at $M_m(\mathrm{H}) = 6.5M_\odot$, the behaviors of the abundances of ^{6}Li and ^{9}Be are similar with those mentioned above.

7.2. Effects of mixing on the isotopic ratios of the X-elements

7.2.1. The ^{6}Li/^{7}Li and ^{9}Be/^{7}Li ratios

As seen in the last subsection, ^{6}Li and ^{9}Be are decomposed in the mixtures with quite small fractions of the H-component. At the same time, ^{7}Li is also decomposed in such mixtures. So we will investigate here how the ^{6}Li/^{7}Li and ^{9}Be/^{7}Li ratios are affected by the nuclear reprocessing due to the mixing.

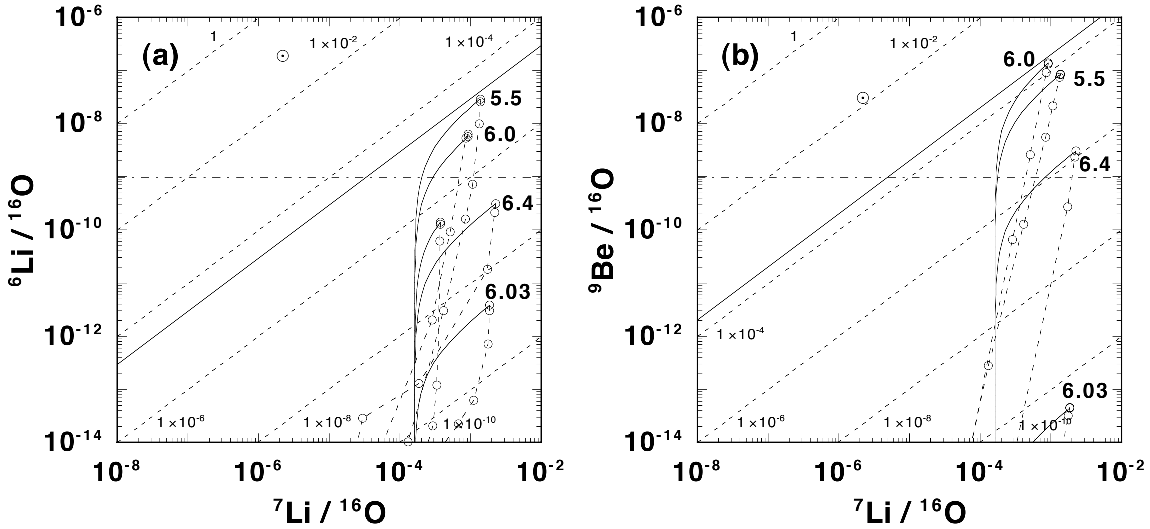

Fig. 7.7. Diagrams between ^{6}Li/^{16}O and ^{7}Li/^{16}O ratios (panel(a)) and between ^{9}Be/^{16}O and ^{7}Li/^{16}O ratios (panel(b)). The ratios are all in number. Markers connected by dashed lines show the ratios in the mixture in the cases with various M_m(He) (M_m(H)= 6.5 $M_\odot$). Original locations of the He-components, M_m(He), are labeled by attached numbers. Thin solid lines indicate the ratios in the corresponding mixtures in the case of the mechanical mixing. The ^{6}Li/^{7}Li ratio equal to 3×10^{-5} (panel (a)) and the ^{9}Be/^{7}Li ratio equal to 2×10^{-4} (panel (b)) are indicated by thick solid lines. Dotted lines indicate values of constant ^{6}Li/^{7}Li ratio (panel (a)) and ^{9}Be/^{7}Li ratio (panel (b)): $1, 1 \times 10^{-2}, 1 \times 10^{-4}, 1 \times 10^{-6}, 1 \times 10^{-8}$ and 1×10^{-10}. A dash-dotted horizontal line indicates the detection limit, i.e., the number ratio of species to ^{16}O equal to 1×10^{-9}. A mark $\odot$ shows the ratios of the solar-system composition.

In Fig. 7.7(a) we show the ^{6}Li/^{16}O-^{7}Li/^{16}O diagram, which is the same as that in Fig. 4.4 (on page 55). Markers linked by dashed curves denote the ratios in the mixtures with various mixing ratio, x. The original locations of the He-components are denoted by attached numbers (the location of the H-component is fixed to be $M_m(\mathrm{H}) = 6.5M_\odot$). For comparison, we also present the distributions of the ratios in the mixtures by thin solid curves when we ignore the nuclear reprocessing after the mixing. With an increase in the mixing ratio, x, the ^{6}Li/^{16}O ratio decreases more rapidly than the ^{7}Li/^{16}O ratio (in the case of the mechanical mixing (thin solid curve), the ^{6}Li/^{16}O and the ^{7}Li/^{16}O ratios decrease similarly but by somewhat different way). As a result, we see that the ^{6}Li/^{7}Li ratios are always below 3×10^{-5} which is the maximum value of the ^{6}Li/^{7}Li ratio found in the previous sections. The behavior in the ^{9}Be/^{16}O-^{7}Li/^{16}O diagram, shown in Fig. 7.7(b), is similar to that in the ^{6}Li/^{16}O-^{7}Li/^{16}O diagram, i.e., as the mixing ratio, x, increases, the ^{9}Be/^{16}O ratio decreases more rapidly than the ^{7}Li/^{16}O ratio and the resultant ^{9}Be/^{7}Li ratio is always smaller than 2×10^{-4}.

Thus, we need not modify the conclusion presented in the previous sections even when we consider the nuclear reprocessing after the mixing between the He-layer and the H-rich envelope, that is, presolar grains with ^{6}Li/^{7}Li less than 3×10^{-5} and with ^{9}Be/^{7}Li less than 2×10^{-4} should be originated from the supernova.

7.2.2. The ^{11}B/^{7}Li ratio

As seen in Figs. 5.2(a) (on page 65) and 6.9(a) (on page 101), the ^{11}B/^{7}Li ratio in the convective He-layer is confined within a range between 0.04 and 2 even if we consider the varieties of the neutrino emission models and initial chemical compositions. On the other hand, we showed in the last section that ^{7}Li and ^{11}B suffers from the nuclear reprocessing due to the mixing. So, it is interesting to investigate how the ^{11}B/^{7}Li ratio is changed by the nuclear reprocessing after the mixing.

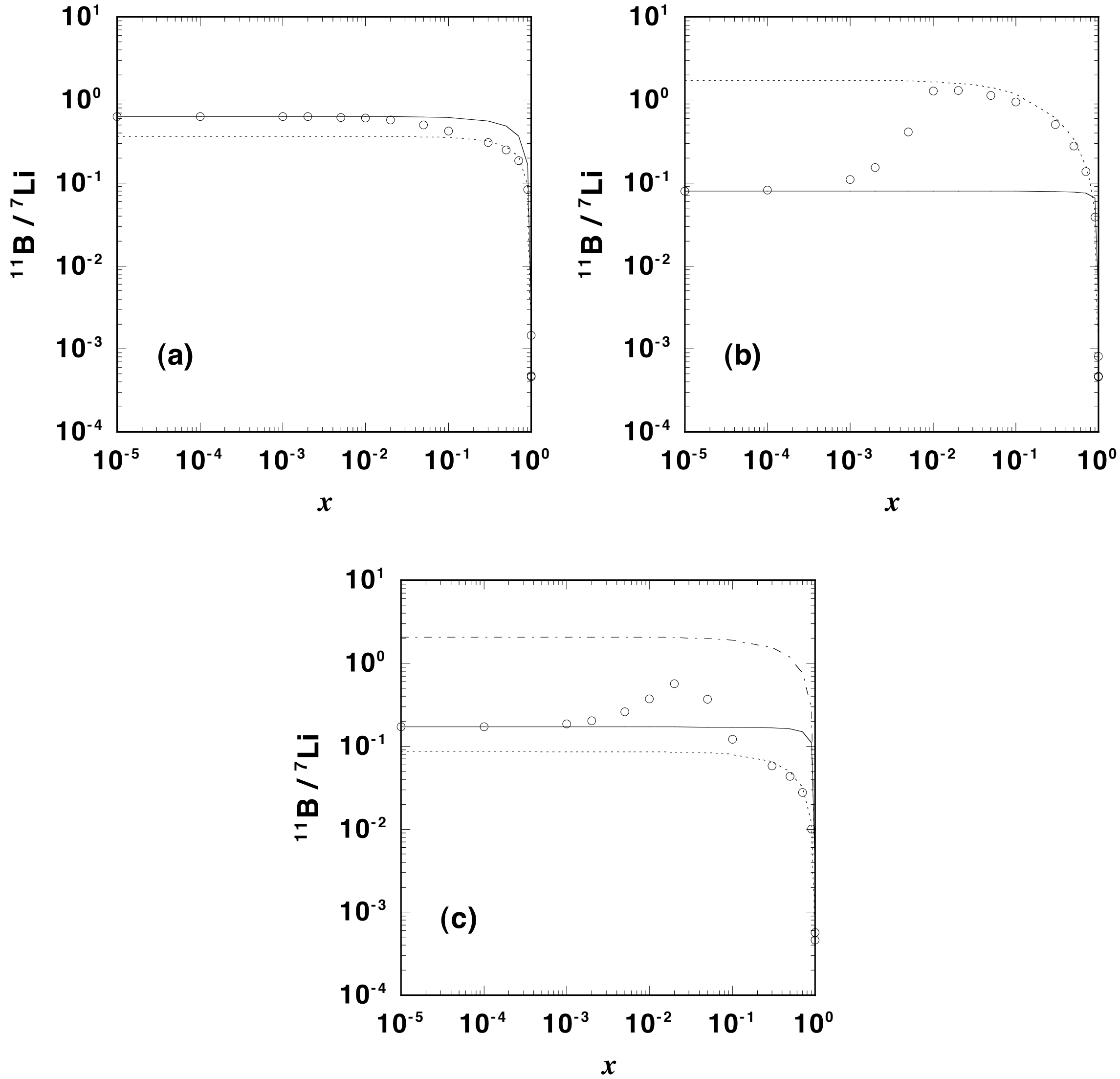

Fig. 7.8. The $^{11}B/^{7}Li$ ratios (open circles) in the mixture in the cases with M_m(He)=3.8 $M_\odot$ (panel (a)), 6.0 $M_\odot$ (panel (b)), and 5.0 $M_\odot$ (panel (c)) (M_m(H)=6.5 $M_\odot$). Solid line and dotted line show the final ratio of $^{11}B/^{7}Li$ and the $^{11}C/^{7}Be$ ratio at the shock arrival to the He/H boundary, respectively, in the case of the mechanical mixing. Dashed-dotted line in panel (c) shows the $^{11}B/^{7}Be$ ratio in the case of the mechanical mixing.

Figures 7.8(a), 7.8(b), and 7.8(c) present the $^{11}B/^{7}Li$ ratios as a function of the the mixing ratio, x, in the mixtures between the H-component and the He-component of $M_m(\mathrm{He}) = 3.8M_\odot$, 6.0 $M_\odot$, and 5.0 $M_\odot$, respectively (the location of the H-component is fixed to be $M_m(\mathrm{H}) = 6.5M_\odot$). Solid curves denote the $^{11}B/^{7}Li$ ratio in the case of only the mechanical mixing and dashed lines show the $^{11}C/^{7}Be$ ratio at a time when the shock arrives at the He/H boundary. We see from Fig. 7.8(a) that the $^{11}B/^{7}Li$ ratio lies on the solid line when $x \lesssim 1 \times 10^{-2}$ and on the dashed line when $x \lesssim 0.5$. It should be noted here that the ratio of $^{11}B/^{7}Li$ is intrinsically determined by the amounts of four isotopes as

$$\frac{^{11}\mathrm{B}}{^{7}\mathrm{Li}} = \frac{n_{^{11}\mathrm{B}} + n_{^{11}\mathrm{C}}}{n_{^{7}\mathrm{Li}} + n_{^{7}\mathrm{Be}}} \tag{7.1}$$

where n_i denotes the number density of ith species. In the case of deep He-component, ^{11}B is produced in the He-component but ^{7}Li is not produced in the He-component nor the H-component (see Fig. 7.2(a) and Fig. 7.4(a)). Furthermore, as mentioned in the last subsection, ^{11}C is never decomposed by the nuclear reprocessing after the mixing. So, when ^{11}B is not decomposed, the final $^{11}B/^{7}Li$ ratio is almost equal to the $^{11}B/^{7}Be$ ratio of the mechanical mixing. Whereas it is equal to that of $^{11}C/^{7}Be$ when ^{11}B is decomposed completely.

Figure. 7.8(b), in the case of $M_m(\mathrm{He}) = 6.0M_\odot$, shows the same feature, in a qualitative sense, as in the previous case. That is, the $^{11}B/^{7}Li$ ratio runs along the $^{11}B/^{7}Li$ curve of the mechanical mixing when $x \ll 1$ and along the $^{11}C/^{7}Be$ curve when $x \gtrsim 1 \times 10^{-2}$. The difference between cases of Figs. 7.8(a) and 7.8(b) comes from the difference in the number ratios of relevant four isotopes in the He-component: in this case, $^{11}B/^{7}Li$, $^{11}C/^{7}Li$, and $^{7}Be/^{7}Li$ are about 0.1, 0.02, and 0.01, respectively. The $^{11}C/^{7}Be$ ratio of the mechanical mixing (dotted line) is greater than that of $^{11}B/^{7}Li$. As a result, when both ^{11}B and ^{7}Li are almost completely decomposed (i.e., $x \gtrsim 1 \times 10^{-2}$), the resultant $^{11}B/^{7}Li$ (which is nearly equal to the $^{11}C/^{7}Be$ ratio) becomes large compared

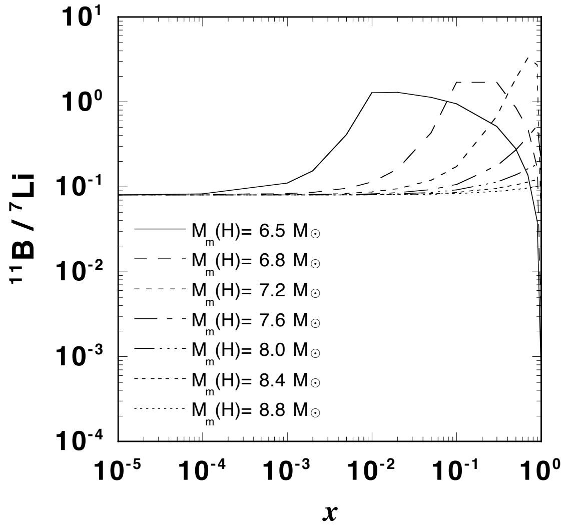

Fig. 7.9. The ^{11}B/^{7}Li ratios in the cases with various M_m(H). The location of the He-component is M_m(He) =6.0 $M_\odot$.

with that of the mechanical mixing (solid line).

In the case of $M_m(\mathrm{He}) = 5.0 M_\odot$, the ^{11}B/^{7}Li ratio behaves somewhat complicatedly as seen in Fig. 7.8(c); the ^{11}B/^{7}Li ratio happens to become larger than not only the ratio of the chemical blend but also the corresponding ^{11}C/^{7}Be ratio. Roughly speaking, with an increase in the mixing ratio, x, the ^{11}B/^{7}Li ratio behaves as

$$\frac{^{11}\mathrm{B}}{^{7}\mathrm{Li}} = \frac{n_{^{11}\mathrm{B}} + n_{^{11}\mathrm{C}}}{n_{^{7}\mathrm{Li}} + n_{^{7}\mathrm{Be}}} \rightarrow \frac{n_{^{11}\mathrm{B}} + n_{^{11}\mathrm{C}}}{n_{^{7}\mathrm{Be}}} \rightarrow \frac{n_{^{11}\mathrm{C}}}{n_{^{7}\mathrm{Be}}}, \tag{7.2}$$

since ^{7}Li is more fragile to protons than ^{11}B.

We will see in brief how the ^{11}B/^{7}Li ratio in the mixture depends on the location of the H-component. Figure 7.9 shows the ^{11}B/^{7}Li ratios in the mixtures with various M_m(H): M_m(H)=6.5 $M_\odot$, 6.8 $M_\odot$, 7.2 $M_\odot$, 8.0 $M_\odot$, and 8.8 $M_\odot$ (the location of the He-component, M_m(He), is fixed to be 6.0 $M_\odot$). As seen from this figure, with an increase in M_m(H) the peak of the ^{11}B/^{7}Li ratio shifts toward the direction of large x as long as we are concerned with the cases of $M_m(\mathrm{H}) \lesssim 7.2 M_\odot$. At the same time, the peak value (i.e., the maximum value of the $^{11}B/^{7}Li$ ratio) becomes large. These comes, mainly, from the following two facts: one is that both ^{7}Li and ^{11}B are possibly decomposed through p-capture reactions but ^{7}Li is more fragile than ^{11}B, and the other is that the shock temperature decreases with an increase in M_m(H). Thus, in the case of large M_m(H) we have a large mixing ratio, x, at which the decomposition processes work appreciably and, at the same time, the decomposition of ^{11}B becomes less important. It should be noted here that the peak values of the $^{11}B/^{7}Li$ ratio is almost equal to its maximum value which is observed previously (compare with Fig. 7.8(b)).

Beyond $M_m(\mathrm{H}) = 7.2M_\odot$, however, the $^{11}B/^{7}Li$ ratio behaves quite differently. The decomposition process does not play an important role and, finally ($M_m(\mathrm{H}) \gtrsim 8.2M_\odot$), the $^{11}B/^{7}Li$ ratio does not suffer at all from the nuclear reprocessing after the mixing. In such a distant mixing, the $^{11}B/^{7}Li$ ratio is determined by that of the mechanical mixing.

As seen in Figs. 7.8 and 7.9, the nuclear reprocessing caused by the mixing brings out the high $^{11}B/^{7}Li$ ratio in most cases compared with that of the mechanical mixing but a degree of the increment is slight. The $^{11}B/^{7}Li$ ratios, obtained in this study, are almost in the region found in Figs. 5.5(a) and 6.10(a) (i.e., $1\times10^{-4} \lesssim {}^{11}B/^{7}Li \lesssim 2$). If we adopt another model of the neutrino emission, the $^{11}B/^{7}Li$ ratio may become to a certain level because the $^{11}B/^{7}Li$ ratio depends sensitively on the relative amounts of ^{11}B, ^{11}C, ^{7}Li, and ^{7}Be before the mixing. The variation of the $^{11}B/^{7}Li$ ratios due to the adopted neutrino emission model will be discussed in Section 7.3.

7.2.3. The $^{11}B/^{10}B$ ratio

The ratios of $^{11}B/^{10}B$ in the mixtures between the He-components at $M_m(\mathrm{He}) = 3.8$ $M_\odot$, 5.0 $M_\odot$, and 6.0 $M_\odot$ and the H-component at $M_m(\mathrm{H}) = 6.5$ $M_\odot$ (at the bottom of the H-rich envelope) are presented in Fig. 7.10. Circles, squares, and triangles denote the $^{11}B/^{10}B$ ratios in the mixture with the He-component at $M_m(\mathrm{He}) = 3.8$ $M_\odot$, 5.0

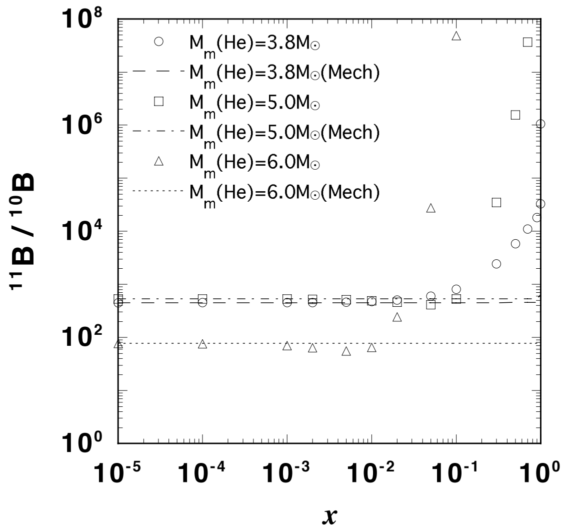

Fig. 7.10. The number ratios of ^{11}B/^{10}B in the mixture. Circles, squares, and triangles denote the ^{11}B/^{10}B ratios in the mixtures in the cases of M_m(He)=3.8 $M_\odot$, 5.0 $M_\odot$, and 6.0 $M_\odot$, respectively. Dashed line, dash-dotted line, and dotted line denote the ratios in the mixture with the He-component at the corresponding locations in the case of the mechanical mixing.

$M_\odot$, and 6.0 $M_\odot$ and a dashed line, a dash-dotted line, and a dotted line denote the corresponding ratios in the case of the mechanical mixing. We see that the ^{11}B/^{10}B ratio at a given mixing ratio, x, becomes larger than the corresponding line when $x \gtrsim 0.1$, 0.1 and 2×10^{-2} in the cases of the He-components at $M_m(\mathrm{He}) = 3.8\ M_\odot$, 5.0 $M_\odot$, and 6.0 $M_\odot$, respectively. When $x > 0.1$, the ^{11}B/^{10}B ratio in the mixture becomes large compared with that in the He-component with an increase in the mixing ratio, x. The increase of the ^{11}B/^{10}B ratio is due to the fact that ^{10}B in the He-component is decomposed by protons in the H-component through ^{11}B$(p,\alpha)^7$Be (see 7.1.2). On the other hand, in the case of the mechanical mixing, the ^{11}B/^{10}B ratio in the mixture is almost equal to the ratio in the He-component when $x < 0.9$ though the ^{11}B/^{10}B ratio in the H-component is very large (i.e., ^{11}B/^{10}B=4.2×10^{29}). This is because the amounts of ^{10}B and ^{11}B in the He-component are much larger than those at the bottom of the H-rich envelope (see Fig.

4.3 on page 52). Thus, the rapid increase of the $^{11}B/^{10}B$ ratio with a small mixing ratio ($x \lesssim 0.1$) is characteristic of the nuclear reprocessing after the mixing. In the case of the He-component at $M_m(\mathrm{He}) = 6.0\ M_\odot$ the $^{11}B/^{10}B$ ratio is slightly smaller than that in the mechanical mixing case when $1 \times 10^{-3} \lesssim x \lesssim 1 \times 10^{-2}$. This is due to the decomposition of ^{11}B in the He-component by protons in the H-component through $^{11}B(p, \alpha\alpha)^4He$ (see Section 7.1.2).

In the case of a distant mixing, i.e., the mixing between the He-component and the H-component at the location outer than the bottom of the H-rich envelope, the nuclear reprocessing after the mixing scarcely changes the $^{11}B/^{10}B$ ratio. In the case of the H-component at $M_m(\mathrm{H}) > 7.2M_\odot$, the $^{11}B/^{10}B$ ratio in the mixture is equal to that in the case of the mechanical mixing, although ^{10}B in the H-component has been decomposed before the mixing (the mass fraction of ^{10}B at $M_m(\mathrm{H}) = 7.2M_\odot$ is equal to 1.1×10^{-41}).

7.2.4. The ratios of $^{12}C/^{13}C$, $^{14}N/^{15}N$, and $^{16}O/^{17}O$

Since the CNO-elements are less fragile to protons than the X-elements, the CNO-elements are scarcely expected to suffer the nuclear reprocessing after the mixing. Here, we show behaviors of $^{12}C/^{13}C$, $^{14}N/^{15}N$, and $^{16}O/^{17}O$ ratios in the mixtures together with the behaviors in the case of the mechanical mixing. The locations of the He-components, $M_m(\mathrm{He})$, are 3.8 $M_\odot$, 5.0 $M_\odot$, 6.0 $M_\odot$, and 6.4 $M_\odot$. The location of the H-component, $M_m(\mathrm{H})$, is fixed to be 6.5 $M_\odot$.

Figure 7.11(a) shows the $^{12}C/^{13}C$ ratios in the mixture. In most cases, the $^{12}C/^{13}C$ ratios are on the corresponding lines, i.e., the $^{12}C/^{13}C$ ratios do not suffer the nuclear reprocessing. Only in the case of $M_m(\mathrm{He}) = 6.0M_\odot$, the $^{12}C/^{13}C$ ratio becomes larger than the corresponding ratio in the case of the mechanical mixing within a factor of 2. In the mixture, ^{13}C is produced from ^{12}C in the He-component and protons in the H-component through $^{12}C(p, \gamma)^{13}N(,e^+\nu_e)^{13}C$. Even in the case of $c_m = 1/2$ (see Section

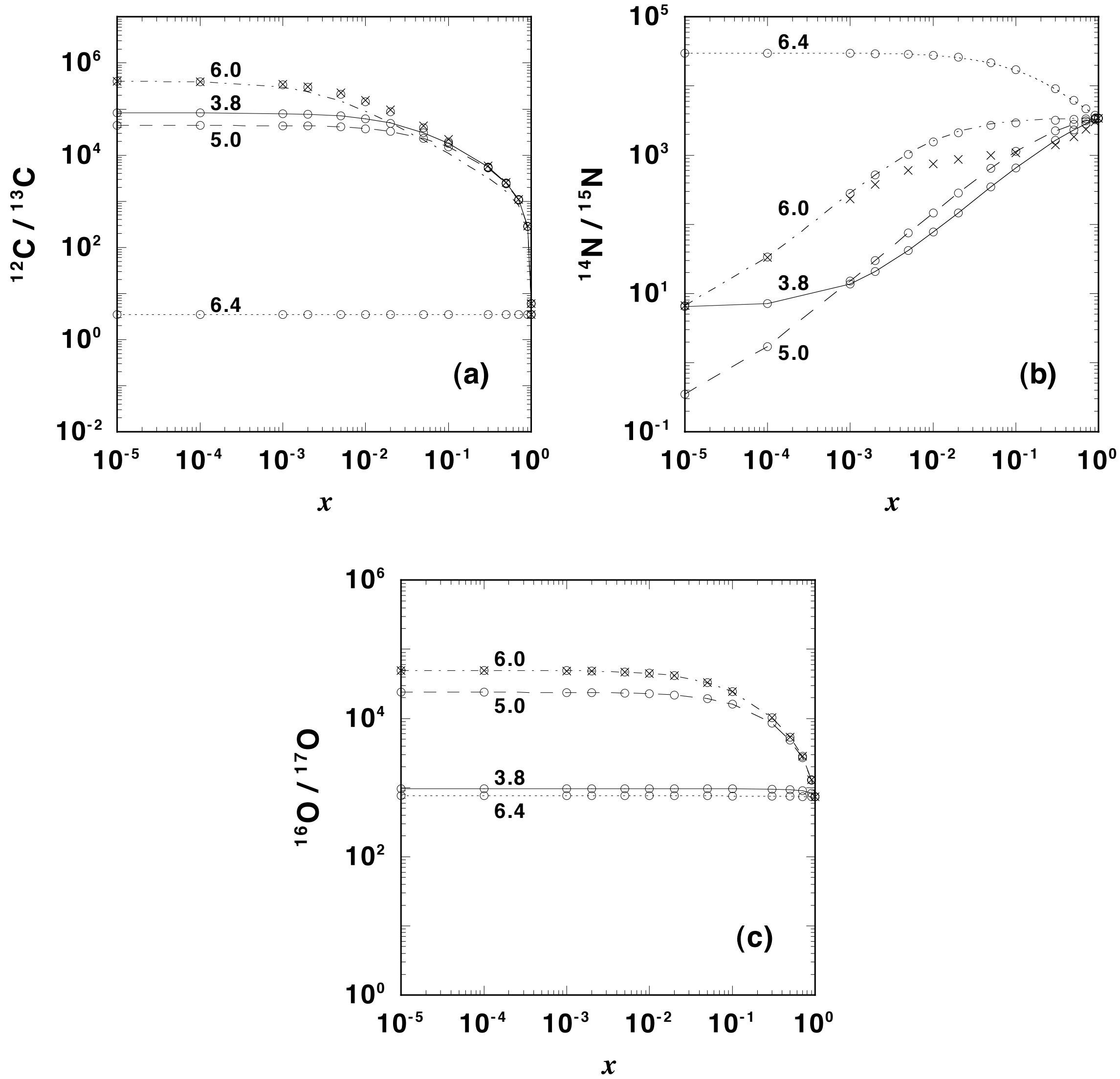

Fig. 7.11. The number ratios of ^{12}C/^{13}C (panel(a)), ^{14}N/^{15}N (panel(b)), and ^{16}O/^{17}O (panel(c)) in the mixture in the various M_m(He). Numbers attached to circles and lines are the location of the He-component, M_m(He). The location of the H-component is fixed to be $M_m(\mathrm{H}) = 6.5\ M_\odot$. Crosses denote the isotopic ratios with $M_m(\mathrm{He}) = 6.0\ M_\odot$ and $c_m = 0.5$.

3.4 on page 42), the additional amount of ^{13}C through the nuclear reprocessing after the mixing is the same as in the case of $c_m = 1$. When the He-component in the convective He-layer and the H-component mix equivalently, the ^{12}C/^{13}C ratio is different from the values of the He-component nor that of the H-component: the ratio is mainly determined by the ratio of the amount of ^{12}C in the He-component to that of ^{13}C in the H-component because ^{12}C is abundant in the convective He-layer and ^{13}C is abundant in the H-rich envelope. In the mixture between the radiative He-component and the H-component, the ^{12}C/^{13}C ratio does not depend on the mixing ratio. The amount of ^{12}C and ^{13}C in the radiative He-layer are equal to those in the H-component.

The ^{14}N/^{15}N ratios in the mixture are presented in Fig. 7.11(b). In each location of the He-component, circles lie on the corresponding line. So, the nuclear reprocessing after the mixing does not affect the ^{14}N/^{15}N ratio. Only when $c_m = 0.5$, the ^{14}N/^{15}N ratio becomes smaller than the ratio in the case of the mechanical mixing by a factor of 3 at the maximum. The decrease of the ^{14}N/^{15}N ratio is brought about by the production of ^{15}N in the mixture; ^{15}N is produced from ^{18}O in the He-component and protons in the H-component through $^{18}\mathrm{O}(p,\alpha)^{15}\mathrm{N}$. However, this nuclear reprocessing occurs only in a short mixing time case. In the case of the mechanical mixing between the convective He-component and the H-component, the ^{14}N/^{15}N ratio is almost equal to that of the H-component when $x < 0.1$. This is due to the fact that the amounts of ^{14}N and ^{15}N in the H-component are larger than those in the He-component. The nuclear reprocessing after the mixing does not affect the ^{14}N/^{15}N ratio in the mixture of the radiative He-component. Even in the cases of a short time mixing, the reaction of $^{14}\mathrm{N}(p,\gamma)^{15}\mathrm{O}(,e^{+}\nu_{\mathrm{e}})^{15}\mathrm{N}$ does not proceed in the low temperature and the amount of ^{15}N produced through $^{18}\mathrm{O}(p,\alpha)^{15}\mathrm{N}$ is too small because of the small amount of ^{18}O in these components.

The ^{16}O/^{17}O ratios in the mixture are presented in Fig. 7.11(c). In this figure, all circles and all crosses lie on the corresponding lines, i.e., there occurs no nuclear reprocessing after the mixing. In the mixture between the He-component in most region of the convective He-layer except the innermost region, and the H-rich envelope, the $^{16}O/^{17}O$ ratio become different from those of the He-component and the H-component when $0.1 \lesssim x \lesssim 0.9$. On the other hand, the $^{16}O/^{17}O$ ratio in the mixture is almost same as the ratio in the He-component and the H-component in the case of the He-component in the innermost region or the radiative He-layer.

At last, the nuclear reprocessing after the mixing scarcely affects the isotopic ratios of the CNO-elements in the mixture. There occurs the nuclear reprocessing only in the case of a short distance mixing, such as the mixing between the He-component at $M_m(\mathrm{He}) = 6.0 M_\odot$ and the H-component at $M_m(\mathrm{H}) = 6.5 M_\odot$. Further, the variation of the isotopic ratio due to the nuclear reprocessing is confined within a factor of 3. There occurs no nuclear reprocessing after the mixing between the radiative He-component and the H-component, because the compositions of the CNO-elements are almost same (except ^{15}N and ^{18}O).

7.3. Summary and diagrams between two isotopic/elemental ratios

In this section, we investigated explosive nucleosynthesis of the light elements during the supernova explosion taking account of the nuclear reprocessing caused by the mixing between the He-layer and the H-rich envelope. The nuclear reprocessing modifies the abundances of the light elements formed before the mixing; the degree of the reprocessing depends on the parameters of the mixing model such as the mixing ratio, the mixing time, and the original locations of the He- and the H-components as well as the nuclear stability of individual element. The results of our present study are summarized as follows:

1. After the mixing, the X-elements relatively abundant in the He-layer are decomposed by protons in the H-rich envelope. The degree of the decomposition depends on original locations of components of the mixture, their mixing ratio, and the

mixing time. Especially, the nuclear reprocessing becomes important in the short range mixing where the upper He-component mixes with the H-component near the bottom of the H-rich envelope.

2. Both ^{7}Li and ^{11}B originally produced in the shock-induced burning stage in the He-layer are decomposed by protons in the mixtures even when the mixing ratio of the H-component is as small as 2×10^{-3} or so. Their unstable isobars, ^{7}Be and ^{11}C are hardly decomposed in the mixture and, thus, the ^{11}B/^{7}Li ratio is determined by the ratio of ^{11}C/^{7}Be when ^{7}Li and ^{11}B are decomposed completely.

3. The abundances of ^{6}Li and ^{9}Be are decreased steeply by p-capture reactions and decomposed completely in the mixture when the mixing ratio of the H-component is larger than the orders of 10^{-3}. In the case of ^{10}B, the nuclear reprocessing is important but not so effective compared with the case of ^{6}Li and ^{9}Be because ^{10}B is less fragile to protons in the mixture.

4. Nuclear reprocessing after the mixing do not affect the abundances of the CNO-elements effectively.

In Sections 5 and 6, we made three diagrams between two isotopic/elemental ratios: ^{11}B/^{7}Li-^{12}C/^{13}C, ^{14}N/^{15}N-^{12}C/^{13}C, and ^{16}O/^{17}O-^{12}C/^{13}C diagrams. Of these three, according to result (4) mentioned above, we are interested in the ^{11}B/^{7}Li-^{12}C/^{13}C diagram but not in the latter two, i.e., we should know how the ^{11}B/^{7}Li-^{12}C/^{13}C diagram is affected by the nuclear reprocessing after the mixing. As pointed out in Section 5, there is a possibility that both the nuclear reprocessing and the ν-process work cooperatively on the formation/destruction of ^{7}Li and ^{11}B. So, as for the neutrino emission models, we consider the cases given by Eqs. (3.33) and (3.34) in addition to the case of Eq. (3.32) (see page 35). The results are overwritten in Fig. 7.12. In this figure, the light shaded region

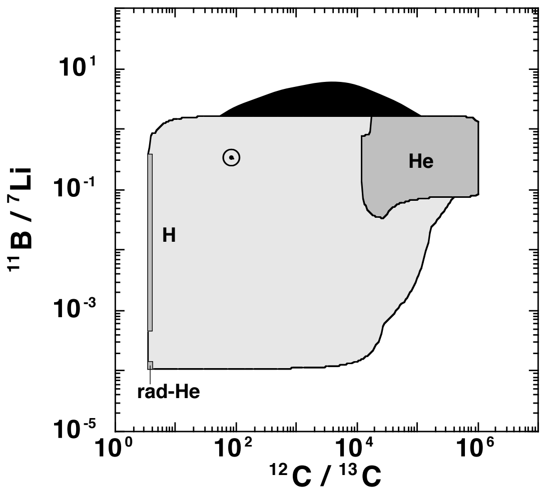

Fig. 7.12. The number ratios of ^{11}B/^{7}Li versus ^{12}C/^{13}C. Three regions with a dark shade are of the convective He-layer (denoted by He), the radiative He-layer (denoted by rad-He), and the H-rich envelope (denoted by H) whereas a region with a light shade denotes the ratios made of the mechanical mixing between these regions. A region coated by black denotes an additional region of the ratios due to the nuclear reprocessing after the mixing. A mark $\odot$ shows the ratio of the solar-system composition. Note that exceptional spike appeared in Fig. 5.2(a) is excluded.

shows the ratios due to the mechanical mixing and a new region coated by black denotes contribution from the nuclear reprocessing due to the mixing. This region comes from the results in the cases of the mixing between the He-component at $M_m(\mathrm{He}) = 5.0 \sim 5.5 M_\odot$ and the H-component at $M_m(\mathrm{H}) = 6.8 \sim 7.2 M_\odot$. As seen in Section 7.2.2, a wide variety is brought about by the nuclear reprocessing but most of it is embedded in the light shaded region. As a result, the new region due to the nuclear reprocessing seems to be limited in the very small area. In other words, the conclusions obtained in the previous sections are proper without any significant modifications even if we consider the nuclear reprocessing induced by the mixing between the He-layer and the H-rich envelope.

8. Variety of the Light Element Synthesis due to the Stellar Mass

In Sections 4, 5, 6, and 7, we investigated the varieties of the light element synthesis of the 16.2 $M_\odot$ supernova due to the neutrino emission model, the chemical compositions in the presupernova stage, and the nuclear reprocessing after the mixing. In these sections, we fixed the mass of the progenitor to be 16.2 $M_\odot$. In practice, however, massive stars with various masses end their lives as type II supernova explosions. The stars evolve on various evolutionary paths and, hence, their stellar structures in the presupernova stage also have a variety due to the stellar mass. Because of the variety, the abundance distribution of the light elements is expected to vary owing to the mass of the progenitor. In this section, we will investigate how the light element synthesis of the supernova explosion varies among the progenitors with different masses. We will use three kinds of supernova explosion models on the basis of numerical models of 25 $M_\odot$ and 20 $M_\odot$ progenitors (Iwamoto 1998) and a 15 $M_\odot$ progenitor (Nomoto *et al.* 1993). The neutrino emission models of the 25 $M_\odot$, 20 $M_\odot$, and 15 $M_\odot$ supernovae are described in Section 3.3 (on page 38) and the initial chemical compositions are presented in Fig. 3.5 on page 47.

8.1. 25 $M_\odot$, 20 $M_\odot$, and 15 $M_\odot$ supernova explosion models

In Section 3.1, we evaluated the approximated power-law density profiles of 25 $M_\odot$, 20 $M_\odot$, and 15 $M_\odot$ progenitors (see Tables 3.1 and 3.2 on page 25) and in Section 3.2 we obtained the relation of the radius to the mass coordinate (see Table 3.3 on page 32). Hereafter, we will present characteristics of the structure of the 25 $M_\odot$, 20 $M_\odot$, and 15 $M_\odot$ progenitor models. We also show their temperature evolutions during the supernova explosions.

Schematic pictures of the stellar structure in the He-layer and the H-rich envelope of the 25 $M_\odot$, 20 $M_\odot$, and 15 $M_\odot$ progenitors are illustrated in Fig. 8.1. Density distributions of the numerical models of the 25 $M_\odot$ and 20 $M_\odot$ progenitors (Iwamoto 1998) and the 15 $M_\odot$ progenitor (Nomoto *et al.* 1993) and the approximated power-law density distributions corresponding to the numerical progenitor models (see Table 3.1 on page 25) are presented in Fig. 8.2. The approximated density profiles are well fitted to the numerical models of the density profiles in the cases of the 25 $M_\odot$ and 20 $M_\odot$ progenitors. In the case of the 15 $M_\odot$ progenitor, the power-law density profile is well approximated to that of the numerical model where the radius is smaller than 8×10^{10} cm. Note that in the outer region of the radiative He-layer, the density of the 15 $M_\odot$ progenitor decreases steeply with an increase in the radius. In the H-rich envelope, the density profile obtained from our model is larger than the corresponding density of the numerical progenitor model by a factor of 20. On studying the nucleosynthesis in the H-rich envelope of the 15 $M_\odot$ supernova, we will investigate only at the bottom of the H-rich envelope.

We pay attention to the radius at the inner boundary of the He-layer. From Fig. 8.1, the radius of the inner boundary of the He-layer is 7.7×10^9 cm, 6.0×10^9 cm, and 3.6×10^9 cm in the cases of the 25 $M_\odot$, 20 $M_\odot$, and 15 $M_\odot$ progenitors, respectively. The radius of the boundary of the 25 $M_\odot$ progenitor is large and that of the 15 $M_\odot$ progenitor is small compared with that of the 20 $M_\odot$ progenitor. The radius of the 20 $M_\odot$ progenitor is equal to that of the 16.2 $M_\odot$ progenitor at the inner boundary of the He-layer because both progenitor models consist of a 6.0 $M_\odot$ He star model calculated by Nomoto and Hashimoto (1988) commonly and H-rich envelope models. In practice, the structure of the convective He-layer of the 20 $M_\odot$ progenitor and that of the 16.2 $M_\odot$ progenitor are identical each other.

The radii of the boundaries between the convective He-layer and the radiative He-layer of the 25 $M_\odot$, 20 $M_\odot$, and 15 $M_\odot$ progenitors are 3.5×10^{10} cm, 4.0×10^{10} cm, and 5.8×10^{10} cm, respectively. Contrary to the case of the inner boundary of the He-layer,

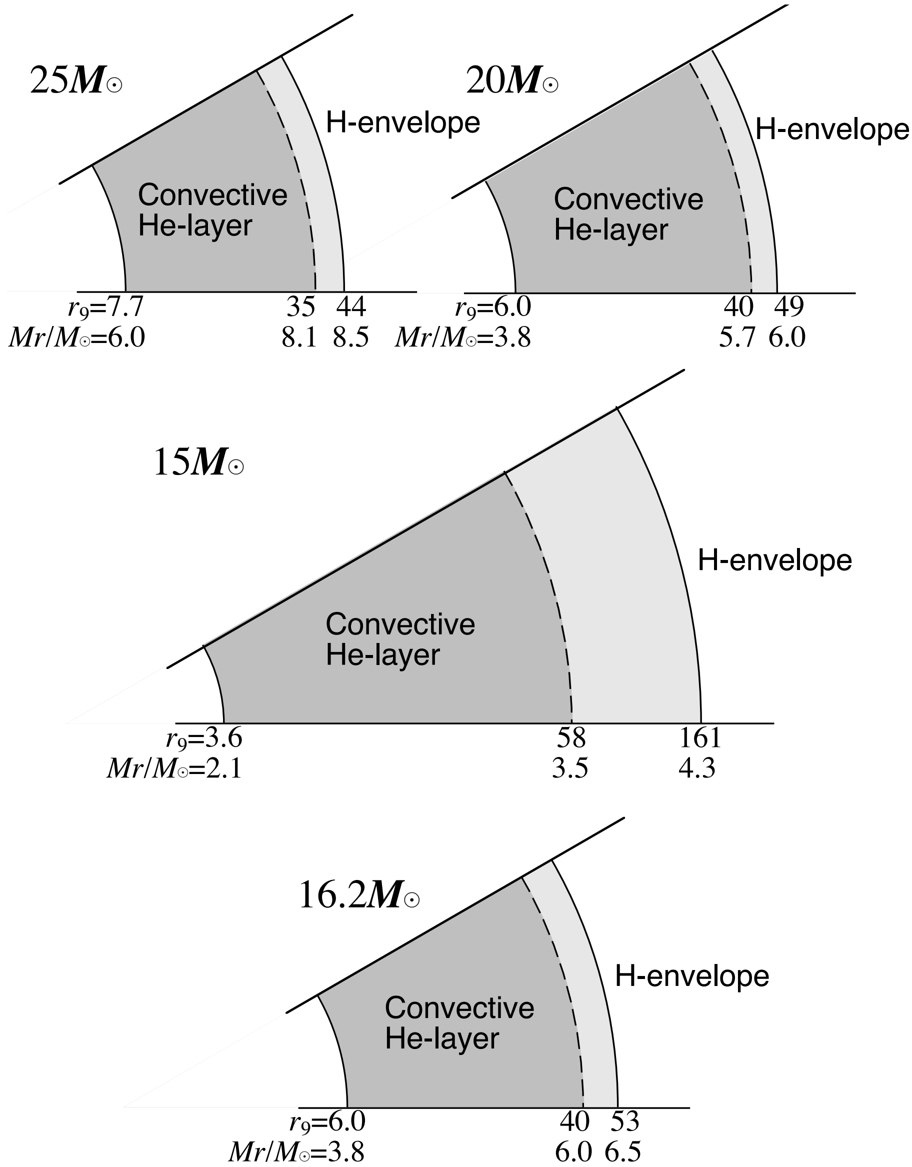

Fig. 8.1. Schematic pictures of the stellar structure in the He-layer and the H-rich envelope of the 25 $M_\odot$, 20 $M_\odot$, and 15 $M_\odot$ progenitors together with the 16.2 $M_\odot$ progenitor (see Fig. 3.1 on page 24). Dark shaded region, light shaded region, and a region outside the light shaded region denote the convective He-layer, the radiative He-layer, and the H-rich envelope, respectively. Radii, r_9, and the internal mass coordinates, M_r, of the boundaries between layers are shown in the units of 1×10^9 cm and the solar mass, $M_\odot$, respectively.

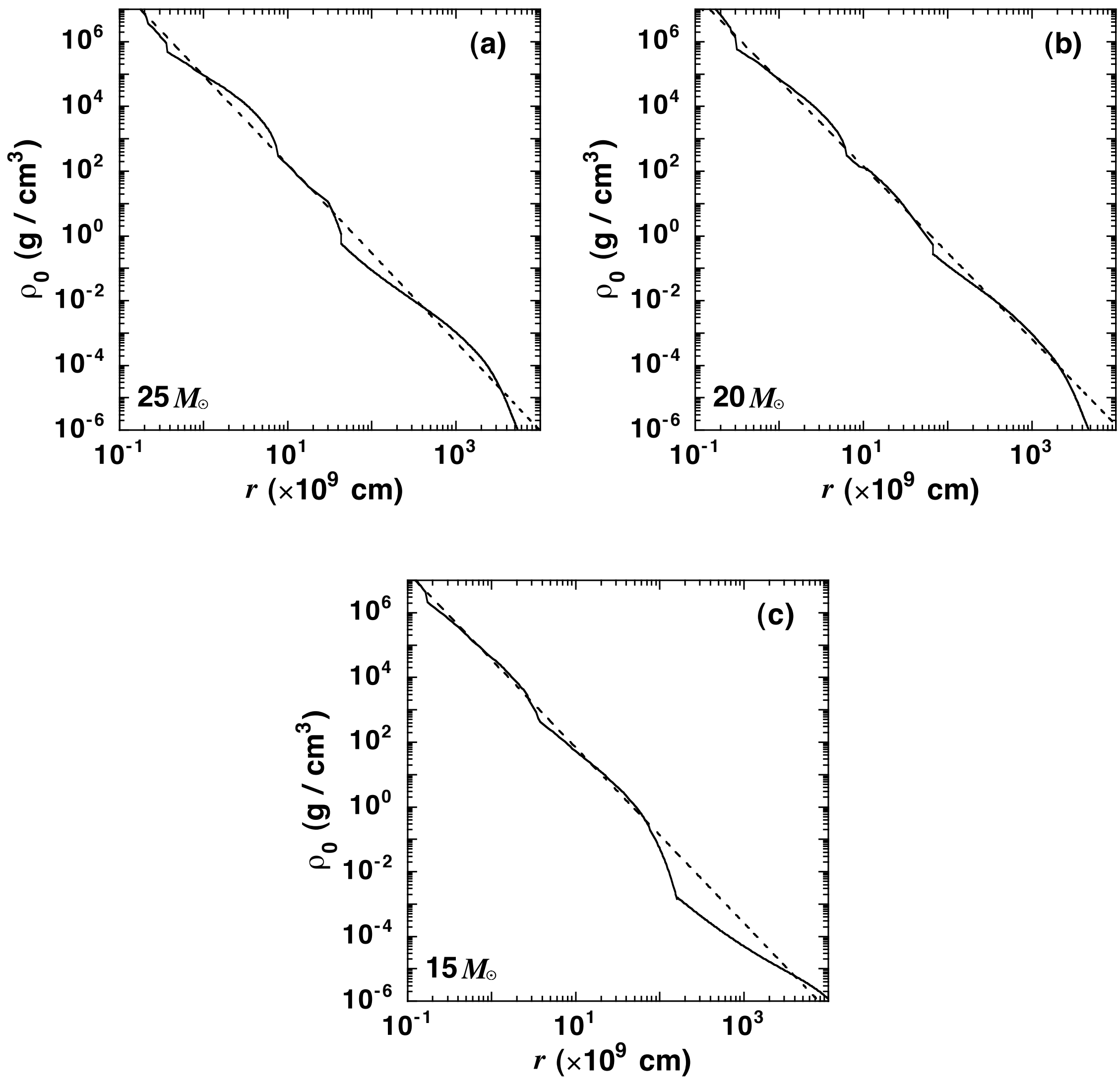

Fig. 8.2. Stellar density distribution $\rho_0(r)$, of the 25 $M_\odot$ (panel (a)) and 20 $M_\odot$ (panel (b)) progenitor models (Iwamoto 1998) and the 15 $M_\odot$ progenitor model (Nomoto *et al.* 1993) (panel (c)). The corresponding approximated power-law density distribution given by Eqs. (3.1) (on page 23) and Table 3.1 (on page 25) are also shown by the dashed line.

the radius of the 25 $M_\odot$ progenitor is small and that of the 15 $M_\odot$ progenitor is large compared with that of the 20 $M_\odot$ progenitor. The radius of the 20 $M_\odot$ progenitor is equal to that of the 16.2 $M_\odot$ progenitor.

The relation of the radius of the bottom of the H-rich envelope to the mass of the progenitor is similar to the relation in the case of the boundary between the convective He-layer and the radiative He-layer. The radius of the bottom of the H-rich envelope is 4.4×10^{10} cm, 4.9×10^{10} cm, and 1.6×10^{11} cm in the cases of the 25 $M_\odot$, 20 $M_\odot$, and 15 $M_\odot$ progenitors, respectively. In the case of the 15 $M_\odot$ progenitor, the radius of the 15 $M_\odot$ progenitor is more than three times larger than those of the 25 $M_\odot$ and the 20 $M_\odot$ progenitors. The radius of the 20 $M_\odot$ progenitor is slightly smaller than that of the 16.2 $M_\odot$ progenitor.

From the above description, we observed the difference of the ranges in the radius of the discrete layers in these progenitors. The difference of the range in the radius affects the peak temperature owing to the following reason. During supernova explosions, the density and the temperature behind the shock front at any given times are roughly constant. In addition, the pressure behind the shock front is almost supported by the radiative pressure because of the high temperature. So, the peak temperature is approximately obtained by setting the volume behind the shock front times the radiation energy density equal to the expansion energy (Weaver and Woosley 1980). In this study, the explosion energy is set to be 1×10^{51} erg in all cases of the explosion model. Thus, the peak temperature is determined by the radius of the shock front and the ranges of the discrete layers reflect the range of the peak temperature in each layer.

Figure 8.3 presents peak temperatures during the supernova explosions and the temperature distributions in the presupernova stages in the cases of the 25 $M_\odot$, 20 $M_\odot$, and 15 $M_\odot$ star models. We see from Fig. 8.3 that the peak temperature at a given radius reflects the radius independently of the stellar mass. At the bottom of the He-layer, the

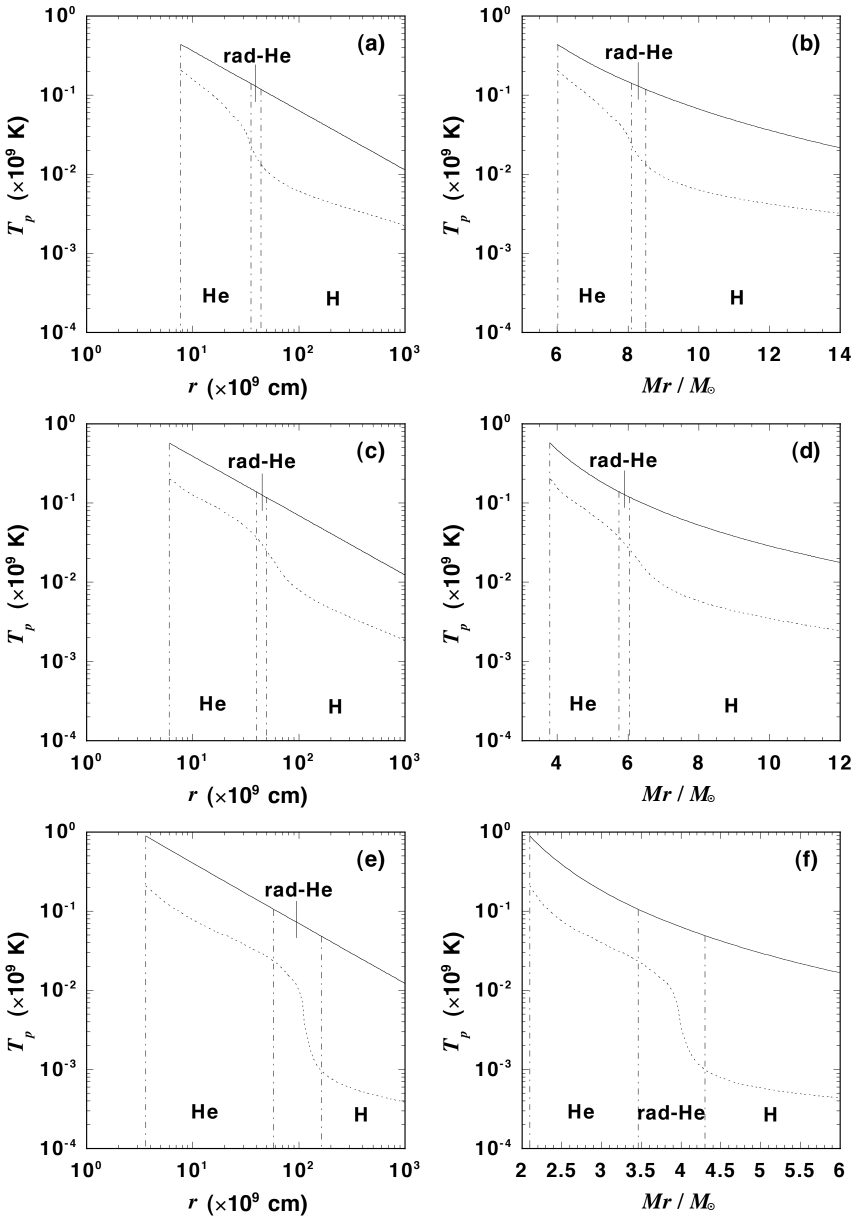

Fig. 8.3. The peak temperatures, T_p, (solid line) and the temperature distributions in the presupernova stage (dashed line in the cases of the 25 $M_\odot$ (panels (a) and (b)), 20 $M_\odot$ (panels (c) and (d)), and 15 $M_\odot$ (panels (e) and (f)) supernovae. Panels (a), (c), and (e) show the relation to the radius, r, and panels (b), (d), and (f) show the relation to the mass coordinate, M_r. Regions between two vertical dash-dotted lines and denoted by "He", "rad-He", and "H" indicate the convective He-layer, the radiative He-layer, and the H-rich envelope, respectively.

peak temperatures of the 25 $M_\odot$, 20 $M_\odot$, and 15 $M_\odot$ supernovae are 4.3×10^8 K, 5.8×10^8 K, and 7.9×10^8 K, respectively. The peak temperature at the bottom of the He-layer of the 20 $M_\odot$ supernova is equal to that of the 16.2 $M_\odot$ supernova. The small radius of the 15 $M_\odot$ progenitor brings about the high peak temperature during the explosion. Owing to the high temperature, α-capture reactions proceed effectively in inner region of the He-layer of the 15 $M_\odot$ supernova compared with the cases of the 25 $M_\odot$ and 20 $M_\odot$ supernovae.

The peak temperatures at the boundary between the convective He-layer and the radiative He-layer of the 25 $M_\odot$, 20 $M_\odot$, and 15 $M_\odot$ supernovae are 1.4×10^8 K, 1.4×10^8 K, and 1.1×10^8 K, respectively. The peak temperature of the 25 $M_\odot$ supernova is almost equal to the 20 $M_\odot$ supernova, so that the light element production in the outer region of the convective He-layer is not so different between them. In the case of the 15 $M_\odot$ supernova, the peak temperature at the boundary is small compared with those in the other two supernovae. We expect that the explosive nucleosynthesis of the light elements scarcely proceeds near the outer boundary of the convective He-layer of the 15 $M_\odot$ supernova (see Figs. 8.3 (c), (e), and (f)).

At the bottom of the H-rich envelope, the peak temperatures of the 25 $M_\odot$, 20 $M_\odot$, and 15 $M_\odot$ supernovae are 1.2×10^8 K, 1.2×10^8 K, and 4.9×10^7 K, respectively. Owing to the similar ranges in the radius of the radiative He-layers between the 25 $M_\odot$ progenitor and the 20 $M_\odot$ progenitor, the ranges of the peak temperatures are similar and, thus, there occurs the light element synthesis in the radiative He-layer similarly. On the other hand, the ranges in the radius of the radiative He-layer of the 15 $M_\odot$ progenitor is much larger. So, the behavior of the light element production in the radiative He-layer of the 15 $M_\odot$ supernova is expected to be different from those in the cases of the 25 $M_\odot$ and 20 $M_\odot$ supernovae. The low peak temperature of the 15 $M_\odot$ supernova also affects the explosive nucleosynthesis in the H-rich envelope. In such a low temperature, it is not expected that the explosive nucleosynthesis proceeds.

8.2. Light element synthesis in the 25 $M_\odot$, 20 $M_\odot$, and 15 $M_\odot$ supernovae

8.2.1. ^{7}Li, ^{10}B, and ^{11}B

Taking account of the ranges of the radius and the peak temperature in each burning layer, we investigate the synthetic processes of the X-elements and their abundance distributions in the 25 $M_\odot$, 20 $M_\odot$, and 15 $M_\odot$ supernovae. Figure 8.4 shows the abundance distributions of the X-elements produced in the He-layer and the H-rich envelope of the 25 $M_\odot$ (panel (a)), 20 $M_\odot$ (panel (b)), and 15 $M_\odot$ (panel (c)) supernovae. Table 8.1 presents typical key reactions of the X-element production of these supernovae.

In the inner region of the convective He-layer, ^{7}Li, ^{10}B, and ^{11}B are commonly in the steady-flow equilibrium of the α-captures and the ν-process during the supernova explosions. The regions, where the abundances are determined by the steady-flow equilibrium condition, are 6.0 $M_\odot \lesssim M_r \lesssim$ 6.1 $M_\odot$, 3.8 $M_\odot \lesssim M_r \lesssim$ 4.1 $M_\odot$, and 2.1 $M_\odot \lesssim M_r \lesssim$ 2.6 $M_\odot$ in the cases of the 25 $M_\odot$, 20 $M_\odot$, and 15 $M_\odot$ supernovae, respectively: the steady-flow equilibrium region is large in the case of the 15 $M_\odot$ supernova and small in the case of the 25 $M_\odot$ supernova. The peak temperatures corresponding to the regions in the cases of the these supernovae are also evaluated by the use of Figs. 8.3(b), (d), and (f); the steady-flow equilibrium between the production and the decomposition of ^{7}Li, ^{10}B, and ^{11}B is achieved when the peak temperature is higher than about 4×10^8 K. So, for example, in the case of the 25 $M_\odot$ supernova of which radius of the inner He-layer boundary is large, the region where the steady-flow equilibrium is achieved is narrow because the peak temperature rises to slightly higher than 4×10^8 K even at the bottom of the He-layer.

In the regions where 6.1 $M_\odot \lesssim M_r \lesssim$ 8.0 $M_\odot$, 4.1 $M_\odot \lesssim M_r \lesssim$ 5.7 $M_\odot$, and 2.6

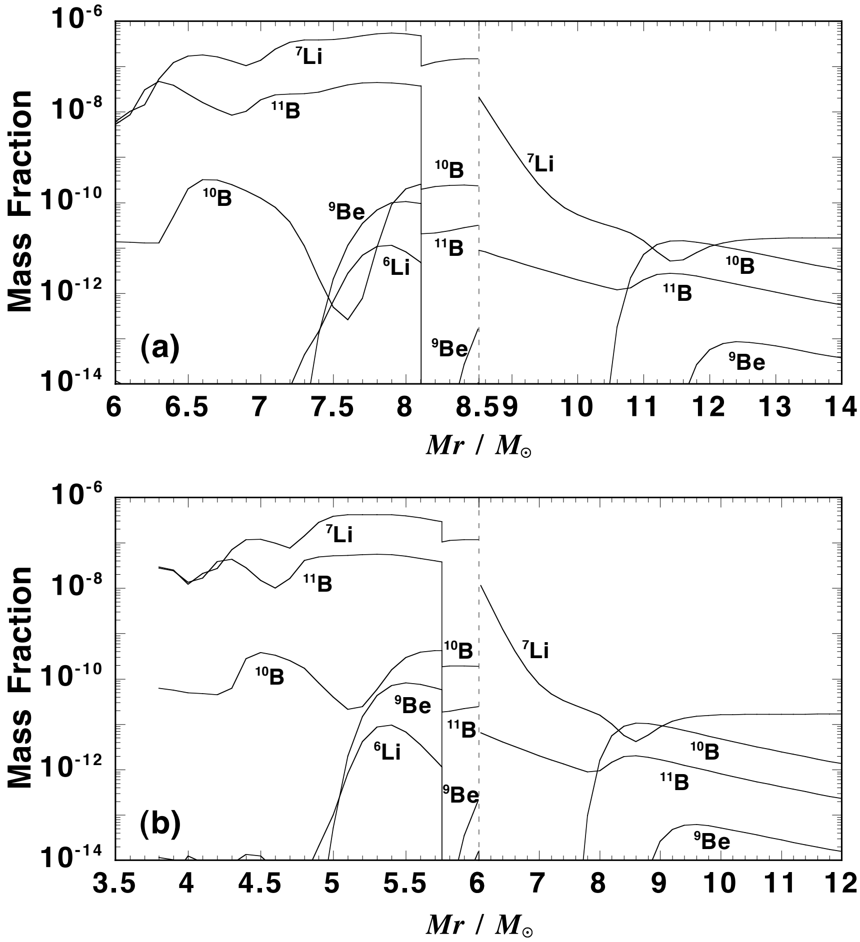

Fig. 8.4. Distributions of the final abundances of the X-elements in the cases of the 25 $M_\odot$ (panel (a)), 20 $M_\odot$ (panel (b)), and 15 $M_\odot$ (panel (c)) supernovae. Discontinuities of the curves appear at the boundaries between the convective and the radiative He-layers (M_r = 8.0 $M_\odot$ (panel (a)), 5.7 $M_\odot$ (panel (b)), and 3.5 $M_\odot$ (panel (C))) and between the radiative He-layer and the H-rich envelope (M_r = 8.5 $M_\odot$ (panel (a)), 6.0 $M_\odot$ (panel (b)), and 4.3 $M_\odot$ (panel(c))). In panel(c), circle, triangle, square, and diamond denote the abundances of ^{7}Li, ^{9}Be, ^{10}B, and ^{11}B, respectively, at the bottom of the H-rich envelope. The abundance of ^{6}Li is below the lowest scale of this figure.

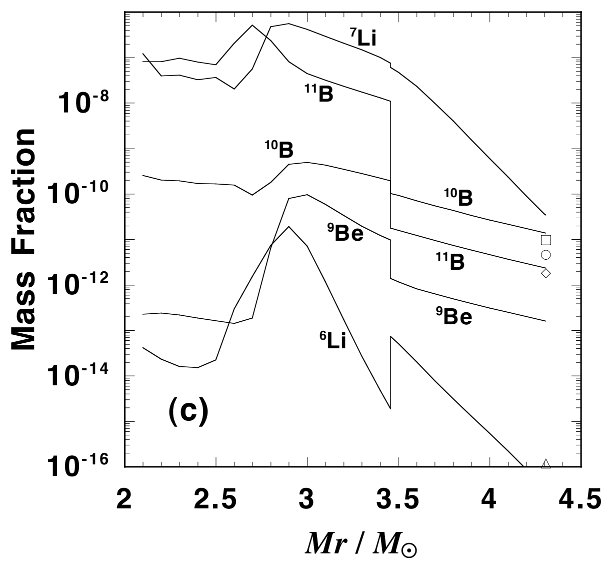

Fig. 8.4. *Continued*

$M_\odot \lesssim M_r \lesssim$ 3.0 $M_\odot$ in the cases of the 25 $M_\odot$, 20 $M_\odot$, and 15 $M_\odot$ supernovae, the abundance distributions of ^{7}Li and ^{11}B are similar among these supernovae. Most of key reactions tabulated in Table 8.1 are in common in the regions. The productions and the decompositions of ^{7}Li and ^{11}B are not affected by the difference of the total neutrino flux due to the stellar mass. In the region where $M_r \gtrsim$ 3.0 $M_\odot$ of the convective He-layer in the case of the 15 $M_\odot$ supernova, decompositions of ^{7}Li, ^{10}B, and ^{11}B do not occur effectively because of low peak temperature.

Note that a large decrease of the ^{10}B abundance is seen in the region where $M_r \gtrsim$ 7.0 $M_\odot$ of the convective He-layer of the 25 $M_\odot$ supernova. Although the decrease is seen in the 20 $M_\odot$ supernova, in the case of the 25 $M_\odot$ supernova the abundance of ^{10}B becomes lower than those of ^{9}Be and ^{6}Li (7.5 $M_\odot \lesssim M_r \lesssim$ 7.8 $M_\odot$). In this region, ^{10}B is decomposed by neutrons during the ν-process. The neutrons are mainly produced through ^{4}He$(\nu,\nu' n)^3$He and ^{3}H$(t,nn)^4$He. The neutrino flux of the 25 $M_\odot$ supernova is larger than that of the 20 $M_\odot$ supernova (see Table 3.4 on page 38), so that larger amount of neutrons are provided in the case of the 25 $M_\odot$ supernova than that of the 20 $M_\odot$ supernova. As a result, the decrease of ^{10}B due to the n-capture proceeds more rapidly in the region of the 25 $M_\odot$ supernova. On the other hand, the corresponding decrease of the ^{10}B abundance is not seen in the convective He-layer of the 15 $M_\odot$ supernova. This is probably because the total neutrino flux is small compared with the 25 $M_\odot$ and 20 $M_\odot$ supernovae and, thus, the amount of the neutrons produced through the ν-process is small.

In the radiative He-layer, the abundances of ^{7}Li, ^{10}B, and ^{11}B produced in the 25 $M_\odot$ supernova are almost equal to those of ^{7}Li, ^{10}B, and ^{11}B produced in the 20 $M_\odot$ supernova, respectively. In both supernovae, ^{7}Li and ^{11}B are slightly decomposed by protons and ^{10}B is decomposed by neutrons (see Table 8.1). In the cases of the 15 $M_\odot$ supernova, decomposition processes of ^{7}Li, ^{10}B, and ^{11}B are not effective. The abundances of ^{10}B and ^{11}B are confined within a factor of 9. On the other hand, the abundances of ^{7}Li has a variety more than three orders of magnitude. Before the shock arrival to the radiative He-layer, ^{10}B and ^{11}B are produced through $^{14}\mathrm{N}(\nu,\nu'\alpha)^{10}\mathrm{B}$ and $^{12}\mathrm{C}(\nu,\nu'p)^{11}\mathrm{B}$, respectively. Since the reaction rates of the ν-process are in inverse proportion to the square of the radius in the progenitor (see Eq. (3.31) on page 35) and the radius of the bottom of the H-rich envelope is 2.8 times larger than that of the inner boundary of the radiative He-layer, it is natural that the varieties of the abundances of ^{10}B and ^{11}B are within a factor of 9. On the other hand, ^{7}Li is produced through $^4\mathrm{He}(\nu,\nu'p)^3\mathrm{H}(\alpha,\gamma)^7\mathrm{Li}$. The peak temperature at the bottom of the H-rich envelope is less than a half of the peak temperature at the inner boundary of the radiative He-layer (see Fig. 8.3(f)). The reaction rate of $^3\mathrm{H}(\alpha,\gamma)^7\mathrm{Li}$ strongly depends on temperature, so that such large varieties of the abundance of ^{7}Li is seen in the radiative He-layer.

In the H-rich envelope, the abundances of ^{7}Li, ^{10}B, and ^{11}B in the case of the 25 $M_\odot$ supernova are almost the same as those of the 20 $M_\odot$ supernova. Slight increase in

Table 8.1. Typical key reactions of the X-element production of the 25 $M_\odot$, 20 $M_\odot$, and 15 $M_\odot$ supernovae. The upper and lower columns show the formation and decomposition reactions, respectively. Furthermore, empty columns mean that there are no appreciable formation (or decomposition) processes.

(a) 25 $M_\odot$ supernova

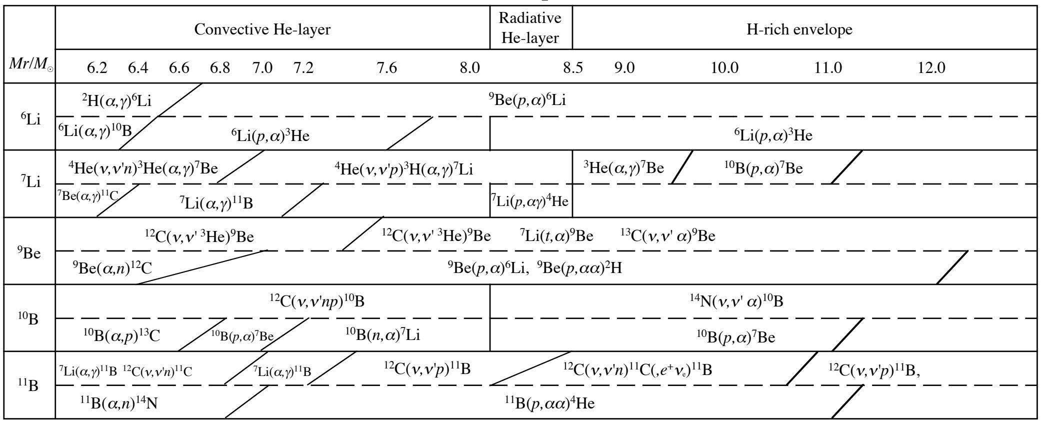

(b) 20 $M_\odot$ supernova

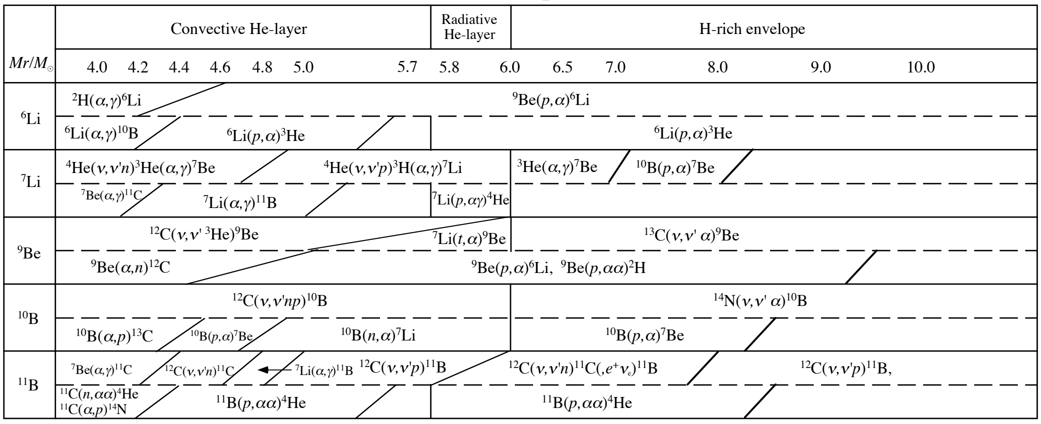

(c) 15 $M_\odot$ supernova

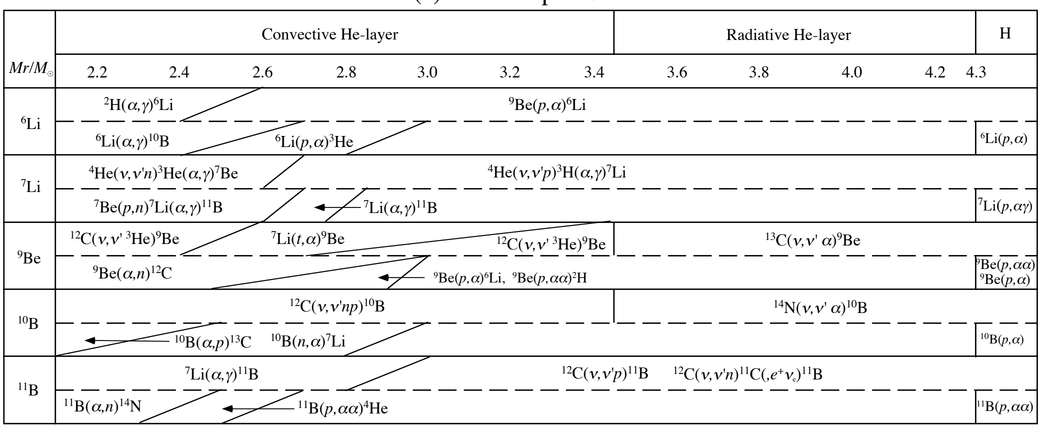

the abundances of these elements is seen because of the larger neutrino flux in the case of the 25 $M_\odot$ supernova (see Table 3.4 on page 38). As mentioned in Section 8.1, when we investigate the light element synthesis in the H-rich envelope of the 15 $M_\odot$ supernova, we only take account of the bottom of the H-rich envelope. The abundances of ^{10}B and ^{11}B at the bottom of the H-rich envelope are near to those in the outer region of the radiative He-layer. So we can say that ^{10}B and ^{11}B are scarcely decomposed even at the bottom of the H-rich envelope and, thus, in the entire region of the H-rich envelope. Although ^{7}Li is decomposed at the bottom of the H-rich envelope, we expect that ^{7}Li probably keeps its abundance before the explosion by considering that the density determined by the power-law density profile is larger than that of the numerical progenitor model by a factor of 20 (see Fig. 8.2(c)).

8.2.2. ^{6}Li and ^{9}Be

Hereafter, we investigate the productions of ^{6}Li and ^{9}Be in the 25 $M_\odot$, 20 $M_\odot$, and 15 $M_\odot$ supernovae. Figure 8.4 also presents the abundance distributions of ^{6}Li and ^{9}Be as well as ^{7}Li, ^{10}B, and ^{11}B. Typical key reactions of ^{6}Li and ^{9}Be are tabulated in Table 8.1. In the convective He-layer, ^{6}Li and ^{9}Be are produced only in the outer region where $M_r \gtrsim$ 7.5 $M_\odot$, 5.1 $M_\odot$, and 2.8 $M_\odot$ in the cases of the 25 $M_\odot$, 20 $M_\odot$, and 15 $M_\odot$ supernovae. In the inner region, ^{6}Li and ^{9}Be are commonly decomposed during the explosions (see Table 8.1). In the outermost region where $M_r \gtrsim$ 3.1 $M_\odot$ of the 15 $M_\odot$ supernova, the abundance of ^{6}Li rapidly decreases with an increase in the mass coordinate. In this region the peak temperature is low, so that only a little amount of ^{6}Li is produced during the explosion. In the radiative He-layer of the 25 $M_\odot$ and 20 $M_\odot$ supernovae, the amounts of ^{6}Li and ^{9}Be are small. In this layer, only a small amount (about 1×10^{-12} or less) of ^{9}Be is produced through the ν-process (see Figs. 8.4(a) and (b) and Table 8.1). Further, the produced ^{9}Be is decomposed rapidly through ^{9}Be$(p,\alpha)^6$Li and ^{9}Be$(p,\alpha\alpha)^2$H (see Table

8.1). The slightly produced ^{6}Li is also decomposed rapidly through ^{6}Li$(p,\alpha)^3$He, so that the amount of ^{6}Li is much smaller than that of ^{9}Be. In the case of the 15 $M_\odot$ supernova, the variety of the amount of ^{9}Be is confined within a factor of 9 as same as ^{10}B and ^{11}B. On the other hand, the amount of ^{6}Li have a variety more than three orders of magnitude as same as ^{7}Li. Hence, it is expected that the ^{9}Be/^{7}Li ratio in the 15 $M_\odot$ supernova becomes large compared with the ratios in the 25 $M_\odot$ and 20 $M_\odot$ supernovae. However, the ^{6}Li/^{7}Li ratio is small commonly in these supernovae. In the H-rich envelope inner than 11.8 $M_\odot$ and 9.0 $M_\odot$ in the cases of the 25 $M_\odot$ and 20 $M_\odot$ supernovae, the amount of ^{9}Be is less than 1×10^{-14}; the ^{9}Be is completely decomposed during the explosions (see Table 8.1). The amount of ^{6}Li is always less than 1×10^{-14} since ^{6}Li is decomposed more rapidly than ^{9}Be.

On the basis of the above behaviors of ^{6}Li and ^{9}Be, we investigate the varieties of the ^{6}Li/^{7}Li and ^{9}Be/^{7}Li ratios in the cases of the 25 $M_\odot$, 20 $M_\odot$, and 15 $M_\odot$ supernovae. The ratios of ^{6}Li/^{16}O-^{7}Li/^{16}O are illustrated in Figs. 8.5(a)-(c) and the ^{9}Be/^{16}O-^{7}Li/^{16}O ratios are illustrated in Figs. 8.5(d)-(f). Figures 8.5(a) and (d), 8.5(b) and (e), and 8.5(c) and (f) correspond to the cases of the 25 $M_\odot$, 20 $M_\odot$, and 15 $M_\odot$ supernovae, respectively.

We see from Figs. 8.5(a) to (c) that the amount of ^{6}Li produced in the convective He-layer (and a small region in the radiative He-layer in the case of 15 $M_\odot$ supernova) is larger than a level of the detection limit (the number ratio to ^{16}O is larger than 1×10^{-9}). Only in the case of 15 $M_\odot$ supernova, which has smaller amount of ^{16}O in the convective He-layer, the ^{6}Li/^{16}O ratio becomes more than 1×10^{-7}. The maximum ^{6}Li/^{7}Li ratio is 3×10^{-5}, 3×10^{-5}, and 4×10^{-5} in the cases of the 25 $M_\odot$, 20 $M_\odot$, and 15 $M_\odot$ supernovae, respectively. The ratio of ^{6}Li/^{7}Li in the supernovae is less than 4×10^{-5} and, thus, we can say that the ^{6}Li/^{7}Li ratio in the supernovae is always three orders of magnitude smaller than that of the solar-system composition.

Next, we investigate the varieties of ^{9}Be/^{7}Li ratios in the 25 $M_\odot$, 20 $M_\odot$, and 15 $M_\odot$

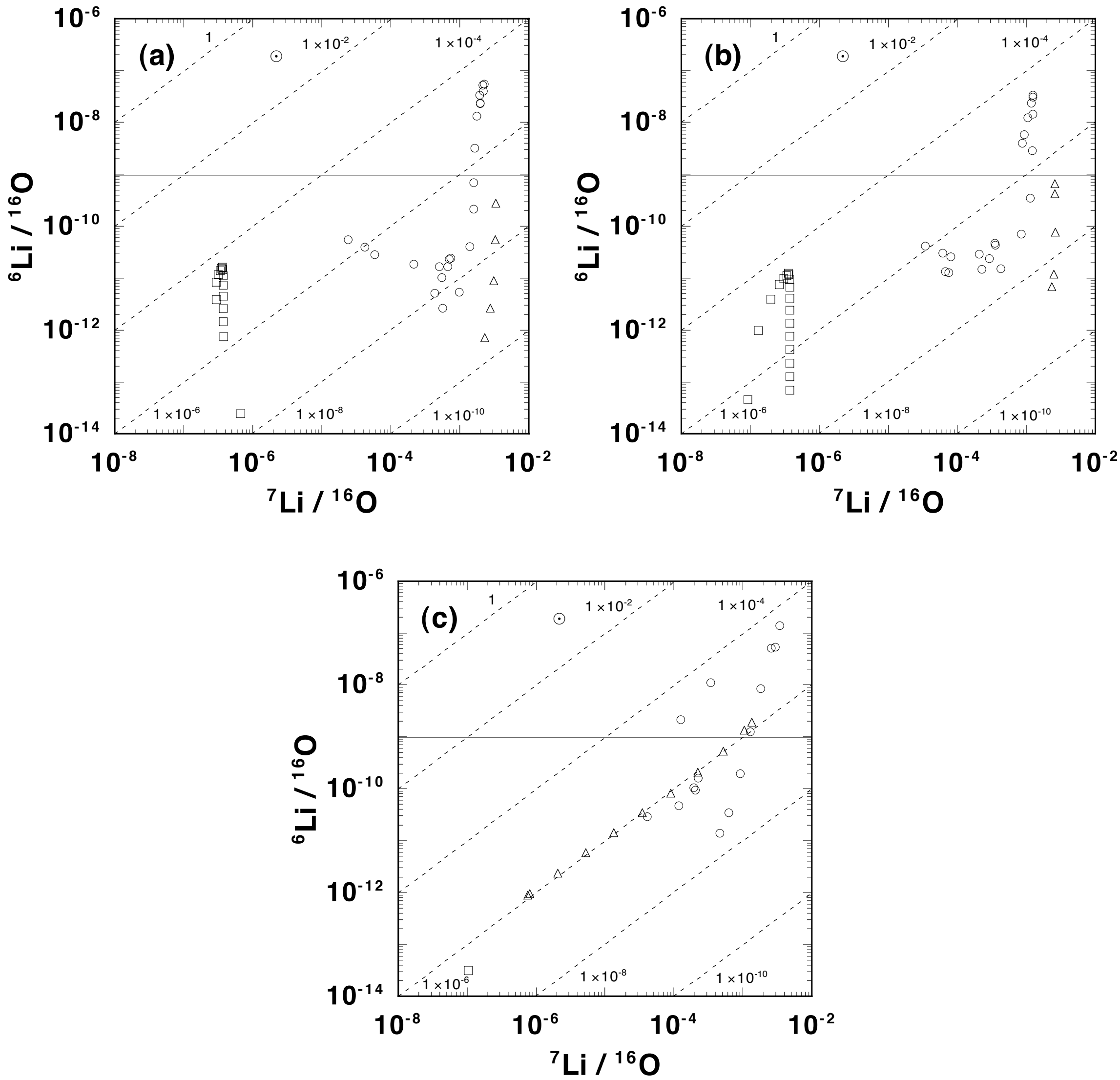

Fig. 8.5. Diagrams between ^{6}Li/^{16}O and ^{7}Li/^{16}O ratios (panels(a) to (c)) and between ^{9}Be/^{16}O and ^{7}Li/^{16}O ratios (panels(d) to (f)). Panels (a) and (d), (b) and (e), and (c) and (f) correspond to the cases of the 25 $M_\odot$, 20 $M_\odot$, and 15 $M_\odot$ supernovae, respectively. The ratios are all in number. Circles, triangles, and squares show the ratios in the convective He-layer, in the radiative He-layer, and in the H-rich envelope, respectively. A mark $\odot$ shows the ratios of solar-system composition. A solid horizontal line indicates the detection limit, i.e., the number ratio of species to ^{16}O equal to 1×10^{-9}. Dotted lines indicate values of constant ^{6}Li/^{7}Li ratios ((a) to (c)) and ^{9}Be/^{7}Li ratios ((d) to (f)): $1, 1 \times 10^{-2}$, 1×10^{-4}, 1×10^{-6}, 1×10^{-8} and 1×10^{-10}.

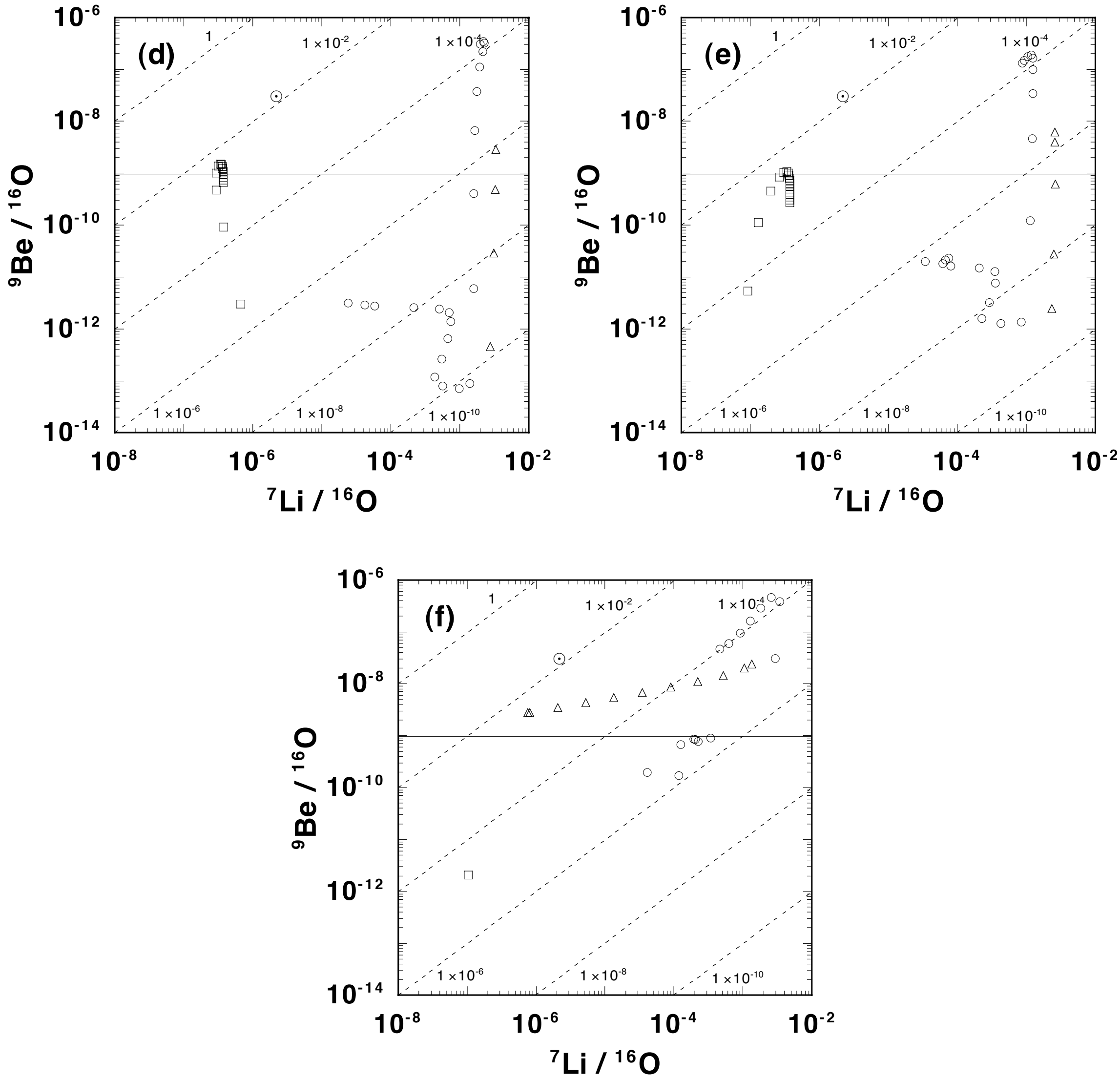

Fig. 8.5. *Continued*

supernovae. The maximum ^{9}Be/^{7}Li ratio in the convective He-layer is 2×10^{-4} commonly in these supernovae and the ^{9}Be/^{7}Li ratio commonly becomes of the order of 1×10^{-4} in the outer region of the convective He-layer. In the radiative He-layer, although the amount of ^{9}Be is smaller than the level of the detection limit in most regions of the 25 $M_\odot$ and 20 $M_\odot$ supernovae, the amount of ^{9}Be is detectable and the ^{9}Be/^{7}Li ratio becomes large in the case of the 15 $M_\odot$ supernova. In the former case, ^{9}Be is decomposed during the explosion. In the latter case, since the radiative He-layer is expanded and the peak temperature is low (see Figs. 8.1 and 8.3), ^{9}Be is not decomposed and ^{7}Li is scarcely produced even after the shock passage. Thus, the variety of the ^{9}Be/^{7}Li ratio in the radiative He-layer of the 15 $M_\odot$ supernova is between 2×10^{-5} and 4×10^{-3}, i.e., the ^{9}Be/^{7}Li ratio become larger by a factor of 20 than the maximum value in the radiative He-layers of the 25 $M_\odot$ and 20 $M_\odot$ supernovae. Note that even in the 15 $M_\odot$ supernova the ^{9}Be/^{7}Li ratio is always smaller than that of the solar-system composition.

We should note that in the ^{9}Be/^{7}Li ratio becomes large in the H-rich envelope in the cases of the 25 $M_\odot$ and 20 $M_\odot$ supernovae. When ^{7}Li/^{16}O ratio is of the order of 1×10^{-6}, ^{9}Be may be detectable and ^{9}Be/^{7}Li ratio attains to 6×10^{-4} and 3×10^{-3} in the cases of the 25 $M_\odot$ and 20 $M_\odot$ supernovae, respectively. However, the region where the ^{9}Be/^{7}Li ratio shows such a large value is the outer region of the H-rich envelope where ^{7}Li keep the amount at the presupernova stage. So, if the amount of ^{7}Li and ^{9}Be expected from observations remain at the presupernova stage, the above ratios of ^{9}Be/^{7}Li are not expected to be seen (see Section 6.3.2 on page 97).

8.2.3. ^{13}C

We change a point of view to the production of the CNO-elements. Figure 8.6 shows the abundance distributions of the CNO-elements produced in the 25 $M_\odot$ (a), 20 $M_\odot$ (b), and 15 $M_\odot$ (c) supernovae and Table 8.2 tabulates typical production and decomposition reactions of the CNO-elements in these supernovae.

From Table 8.2, production and decomposition reactions of ^{13}C in the He-layer and the H-rich envelope do not depend on the stellar mass. The efficiencies of the reactions are affected by the peak temperature of which range depends on the stellar mass. The abundance distributions of the CNO-elements in the cases of the 25 $M_\odot$, 20 $M_\odot$, and 15 $M_\odot$ supernovae are presented in Fig. 8.6(a), 8.6(b), and 8.6(c), respectively. From these figures, decrease of the ^{13}C abundance is seen in the region where $M_r \lesssim$ 6.1 $M_\odot$, $M_r \lesssim$ 4.1 $M_\odot$, and $M_r \lesssim$ 2.5 $M_\odot$ in the cases of the 25 $M_\odot$, 20 $M_\odot$, and 15 $M_\odot$ supernovae, respectively. The decrease in the case of the 25 $M_\odot$ supernova is small compared with that in the case of the 20 $M_\odot$ supernova. On the other hand, not only the decrease but also an increase of the ^{13}C abundance are seen in the region of the 15 $M_\odot$ supernova. The peak temperature and the large neutrino flux after the shock passage in the inner He-layer make the behavior of the ^{13}C abundance complex. At the inner boundary of the He-layer, the abundance of ^{13}C is relatively large owing to the reproduction through the n-capture despite the decomposition through ^{13}C$(\alpha, n)^{16}$O (see Table 8.2). In the regions outer than 6.1 $M_\odot$, 4.1 $M_\odot$, and 2.5 $M_\odot$, the abundance distributions of the ^{13}C scarcely change by the stellar mass in the cases of the 25 $M_\odot$, 20 $M_\odot$, and 15 $M_\odot$ supernovae. In the radiative He-layer and the H-rich envelope, the abundance of ^{13}C commonly keeps its initial abundance during the supernova explosions.

8.2.4. ^{14}N

The variety of the abundance distributions of the ^{14}N due to the stellar mass is mainly brought about by the efficiency of the decomposition reaction and the initial compositions. The production process of the ^{14}N is commonly ^{11}B$(\alpha, n)^{14}$N (see Table 8.2). The effective decomposition of ^{14}N occurs only in the region where $M_r \lesssim$ 2.2 $M_\odot$ of the 15 $M_\odot$ supernova. In this region, the peak temperature rises to more than 7.1×10^8

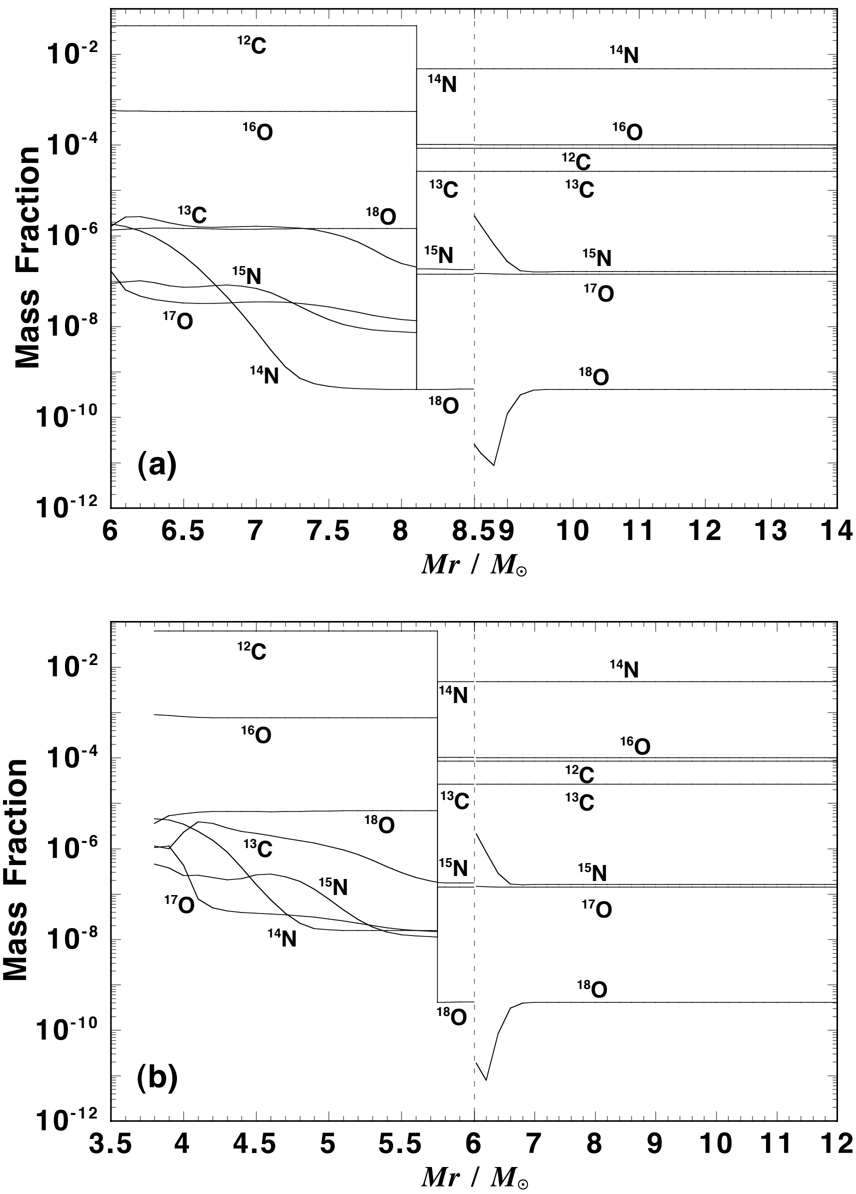

Fig. 8.6. Distributions of the final abundances of the CNO-elements in the cases of the 25 $M_{\odot}$ (panel (a)), 20 $M_{\odot}$ (panel (b)), and 15 $M_{\odot}$ (panel (c)) supernovae. Discontinuities of the curves appear at the boundaries between the convective and the radiative He-layers (M_r = 8.0 $M_{\odot}$ (panel (a)), 5.7 $M_{\odot}$ (panel (b)), and 3.5 $M_{\odot}$ (panel (C))) and between the radiative He-layer and the H-rich envelope (M_r = 8.5 $M_{\odot}$ (panel (a)), 6.0 $M_{\odot}$ (panel (b)).

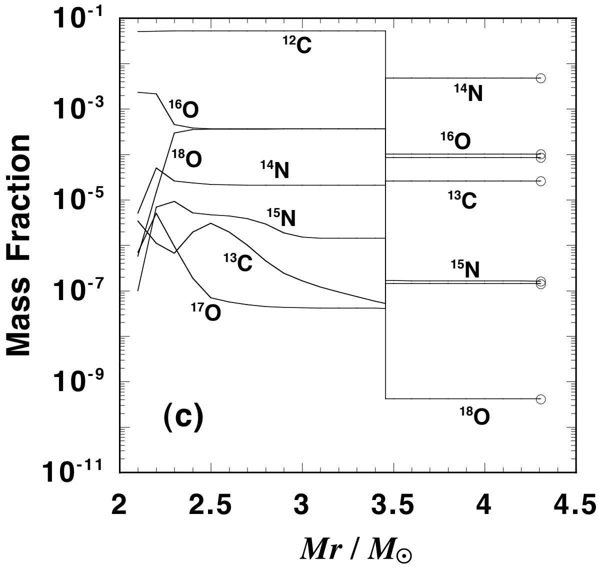

Fig. 8.6. *Continued*

K during the explosion (see Fig. 8.3(f)), so that ^{14}N$(n,p)^{14}$C$(\alpha,\gamma)^{18}$O reactions proceed. Since the peak temperatures at the inner He-layer boundaries of the 25 $M_{\odot}$ and 20 $M_{\odot}$ supernovae do not rise to such a high temperature, such a decomposition is not effective. As seen from Fig. 3.5 (see page 47), the initial abundance of ^{14}N in the convective He-layer has a variety in the progenitors. The variety of the initial abundance reflects the region where the production process is effective. In practice, although the abundance of ^{14}N keep its initial composition in the outer 1/4 region of the convective He-layer in the case of the 25 $M_{\odot}$ supernova, the initial abundance is kept during the explosion in a half of the convective He-layer of the 20 $M_{\odot}$ supernova and most of the He-layer of the 15 $M_{\odot}$ supernova ($M_r \gtrsim 2.4 M_{\odot}$). In the radiative He-layer and the H-rich envelope, no effective production of ^{14}N occurs.

Table 8.2. Typical key reactions of the CNO-element production of the 25 $M_\odot$, 20 $M_\odot$, and 15 $M_\odot$ supernovae. The upper and lower columns show the formation and decomposition reactions, respectively. Empty columns mean that there are no appreciable formation (or decomposition) processes.

(a) 25 $M_\odot$ supernova

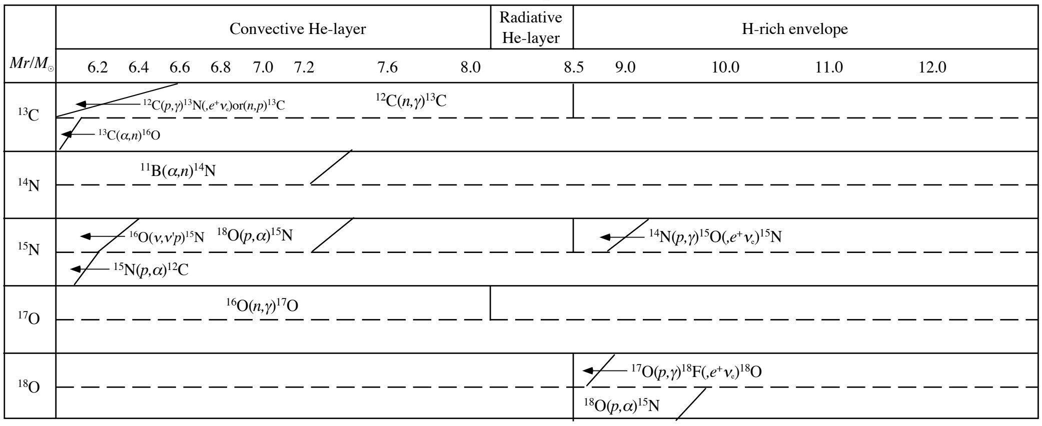

(b) 20 $M_\odot$ supernova

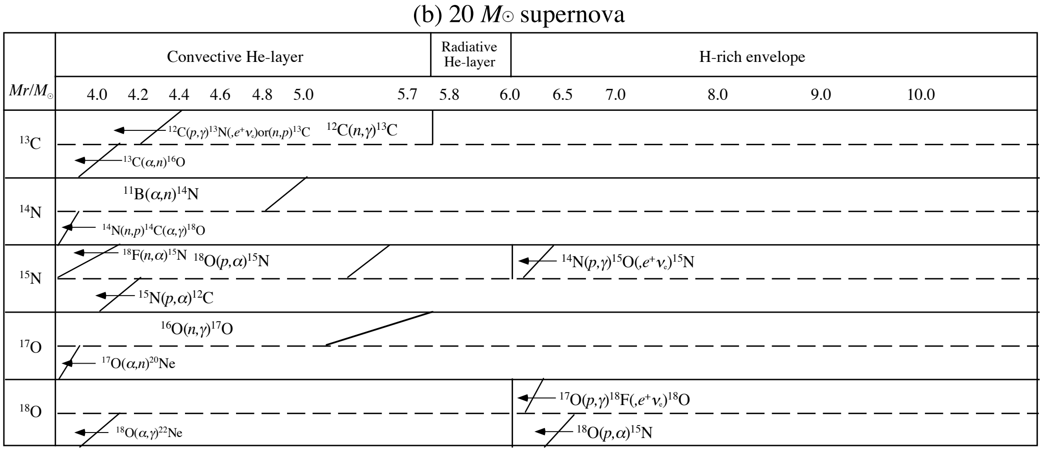

(c) 15 $M_\odot$ supernova

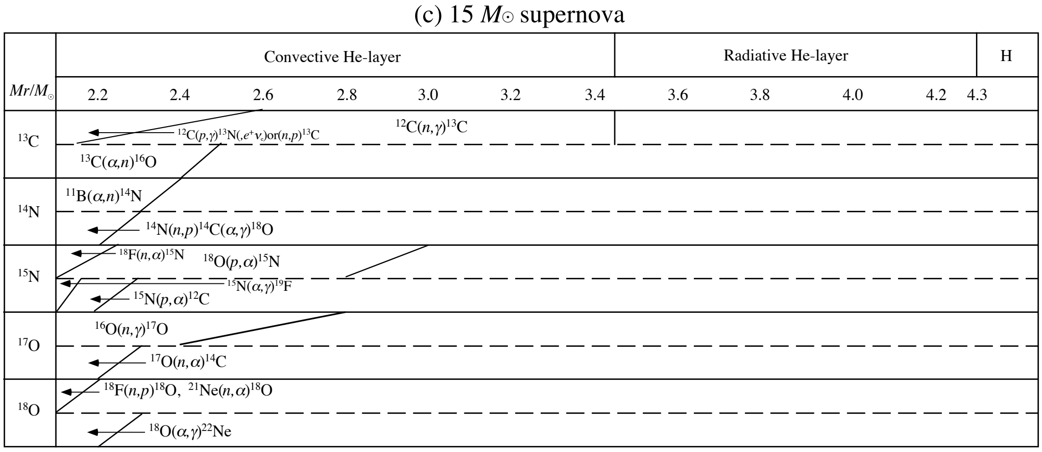

8.2.5. ^{15}N

In most of the region in the convective He-layer, ^{15}N is produced through ^{18}O(p, α) ^{15}N commonly in the cases of the 25 $M_{\odot}$, 20 $M_{\odot}$, and 15 $M_{\odot}$ supernovae. So, the initial abundance of ^{18}O affects the final abundance of ^{15}N in these supernovae. Although the abundance distribution of ^{15}N is different between the 25 $M_{\odot}$ and 20 $M_{\odot}$ supernovae, roughly speaking, the distribution of the ^{15}N/^{18}O ratio is similar between them. In the case of the 15 $M_{\odot}$ supernova, the abundance of ^{15}N relative to that of ^{18}O is small because the number ratio of protons produced through the ν-process to ^{18}O is small compared with those in the cases of the other two supernovae. In the region inner than 2.3 $M_{\odot}$, large decrease of the abundance of ^{15}N occurs (see Fig. 8.6(c)). This is brought about by the decrease of the ^{15}N production and by the decomposition through ^{15}N$(p, \alpha)^{12}$C and ^{15}N$(\alpha, \gamma)^{19}$F proceeded owing to the high temperature. In the radiative He-layer, ^{15}N commonly keeps its initial abundance during the supernova explosions. In the region where $M_r \lesssim$ 9.2 $M_{\odot}$ and $M_r \lesssim$ 6.6 $M_{\odot}$ in the cases of the 25 $M_{\odot}$ and 20 $M_{\odot}$ supernovae of the H-rich envelope, respectively, ^{15}N is produced through ^{14}N$(p, \gamma)^{15}$O$(,e^{+}\nu_{e})^{15}$N during the explosions. The peak temperatures of these regions are commonly higher than 9×10^{7} K. In the case of the 15 $M_{\odot}$ supernova, ^{15}N is not produced in the H-rich envelope. The peak temperature at the bottom of the H-rich envelope is too low to bring about the ^{15}N production through the p-capture.

8.2.6. ^{17}O

In the convective He-layer, the variation of the ^{17}O abundance is obtained mainly in the innermost regions, i.e., $M_r \lesssim$ 6.1 $M_{\odot}$, 4.0 $M_{\odot}$, and 2.4 $M_{\odot}$ in the cases of the 25 $M_{\odot}$, 20 $M_{\odot}$, and 15 $M_{\odot}$ supernovae, respectively. In the cases of the 20 $M_{\odot}$ and 15 $M_{\odot}$ supernovae, the increase in the abundance of ^{17}O commonly occurs. In the case of the 25

$M_\odot$ supernova, the increase in the ^{17}O abundance is small compared with that of the 20 $M_\odot$ supernova. In the region where $M_r \lesssim 2.2\ M_\odot$ in the case of the 15 $M_\odot$ supernova, ^{17}O is decomposed through $^{17}\mathrm{O}(n,\alpha)^{14}\mathrm{C}(\alpha,\gamma)^{18}\mathrm{O}$ (see Table 8.2). In the radiative He-layer and the H-rich envelope, ^{17}O commonly keeps its initial abundance in the cases of these supernovae.

8.2.7. ^{12}C, ^{16}O, and ^{18}O

In most regions of the He-layer and the H-rich envelope except near boundaries, ^{12}C, ^{16}O, and ^{18}O keep their abundances during the supernova explosions commonly in the cases of the 25 $M_\odot$, 20 $M_\odot$, and 15 $M_\odot$ supernovae. Just above the inner boundaries of the He-layer and the H-rich envelope, several productions and decompositions occur practically during the explosions. In the innermost region where $M_r \lesssim 2.2\ M_\odot$ in the case of the 15 $M_\odot$ supernova, ^{16}O is produced through $^{12}\mathrm{C}(\alpha,\gamma)^{16}\mathrm{O}$ and ^{18}O is rapidly captured to ^{22}Ne through $^{18}\mathrm{O}(\alpha,\gamma)^{22}\mathrm{Ne}$. In such a region the peak temperature becomes high ($T_p \gtrsim 7.1 \times 10^8$ K) enough to activate these reactions (see also Fig. 8.3(f)). In the cases of the 25 $M_\odot$ and 20 $M_\odot$ supernovae, the abundance of ^{18}O also decreases during the explosions in the inner region of the H-rich envelope where $M_r \lesssim 9.4\ M_\odot$ and 6.8 $M_\odot$, respectively. When the peak temperature higher than 8.3×10^7 K (the corresponding radius is about 8×10^{10} cm), ^{18}O is decomposed through $^{18}\mathrm{O}(p,\alpha)^{15}\mathrm{N}$. In the case of the 15 $M_\odot$ supernova, the abundance of ^{18}O in the H-rich envelope does not change during the explosions because of low peak temperature ($T_p < 4.9 \times 10^7$ K).

8.3. Influence of the decay time of the neutrino emission

In the case of the 16.2 $M_\odot$ supernova, the X-element production is affected by the decay time of the neutrino emission in the inner region of the He-layer. This is because the explosive nucleosynthesis starts before the X-element production due to the neutrino irradiation terminates in the inner region of the He-layer (see Section 5 on page 60). Now, we pay attention to the influence of the decay time of the neutrino emission on the number ratio of ^{11}B/^{7}Li in the supernovae with masses of 25 $M_\odot$, 20 $M_\odot$, and 15 $M_\odot$. The final number ratios of ^{11}B/^{7}Li in the He-layer of the 25 $M_\odot$, 20 $M_\odot$, and 15 $M_\odot$ supernovae are presented in Figs. 8.7(a), 8.7(b), and 8.7(c), respectively.

From these figures we see that there are three characteristic regions in the mass coordinates; the first region are $M_r \lesssim 4.0 M_\odot$ and $M_r \lesssim 2.5 M_\odot$ in the cases of the 20 $M_\odot$ and 15 $M_\odot$ supernovae, respectively. In these regions, the ^{11}B/^{7}Li ratio is confined within one order of magnitude except spikes. The abundances of ^{7}Li and ^{11}B are determined by the steady-flow equilibrium condition; ^{7}Li and ^{11}B are produced through two reaction sequences: ^{4}He$(\nu,\nu'p)^{3}$H$(\alpha,\gamma)^{7}$Li$(\alpha,\gamma)^{11}$B$(\alpha,n)^{14}$N and ^{4}He$(\nu,\nu'n)^{3}$He$(\alpha,\gamma)^{7}$Be$(\alpha,\gamma)^{11}$C $(\alpha,p)^{14}$N (see also Table 8.1). Since peak temperature is high enough to proceed α-capture reactions in a short time scale, the change of the reaction rates of ^{4}He$(\nu,\nu'p)^{3}$H and ^{4}He$(\nu,\nu'n)^{3}$He due to the change of the neutrino flux affects the abundances of ^{7}Li and ^{11}B similarly and, as a result, the ^{11}B/^{7}Li ratio scarcely changes owing to the change of the neutrino flux. This region is small ($M_r \lesssim 6.1 M_\odot$) in the case of 25 $M_\odot$ supernova because the peak temperature is low even at the inner boundary of the He-layer (see Fig. 8.3(b)).

The second region is $6.4 M_\odot \lesssim M_r \lesssim 7.0 M_\odot$ and $4.3 M_\odot \lesssim M_r \lesssim 4.8 M_\odot$ in the cases of the 25 $M_\odot$ and 20 $M_\odot$ supernovae, respectively. The ^{11}B/^{7}Li ratio is different only in the case of τ_ν=10 s and the difference is within a factor of 5. Production processes of ^{7}Li and ^{11}B are ^{4}He$(\nu,\nu'n)^{3}$He$(\alpha,\gamma)^{7}$Be$(e^-,\nu_{\rm e})^{7}$Li and ^{12}C$(\nu,\nu'n)^{11}$C$(,e^+\nu_{\rm e})^{11}$B, respectively. However, a part of ^{11}C produced by this process is decomposed through ^{11}C$(n,\alpha\alpha)^{4}$He before the shock arrival. Only in the case of τ_ν=10 s, ^{11}B is re-produced through ^{12}C$(\nu,\nu'n)^{11}$C$(,e^+\nu_{\rm e})$ ^{11}B after the shock arrival (see also Section 5.2 on page 63). In the case of the 15 $M_\odot$ supernova, the above process does not occur. The amount of

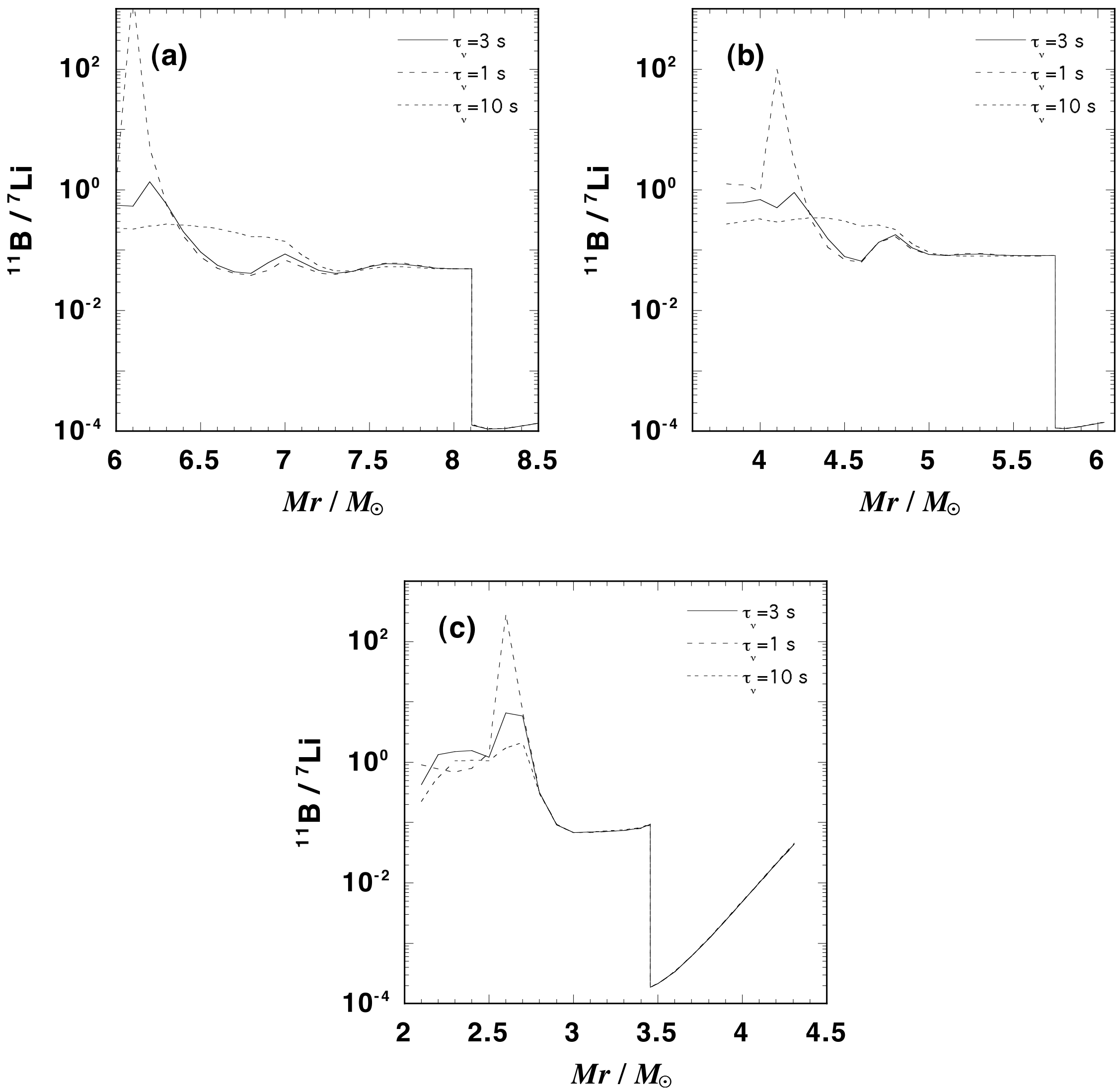

Fig. 8.7. Distributions of the number ratios of ^{11}B/^{7}Li in the He-layer of the 25 $M_\odot$ (panel (a)), 20 $M_\odot$ (panel (b)), and 15 $M_\odot$ (panel (c)) supernovae. Dashed curves, solid curves, and dotted curves denote the cases of τ_ν=1 s, 3 s, and 10 s, respectively.

^{11}B produced originally through ^{12}C$(\nu, \nu' p)^{11}$B is larger than the amount of ^{11}C.

The third region is outer than the second region of each supernova. In this region, the ^{11}B/^{7}Li ratio is almost independent of τ_ν. Almost all neutrinos pass through the region before the shock arrival even in the case of τ_ν=10 s.

Note that there are exceptional spikes in narrow regions in the mass coordinates in each figure. In the mass region, neutrino irradiation stops before the shock arrival and both ^{7}Be and ^{11}C (or ^{11}B) decrease exponentially in the post shock stage as mentioned in Section 5. Since the decomposition rate of ^{7}Be is larger than that of ^{11}C, the ^{11}B/^{7}Li ratio becomes very large. At last, the varieties of ^{11}B/^{7}Li ratios in the 25 $M_\odot$, 20 $M_\odot$, and 15 $M_\odot$ supernovae are confined between 0.04 and 7 except the spikes. We can say that the ^{11}B/^{7}Li ratio is commonly insensitive to the neutrino emission model in these supernovae.

In constructing diagrams of two isotopic ratios, we have used the ^{12}C/^{13}C ratio in most cases. So, we will mention the influence of the decay time of the neutrino flux on the ^{12}C/^{13}C ratios. The final number ratios of ^{12}C/^{13}C in the convective He-layer of the 25 $M_\odot$, 20 $M_\odot$, and 15 $M_\odot$ supernovae are presented in Figs. 8.8(a), 8.8(b), and 8.8(c), respectively.

In the case of the 25 $M_\odot$ supernova (Fig. 8.8(a)), the variety of ^{12}C/^{13}C ratios due to τ_ν at a fixed mass coordinate is confined within a factor of 3. As shown in Section 8.2.3, ^{13}C is scarcely decomposed through ^{13}C$(\alpha, n)^{16}$O even near the bottom of the He-layer. Although ^{13}C is produced after the shock passage, the produced abundance of ^{13}C is smaller than the abundance of ^{13}C produced before the shock arrival (in the case of τ_ν=10 s, the abundance of ^{13}C produced after the shock passage is larger than that before the shock arrival). In the case of the 20 $M_\odot$ supernova (Fig. 8.8(b)), the variety of ^{12}C/^{13}C ratios due to τ_ν is within a factor of 50. Near the inner boundary of the He-layer, ^{13}C is decomposed through ^{13}C$(\alpha, n)^{16}$O more than two orders of magnitude independently

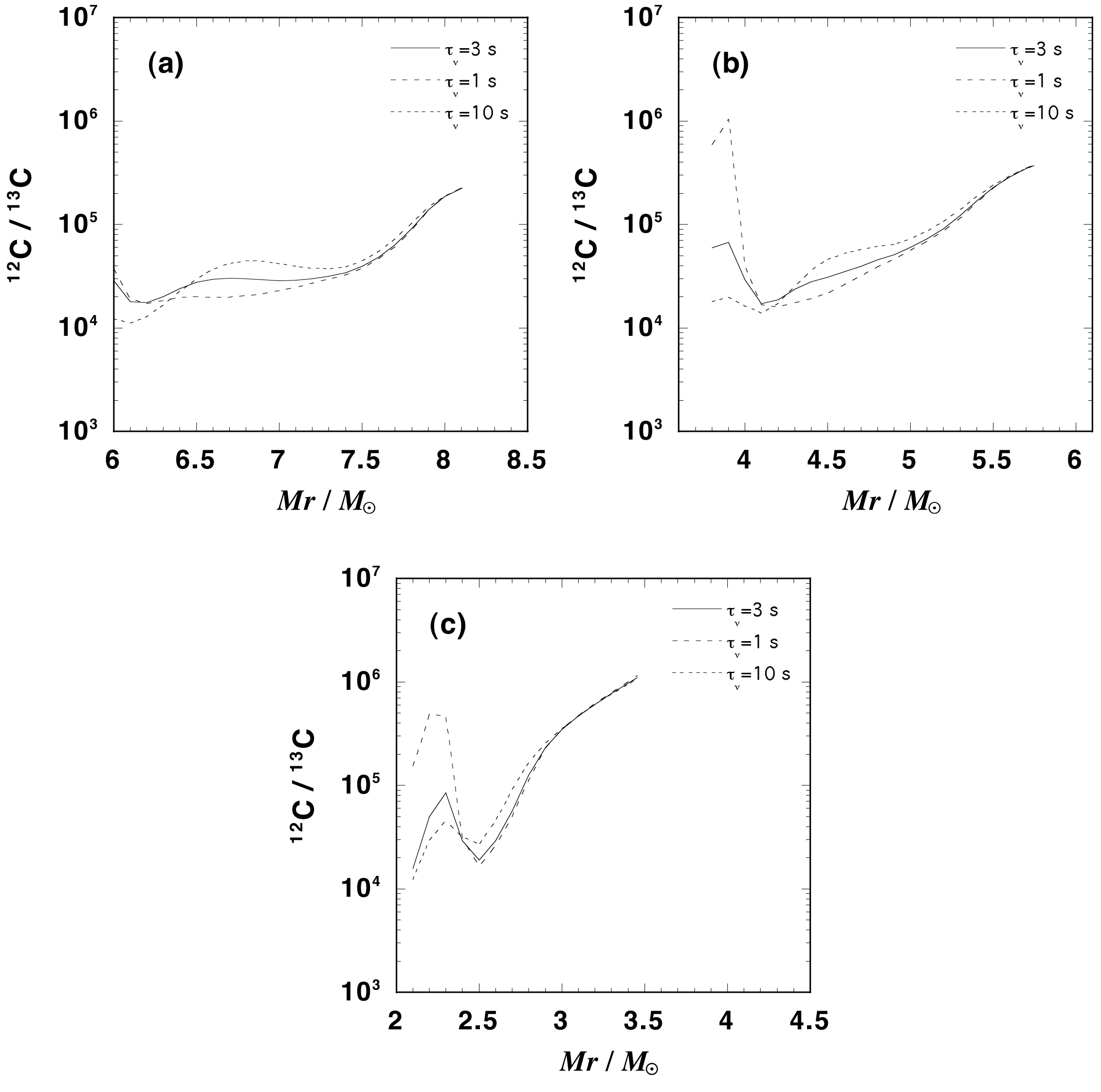

Fig. 8.8. As same as Fig. 8.7 but for the $^{12}C/^{13}C$ ratio.

of τ_ν. So, when τ_ν=3 s and 10 s the amount of ^{13}C produced through ^{12}C$(n,\gamma)^{13}$C and ^{12}C$(p,\gamma)^{13}$N$(n,p)^{13}$C after the shock arrival is much larger than the amount of ^{13}C just after the decomposition. Note that the ^{12}C/^{13}C ratio in the inner region of the He-layer ($M_r \sim 3.9 M_\odot$) become larger than that in the outer region of the He-layer ($M_r \sim 6.0 M_\odot$) in the case of τ_ν=1 s. This large ^{12}C/^{13}C ratio gives a large region of the convective He-layer in the diagram of the ^{16}O/^{17}O-^{12}C/^{13}C ratios (see Fig. 8.11(b)). In the case of the 15 $M_\odot$ supernova (Fig. 8.8(c)), the variety due to τ_ν is within a factor of 20, which is smaller than that of the 20 $M_\odot$ supernova. Similarly to the case of the 20 $M_\odot$ supernova, the decomposition of ^{13}C occurs in the inner region of the He-layer ($M_r \lesssim 2.4 M_\odot$). Since, however, the radius of the inner He-layer boundary of the 15 $M_\odot$ progenitor is small (see Fig. 8.1) and, as a result, the shock arrives at the boundary in a very short time (2.3 s after the neutrino irradiation), appreciable amount of ^{13}C is produced after the shock passage even in the case of τ_ν= 1 s.

8.4. Nuclear reprocessing after the mixing

Now, we will mention the behavior of ^{11}B/^{7}Li ratio due to nuclear reprocessing after the mixing between the He-component and the H-component. Basically, the behavior of ^{11}B/^{7}Li ratio due to the reprocessing after the mixing in the cases of the 25 $M_\odot$ and 20 $M_\odot$ supernovae are similar to that in the case of the 16.2 $M_\odot$ supernova; ^{7}Li and ^{11}B are decomposed through p-captures in the mixture and the final ^{7}Li and ^{11}B abundances are determined by the contents of ^{7}Be and ^{11}C undecomposed in the mixture. The other X-elements, ^{6}Li, ^{9}Be, and ^{10}B are also decomposed rapidly by a small amount of protons in the mixture. On the other hand, nuclear reprocessing after the mixing does not affect the abundances of the CNO-elements. In the case of long distance mixing beyond M_m(H) = 10.4 $M_\odot$ and 8.0 $M_\odot$ of the 25 $M_\odot$ and 20 $M_\odot$ supernovae, respectively, there occurs no appreciable nuclear reprocessing after the mixing.

In the case of the 15 $M_\odot$ supernova, although we consider the mixing between the He-component and the H-component at the bottom of the H-rich envelope, the nuclear reprocessing after the mixing does not proceed effectively. As mentioned in Section 8.1, the fitted value of the density is larger than the density of the numerical 15 $M_\odot$ progenitor model (Nomoto *et al.* 1993) by a factor of 20 at the bottom of the H-rich envelope. So, at the bottom of the H-rich envelope nuclear reactions proceeds more effectively those in the numerical progenitor model. Thus, we confirm that the nuclear reprocessing after the mixing does not occur effectively in the 15 $M_\odot$ supernova.

8.5. Summary and diagrams between two isotopic/elemental ratios

We investigated the variety of the light element synthesis due to the stellar mass of the progenitor using 25 $M_\odot$, 20 $M_\odot$, and 15 $M_\odot$ supernova models. We also investigated the varieties of the isotopic/elemental ratios of the light elements produced in the supernovae due to the decay time of the neutrino flux and the nuclear reprocessing after the mixing. Here, we summarize results obtained the above as follows:

1. The maximum temperature at a given radius, i.e., the temperature just after the shock passage, is almost independent of the total mass of a progenitor. The difference of the ranges in the radius of the He-layer and the H-rich envelope brings about the variety of the abundances of the light elements due to the mass of the progenitor;

   (a) The stellar structure of the 20 $M_\odot$ supernova is similar to that of the 16.2 $M_\odot$ progenitor in the region inner than 1×10^{12} cm. Owing to the similar structures, the abundance distributions of the light elements in the He-layer and the H-rich envelope of the 20 $M_\odot$ supernova is almost same as that of the 16.2 $M_\odot$ supernova.

(b) The large radius of the inner boundary of the He-layer of the 25 $M_\odot$ progenitor brings about low peak temperature in the inner region of the He-layer. So, the steady-flow equilibrium of the X-elements, the ^{13}C decomposition, and the ^{17}O production, which occur during the explosion of the 20 $M_\odot$ supernova, scarcely occur. The production of the X-elements and the CNO-elements is scarcely different from that in the case of the 20 $M_\odot$ supernova.

(c) In the case of the 15 $M_\odot$ supernova, the peak temperature rises to about 8×10^8 K in the innermost region of the He-layer, many kinds of α-capture reactions proceed just after the shock passage. In the radiative He-layer and the H-rich envelope, the explosive nucleosynthesis scarcely proceeds. The radii of the inner boundaries of these layers are so large that the temperature in these layers does not become high enough to arise the explosive nucleosynthesis.

2. The variety due to the decay time of the neutrino emission is seen in the innermost region of the He-layer independently of the stellar mass. The ^{11}B/^{7}Li ratio is commonly confined between 0.04 and 7 in these supernovae. The ^{12}C/^{13}C ratio changes within a factor of 50 in the 20 $M_\odot$ and 15 $M_\odot$ supernovae and is confined within a factor of 3 in the 25 $M_\odot$ supernova.

3. Nuclear reprocessing occurs after the mixing between the He-component and the H-component in the cases of 25 $M_\odot$ and 20 $M_\odot$ supernovae as same as 16.2 $M_\odot$ supernova. However, there occurs no effective nuclear reprocessing in the mixture in the case of 15 $M_\odot$ supernova. The radius of the bottom of the H-rich envelope of 15 $M_\odot$ progenitor is large compared with more massive progenitors and, as a result, the temperature in the mixture is too low to proceed the nuclear reprocessing after the mixing.

4. In all models, the abundances of ^{6}Li and ^{9}Be produced during supernova explosions are very small. Only in the case of 15 $M_{\odot}$ supernova, ^{9}Be/^{7}Li ratio shows large value by a factor of 20 compared with the those of the other supernovae.

We present the three diagrams of the isotopic/elemental ratios, i.e., ^{11}B/^{7}Li-^{12}C/^{13}C, ^{14}N/^{15}N-^{12}C/^{13}C, and ^{16}O/^{17}O-^{12}C/^{13}C ratios in the cases of the 25 $M_{\odot}$, 20 $M_{\odot}$, and 15 $M_{\odot}$ supernovae and investigate the varieties in each supernova.

First, the diagrams of ^{11}B/^{7}Li-^{12}C/^{13}C ratios in the cases of the 25 $M_{\odot}$, 20 $M_{\odot}$, and 15 $M_{\odot}$ supernovae are illustrated in Figs. 8.9(a), 8.9(b), and 8.9(c), respectively. Roughly speaking, the varieties of the abundance ratios are almost same among these diagrams; the variety of ^{12}C/^{13}C ratio is between 3 and 1×10^{6} and that of ^{11}B/^{7}Li is between 1×10^{-4} and 7. We see that the area of the ratios in the convective He-layer of the 25 $M_{\odot}$ supernova in Fig. 8.9(a) is small compared with those of the other two supernovae. This is due to the fact that the ^{12}C/^{13}C ratios in the 25 $M_{\odot}$ supernova is less sensitive to the decay time of the neutrino flux (see Section 8.3). The variety of the ratios in the radiative He-layer or the H-rich envelope is almost same in these supernovae. It should be noted that the region due to the nuclear reprocessing after the mixing are different between the 25 $M_{\odot}$ and 20 $M_{\odot}$ supernovae (see regions coated by black); the region where the ^{12}C/^{13}C ratio is larger than the ratio in the convective He-layer is formed in the case of the 25 $M_{\odot}$ supernova and the region where ^{11}B/^{7}Li ratio is larger than that in the mixture is formed in the case of the 20 $M_{\odot}$ supernova. Unfortunately, most of the region made by the nuclear reprocessing overlaps with the region in the supernovae with the other masses. So, it is difficult to find an evidence for the nuclear reprocessing after the mixing in presolar grains by the use of these diagrams.

Next, the diagrams of ^{14}N/^{15}N-^{12}C/^{13}C ratio in the cases of the 25 $M_{\odot}$, 20 $M_{\odot}$, and 15 $M_{\odot}$ supernovae are illustrated in Fig. 8.10(a), 8.10(b), and 8.10(c), respectively. These

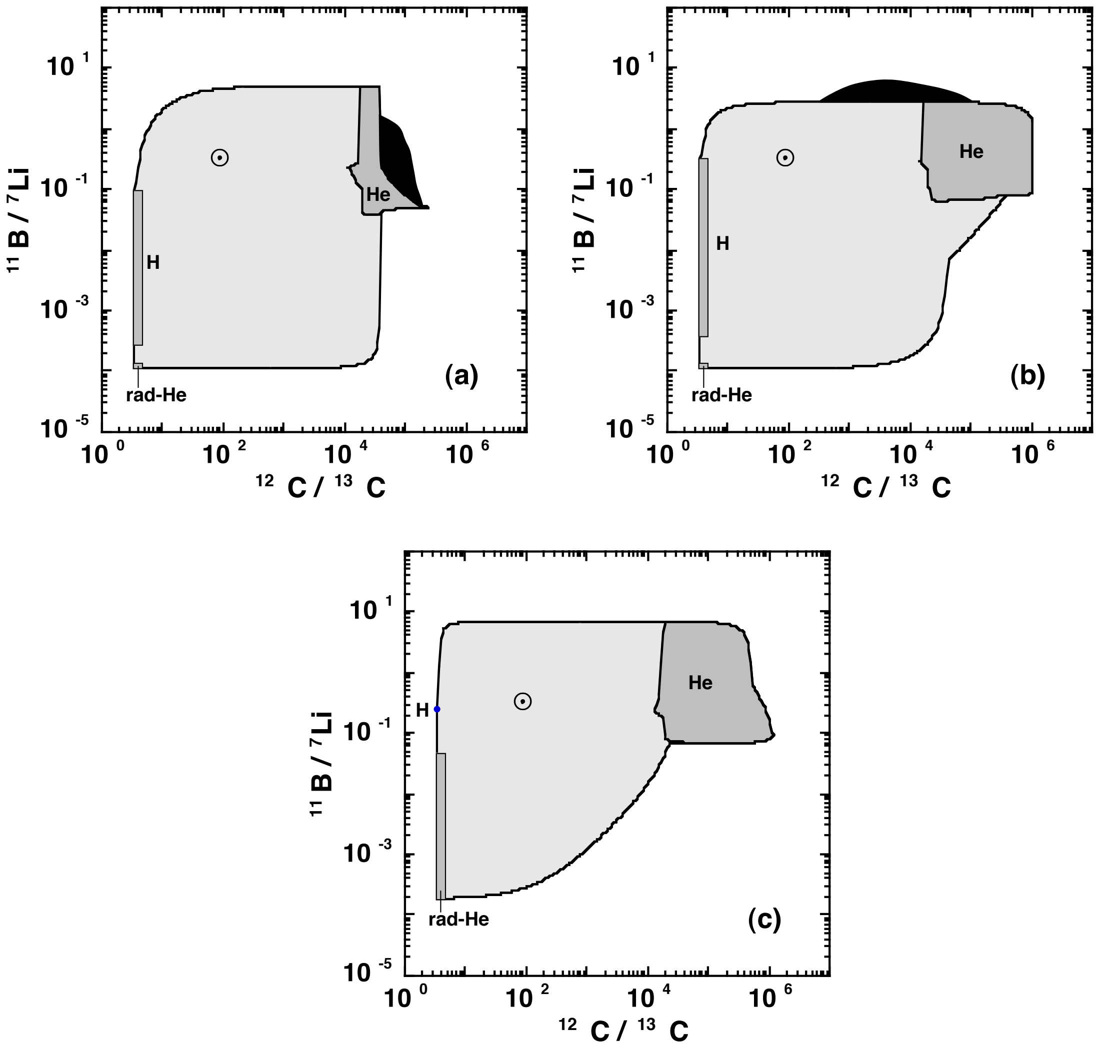

Fig. 8.9. The number ratios of ^{11}B/^{7}Li versus ^{12}C/^{13}C in the cases of the 25 $M_{\odot}$ (panel(a)), 20 $M_{\odot}$ (panel(b)), and 15 $M_{\odot}$ (panel(c)) supernovae. Three regions with a dark shade are of the convective He-layer (denoted by He), the radiative He-layer (denoted by rad-He), and the H-rich envelope (denoted by H) whereas a region with a light shade denotes the ratios made of the mechanical mixing between these regions. A region coated by black denotes the ratios made of the nuclear reprocessing after the mixing. A mark $\odot$ shows the ratio of the solar-system composition. (Exceptional spikes appeared in Fig. 8.7 are excluded.)

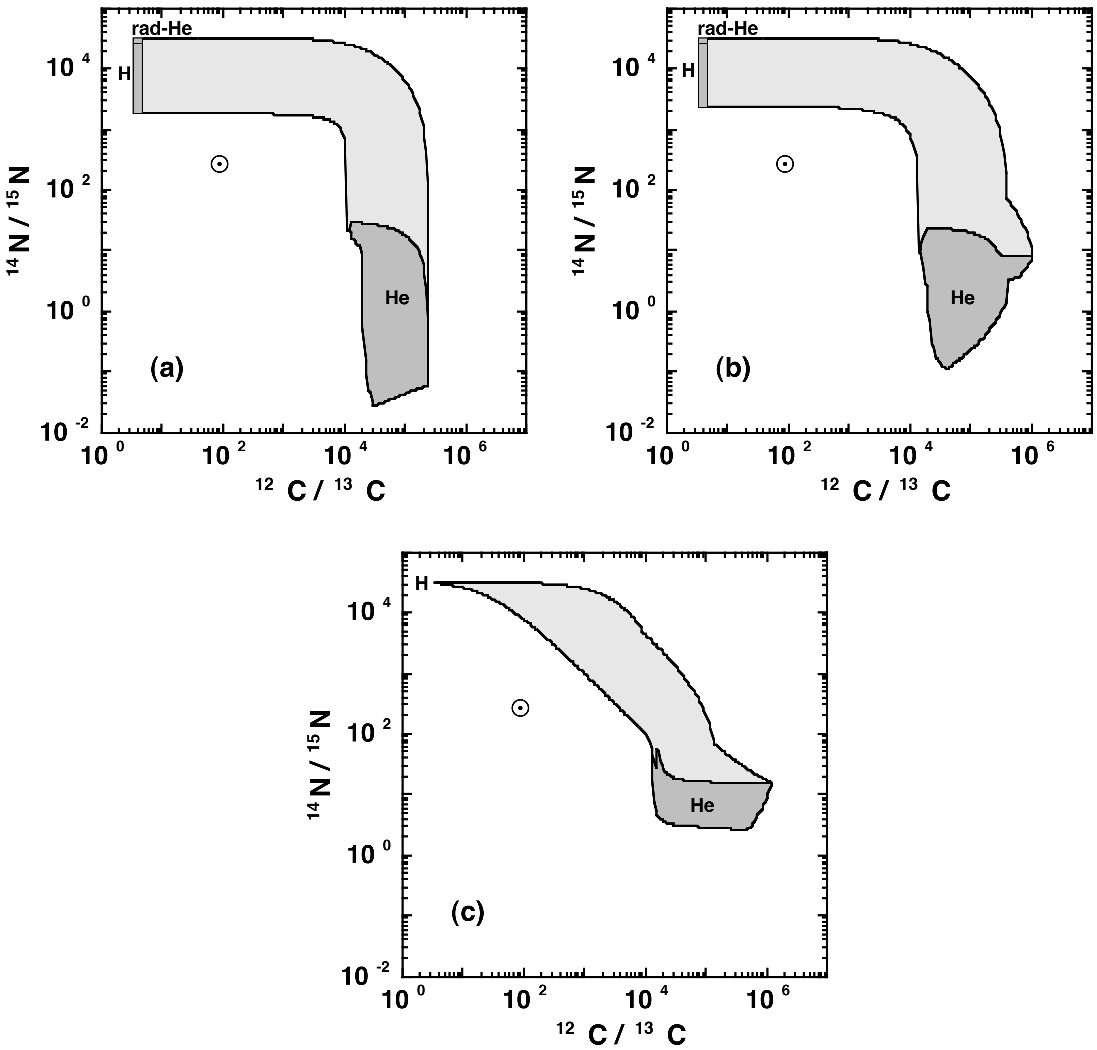

Fig. 8.10. As same as Fig. 8.9 but for $^{14}N/^{15}N$ versus $^{12}C/^{13}C$. In panel(c), the region of the radiative He-layer overlaps with that of the H-rich envelope.

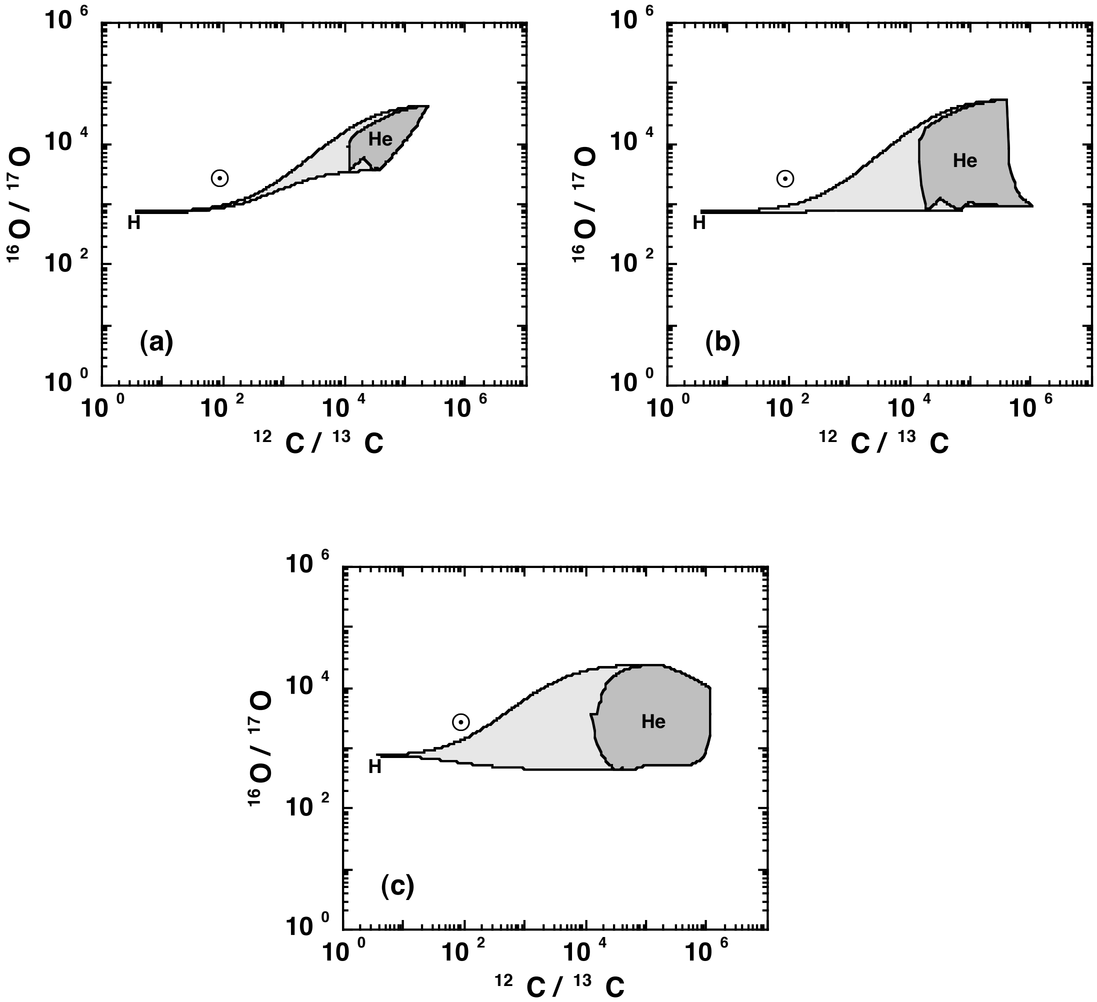

Fig. 8.11. As same as Fig. 8.9 but for $^{16}O/^{17}O$ versus $^{12}C/^{13}C$. The region of the radiative He-layer overlaps with that of the H-rich envelope.

three diagrams have also similar varieties each other. Only the diagram of the 15 $M_\odot$ supernova has smaller ^{14}N/^{15}N ratio with the ^{12}C/^{13}C ratio between 10^3 and 10^4. This is due to the fact that the amounts of ^{14}N and ^{15}N in the convective He-layer of the 15 $M_\odot$ supernova are larger than those of the other supernovae. In addition, the ^{14}N/^{15}N ratio in the H-rich envelope is equal to that in the radiative He-layer, i.e., the ratio at the presupernova stage. The large radius of the bottom of the H-rich envelope prevents from the explosive ^{15}N production during the explosion (see Section 8.2.5).

Finally, the diagrams of ^{16}O/^{17}O-^{12}C/^{13}C ratio in the cases of the 25 $M_\odot$, 20 $M_\odot$, and 15 $M_\odot$ supernovae are illustrated in Fig. 8.11(a), 8.11(b), and 8.11(c), respectively. We see that these three diagrams have a common correlation between the ^{16}O/^{17}O ratio and the ^{12}C/^{13}C ratio but the region of the 25 $M_\odot$ supernova is smaller than those of the other two supernovae. Especially, the region of the convective He-layer of the 25 $M_\odot$ supernova is smaller. One reason is the low peak temperature near the inner He-layer boundary and the other reason is that the both isotopic ratios are insensitive to the decay time of the neutrino flux in the case of the 25 $M_\odot$ supernova. The ratios in the radiative He-layer and the H-rich envelope keep their ratios at the presupernova stage commonly. Thus, the region of the ^{16}O/^{17}O-^{12}C/^{13}C diagram is in almost common between the 20 $M_\odot$ and the 15 $M_\odot$ supernovae but that of the 25 $M_\odot$ supernova is small.

9. Light Element Synthesis in the AGB Stars and by the Galactic Cosmic Rays

9.1. Low and intermediate mass stars on the RGB and the AGB

Stars with masses smaller than 9 $M_\odot$ on the main sequence end their lives not as supernova explosions but as the formation of white dwarfs. After the main sequence stage till the formation of the white dwarfs, the stars lose most of their envelopes. The envelopes are mixed with the internal material processed the H- and He-burnings and the compositions of the envelopes are changed during their evolutions. Until now, most ("mainstream") presolar grains are thought to be formed in the envelopes of such stars (Hoppe *et al.* 1994a). So, it is worth while deducing the surface compositions of these stars and comparing them with the compositions of supernovae. Calculations of stellar evolutions after stars leave the main sequence stage have been conducted by many authors after Hayashi *et al.* (1962) and, recently, the change of the abundances of the CNO-elements of low and intermediate mass stars after the main sequence stage also have been investigated for comparison with observations of surface of evolved stars (e.g., El Eid 1994; Forestini and Charbonnel 1997; Boothroyd and Sackmann 1999).

Hereafter, we will explain briefly stellar evolution after the main sequence stage and change of the surface composition. After a star leaves the main sequence, the star starts the H-shell burning and attains to the red giant branch (RGB). On the RGB, surface convective layer penetrates inward and the maximum depth of the convective layer reaches the region where partial H-burning has occurred earlier in the evolution. So, the surface chemical composition changes by the addition of ^{4}He together with the products of the CNO-cycles. This is known as the "first dredge-up". Mass loss of the envelope partially occurs on the RGB, so that it is expected that some presolar grains have the composition processed the "first dredge-up".

After the H-shell burning, core He-burning starts and ^{4}He at the central core changes to ^{12}C. Following the ^{4}He exhaustion at the center and the termination of the core He-burning, the ^{4}He surrounding the C-core starts to burn (shell He-burning). In the shell He-burning stage, the region outside the He-burning shell expands and the H-shell is extinguished. This stage is known as the early asymptotic giant branch (E-AGB) stage. On this stage, the surface convection penetrates into the extinguished H-shell and the H-burning products mix to the surface (in the case of the star with the mass larger than 4 $M_\odot$). This mixing is called the "second dredge-up". However, the surface composition scarcely changes by the second dredge-up.

Following the second dredge-up, the shell He-burning and the shell H-burning turn on alternatively and periodically. This stage is known as the thermally-pulsing asymptotic giant branch (TP-AGB) stage. The regions inside and outside the He-burning shell mix by convection during the shell He-burning. After the He-burning turns off, surface convection penetrates into inside the H-burning shell. As a result, the C-rich material produced through the shell He-burning is carried to the stellar surface. This injection of the C-rich material into the envelope is called the "third dredge-up". The third dredge-up occurs periodically. Most of the envelope is ejected on this stage and some presolar grains are also expected to be formed on this stage.

We obtained the ranges of the surface ^{12}C/^{13}C, ^{14}N/^{15}N, and ^{16}O/^{17}O ratios of stars on the RGB (till the first dredge-up) from El Eid (1994) and those of ^{12}C/^{13}C and ^{16}O/^{17}O ratios from Boothroyd and Sackmann (1999). El Eid (1994) investigated the abundances of the CNO-elements from the main sequence stage till the second dredge-up in eight stars with masses between 1.7 $M_\odot$ and 15 $M_\odot$ (we do not adopt the ratios in a 15 $M_\odot$ star). Boothroyd and Sackmann (1999) investigated the abundances of the CNO-elements till the second dredge-up in twenty-seven stars with masses between 0.85 $M_\odot$ and 9.0 $M_\odot$. Combined with their results, the ranges of the number ratios of ^{12}C/^{13}C, ^{14}N/^{15}N, and

$^{16}O/^{17}O$ of stars on the RGB are given by

$$19 \leq {}^{12}C/^{13}C \leq 90, \tag{9.1}$$

$$270 \leq {}^{14}N/^{15}N \leq 1.7 \times 10^3, \tag{9.2}$$

and

$$170 \leq {}^{16}O/^{17}O \leq 2.7 \times 10^3. \tag{9.3}$$

In this study, we do not adopt the surface ratios till the second dredge-up because the ratios are almost equivalent to those on the RGB.

We obtained the ranges of the surface ratios of the CNO-elements of stars on the TP-AGB (during the third dredge-up) from Forestini and Charbonnel (1997). They investigated the abundances and the isotopic ratios of the CNO-elements of four stars on the TP-AGB with masses between 3 $M_\odot$ and 6 $M_\odot$. The obtained ranges of the $^{12}C/^{13}C$, $^{14}N/^{15}N$, and $^{16}O/^{17}O$ ratios are given by

$$3.2 \leq {}^{12}C/^{13}C \leq 170, \tag{9.4}$$

$$1.4 \times 10^3 \leq {}^{14}N/^{15}N \leq 3.4 \times 10^4, \tag{9.5}$$

and

$$220 \leq {}^{16}O/^{17}O \leq 690. \tag{9.6}$$

We will compare the ranges of these ratios of the stars on the RGB and the TP-AGB in the forms of diagrams of $^{14}N/^{15}N$-$^{12}C/^{13}C$ and $^{16}O/^{17}O$-$^{12}C/^{13}C$ ratios with those obtained from supernovae in Section 9.3.

9.2. Galactic cosmic rays

Cosmic ray interactions have been considered as main sources of the X-elements (after Reeves *et al.* 1970). The galactic cosmic rays, most of which kinetic energy is between 100 MeV and 2 GeV (Reeves, 1994), decompose nuclei in the interstellar medium and form lighter nuclei. So it is thought that the energetic nuclei such as protons and α-particles decompose ^{12}C and ^{16}O in the interstellar medium and, as a result, that the X-elements are formed as their fragments. We deduce the isotopic/elemental ratios of the X-elements produced by the cosmic ray interactions. Here, we adopt the production rates of the X-elements produced through the galactic cosmic ray interactions with the interstellar medium in Walker *et al.* (1985). They considered nucleosynthesis of the X-elements in reactions of energetic ^{1}H and ^{4}He nuclei with ^{4}He, ^{12}C, ^{13}C, ^{14}N, and ^{16}O nuclei in the interstellar medium. They took the chemical composition in the interstellar nuclei to be the solar-system composition and used energy spectra of the energetic particles as same as in Meneguzzi *et al.* (1971). The obtained result is as follows: ^{6}Li/^{7}Li=0.70, ^{9}Be/^{7}Li=0.15, ^{11}B/^{7}Li=1.82, and ^{11}B/^{10}B=2.54.

In order to explain the solar-system abundances of the X-elements by the cosmic rays, low-energy cosmic rays interacting with the interstellar medium also have been considered (e.g., Walker *et al.* 1985). Evidence for the cosmic-rays ($\sim$ 10 Mev/nucleon) provided by the observations of γ-ray emission from the Orion complex of molecular cloud and star-forming regions with the COMPTEL telescope (Bloemen *et al.* 1994). The detected lines are nuclear de-excitation lines of ^{12}C and ^{16}O of 4.44 MeV and 6.13 MeV, respectively, which can be produced only by interactions of energetic C and O nuclei rather than protons and α-particles.

Ramaty *et al.* (1996) carried out calculations of γ-ray lines, the X-elements, and radioactive isotope production by low-energy cosmic rays. They assumed six kinds of accelerated particle composition such as the solar-system composition (Anders and Grevesse 1989) and supernova explosion (Weaver and Woosley 1993) and the solar-system composition and proto-galaxy composition as interstellar medium composition. The chemical compositions of accelerated particles and the interstellar medium and energy spectra of the cosmic rays are poorly understood since evidence for low-energy cosmic rays are limited to the observation of the COMPTEL (e.g., Bloemen *et al.* 1994). They calculated by the use of two kinds of assumed energy spectra. From the results of their calculations, we adopted the following cases. Particle composition is set to be the solar-system composition, cosmic ray composition, and 35 $M_\odot$ supernova composition. Interstellar medium composition is set to be the solar-system composition. Energy spectra are assumed on the basis of the consequence of shock acceleration. Note that by the use of the other parameters, results do not change so much the range of the isotopic ratios we adopted. The adopted isotopic/elemental ratios of the X-elements are given by

$$8.4 \times 10^{-2} \leq \ {}^{11}\mathrm{B}/{}^{7}\mathrm{Li} \ \leq 7.4, \tag{9.7}$$

$$0.12 \leq \ {}^{6}\mathrm{Li}/{}^{7}\mathrm{Li} \ \leq 0.71, \tag{9.8}$$

and

$$1.2 \times 10^{-3} \leq {}^{9}\mathrm{Be}/{}^{7}\mathrm{Li} \leq 5.5 \times 10^{-2}. \tag{9.9}$$

9.3. Comparison with our numerical results

We will compare the varieties of the isotopic/elemental ratios of the light elements in supernovae with those obtained from stars on the RGB and the AGB, and the galactic cosmic rays.

First, we will pay attention to the varieties of the isotopic ratios of the CNO-elements at the surface of the RGB stars and the AGB stars. In Fig. 9.1(a) we present the diagrams of ${}^{14}\mathrm{N}/{}^{15}\mathrm{N}$-${}^{12}\mathrm{C}/{}^{13}\mathrm{C}$ obtained from the RGB stars and the AGB stars together with the ratios obtained from a 25 $M_\odot$ supernova model (see Section 8.1 on page 134). We see from Fig. 9.1(a) that all region obtained in this study does not overlap with the region of the RGB stars and that most of the region does not overlap with those of the AGB stars. Only grains with the ${}^{12}\mathrm{C}/{}^{13}\mathrm{C}$ ratio smaller than 170 are not distinguishable from

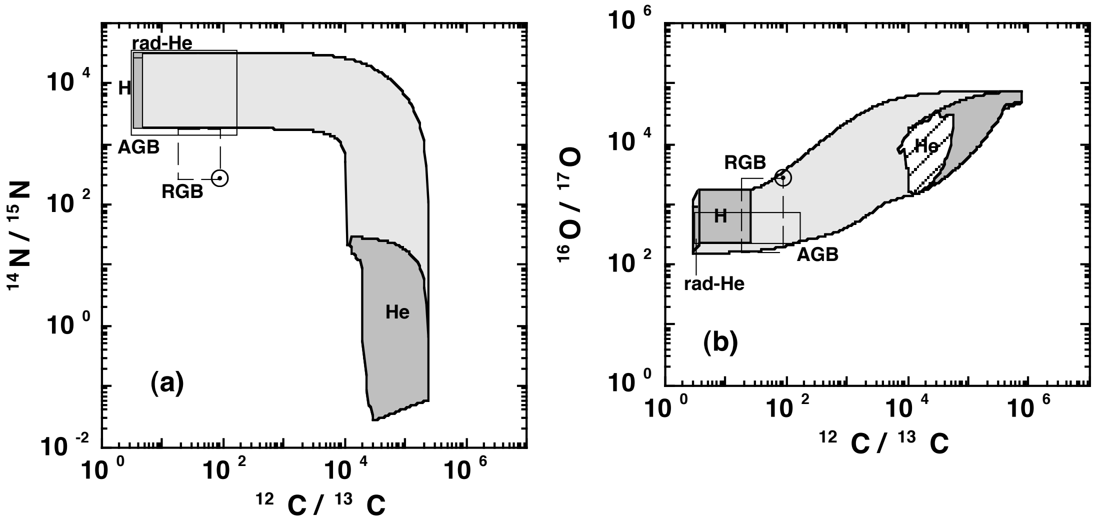

Fig. 9.1. The number ratio of $^{14}N/^{15}N$ (panel(a)) and $^{16}N/^{17}O$ (panel(b)) versus $^{12}C/^{13}C$. A region closed by a dashed line is of stars on the RGB (denoted by RGB) and a region enclosed by a solid line is of stars on the AGB (denoted by AGB). Panel (a) also presents the ratios in the 25 $M_{\odot}$ supernova (see Fig. 8.10(a) on page 166) and panel(b) presents the diagram of the ratios in the 16.2 $M_{\odot}$ supernova considered the uncertainties on the initial chemical compositions (see Fig. 6.10(c) on page 109).

those of the AGB star origin. We found that in Section 8.5 the range of $^{14}N/^{15}N$ in the H-rich envelope depends on the stellar mass. Despite the low $^{14}N/^{15}N$ ratio in the case of 25 $M_{\odot}$ supernova, the region of the RGB stars does not overlap with that of 25 $M_{\odot}$ supernova. In Fig. 9.1(b), we compare the region of $^{16}O/^{17}O$-$^{12}C/^{13}C$ ratios obtained in Fig. 6.10(c) with that of the AGB stars and the RGB stars. We see that the region, where $^{12}C/^{13}C$ ratio is larger than 170, in the supernova does not overlap with those of the AGB and the RGB stars, as same as $^{14}N/^{15}N$-$^{12}C/^{13}C$ diagram. So, although it is difficult to distinguish grains formed in the H-component of the supernova from those formed in the AGB stars, we can distinguish grains formed in the He-component or the mixture of the supernovae. So, we can say that these combinations of the isotopic ratios are useful to identify presolar grains originated from supernovae.

Next, we will change a point of view to the elemental ratios of the light elements produced by the cosmic rays. Figure 9.2(a) shows the range of $^{6}Li/^{7}Li$ ratio predicted by the study of the galactic cosmic rays (thick dashed line), the low-energy cosmic rays (hatched region) together with Fig. 8.5(b) (see page 148). The $^{6}Li/^{7}Li$ ratio expected to be detectable in the supernovae is more than three orders of magnitude smaller than that obtained from the cosmic rays. So we can say that $^{6}Li/^{7}Li$ ratio is suitable for determining whether a given grain is originated from supernovae or the cosmic rays; presolar grains with the $^{6}Li/^{7}Li$ ratio less than 3×10^{-5} should be originated from supernovae. Figure 9.2(b) shows the range of $^{9}Be/^{7}Li$ ratios together with Fig. 8.5(f) (the 15 $M_{\odot}$ supernova). In most cases $^{9}Be/^{7}Li$ ratio of the supernovae are much smaller than that of the cosmic rays. Only in a small region in the radiative He-layer of the 15 $M_{\odot}$ supernova, $^{9}Be/^{7}Li$ ratio is overlapped with the range of the cosmic rays. Thus, $^{9}Be/^{7}Li$ ratio is also good for distinguishing from supernova originated grains; presolar grains with the $^{9}Be/^{7}Li$ ratio less than 1×10^{-3} should be originated from supernovae. Only in the case of the $^{9}Be/^{7}Li$ ratio between 1×10^{-3} and 4×10^{-3}, we had better investigate whether the grains are

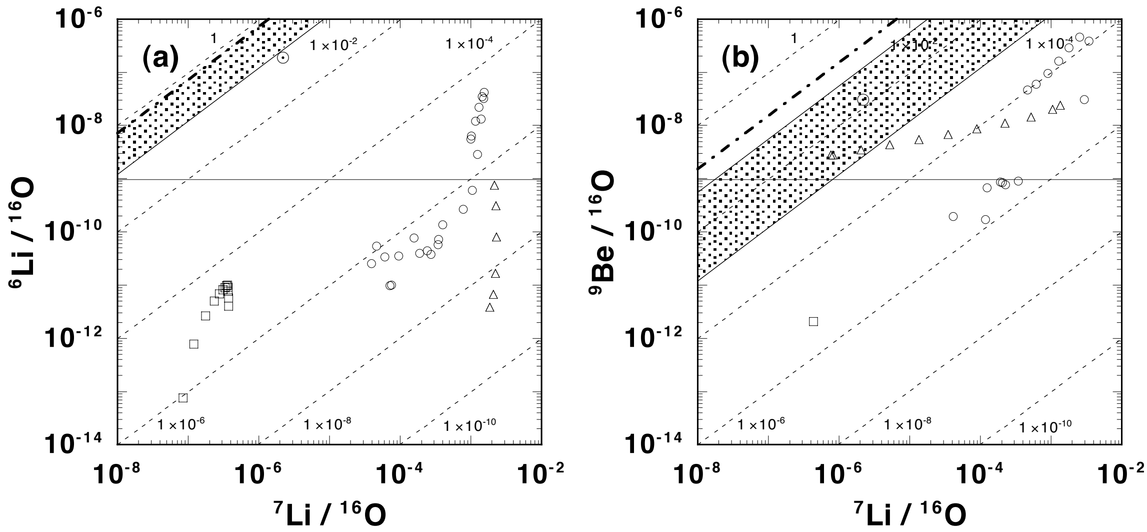

Fig. 9.2. Diagrams between ^{6}Li/^{16}O and ^{7}Li/^{16}O ratios (panel(a)) and between ^{9}Be/^{16}O and ^{7}Li/^{16}O ratios (panel(b)) of the galactic cosmic rays (a thick dash-dotted line) and of the low-energy cosmic rays (a hatched region). Panel(a) also presents the ratios of the 20 $M_{\odot}$ supernova (see Fig. 8.5(b)) and panel(b) presents the ratios of the 15 $M_{\odot}$ supernova (see Fig. 8.5(f)).

originated from the supernovae or the low-energy cosmic rays by the use of the other isotopic/elemental ratios.

Finally, the region of ^{11}B/^{7}Li ratio of the cosmic rays is presented in Fig. 9.3 together with ^{11}B/^{7}Li-^{12}C/^{13}C diagram of the 20 $M_{\odot}$ supernova (Fig. 8.9(b) on page 165). Thick dash-dotted line denotes the ^{11}B/^{7}Li ratio of the galactic cosmic rays and a region with oblique lines shows the region of the low-energy cosmic rays. The variety of the ^{11}B/^{7}Li ratios of the low-energy cosmic rays is about two orders of magnitude. On the other hand, the variety of the ^{11}B/^{7}Li ratios of the supernova is more than four orders of magnitude. The variety of the ^{11}B/^{7}Li ratios of the supernova is small compared with those of the isotopic/elemental ratios of the other X-elements produced in the supernova (the variety

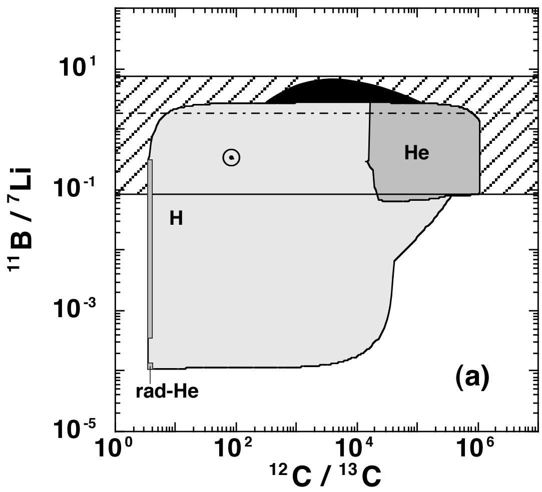

Fig. 9.3. The number ratio of $^{11}B/^{7}Li$ versus $^{12}C/^{13}C$ of the galactic cosmic rays (a thick dash-dotted line) and of the low-energy cosmic rays (a region with oblique lines) together of the 20 $M_{\odot}$ supernova (see Fig. 8.9(b)).

of the other ratios are mainly restricted by the detection limit). Despite small variety of the $^{11}B/^{7}Li$ ratios of the supernova compared with those of the elemental ratios of the other X-elements, the variety of the $^{11}B/^{7}Li$ ratio is still much larger than that of the cosmic rays. Thus, this diagram, $^{11}B/^{7}Li$-$^{12}C/^{13}C$ ratios is still useful for distinguishing presolar grains originated from supernovae.

10. Conclusions and Discussion

We studied explosive nucleosynthesis of the light elements in the He-layer and the H-rich envelope of type II supernovae, by changing parameters expected to affect supernova nucleosynthesis such as the model of the neutrino emission, the initial chemical compositions, the nuclear reprocessing after the mixing, and the mass of a progenitor. We evaluated the varieties of the abundances and the isotopic/elemental ratios of the light elements produced in the supernovae and made diagrams between two isotopic/elemental ratios. Our results are summarized as follows:

1. The amounts of ^{6}Li and ^{9}Be produced in supernovae are very small. The ratios of ^{6}Li/^{7}Li and ^{9}Be/^{7}Li are smaller than 4×10^{-5} and 4×10^{-3}, respectively when the abundances of ^{6}Li and ^{9}Be are beyond the detection limit (i.e., the number ratio to ^{16}O is larger than 1×10^{-9}). Except the ^{9}Be/^{7}Li ratio in the radiative He-layer of a 15 $M_{\odot}$ supernova, the ^{9}Be/^{7}Li ratio is smaller than 2×10^{-4}.

2. The other X-elements are produced appreciably in the He-layer and the inner H-rich envelope (except ^{10}B) of supernovae. Their abundances vary over several orders of magnitude with the internal mass coordinate and by changing the model of the neutrino emission. However, the ^{11}B/^{7}Li ratio in the convective He-layer is confined within a factor of 180.

3. The tightly bounded isotopes, ^{12}C and ^{16}O keep their initial abundances during the supernova explosions. Exceptional increase of the abundance of ^{16}O is seen near the inner He-layer boundary of a 15 $M_{\odot}$ supernova.

4. The other CNO-elements are synthesized in the convective He-layer by small fractions. Their amounts depend on the neutrino emission model but are confined

within a factor of 10 or so. In the radiative He-layer and the H-rich envelope their abundances are governed by the chemical composition in the presupernova stage in a sense that pre-existing elements survive as they were.

5. The X-elements suffer from the nuclear reprocessing after the mixing; the X-elements abundant in the He-component are decomposed by protons in the H-component through p-captures in the mixture. The amounts of ^{6}Li, ^{9}Be, and ^{10}B decrease steeply with a small mixing ratio ($x \lesssim 0.1$). When ^{7}Li and ^{11}B are decomposed, the final abundances of ^{7}Li and ^{11}B are determined by those of their isobars, ^{7}Be and ^{11}C, respectively, undecomposed in the mixture. In the case of the distant mixing, there occurs no nuclear reprocessing after the mixing. The nuclear reprocessing does not affect the abundances of the CNO-elements.

6. The difference of radial structure due to the stellar mass brings about the varieties of the light element abundances; in the case of 25 $M_{\odot}$ supernova which has a large radius of the C/He boundary, the influence of the neutrino emission on the light element production is small. In the case of 15 $M_{\odot}$ supernova which has a large radius of the He/H boundary, there occurs no nuclear reprocessing after the mixing.

On the basis of the above results of the numerical simulations, we constructed the diagrams of two isotopic/elemental ratios of the light elements in Sections 5.5, 6.5, 7.3, and 8.5. We also compared the probable regions of the isotopic/elemental ratios of the light elements in these diagrams with those at the surface of the RGB stars, the AGB stars, and the produced by the galactic cosmic rays in Section 9. Finally, in order to find a suitable manner for identifying supernova originated presolar grains, we propose conditions for the composition of the light elements in presolar grains originated from the supernovae:

(a) Presolar grains with ^{6}Li/^{7}Li less than 4×10^{-5} and ^{9}Be/^{7}Li less than 1×10^{-3} should be originated from supernovae.

(b) Presolar grains originated from supernovae should have the isotopic/elemental ratios inside the regions we predicted in diagrams of ^{11}B/^{7}Li-^{12}C/^{13}C, ^{14}N/^{15}N-^{12}C/^{13}C, and ^{16}O/^{17}O-^{12}C/^{13}C ratios.

Since Amari *et al.* (1992), supernova originated presolar grains have been identified. The isotopic ratios of the elements in the grains qualitatively match with those in supernovae: wide range of the ^{12}C/^{13}C ratios, the ^{15}N excesses, large ^{26}Al/^{27}Al ratios, the ^{28}Si excesses. Some of the grains show the ^{44}Ca excesses due to the decays of ^{44}Ti and the ^{49}Ti excesses due to the decays of ^{49}V. In this study we also obtained the above characteristics of the isotopic ratios of the light elements. The mixtures between the ^{12}C rich convective layer and the H-rich envelope where the ^{12}C/^{13}C ratio is about three showed the wide range of the ^{12}C/^{13}C ratios. The ^{15}N excesses were shown in the convective He-layer.

Quantitative comparison of the isotopic ratios of the supernova originated grains, which had been identified qualitatively, with those in supernova models were also performed in Travaglio *et al.* (1996) and (1999). Travaglio *et al.* (1999) evaluated the ranges of the isotopic ratios of C, N, O, Al, Si, Ca, and Ti in the mixtures of a 15 $M_\odot$ supernova using numerical results of the explosive nucleosynthesis of the supernova in Woosley and Weaver (1995). Travaglio *et al.* (1999) divided the supernova into several regions and they mixed the different ratios of the averaged compositions of the discrete regions. We will compare the range of the ^{14}N/^{15}N-^{12}C/^{13}C ratios of a 15 $M_\odot$ supernova in this study with that shown in Fig. 11 in Travaglio *et al.* (1999). We present the diagram of ^{14}N/^{15}N-^{12}C/^{13}C in Fig. 10.1. In this figure we consider two cases of the abundances of ^{14}N and ^{15}N in the radiative He-layer and the H-rich envelope: one case is that all of the abundances of N are incorporated into the mixture. The other case is that only

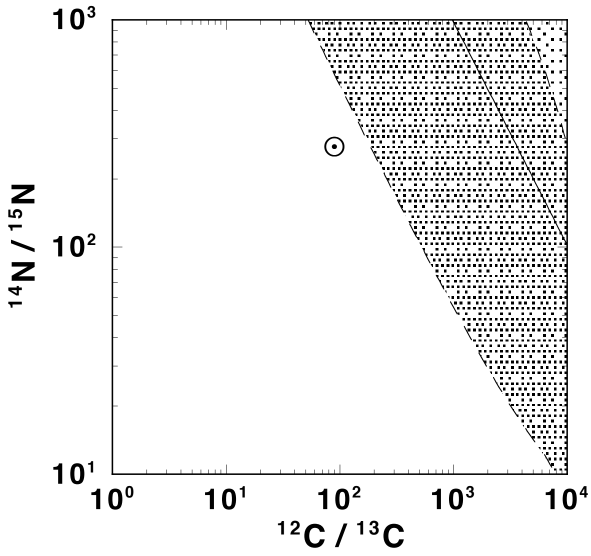

Fig. 10.1. The number ratios of $^{14}N/^{15}N$ versus $^{12}C/^{13}C$ in the case of the 15 $M_\odot$ supernova. A region with a light shade above solid line of is of the mixture. (Most of the region is overlapped with a dark shaded region.) The region is identical to a part of the region shown in Fig. 8.10(c). A region with a dark shade between two dashed lines is of the mixture but only 1/20 of the amounts of N in the radiative He-layer and the H-rich envelope are incorporated into the mixture. A mark $\odot$ shows the ratio of the solar-system composition.

1/20 of those are incorporated since, in most cases of Travaglio *et al.* (1999), 1/20 of all the nitrogen in the He/N layer was incorporated into mix. In Fig. 11 of Travaglio *et al.* (1999), the isotopic ratios in the cases of several parameter sets are shown in the form of lines. On the other hand, in Fig. 10.1 the isotopic ratios are shown in the form of a region; the region is obtained by considering not only the different mixing ratios but also the uncertainties of the neutrino emission model. All lines shown in Fig. 11(b) (in the case of C/O=3) of Travaglio *et al.* (1999) are inside the dark shaded region in Fig. 10.1. So, the diagram shows the ranges of the isotopic/elemental ratios of the light elements produced in supernovae more clearly than the diagrams of Travaglio *et al.* (1999). In order to clarify the regions of the isotopic/elemental ratios in supernovae, the diagram of the isotopic/elemental ratios obtained in this study are preferred.

Travaglio *et al.* (1999) considered the mixing of the inner O-rich regions in order to reproduce the isotopic ratios of the presolar grains qualitatively predicted to be supernova origin. So, hereafter, we roughly estimate how the varieties of the isotopic ratios change owing to the addition of the matter in the inner regions to the mixture between the He-layer and the H-rich envelope. Unfortunately, the light element compositions in the inner regions of supernova ejecta are not described in most of published manuscripts on supernova nucleosynthesis. We discuss the isotopic/elemental ratios of the light elements produced in the inner O-rich layer on the basis of our preliminary result of explosive nucleosynthesis of the light elements in the O/C- and O/Ne-layers and the light element compositions of Si/S-, O/Si-, O/Ne-, and O/C-layers of a 25 $M_\odot$ supernova tabulated in Meyer *et al.* (1995).

First, we will consider the X-element production in the inner O-rich layers. In the O/C- and O/Ne-layers, the final abundance of ^{11}B is of the orders of 1×10^{-7} or less. The ^{11}B/^{7}Li ratio is within a range from 10 to 20. In these layers, the final abundance of ^{11}B is determined by that of ^{11}C produced through ^{12}C$(\nu, \nu' n)^{11}$C because ^{11}B produced through ^{12}C$(\nu, \nu' p)^{11}$B is rapidly decomposed through ^{11}B$(p, \alpha\alpha)^{4}$He. In the O/C-layer, ^{7}Li is produced as ^{7}Be through ^{12}C$(\nu, \nu' np)^{10}$B$(p, \alpha)^{7}$Be and in the O/Ne-layer the final abundance of ^{7}Li is determined by those of ^{7}Li and ^{7}Be produced through the ν-process of ^{12}C. The obtained range of the ^{11}B/^{7}Li is roughly consistent with the ratios obtained from ^{12}C de-excitation branching ratios. Meyer *et al.* (1995) obtained that the ^{11}B/^{7}Li ratio in the O/C- and O/Ne-layers is larger than 100. However, the decomposition processes of ^{7}Li and ^{7}Be were not shown. Thus, the variety of the ^{11}B/^{7}Li does not become so wide even if the ^{11}B/^{7}Li ratio in the inner O-rich layer is considered. From our preliminary calculation, the $^{12}C/^{13}C$ ratio is of the orders of 1×10^4 in the O/C- and O/Ne-layers. So, the variety of the $^{11}B/^{7}Li$-$^{12}C/^{13}C$ ratio is not so changed even if the mixing of the inner O-rich layer is considered.

We showed in this study that the amounts of ^6Li and ^9Be is very small in the He-layer and the H-rich envelope. Since the abundances of ^6Li and ^9Be in the O/C- and O/Ne-layers are less than the lowest scale (1×10^{-13}) of Fig. 11 of Woosley and Weaver (1995), the abundances are of the orders of or less than 10^{-13}. From our preliminary result we obtained that the abundances of ^6Li and ^9Be are of the orders of or less than 10^{-12} in the O/C- and O/Ne-layers. Combined with the above two results, the abundances of ^6Li and ^9Be in the inner O-rich layer are probably less than 10^{-12}. The amount of ^{16}O in the inner region is of the orders of 0.1, so that ^6Li and ^9Be from the inner layers are not detectable in supernova originate presolar grains. Thus, the result that the abundances of ^6Li and ^9Be in supernovae are very small is not altered even if the mixing with the inner O-rich layer is considered.

We will next consider the $^{14}N/^{15}N$-$^{12}C/^{13}C$ ratios. The O-rich matter in the inner regions is rich in ^{15}N. From Meyer *et al.* (1995), the $^{12}C/^{13}C$ ratios in the Si/S- and O/Si-layers are 30 and 500, respectively, and the $^{14}N/^{15}N$ ratios are of the orders of 10^{-3} in these layers. In the O/Ne- and O/C-layers, the $^{12}C/^{13}C$ and $^{14}N/^{15}N$ ratios are inside the region of the He-layer obtained in this study. Since, however, the isotopic ratios in the Si/S- and O/Si-layers are outside the region we obtained, the region of the $^{14}N/^{15}N$-$^{12}C/^{13}C$ ratios in the mixture of the inner layers is different from the region we obtained. In Travaglio *et al.* (1999), the ratios of $^{14}N/^{15}N$-$^{12}C/^{13}C$ in the mixture under the condition of C/O > 1 were evaluated because of the reproduction of the isotopic ratios of the supernova originated graphite grains. So, we will also consider the region of the $^{14}N/^{15}N$-$^{12}C/^{13}C$ ratios under the condition of C/O > 1. The obtained result is that the region of the isotopic ratios of the mixture between the inner regions and the C-rich layers under the condition of C/O $>$ 1 is not so changed from our obtained region in Fig. 8.10(a) on page 166: the lower limit of the ^{14}N/^{15}N ratio where the ^{12}C/^{13}C ratio is $10^3 \sim 2 \times 10^4$ decreases by a factor of two or less and the lower limit of the ^{14}N/^{15}N ratio decreases to 2×10^{-3} where the ^{12}C/^{13}C ratio is in the region of the convective He-layer. Thus, we expect that the probable region of the ^{14}N/^{15}N-^{12}C/^{13}C ratios of the C-rich supernova ejecta is scarcely changed by the mixing of the inner layers.

Finally, we consider the ^{16}O/^{17}O ratios in the inner region. In the region inner than the He-layer, the ^{16}O/^{17}O ratio is larger than 10^6 (Meyer *et al.* 1995), so that the ^{16}O/^{17}O ratio becomes large by the mixing of small amount of the matter in the inner layers. By the mixing between the C-rich mixture and the O/C-layer, the maximum value of the ^{16}O/^{17}O ratio becomes 6×10^6 even under the condition of C/O $>$ 1. In practice, this mixing process is like the mixing between the C-rich material and pure ^{16}O. Thus, we should take account of the mixing of the inner O-rich region in the case of the diagrams of ^{16}O/^{17}O-^{12}C/^{13}C ratios.

We compare the region of ^{14}N/^{15}N-^{12}C/^{13}C and ^{16}O/^{17}O-^{12}C/^{13}C ratios in the diagrams presented in Sections 5, 6, and 8 with summarized data of the isotopic ratios in low density graphite grains tabulated in Table 3 in Travaglio *et al.* (1999). The summarized data are originally reported in Amari *et al.* (1995a), (1996a), (1996b), and Nittler *et al.* (1996) and unpublished data are included. In our present study, 35 low density graphite grains, of which ^{12}C/^{13}C, ^{14}N/^{15}N, and ^{16}O/^{17}O ratios are measured, are contained. The range of the ^{12}C/^{13}C, ^{14}N/^{15}N, and ^{16}O/^{17}O ratios among these grains are $6 \sim 1493$, $28 \sim 306$, and $655 \sim 11140$, respectively.

By the use of ^{14}N/^{15}N-^{12}C/^{13}C ratio diagrams, all grains except one have the isotopic ratios plotted outside the region obtained from our present study when the uncertainty of the initial chemical compositions is considered. Although our present study predicts that the ^{14}N/^{15}N ratio is larger than 1×10^3 in supernova originated grains with the

$^{12}C/^{13}C$ ratio smaller than 1500, the $^{14}N/^{15}N$ ratios in the low density graphite grains are smaller than about 300. In the case of $^{16}O/^{17}O$-$^{12}C/^{13}C$ ratio diagrams, the isotopic ratios of several grains are inside the region of supernovae we predicted. All of the grains have the $^{12}C/^{13}C$ ratios larger than the solar-system ratio of $^{12}C/^{13}C$ and their $^{16}O/^{17}O$ and $^{12}C/^{13}C$ ratios are inside the region of the ratios obtained from 15 $M_\odot$ to 20 $M_\odot$ supernovae considered the uncertainty of the initial chemical compositions. The other grains, most of which have the $^{12}C/^{13}C$ ratios smaller than the solar-system ratio of $^{12}C/^{13}C$, have the $^{16}O/^{17}O$ and $^{12}C/^{13}C$ ratios outside the region of supernova originated grains we predicted. Considering the mixing of the inner O-rich layer, we obtained that 31 grains show their isotopic ratios inside the predicted region. So, we should consider again the inner O-rich layer when we evaluate the variety of the $^{16}O/^{17}O$ ratio.

A trace of the radioactive decays of ^{44}Ti found in presolar grains is one of the strong evidences of supernova originated presolar grains (Nittler *et al.* 1996). This is because ^{44}Ti is predicted to be produced by the α-rich freeze-out in the innermost layers of massive stars (Woosley and Weaver 1995). However, such a strong evidence for the supernova originated grains have been found in only four graphite grains in eighty-nine grains (Nittler *et al.* 1996; Travaglio *et al.* 1999) and seven SiC grains (Amari *et al.* 1992; Hoppe *et al.* 1996; Nittler *et al.* 1996). So it is important to find the elements or the isotopic/elemental ratios which show characteristic behaviors of supernova nucleosynthesis other than ^{44}Ti. In this study we obtained that the isotopic/elemental ratios of the X-elements show the characteristic behaviors of the supernova nucleosynthesis. Until now, presolar grains originated from supernovae have not been identified by the analyses of the isotopic/elemental ratios of the X-elements. However, if presolar grains which contain the X-elements of which $^{11}B/^{7}Li$, $^{9}Be/^{7}Li$, and $^{6}Li/^{7}Li$ ratios show the ratios inside the region we predicted in this study, the presolar grains are strongly suggested to be supernova origin.

Acknowledgements

The author acknowledges Prof. Kiyoshi Nakazawa and Dr. Hiroyuki Emori for their great deal of valuable advice, continuing encouragement for a long time and critical reading of this manuscript. By the courtesy of the collaborators, Prof. K. Nakazawa and Dr. H. Emori, he was permitted to reprint "*Light Elements Synthesized in the He-layer and the H-rich Envelope of a Type II Supernova -Influence of the Adopted Neutrino Emission Model-*" (Yoshida, Emori, and Nakazawa 2000) and "*Light Elements Synthesized in the He-layer and the H-rich Envelope of a Type II Supernova, II -Influence of Initial Chemical Compositions-*" (Yoshida, Nakazawa, and Emori 1999) in this thesis. He express his gratitude to Kohichi Iwamoto for giving data of internal structure for 25 $M_\odot$ and 20 $M_\odot$ progenitor models and Ken'ichi Nomoto and Toshikazu Shigeyama for giving the data of internal structure for 16.2 $M_\odot$ and 15 $M_\odot$ progenitor models and helpful discussion. He is also indebted to Takafumi Hirata for useful advice from cosmochemical viewpoints. He also thanks Shigeru Ida and Hidekazu Tanaka for useful advice and Kei Kudo for her help in preparing the reprinted manuscript (Yoshida, Emori, and Nakazawa 2000). This work has been supported, in part, by Grand-in-Aid for General Scientific Research (B) (Nos. 07454114 and 09440089). The computation has been made by Cray C916 and NEC SX-5 at the Computer Center of Tokyo Institute of Technology.

References

Ajzenberg-Selove, F. 1987, Energy Levels of Light Nuclei A=18-20, *Nucl. Phys.*, **A475**, 1-198 (AJ87).

Ajzenberg-Selove, F. 1990, Energy Levels of Light Nuclei A=11-12, *Nucl. Phys.*, **A506**, 1-158 (AJ90).

Ajzenberg-Selove, F. 1991, Energy Levels of Light Nuclei A=13-15, *Nucl. Phys.*, **A523**, 1-196 (AJ91).

Amari, S. and E. Zinner 1997a, Presolar grains in meteorites: stardust in the laboratory, *Nucl. Phys.*, **A621**, 99c-112c.

Amari, S. and E. Zinner 1997b, Supernova grains from meteorites, pp.287-305 in *Astrophysical Implications of the Laboratory Study of Presolar Materials*, AIP Conference Proceedings 402.

Amari, S., E. Anders, A. Virag, and E. Zinner 1990, Interstellar graphite in meteorites, *Nature*, **345**, 238-240.

Amari, S., P. Hoppe, E. Zinner, and R. S. Lewis 1992, Interstellar SiC with unusual isotopic compositions: grains from a supernova?, *Astrophys. J.*, **394**, L43-L46.

Amari, S., E. Zinner, and R. S. Lewis 1994, C-, N-, O-, Si-, and Ti-isotopic ratios of low density graphite grains from Murchison indicate a supernova origin, *Lunar Planet. Sci.*, **XXV**, 27-28.

Amari, S., E. Zinner, and R. S. Lewis 1995a, Large ^{18}O excesses in circumstellar graphite grains from the Murchison meteorite: indication of a massive-star origin, *Astrophys. J.*, **447**, L147-L150.

Amari, S., E. Zinner, and R. S. Lewis 1995b, Interstellar graphite from the Murchison meteorite, pp.581-584 in *Nuclei in the Cosmos III*, AIP Conference Proceedings 327.

Amari, S., E. Zinner, and R. S. Lewis 1995c, Calcium-41 in circumstellar graphite from supernovae, *Meteoritics*, **30**, 480.

Amari, S., E. Zinner, and R. S. Lewis 1996a, ^{41}Ca in presolar graphite of supernova origin, *Astrophys. J.*, **470**, L101-104.

Amari, S., E. Zinner, and R. S. Lewis 1996b, A presolar graphite grain with unusual isotopic compositions, *Meteoritics & Plant. Sci. Suppl.*, **31**, A7-A8.

Anders, E. and N. Grevesse 1989, Abundances of the elements: meteoritic and solar, *Geochim. Cosmochim. Acta*, **53**, 197-214.

Andersen, J., B. Gustafsson, and D. L. Lambert 1984, The lithium isotope ratio in F and G stars, *Astron. Astrophys.*, **136**, 65-73.

Arnett, W. D. 1969, Explosive nucleosynthesis in stars, *Astrophys. J.*, **157**, 1369-1380.

Arnett, W. D., J. N. Bahcall, R. P. Kirshner, and S. E. Woosley 1989a, Supernova 1987A, *Annu. Rev. Astron. Astrophys.*, **27**, 629-700.

Arnett, D., B. Fryxell, and E. Müller 1989b, Instabilities and nonradial motion in SN 1987A, *Astrophys. J.*, **341**, L63-L66.

Audi, G. and A. H. Wapstra 1993, The 1993 atomic mass evaluation (I) Atomic mass table, *Nucl. Phys.*, **A565**, 1-65.

Audi, G. and A. H. Wapstra 1995, The 1995 update to the atomic mass evaluation, *Nucl. Phys.*, **A595**, 409-480.

Bahcall, J. N. 1989, *Neutrino Astrophysics*, pp.428-432, Cambridge University Press, Cambridge.

Beer, H., F. Voss, and R. R. Winters 1992, On the calculation of maxwellian-averaged capture cross sections, *Astrophys. J. Suppl.*, **80**, 403-424 (BV92).

Beer, H., M. Wiescher, F. Käppeler, J. Görres, and P. E. Koehler 1992, A measurement of the ^{14}C$(n,\gamma)^{15}$C cross section at a stellar temperature of $kT = 23.3$ keV, *Astrophys. J.*, **387**, 258-262 (BW92).

Bethe, H. A. 1990, Supernova mechanisms, *Rev. Modern Phys.*, **62**, 801-866.

Blackmon, J. C., A. E. Champagne, M. A. Hofstee, M. S. Smith, R. G. Downing, and G. P. Lamaze 1995, Measurement of the $^{17}O(p,\alpha)^{14}N$ cross section at stellar energies, *Phys. Rev. Lett.*, **74**, 2642-2645.

Bloemen, H., R. Wijnands, K. Bennett, R. Diehl, W. Hermsen, G. Lichti, D. Morris, J. Ryan, V. Schönfelder, A. W. Strong, B. N. Swanenburg, C. de Vies, and C. Winkler 1994, COMPTEL observations of the Orion complex: evidence for cosmic-ray induced gamma-ray lines, *Astron. Astrophys.*, **281**, L5-L8.

Boesgaard, A. M. and K. G. Budge 1989, Beryllium abundances in the lithium-deficient Hyades F stars, *Astrophys. J.*, **338**, 875-887.

Boesgaard, A. M., C. P. Deliyannis, A. Stephens, and D. L. Lambert 1998, Boron in lithium- and beryllium-deficient F stars, *Astrophys. J.*, **492**, 727-742.

Boothroyd, A. I. and I.-J. Sackmann 1999, The CNO isotopes: deep circulation in red giants and first and second dredge-up, *Astrophys. J.*, **510**, 232-250.

Buchmann, L. 1996, New stellar reaction rate for $^{12}C(\alpha,\gamma)^{16}O$, *Astrophys. J.*, **468**, L127-L130 (BU96).

Buchmann, L. 1997, Erratum, *Astrophys. J.*, **479**, L153.

Burrows, A. and J. M. Lattimer 1987, Neutrinos from SN 1987A, *Astrophys. J.*, **318**, L63-L68.

Caughlan, G. R. and W. A. Fowler 1988, Thermonuclear reaction rates V, *Atom. Data Nucl. Data Tables*, **40**, 283-334 (CF88).

Cayrel, R., M. Spite, F. Spite, E. Vangioni-Flam, M. Cassé, and J. Audouze 1999, New high S/N observations of the $^6Li/^7Li$ blend in HD84937 and two other metal-poor stars, *Astron. Astrophys.*, **343**, 923-932.

Chandrasekhar, S. 1981, *Hydrodynamic and Hydromagnetic Stability*, pp.428-436, Dover, New York.

Chevalier, R. A. 1976, The hydrodynamics of Type II supernovae, *Astrophys. J.*, **207**, 872-887.

Cooperstein, J. 1988, Neutrinos in supernovae, *Phys. Rep.*, **163**, 95-126.

Domogatsky, G. V., R. A. Eramzhyan, and D. K. Nadyozhin 1977, Neutrino contribution to nucleosynthesis, *Proc. Intl. Conf. Neutrino Phys. and Astrophy.*, 115-120.

Drotleff, H. W., A. Denker, H. Knee, M. Soiné, G. Wolf, J. W. Hammer, U. Greife, C. Rolfs, and H. P. Trautvetter 1993, Reaction rates of the s-process neutron sources ^{22}Ne$(\alpha, n)^{25}$Mg and ^{13}C$(\alpha, n)^{16}$O, *Astrophys. J.*, **414**, 735-739 (DD93).

Ebisuzaki, T., T. Shigeyama, and K. Nomoto 1989, Rayleigh-Taylor instability and mixing in SN 1987A, *Astrophys. J.*, **344**, L65-L68.

El Eid, M. F. 1994, CNO isotopes in red giants: theory versus observations, *Astron. Astrophys.*, **285**, 915-928.

Epstein, R. I., S. A. Colgate, and W. C. Haxton 1988, Neutrino-induced r-process nucleosynthesis, *Phys. Rev. Lett.*, **61**, 2038-2041.

Forestini, M. and C. Charbonnel 1997, Nucleosynthesis of light elements inside thermally pulsing AGB stars I. The case of intermediate-mass stars, *Astron. Astrophys. Suppl.*, **123**, 241-272.

Fryxell, B., E. Müller, and D. Arnett 1991, Instabilities and clumping in SN 1987A. I. Early evolution in two dimensions, *Astrophys. J.*, **367**, 619-634.

García, A., E. G. Adelberger, P. V. Magnus, D. M. Markoff, K. B. Swartz, M. S. Smith, K. I. Hahn, N. Bateman, and P. D. Parker 1991, The "missing" 3^+ state of ^{18}Ne and explosive ^{17}F(p, γ) burning, *Phys. Rev. C*, **43**, 2012-2019 (GA91).

Giesen, U., C. P. Browne, J. Görres, J. G. Ross, M. Wiescher, R. E. Azuma, J. D. King, J. B. Vise, and M. Buckby 1994, The influence of low-energy resonances on the reaction rate of ^{18}O$(\alpha, \gamma)^{22}$Ne, *Nucl. Phys.*, **A567**, 146-164.

Hachisu, I., T. Matsuda, K. Nomoto, and T. Shigeyama 1990, Nonlinear growth of Rayleigh-Taylor instabilities and mixing in SN 1987A, *Astrophys. J.*, **358**, L57-L61.

Hachisu, I., T. Matsuda, K. Nomoto, and T. Shigeyama 1991, Rayleigh-Taylor instabilities and mixing in the helium star model for type Ib/Ic supernovae, *Astrophys. J.*, **368**, L27-L30.

Hachisu, I., T. Matsuda, K. Nomoto, and T. Shigeyama 1992, Mixing in ejecta of supernovae. I. General properties of two-dimensional Rayleigh-Taylor instabilities and mixing width in ejecta of supernova, *Astrophys. J.*, **390**, 230-252.

Hachisu, I., T. Matsuda, K. Nomoto, and T. Shigeyama 1994, Mixing in ejecta of supernovae. II. Mixing width of 2D Rayleigh-Taylor instabilities in the helium star models for type Ib/Ic supernovae, *Astron. Astrophys. Suppl.*, **104**, 341-364.

Hashimoto, M. 1999, private communication.

Hashimoto, M., K. Nomoto, and T. Shigeyama 1989, Explosive nucleosynthesis in supernova 1987A, *Astron. Astrophys.*, **210**, L5-L8.

Hayashi, C., R. Hoshi, and D. Sugimoto 1962, Evolutions of the stars, *Prog. Theor. Phys. Suppl.*, **22**, 1-183.

Herant, M. and S. E. Woosley 1994, Postexplosion hydrodynamics of supernovae in red supergiants, *Astrophys. J.*, **425**, 814-828.

Hobbs, L. M. and J. A. Thorburn 1997, Lithium isotope ratios in halo stars. II., *Astrophys. J.*, **491**, 772-788.

Hoffman, R. D. and S. E. Woosley 1992, Tables of reaction rates for nucleosynthesis for charged particle, weak, and neutrino interactions ($Z < 45$), (unpublished; http://isotopes.lbl.gov/isotopes/hw92_1.html).

Hoppe, P., S. Amari, E. Zinner, and R. S. Lewis 1992, Large oxygen isotopic anomalies in graphite grains from the Murchison meteorite, *Meteoritics*, **27**, 235.

Hoppe, P., S. Amari, E. Zinner, T. Ireland, and R. S. Lewis 1994a, Carbon, nitrogen, magnesium, silicon, and titanium isotopic compositions of single interstellar silicon carbide grains from the Murchison carbonaceous chondrite, *Astrophys. J.*, **430**, 870-890.

Hoppe, P., B. Pungitore, P. Eberhardt, S. Amari, and R. S. Lewis 1994b, Ion imaging of small interstellar grains, *Meteoritics*, **29**, 474-475.

Hoppe, P., S. Amari, E. Zinner, and R. S. Lewis 1995a, Isotopic compositions of C, N, O, Mg, and Si, trace element abundances, and morphologies of single circumstellar graphite grains in four density fractions from the Murchison meteorite, *Geochim. Cosmochim. Acta*, **59**, 4029-4056.

Hoppe, P., R. Strebel, B. Pungitore, and P. Eberhardt 1995b, Interstellar SiC of type X: how many distinct stellar sources?, *Lunar and Plant. Sci.*, **XXVI**, 621-622.

Hoppe, P., R. Strebel, P. Eberhardt, S. Amari, and R. S. Lewis 1996, Type II supernova matter in a silicon carbide grain from the Murchison meteorite, *Science*, **272**, 1314-1316.

Hutcheon, I. D., G. R. Huss, A. J. Fahey, and G. J. Wasserburg 1994, Extreme ^{26}Mg and ^{17}O enrichments in an Orgueil corundum: identification of a presolar oxide grain, *Astrophys. J.*, **425**, L97-L100.

Igashira, M., Y. Nagai, K. Masuda, T. Ohsaki, and H. Kitazawa 1995, Measurement of the $^{16}\mathrm{O}(n,\gamma)^{17}\mathrm{O}$ reaction cross section at stellar energy and the critical role of nonresonant p-wave neutron capture, *Astrophys. J.*, **441**, L89-L92 (IN95).

Iwamoto, K. 1998, private communication.

Iwamoto, K., T. R. Young, N. Nakasato, T. Shigeyama, K. Nomoto, I. Hachisu, and H. Saio 1997, Instabilities and mixing in SN 1993J, *Astrophys. J.*, **477**, 865-875.

Kawano, L. H., W. A. Fowler, R. W. Kavanagh, and R. A. Malaney 1991, Signatures of inhomogeneity in the early universe, *Astrophys. J.*, **372**, 1-7 (KF91).

Kawano, L. H., W. A. Fowler, R. W. Kavanagh, and R. A. Malaney 1991, Erratum, *Astrophys. J.*, **382**, 358.

Käppeler, F., M. Wiescher, U. Giesen, J. Görres, I. Baraffe, M. El Eid, C. M. Raiteri, M. Busso, R. Gallino, M. Limongi, and A. Chieffi 1994, Reaction rates for $^{18}O(\alpha,\gamma)^{22}Ne$, $^{22}Ne(\alpha,\gamma)^{26}Mg$, and $^{22}Ne(\alpha,n)^{25}Mg$ in stellar helium burning and s-process nucleosynthesis in massive stars, *Astrophys. J.*, **437**, 396-409 (KW94).

Kikuchi, T., Y. Nagai, T. S. Suzuki, T. Shima, T. Kii, M. Igashira, A. Mengoni, and T. Otsuka 1998, Nonresonant direct p- and d-wave neutron capture by ^{12}C, *Phys. Rev. C*, **57**, 2724-2730 (KN98).

Koehler, P. E. and S. M. Graff 1991, $^{17}O(n,\alpha)^{14}C$ cross section from 25 meV to approximately 1 MeV, *Phys. Rev. C*, **44**, 2788-2793 (KG91).

Kunz, R., S. Barth, A. Denker, H. W. Drotleff, J. W. Hammer, H. Knee, and A. Meyer 1996, Determination of $^{9}Be(\alpha,n)^{12}C$ reaction rate, *Phys. Rev. C*, **53**, 2486-2495 (KB96).

Lamb S. A., I. Iben, Jr., and W. M. Howard 1976, On the evolution of massive stars through the core carbon-burning phase, *Astrophys. J.*, **207**, 209-232.

Landré, V., N. Prantzos, P. Aguer, G. Bogaert, A. Lefebvre, and J. P. Thibaud 1990, Revised reaction rates for the H-burning of ^{17}O and the oxygen isotopic abundances in red giants, *Astron. Astrophys*, **240**, 85-92 (LA90).

Lattimer, J. M. and A. Yahil 1989, Analysis of the neutrino events from supernova 1987A, *Astrophys. J.*, **340**, 426-434.

Lattimer, J. M., D. N. Schramm, and L. Grossman 1978, Condensation in supernova ejecta and isotopic anomalies in meteorites, *Astrophys. J.*, **219**, 230-249.

Lemke, M., D. L. Lambert, and B. Edvardsson 1993, The boron abundance of Procyon, *Pub. Astron. Soc. Pacific*, **105**, 468-475.

Lemoine, M, D. N. Schramm, J. W. Truran, and C. J. Copi 1997, On the significance of population II ^{6}Li abundances, *Astrophys. J.*, **478**, 554-562.

Malaney, R. A. and W. A. Fowler 1989, On nuclear reactions and ^{9}Be production in inhomogeneous cosmologies, *Astrophys. J.*, **345**, L5-L8 (MF89).

Mckeegan, K. D., R. M. Walker, and E. Zinner 1985, Ion microprobe isotopic measurements of individual interplanetary dust particles, *Geochim. Cosmochim. Acta*, **49**, 1971-1987.

Meissner, J., H. Schatz, J. Görres, H. Herndl, M. Wiescher, H. Beer, and F. Käppeler 1996, Neutron capture cross section of ^{18}O and its astrophysical implications, *Phys. Rev. C*, **53**, 459-468 (MS96a).

Meissner, J., H. Schatz, H. Herndl, M. Wiescher, H. Beer, and F. Käppeler 1996, Neutron capture cross section of ^{15}N at stellar energies, *Phys. Rev. C*, **53**, 977-981 (MS96b).

Meneguzzi, M., J. Audouze, and H. Reeves 1971, The production of the elements Li, Be, B by galactic cosmic rays in space and its relation with stellar observations, *Astron. Astrophys.*, **15**, 337-359.

Meyer, B. S., T. A. Weaver, and S. E. Woosley 1995. Isotopic source table for a 25 $M_\odot$ supernova, *Meteoritics*, **30**, 325-334.

Nagai, Y., M. Igashira, N. Mukai, T. Ohsaki, F. Uesawa, K. Takeda, T. Ando, H. Kitazawa, S. Kubono, and T. Fukuda 1991, Capture rate of the ^{7}Li$(n,\gamma)^8$Li reaction by prompt gamma-ray detection, *Astrophys. J.*, **381**, 444-448 (NI91).

Nittler, L. R., S. Amari, R. M. Walker, E. K. Zinner, and R. S. Lewis 1993, Identification of exotic SiC grains from the Murchison meteorite by ion imaging, *Meteorites*, **28**, 413.

Nittler, L. R., P. Hoppe, C. M. O.'D. Alexander, S. Amari, P. Eberhardt, X. Gao, R. S. Lewis, R. Strebel, R. M. Walker, and E. Zinner 1995, Silicon nitride from supernovae, *Astrophys. J.*, **453**, L25-L28.

Nittler, L. R., S. Amari, E. Zinner, S. E. Woosley, and R. S. Lewis 1996, Extinct ^{44}Ti in presolar graphite and SiC: proof of a supernova origin, *Astrophys. J.*, **462**, L31-34.

Nittler, L. R., C. M. O.'D. Alexander, J. Wang, and X. Gao 1998, Meteoritic oxide grain from supernova found, *Nature*, **393**, 222.

Nomoto, K. and M. Hashimoto 1988, Presupernova evolution of massive stars, *Phys. Rep.*, **163**, 13-36.

Nomoto, K., T. Suzuki, T. Shigeyama, S. Kumagai, H. Yamaoka, and H. Saio 1993, A type IIb model for supernova 1993J, *Nature*, **364**, 507-509.

Ramaty, R., B. Kozlovsky, and R. I. Lingenfelter 1996, Light isotopes, extinct radioisotopes, and gamma-ray lines from low-energy cosmic-ray interactions, *Astrophys. J.*, **456**, 525-540.

Rauscher, T., J. H. Applegate, J. J. Cowan, F.-K. Thielemann, and M. Wiescher 1994, Production of heavy elements in inhomogeneous cosmologies, *Astrophys. J.*, **429**, 499-530 (RA94).

Rauscher, T. and G. Raimann 1996, Astrophysical reaction rates for ^{10}B$(p, \alpha)^{7}$Be and ^{11}B$(p, \alpha)^{8}$Be from a direct model, *Phys. Rev. C*, **53**, 2496-2504 (RR96).

Rebolo, R., L. Crivellari, F. Castelli, B. Foing, and J. E. Beckman 1986, Lithium abundances and ^{7}Li/^{6}Li ratios in late-type population I field dwarfs, *Astron. Astrophys.*, **166**, 195-203.

Reeves, H. 1994, On the origin of the light elements ($Z < 6$), *Rev. Modern Phys.*, **66**, 193-216.

Reeves, H., W. A. Fowler, and F. Hoyle 1970, Galactic cosmic ray origin of Li, Be, and B in stars, *Nature*, **226**, 727-729.

Rolfs, C. E. and W. S. Rodney 1988, *Cauldrons in the Cosmos*, pp.376-379, Chicago Press, Chicago and London.

Saio, H., K. Nomoto, and M. Kato 1988, Nitrogen and helium enhancement in the progenitor of supernova 1987A, *Nature*, **334**, 508-510.

Sato, H. 1967, Formation of Li, Be, B in the expanding hot universe, *Prog. Theor. Phys.*, **38**, 1083-1094 (SA67).

Sedov, L. I. 1959, *Similarity and Dimensional Methods in Mechanics*, pp.260-270, Academic Press, New York and London.

Shigeyama, T. and K. Nomoto 1990, Theoretical light curve of SN 1987A and mixing of hydrogen and nickel in the ejecta, *Astrophys. J.*, **360**, 242-256.

Shigeyama, T., K. Nomoto, M. Hashimoto, and D. Sugimoto 1987, Light-curve models for supernova SN1987A in the Large Magellanic Cloud, *Nature*, **328**, 320-323.

Shigeyama, T., K. Nomoto, and M. Hashimoto 1988, Hydrodynamical models and the light curve of Supernova 1987A in the Large Magellanic Cloud, *Astron. Astrophys.*, **196**, 141-151.

Smith, M. S., L. H. Kawano, and R. A. Malaney 1993. Experimental, computational, and observational analysis of primordial nucleosynthesis, *Astrophys. J. Suppl.*, **85**, 219-247 (SK93).

Smith, V. V., D. L. Lambert, and P. E. Nissen 1998, Isotopic lithium abundances in nine halo stars, *Astrophys. J.*, **506**, 405-423.

Soderblom, D. R., B. F. Jones, S. Balachandran, J. R. Stauffer, D. K. Duncan, S. B, Fedele, and J. D. Hudon 1993, The evolution of the lithium abundances of solar-type stars. III. The pleiades, *Astron. J.*, **106**, 1059-1086.

Swart, P. K., M. M. Grady, C. T. Pillinger, R. S. Lewis, and E. Anders 1983, Interstellar carbon in meteorites, *Science*, **220**, 406-410.

Thielemann, F.-K., M. Hashimoto, and K. Nomoto 1990, Explosive nucleosynthesis in SN 1987A. II. Composition, radioactivities, and the neutron star mass, *Astrophys. J.*, **349**, 222-240.

Thielemann, F.-K., K. Nomoto, and M. Hashimoto 1996, Core-collapse supernovae and their ejecta, *Astrophys. J.*, **460**, 408-436.

Thielemann, F.-K., M. Wiescher, and Ch. Freiburghaus 1991, Stellar reaction rates, (unpublished; http://ie.lbl.gov/astro/friedel.html) (TH91).

Thomas, D., D. N. Schramm, K. A. Olive, and B. D. Fields 1993, Primordial nucleosynthesis and the abundances of beryllium and boron, *Astrophys. J.*, **406**, 569-579 (TS93).

Timmes, F. X., S. E. Woosley, and T. A. Weaver 1995, Galactic chemical evolution: hydrogen through zinc, *Astrophys. J. Suppl.*, **98**, 617-658.

Travaglio, C., R. Gallino, S. Amari, E. Zinner, and S. E. Woosley 1996, Isotopic compositions of meteoritic graphite grains and supernova mixing, pp. 469-474 in *Stellar Evolution: What should Be Done*, 32^{nd} Liège Int. Astrophys. Coll., Liège.

Travaglio, C., R. Gallino, S. Amari, E. Zinner, S. E. Woosley, and R. S. Lewis 1999, Low-density graphite grains and mixing in type II supernovae, *Astrophys. J.*, **510**, 325-354.

Utku, S., J. G. Ross, N. P. T. Bateman, D. W. Bardayan, A. A. Chen, J. Görres, A. J. Howard, C. Iliadis, P. D. Parker, M. S. Smith, R. B. Vogelaar, M. Wiescher, and K. Yildiz 1998, Breakout from the hot CNO cycle: the ^{18}F(p,γ) vs ^{18}F(p,α) branching ratio, *Phys. Rev. C*, **57**, 2731-2739 (UR98).

Wagoner, R. V. 1969, Synthesis of the elements within objects exploding from very high temperatures, *Astrophys. J.*, **162**, 247-295 (WA69).

Wagoner, R. V. 1973, Big-Bang nucleosynthesis revisited, *Astrophys. J.*, **179**, 343-360 (WA73).

Wagoner, R. V., W. A. Fowler, and F. Hoyle 1967, On the synthesis of elements at very high temperatures, *Astrophys. J.*, **148**, 3-49 (WF67).

Walker, T. P., G. J. Mathews, and V. E. Viola 1985, Astrophysical production rates for Li, Be, and B isotopes from energetic ^{1}H and ^{4}He reactions with HeCNO nuclei, *Astrophys. J.*, **299**, 745-751.

Walker, F. W., J. R. Parrington, and F. Feiner 1989, *Nuclides and Isotopes*, GE Nuclear Energy (WP89).

Wang, T. R., R. B. Vogelaar, and R. W. Kavanagh 1991, ^{11}B+α reaction rates and primordial nucleosynthesis, *Phys. Rev. C*, **43**, 883-896 (WV91).

Wang, T. R., R. B. Vogelaar, and R. W. Kavanagh 1991, Erratum, *Phys. Rev. C*, **44**, 1226.

Weaver, T. A. and S. E. Woosley 1980, Evolution and explosion of massive stars, *Ann. New York Acad. Sci.*, **336**, 335-357.

Weaver, T. A. and S. E. Woosley 1993, Nucleosynthesis in massive stars and the ^{12}C$(\alpha,\gamma)^{16}$O reaction rate, *Phys. Rep.*, **227**, 65-96.

Weaver, T. A., G. B. Zimmerman, and S. E. Woosley 1978, Presupernova evolution of massive stars, *Astrophys. J.*, **225**, 1021-1029.

Wiescher, M. and K.-U. Kettner 1982, Warm CNO nucleosynthesis as a possible enrichment mechanism for oxygen and fluorine isotopes, *Astrophys. J.*, **263**, 891-901 (WK82).

Wiescher, M., J. Görres, S. Graff, L. Buchmann, and F.-K. Thielemann 1989, The hot proton-proton chains in low-metallicity objects, *Astrophys. J.*, **343**, 352-364 (WG89).

Wiescher, M., V. Harms, J. Görres, F.-K. Thielemann, and L. J. Rybarcyk 1987, Alpha-burning of ^{14}O, *Astrophys. J.*, **316**, 162-171 (WH87).

Wolfs, F. L. H., S. J. Freedman, J. E. Nelson, M. S. Dewey, and G. L. Greene 1989, Measurement of the ^{3}He$(n,\gamma)^{4}$He cross section at thermal neutron energies, *Phys. Rev. Lett.*, **63**, 2721-2724 (WF89).

Woosley, S. E. 1986, Nucleosynthesis and stellar evolution, pp. 1-195 in *Nucleosynthesis and Chemical Evolution*, Observatoire de Genève.

Woosley, S. E. 1988, SN 1987A: After the peak, *Astrophys. J.*, **330**, 218-253.

Woosley, S. E. and W. C. Haxton 1988, Supernova neutrinos, neutral currents and the origin of fluorine, *Nature*, **334**, 45-47.

Woosley, S. E. and T. A. Weaver 1986, The physics of supernova explosions, *Annu. Rev. Astron. Astrophys.*, **24**, 205-253.

Woosley, S. E. and T. A. Weaver 1995, The evolution and explosion of massive stars. II. Explosive hydrodynamics and nucleosynthesis, *Astrophys. J. Suppl.*, **101**, 181-235.

Woosley, S. E., D. H. Hartmann, R. D. Hoffman, and W. C. Haxton 1990, The ν-process, *Astrophys. J.*, **356**, 272-301.

Woosley, S. E., R. D. Hoffman, F. X. Timmes, T. A. Weaver, and F.-K. Thielemann 1997, Nucleosynthesis in massive stars and supernovae, *Nuclear Physics*, **A621**, 445c-452c.

Woosley, S. E., P. A. Pinto, P. G. Martin, T. A. Weaver 1987, Supernova 1987A in the Large Magellanic Cloud - The explosion of AN approximately 20 solar mass star which has experienced mass loss?, *Astrophys. J.*, **318**, 664-673.

Yoshida, T., H. Emori, and K. Nakazawa 2000, Light elements synthesized in the He-layer and the H-rich envelope of a Type II supernova -Influence of the adopted neutrino emission model-, *Earth, Planets and Space*, in press.

Yoshida, T., K. Nakazawa, and H. Emori 1999, Light elements synthesized in the He-layer and the H-rich envelope of a Type II supernova -Influence of initial chemical compositions-, *submitted to Earth, Planets and Space.*

Zinner, E. 1995, Interstellar grains from primitive meteorites: new constraints of nucleosynthesis theory and stellar evolution models, pp.567-579 in *Nuclei in the Cosmos III*, AIP Conference Proceedings 327.

Zinner, E. 1998, Stellar nucleosynthesis and the isotopic composition of presolar grains from primitive meteorites, *Annu. Rev. Earth Planet. Sci.*, **26**, 147-188.

Zinner, E. and S. Amari 1995, The isotopic composition of interstellar graphite from the Murchison meteorite: evidence for supernova mixing, *Lunar and Plant. Sci.*, **XXVI**, 1561-1562.

Zinner, E., M. Tang, and E. Anders 1989, Interstellar SiC in the Murchison and Murray meteorites: isotopic composition of Ne, Xe, Si, C, and N, *Geochim. Cosmochim. Acta*, **53**, 3273-3290.

Zinner E., S. Amari, and R. S. Lewis 1991, Silicon carbide from a supernova?, *Meteoritics*, **26**, 413.

Appendix
Nuclear Reaction Tables

In the following tables we show nuclear reactions, β-decays, and electron captures relevant to the species included in our nuclear reaction network. The Q-value and the reference from which the reaction rate is taken are also listed. Tables are compiled by the following way:

Table A.1. (n, γ) reactions

Table A.2. (p, γ) reactions

Table A.3. (α, γ) reactions

Table A.4. (α, n) reactions and their inverse reactions

Table A.5. (α, p) reactions and their inverse reactions

Table A.6. (n, p) reactions and their inverse reactions

Table A.7. Reactions including deuteron (d) and triton (t)

Table A.8. The other reactions

Table A.9. β-decays and electron captures

Table A.10. The ν-process reactions

In Table A.9, ${}^1\mathrm{n}(\beta^-)^1\mathrm{H}^*$ includes ${}^1\mathrm{n}(\beta^-)^1\mathrm{H}$, ${}^1\mathrm{n}(e^+, \bar{\nu}_e)^1\mathrm{H}$, and ${}^1\mathrm{n}(\nu_e, e^-)^1\mathrm{H}$ reactions. ${}^1\mathrm{H}(e^-, \nu_e)^1\mathrm{n}^{**}$ includes ${}^1\mathrm{H}(e^-, \nu_e)^1\mathrm{n}$, ${}^1\mathrm{H}(e^+, \bar{\nu}_e)^1\mathrm{H}$, and ${}^1\mathrm{H}{+}(e^- \bar{\nu}_e,)^1\mathrm{n}$ reactions. Note that reactions, marked by $*$ in the reference column, are omitted in our present simulations. The Q-values shown in Tables A.1 to A.9 are those evaluated on the basis of the atomic masses listed by Audi and Wapstra (1993).

Table A.1. (n, γ) reactions.

	reaction	Q(MeV)	Ref.		reaction	Q(MeV)	Ref.
1	^{1}H $(n,\gamma)^{2}$H	2.225	SK93	19	^{15}N $(n,\gamma)^{16}$N	2.491	MS96b
2	^{2}H $(n,\gamma)^{3}$H	6.257	WA69	20	^{16}N $(n,\gamma)^{17}$N	5.884	RA94
3	^{3}He $(n,\gamma)^{4}$He	20.578	WF89	21	^{13}O $(n,\gamma)^{14}$O	23.176	*
4	^{6}Li $(n,\gamma)^{7}$Li	7.250	MF89	22	^{14}O $(n,\gamma)^{15}$O	13.222	*
5	^{7}Li $(n,\gamma)^{8}$Li	2.034	NI91	23	^{15}O $(n,\gamma)^{16}$O	15.664	*
6	^{8}Li $(n,\gamma)^{9}$Li	4.063	RA94	24	^{16}O $(n,\gamma)^{17}$O	4.143	IN95
7	^{9}Be $(n,\gamma)^{10}$Be	6.812	RA94	25	^{17}O $(n,\gamma)^{18}$O	8.044	KG91
8	^{10}Be $(n,\gamma)^{11}$Be	0.504	RA94	26	^{18}O $(n,\gamma)^{19}$O	3.957	MS96a
9	^{10}B $(n,\gamma)^{11}$B	11.454	WA69	27	^{17}F $(n,\gamma)^{18}$F	9.150	TH91
10	^{11}B $(n,\gamma)^{12}$B	3.370	WV91	28	^{18}F $(n,\gamma)^{19}$F	10.432	TH91
11	^{11}C $(n,\gamma)^{12}$C	18.722	RA94	29	^{19}F $(n,\gamma)^{20}$F	6.601	WA69
12	^{12}C $(n,\gamma)^{13}$C	4.946	KN98	30	^{18}Ne $(n,\gamma)^{19}$Ne	11.639	TH91
13	^{13}C $(n,\gamma)^{14}$C	8.176	WA69	31	^{19}Ne $(n,\gamma)^{20}$Ne	16.864	TH91
14	^{14}C $(n,\gamma)^{15}$C	1.218	BW92	32	^{20}Ne $(n,\gamma)^{21}$Ne	6.761	BV92
15	^{15}C $(n,\gamma)^{16}$C	4.250	RA94	33	^{21}Ne $(n,\gamma)^{22}$Ne	10.364	WA69
16	^{12}N $(n,\gamma)^{13}$N	20.064	*	34	^{21}Na $(n,\gamma)^{22}$Na	11.069	TH91
17	^{13}N $(n,\gamma)^{14}$N	10.553	RA94	35	^{22}Na $(n,\gamma)^{23}$Na	12.419	TH91
18	^{14}N $(n,\gamma)^{15}$N	10.833	BV92				

Table A.2. (p,γ) reactions.

	reaction	Q(MeV)	Ref.		reaction	Q(MeV)	Ref.
1	^{2}H $(p,\gamma)^{3}$He	5.493	CF88	20	^{16}C $(p,\gamma)^{17}$N	13.112	*
2	^{3}H $(p,\gamma)^{4}$He	19.814	CF88	21	^{12}N $(p,\gamma)^{13}$O	1.516	WG89
3	^{6}He $(p,\gamma)^{7}$Be	9.975	*	22	^{13}N $(p,\gamma)^{14}$O	4.628	CF88
4	^{6}Li $(p,\gamma)^{7}$Be	5.606	CF88	23	^{14}N $(p,\gamma)^{15}$O	7.297	CF88
5	^{8}Li $(p,\gamma)^{9}$Be	16.886	*	24	^{15}N $(p,\gamma)^{16}$O	12.127	CF88
6	^{9}Li $(p,\gamma)^{10}$Be	19.636	*	25	^{16}N $(p,\gamma)^{17}$O	13.780	*
7	^{7}Be $(p,\gamma)^{8}$B	0.137	CF88	26	^{17}N $(p,\gamma)^{18}$O	15.942	CF88
8	^{9}Be $(p,\gamma)^{10}$B	6.586	CF88	27	^{16}O $(p,\gamma)^{17}$F	0.600	CF88
9	^{10}Be $(p,\gamma)^{11}$B	11.228	TS93	28	^{17}O $(p,\gamma)^{18}$F	5.607	LA90
10	^{11}Be $(p,\gamma)^{12}$B	14.094	*	29	^{18}O $(p,\gamma)^{19}$F	7.994	CF88
11	^{8}B $(p,\gamma)^{9}$C	1.296	WG89	30	^{19}O $(p,\gamma)^{20}$F	10.639	*
12	^{10}B $(p,\gamma)^{11}$C	8.690	CF88	31	^{17}F $(p,\gamma)^{18}$Ne	3.922	GA91
13	^{11}B $(p,\gamma)^{12}$C	15.957	CF88	32	^{18}F $(p,\gamma)^{19}$Ne	6.411	UR98
14	^{12}B $(p,\gamma)^{13}$C	17.533	*	33	^{19}F $(p,\gamma)^{20}$Ne	12.843	CF88
15	^{11}C $(p,\gamma)^{12}$N	0.601	WG89	34	^{20}F $(p,\gamma)^{21}$Ne	13.003	*
16	^{12}C $(p,\gamma)^{13}$N	1.944	CF88	35	^{20}Ne $(p,\gamma)^{21}$Na	2.431	CF88
17	^{13}C $(p,\gamma)^{14}$N	7.551	CF88	36	^{21}Ne $(p,\gamma)^{22}$Na	6.739	CF88
18	^{14}C $(p,\gamma)^{15}$N	10.207	KF91	37	^{22}Ne $(p,\gamma)^{23}$Na	8.794	CF88
19	^{15}C $(p,\gamma)^{16}$N	11.480	*	38	^{22}Na $(p,\gamma)^{23}$Mg	7.580	CF88

Table A.3. (α, γ) reactions.

	reaction	Q(MeV)	Ref.		reaction	Q(MeV)	Ref.
1	^{2}H $(\alpha,\gamma)^{6}$Li	1.474	CF88	18	^{12}C $(\alpha,\gamma)^{16}$O	7.162	BU96
2	^{3}H $(\alpha,\gamma)^{7}$Li	2.467	CF88	19	^{13}C $(\alpha,\gamma)^{17}$O	6.359	*
3	^{3}He $(\alpha,\gamma)^{7}$Be	1.587	CF88	20	^{14}C $(\alpha,\gamma)^{18}$O	6.227	CF88
4	^{6}He $(\alpha,\gamma)^{10}$Be	7.412	*	21	^{15}C $(\alpha,\gamma)^{19}$O	8.966	*
5	^{6}Li $(\alpha,\gamma)^{10}$B	4.460	CF88	22	^{13}N $(\alpha,\gamma)^{17}$F	5.819	*
6	^{7}Li $(\alpha,\gamma)^{11}$B	8.665	CF88	23	^{14}N $(\alpha,\gamma)^{18}$F	4.415	CF88
7	^{8}Li $(\alpha,\gamma)^{12}$B	10.001	TH91	24	^{15}N $(\alpha,\gamma)^{19}$F	4.014	CF88
8	^{7}Be $(\alpha,\gamma)^{11}$C	7.544	CF88	25	^{16}N $(\alpha,\gamma)^{20}$F	8.124	*
9	^{9}Be $(\alpha,\gamma)^{13}$C	10.648	*	26	^{14}O $(\alpha,\gamma)^{18}$Ne	5.112	WH87
10	^{10}Be $(\alpha,\gamma)^{14}$C	12.012	TH91	27	^{15}O $(\alpha,\gamma)^{19}$Ne	3.529	CF88
11	^{11}Be $(\alpha,\gamma)^{15}$C	12.726	*	28	^{16}O $(\alpha,\gamma)^{20}$Ne	4.730	CF88
12	^{8}B $(\alpha,\gamma)^{12}$N	8.008	*	29	^{17}O $(\alpha,\gamma)^{21}$Ne	7.348	CF88
13	^{10}B $(\alpha,\gamma)^{14}$N	11.612	*	30	^{18}O $(\alpha,\gamma)^{22}$Ne	9.667	KW94
14	^{11}B $(\alpha,\gamma)^{15}$N	10.991	WV91	31	^{17}F $(\alpha,\gamma)^{21}$Na	6.561	*
15	^{12}B $(\alpha,\gamma)^{16}$N	10.112	*	32	^{18}F $(\alpha,\gamma)^{22}$Na	8.480	*
16	^{9}C $(\alpha,\gamma)^{13}$O	8.228	*	33	^{19}F $(\alpha,\gamma)^{23}$Na	10.467	*
17	^{11}C $(\alpha,\gamma)^{15}$O	10.220	*	34	^{19}Ne $(\alpha,\gamma)^{23}$Mg	9.649	TH91

Table A.4. (α, n) and (n, α) reactions.

	reaction	Q(MeV)	Ref.		reaction	Q(MeV)	Ref.
1	^{6}He $(\alpha, n)^{9}$Be	0.600	*	1	^{6}Li $(n, \alpha)^{3}$H	4.783	CF88
2	^{8}Li $(\alpha, n)^{11}$B	6.629	TS93	2	^{7}Be $(n, \alpha)^{4}$He	18.991	WA69
3	^{9}Li $(\alpha, n)^{12}$B	5.938	TH91	3	^{10}B $(n, \alpha)^{7}$Li	2.790	CF88
4	^{9}Be $(\alpha, n)^{12}$C	5.701	KB96	4	^{14}O $(n, \alpha)^{11}$C	3.003	*
5	^{10}Be $(\alpha, n)^{13}$C	3.835	WA69	5	^{15}O $(n, \alpha)^{12}$C	8.502	CF88
6	^{11}Be $(\alpha, n)^{14}$C	11.508	TS93	6	^{17}O $(n, \alpha)^{14}$C	1.818	KG91
7	^{10}B $(\alpha, n)^{13}$N	1.058	CF88	7	^{17}F $(n, \alpha)^{14}$N	4.735	CF88
8	^{11}B $(\alpha, n)^{14}$N	0.158	WV91	8	^{18}F $(n, \alpha)^{15}$N	6.420	CF88
9	^{12}B $(\alpha, n)^{15}$N	7.621	WA69	9	^{18}Ne $(n, \alpha)^{15}$O	8.111	TH91
10	^{13}C $(\alpha, n)^{16}$O	2.215	DD93	10	^{19}Ne $(n, \alpha)^{16}$O	12.135	WA69
11	^{15}C $(\alpha, n)^{18}$O	5.009	WA69	11	^{21}Ne $(n, \alpha)^{18}$O	0.698	CF88
12	^{16}C $(\alpha, n)^{19}$O	4.714	*	12	^{22}Ne $(n, \alpha)^{19}$F	1.952	CF88
13	^{16}N $(\alpha, n)^{19}$F	1.523	WA69	13	^{21}Na $(n, \alpha)^{18}$F	2.589	TH91
14	^{17}N $(\alpha, n)^{20}$F	2.242	*	14	^{23}Mg $(n, \alpha)^{20}$Ne	7.216	*
15	^{17}O $(\alpha, n)^{20}$Ne	0.587	CF88				
16	^{19}O $(\alpha, n)^{22}$Ne	5.709	WA69				
17	^{20}F $(\alpha, n)^{23}$Na	3.865	WA69				

Table A.5. (α, p) and (p, α) reactions.

	reaction	Q(MeV)	Ref.		reaction	Q(MeV)	Ref.
1	^{8}B $(\alpha,p)^{11}$C	7.406	WG89	1	^{6}He $(p,\alpha)^{3}$H	7.509	*
2	^{10}B $(\alpha,p)^{13}$C	4.061	WA69	2	^{6}Li $(p,\alpha)^{3}$He	4.019	CF88
3	^{11}B $(\alpha,p)^{14}$C	0.784	WV91	3	^{7}Li $(p,\alpha)^{4}$He	17.347	CF88
4	^{9}C $(\alpha,p)^{12}$N	6.711	WG89	4	^{9}Li $(p,\alpha)^{6}$He	12.224	*
5	^{11}C $(\alpha,p)^{14}$N	2.922	WA69	5	^{9}Be $(p,\alpha)^{6}$Li	2.126	CF88
6	^{12}N $(\alpha,p)^{15}$O	9.619	WF67	6	^{10}Be $(p,\alpha)^{7}$Li	2.563	TS93
7	^{13}N $(\alpha,p)^{16}$O	5.218	TS93	7	^{11}Be $(p,\alpha)^{8}$Li	4.094	TS93
8	^{14}O $(\alpha,p)^{17}$F	1.190	CF88	8	^{10}B $(p,\alpha)^{7}$Be	1.146	RR96
9	^{17}F $(\alpha,p)^{20}$Ne	4.129	CF88	9	^{12}B $(p,\alpha)^{9}$Be	6.886	WA69
10	^{18}F $(\alpha,p)^{21}$Ne	1.741	WA69	10	^{15}C $(p,\alpha)^{12}$B	1.368	*
11	^{19}F $(\alpha,p)^{22}$Ne	1.672	CF88	11	^{15}N $(p,\alpha)^{12}$C	4.965	CF88
12	^{18}Ne $(\alpha,p)^{21}$Na	2.627	TH91	12	^{16}N $(p,\alpha)^{13}$C	7.421	WA69
13	^{19}Ne $(\alpha,p)^{22}$Na	2.069	TH91	13	^{17}O $(p,\alpha)^{14}$N	1.192	LA90
				14	^{18}O $(p,\alpha)^{15}$N	3.981	CF88
				15	^{19}O $(p,\alpha)^{16}$N	2.514	WA69
				16	^{18}F $(p,\alpha)^{15}$O	2.883	UR98
				17	^{19}F $(p,\alpha)^{16}$O	8.113	CF88
				18	^{20}F $(p,\alpha)^{17}$O	5.655	WA69
				19	^{23}Na $(p,\alpha)^{20}$Ne	2.377	CF88

Table A.6. (n,p) and (p,n) reactions.

	reaction	Q(MeV)	Ref.		reaction	Q(MeV)	Ref.
1	^{3}He $(n,p)^{3}$H	0.764	CF88	1	^{6}He $(p,n)^{6}$Li	2.726	*
2	^{7}Be $(n,p)^{7}$Li	1.644	CF88	2	^{9}Li $(p,n)^{9}$Be	12.824	*
3	^{10}B $(n,p)^{10}$Be	0.226	*	3	^{11}Be $(p,n)^{11}$B	10.724	TS93
4	^{11}C $(n,p)^{11}$B	2.764	CF88	4	^{12}B $(p,n)^{12}$C	12.586	CF88
5	^{12}N $(n,p)^{12}$C	18.120	TS93(E)	5	^{15}C $(p,n)^{15}$N	8.990	WA69
6	^{13}N $(n,p)^{13}$C	3.003	RA94	6	^{16}C $(p,n)^{16}$N	7.228	*
7	^{14}N $(n,p)^{14}$C	0.626	TS93	7	^{16}N $(p,n)^{16}$O	9.636	WA69
8	^{13}O $(n,p)^{13}$N	18.547	*	8	^{17}N $(p,n)^{17}$O	7.897	*
9	^{14}O $(n,p)^{14}$N	5.925	CF88	9	^{19}O $(p,n)^{19}$F	4.037	WA69
10	^{15}O $(n,p)^{15}$N	3.537	CF88	10	^{20}F $(p,n)^{20}$Ne	6.242	WA69
11	^{17}F $(n,p)^{17}$O	3.542	WA69				
12	^{18}F $(n,p)^{18}$O	2.439	WA69				
13	^{18}Ne $(n,p)^{18}$F	5.228	TH91				
14	^{19}Ne $(n,p)^{19}$F	4.021	CF88				
15	^{21}Na $(n,p)^{21}$Ne	4.330	TH91				
16	^{22}Na $(n,p)^{22}$Ne	3.625	CF88				
17	^{23}Mg $(n,p)^{23}$Na	4.839	CF88				

Table A.7. Reactions including d and t.

	reaction	Q(MeV)	Ref.		reaction	Q(MeV)	Ref.
1	^{2}H$(d,p)^{3}$H	4.033	CF88	10	^{8}Li $(p,d)^{7}$Li	1.012	TS93
2	^{2}H$(d,n)^{3}$He	3.269	CF88	11	^{8}Li $(d,n)^{9}$Be	14.662	TS93
3	^{2}H$(d,r)^{4}$He	23.847	CF88	12	^{9}Be $(d,n)^{10}$B	4.361	SA67
4	^{3}H $(d,n)^{4}$He	17.589	CF88	13	^{9}Be $(t,n)^{11}$B	9.558	TS93
5	^{3}He $(d,p)^{4}$He	18.353	CF88	14	^{10}B $(d,p)^{11}$B	9.230	SA67
6	^{3}He $(t,d)^{4}$He	14.320	CF88	15	^{11}B $(d,n)^{12}$C	13.732	SA67
7	^{6}Li $(d,p)^{7}$Li	5.025	TS93	16	^{14}C $(d,n)^{15}$N	7.983	TS93
8	^{6}Li $(d,n)^{7}$Be	3.381	TS93	17	^{12}N $(n,d)^{11}$C	1.624	TS93(E)
9	^{7}Li $(t,n)^{9}$Be	10.438	TS93				

Table A.8. The other reactions.

	reaction	Q(MeV)	Ref.		reaction	Q(MeV)	Ref.
1	^{1}H$(pn,p)^{2}$H	2.225	CF88	10	^{7}Be$(d,p\alpha)^{4}$He	16.766	CF88
2	^{3}H$(t,nn)^{4}$He	11.332	CF88	11	^{9}Be$(p,d\alpha)^{4}$He	0.651	CF88
3	^{3}He$(^{3}$He$,pp)^{4}$He	12.860	CF88	12	^{11}B$(p,\alpha\alpha)^{4}$He	8.682	CF88
4	^{4}He$(nn,\gamma)^{6}$He	0.975	CF88	13	^{11}C$(n,\alpha\alpha)^{4}$He	11.447	WA69
5	^{4}He$(pn,\gamma)^{6}$Li	3.700	CF88	14	^{13}O$(\alpha,pp)^{15}$O	8.102	WK82
6	^{4}He$(n\alpha,\gamma)^{9}$Be	1.574	CF88	15	^{7}Li$(t,nn\alpha)^{4}$He	8.864	CF88
7	^{4}He$(\alpha\alpha,\gamma)^{12}$C	7.275	CF88	16	^{7}Be$(^{3}$He$,pp\alpha)^{4}$He	11.272	CF88
8	^{7}Li$(d,n\alpha)^{4}$He	15.121	CF88	17	^{12}C$(^{12}$C$,p)^{23}$Na	2.241	CF88
9	^{8}Li$(d,n\alpha)^{4}$He	15.313	TS93	18	^{12}C$(^{12}$C$,\alpha)^{20}$Ne	4.617	CF88

Table A.9. $\beta^{\pm}$-decays and electron captures.

	reaction	Q(MeV)	Ref.		reaction	Q(MeV)	Ref.
1	^{1}n$(\beta^-)^1$H	0.782	TS93	18	^{11}C$(\beta^+)^{11}$B	0.960	TS93
2	^{1}n$(\beta^-)^1$H **	0.782	WA73	19	^{14}C$(\beta^-)^{14}$N	0.157	AJ91
3	^{1}H$(\beta^+)^1$n ***	-1.804	WA73	20	^{15}C$(\beta^-)^{15}$N	9.772	AJ91
4	^{1}H$(e^- p, \nu_e)^2$H	1.442	CF88	21	^{16}C$(\beta^-)^{16}$N	8.012	TS93
5	^{1}H$(p, e^+\nu_e)^2$H	1.442	CF88	22	^{12}N$(\beta^+)^{12}$C	16.316	AJ90
6	^{3}H$(\beta^-)^3$He	0.0185	TS93	23	^{13}N$(\beta^+)^{13}$C	1.198	AJ91
7	^{3}He$(e^-, \nu_e)^3$H	-0.0185	CF88	24	^{16}N$(\beta^-)^{16}$O	10.419	TS93
8	^{3}He$(p, e^+\nu_e)^4$He	19.795	CF88	25	^{17}N$(\beta^-)^{17}$O	8.680	TS93
9	^{6}He$(\beta^-)^6$Li	3.508	TS93	26	^{13}O$(\beta^+)^{13}$N	16.743	WP89
10	^{8}Li$(\beta^-)2^4$He	16.095	TS93	27	^{14}O$(\beta^+)^{14}$N	4.121	TS93
11	^{9}Li$(\beta^-)^9$Be	13.606	TS93	28	15O$(\beta^+)^{15}$N	1.732	TS93
12	^{9}Li$(\beta^- n)2^4$He	12.033	TS93	29	^{19}O$(\beta^-)^{19}$F	4.820	AJ87
13	^{7}Be$(e^-, \nu\gamma)^7$Li	0.862	CF88	30	^{17}F$(\beta^+)^{17}$O	1.739	TS93
14	^{11}Be$(\beta^-)^{11}$B	11.506	TS93	31	^{18}F$(\beta^+)^{18}$O	0.634	TS93
15	^{8}B$(\beta^-)2^4$He	17.050	TS93	32	^{20}F$(\beta^-)^{20}$Ne	7.025	AJ87
16	^{12}B$(\beta^-)^{12}$C	13.369	TS93	33	^{18}Ne$(\beta^+)^{18}$F	3.424	WP89
17	^{9}C$(\beta^+ p)2^4$He	15.753	WP89	34	^{19}Ne$(\beta^+)^{19}$F	2.216	WP89

Table A.10. The ν-process reactions. In the table, superscripts * and † represent the ν-processes accompanied with subsequent β^-- and β^+-decays, respectively; e.g., $^{14}O(\nu,\nu' n)\,^{13}O(,e^+\nu_e)\,^{13}N$. Reaction type $(\nu,\nu'\cdot\cdot)$ includes six kinds of reactions, $(\nu_e,\nu'_e\cdot\cdot)$, $(\bar\nu_e,\bar\nu'_e\cdot\cdot)$, $(\nu_\mu,\nu'_\mu\cdot\cdot)$, $(\bar\nu_\mu,\bar\nu'_\mu\cdot\cdot)$, $(\nu_\tau,\nu'_\tau\cdot\cdot)$, and $(\bar\nu_\tau,\bar\nu'_\tau\cdot\cdot)$. Furthermore, reaction type "others" means $(\nu,\nu'\,^3He)$, $(\nu,\nu' n\alpha)$, $(\nu,\nu' p\alpha)$, $(\nu,\nu' p\,^3H)$, $(\nu,\nu' n\,^3He)$, and $(\nu,\nu'\alpha\alpha)$.

<table>
<tr><th>reaction type</th><th colspan="3">target nucleus</th></tr>
<tr><td>(ν_e,e^-)</td><td colspan="3">^{12}C, ^{13}C, ^{14}C, ^{14}N, ^{15}N, ^{18}O, ^{18}F, ^{19}F, ^{20}F</td></tr>
<tr><td>$(\bar\nu_e,e^+)$</td><td colspan="3">^{1}H, ^{12}N, ^{13}N, ^{14}N, ^{14}O, ^{15}O, ^{17}F, ^{18}F, ^{18}Ne, ^{19}Ne, ^{20}Ne</td></tr>
<tr><td>(ν_e,e^-p)</td><td colspan="2">^{13}C, ^{14}C, $^{14}O^\dagger$, ^{17}O, ^{18}O, ^{20}F, $^{18}Ne^\dagger$, ^{19}Ne, ^{22}Ne, $^{23}Na^\dagger$</td><td rowspan="2">^{4}He, ^{12}C, ^{13}N, ^{14}N, ^{15}N, ^{15}O, ^{16}O, ^{18}F, ^{19}F, ^{20}Ne, ^{21}Ne</td></tr>
<tr><td>$(\bar\nu_e,e^+n)$</td><td colspan="2">^{12}N, $^{13}C^*$, $^{14}C^*$, ^{14}O, $^{17}O^*$, $^{18}O^*$, ^{17}F, $^{20}F^*$, ^{18}Ne, $^{22}Ne^*$, ^{23}Na</td></tr>
<tr><td>(ν_e,e^-n)</td><td colspan="3">^{14}C, ^{18}O</td></tr>
<tr><td>$(\bar\nu_e,e^+p)$</td><td colspan="3">^{14}O, ^{15}O, $^{16}O^*$, ^{18}Ne, ^{19}Ne</td></tr>
<tr><td>(ν_e,e^-pp)</td><td colspan="3">$^{12}N^\dagger$, ^{17}F</td></tr>
<tr><td>$(\nu,\nu' n)$</td><td>^{4}He, ^{12}C, ^{13}N, $^{14}O^\dagger$, ^{20}F, $^{18}Ne^\dagger$, ^{20}Ne, $^{23}Na^\dagger$</td><td rowspan="2">^{13}C, ^{14}C, ^{17}O, ^{18}O, ^{22}Ne</td><td rowspan="3">^{14}N, ^{15}N, ^{15}O, ^{16}O, ^{18}F, ^{19}F, ^{19}Ne, ^{21}Ne</td></tr>
<tr><td>$(\nu,\nu'\alpha)$</td><td>^{12}N, $^{14}O^\dagger$, ^{17}F, $^{20}F^*$, ^{18}Ne, ^{23}Na</td></tr>
<tr><td>$(\nu,\nu' p)$</td><td colspan="2">^{4}He, ^{12}C, $^{13}C^*$, $^{14}C^*$, $^{12}N^*$, ^{13}N, ^{14}O, $^{17}O^*$, $^{18}O^*$, ^{17}F, $^{20}F^*$, ^{18}Ne, ^{20}Ne, $^{22}Ne^*$, ^{23}Na</td></tr>
<tr><td>$(\nu,\nu' pn)$</td><td colspan="3">^{12}C, ^{12}N, ^{17}F</td></tr>
<tr><td>$(\nu,\nu' pp\alpha)$</td><td colspan="3">^{13}N</td></tr>
<tr><td>others</td><td colspan="3">^{12}C</td></tr>
</table>